CORA Cork Open Research Archive
Cartlann Taighde Oscailte Chorcaí

Title	A multifunctional platform for the rapid prototyping of polymeric microneedle devices
Authors	Bocchino, Andrea
Publication date	2025
Original Citation	Bocchino, A. 2025. A multifunctional platform for the rapid prototyping of polymeric microneedle devices. PhD Thesis, University College Cork.
Type of publication	Doctoral thesis
Link to publisher's version	https://zenodo.org/records/15835760
Rights	© 2025, Andrea Bocchino. - https://creativecommons.org/licenses/by/4.0/
Download date	2026-11-17 12:33:46
Item downloaded from	https://hdl.handle.net/10468/17939

UCC
University College Cork, Ireland
Coláiste na hOllscoile Corcaigh

Ollscoil na hÉireann, Corcaigh
National University of Ireland, Cork

A Multifunctional Platform for the Rapid Prototyping of Polymeric Microneedle Devices

Thesis presented by

Andrea Bocchino

for the degree of

Doctor of Philosophy

University College Cork

Tyndall National Institute

Supervisor(s): Dr. Conor O'Mahony, Dr. Paul Galvin

2025

Declaration

This is to certify that the work I am submitting is my own and has not been submitted for another degree, either at University College Cork or elsewhere. All external references and sources are clearly acknowledged and identified within the contents. I have read and understand the regulations of University College Cork concerning plagiarism and intellectual property.

_____

Andrea Bocchino

April 23rd 2025

Foreword

This work has emanated from research conducted with the financial support of the European Union's Horizon 2020 Research and Innovation Programme under grant #825549 (ELSAH project); the Government of Ireland through the Disruptive Technologies Innovation Fund (DT2018 0291-A, HOLISTICS); Research Ireland through the Insight Centre for Data Analytics (SFI/12/RC/2289-P2); Enterprise Ireland under the Commercialisation Fund (CF/2012/2339); the Higher Education Authority under the Programme for Research in Third-Level Institutions; and the European Regional Development Fund.

Abstract

Microneedle (MNs) technology has huge appeal for several biomedical applications. The ability to painlessly penetrate the *stratum corneum*, the uppermost layer of the skin, interfacing with the interstitial fluid (ISF) without drawing any blood, is extremely valuable. Especially when this is coupled with bypassing problems such as rejection of the technology due to needle phobia or need to have trained healthcare personnel for correct application.

MNs can be produced with different materials. Among them, polymer microneedles are becoming more and more predominant due to their low cost and the multitude of different and appealing properties they possess.

However, because of this multitude of properties, many different polymers are used to fabricate MNs. The high variety led to the development of various fabrication processes, which can be difficult to replicate or may require expensive machinery or tools. Moreover, different MN arrays may need additional layers, such as metallization or passivation. Both have little to no dedicated characterization and would further increase the complexity of the manufacturing procedure. Research on polymer MNs can therefore be slow, especially if trying to shift the focus from one application to another. Having a tool able to produce microneedles with different properties using a single process, easily tailorable towards different use cases, would be incredibly valuable to speed up research, potentially bringing new devices to the market.

In this thesis, a platform for the rapid prototyping of polymer MNs is designed, developed and characterised. This platform, based on a core replica moulding process, represents a major advance in the development of a multifunctional process for the laboratory-scale production of microneedles, allowing for easy merging of different polymers and

commercially available substrates together with various functionalities, features and customisable properties. This provides a tool that could drastically speed up MN device research and development. To my knowledge, this is the first platform which enables the merging of several degradable, swellable, and medical polymers with fabric, flexible substrates, and metals. Different metallization and passivation techniques are analysed and compared, providing insights on what is preferrable to use in different applications and how to more efficiently implement it. In fact, although both procedures are commonly used on MN arrays, there is a scarcity of proper characterization tailored specifically towards their implementation on MN devices. The value and usability of the platform has then been demonstrated by several examples focussing on drug delivery, biopotential capturing, and continuous biomarkers monitoring.

Scope of Thesis

The scope of this thesis is to design, characterize, and demonstrate applications of this platform, validating its capabilities and establishing its value for microneedles production and customization. The thesis is divided into Chapters, the first one focussing on introducing MNs technology, the problems this work is tackling, and the novelties which were introduced by it. Subsequently, different journal papers are used as individual Chapters to either describe specific aspects of the platform in detail, or to demonstrate novel medical applications that the technology was used in.

In Chapter 1, an overview of microneedles (MNs) technology together with a review of MN implementations for medical applications is given. Following this review, gaps in the current state of the art were identified, highlighting the need for a multifunctional and versatile process for the production of MN devices. This stemmed majorly from the fact that different applications may require different materials and functionalities, generating numerous fabrication methods, that are at times hyper-specific and difficult to replicate. The main objective of the thesis was stated: the development of a platform able to rapidly prototype MN devices for medical applications, allowing for full customisation of the produced devices. The different modules needed by the platform were then identified and individually presented. Fabrication processes, metallization techniques and passivation methods were introduced, justifying which one were used within the platform. Finally, the key novelties were emphasised, highlighting the challenges that were overcome by this work.

In Chapter 2, the platform developed within this work is presented in detail. The core aspects, and all the different modules the platform is comprised of, are shown. In addition, exemplars demonstrating novel applications of MN devices fabricated with the platform are introduced. Chapter 2 was published as "A Multifunctional Platform for the Production and Customization of Polymer-based Microneedle Devices" in *Sensors and Actuators A: Physical*. This is a multidisciplinary journal covering sensors and transducers research, and ranked in the 88th percentile in its field.

Chapter 3 is focussed on a specific module of the platform, which is one of the main contributions of the thesis: passivation methods for MN-based devices. Within this Chapter, several passivation methods are developed and characterised. The different layers are compared, and the strengths and weaknesses of each passivation option are assessed. Chapter 3 was published as "Strategies for Passivating Microneedle-based Sensors: Development, Characterization and Comparison" in *Sensors and Actuators Reports*. This is a multidisciplinary journal covering sensors and transducers research and ranked in the 93rd percentile in its field.

Chapter 4 provides an initial example of how MNs can be utilized for transdermal delivery. The paper was mainly focused on the transition from laboratory to industrial level production for certain aspects of the platform. Specifically, a coating mechanism for MN arrays was presented, and injection moulding was used to fabricate the needles, hence proving the scalability of a moulding process. This work also served to validate the skin model and the protocol used for MN testing within this thesis. Chapter 4 was published as "Piezoelectric Inkjet Coating of Injection Moulded, Reservoir-Tipped Microneedle

Arrays for Transdermal Delivery" in *Journal of Micromechanics and Microengineering*. This leading journal covering all aspects of nano- and microelectromechanical systems is ranked in the 69th percentile in its field.

In Chapter 5, a second exemplar for transdermal delivery is presented. The platform is used to replicate micro-patterned bio-inspired MNs. This paper served not only to prove that the core production process of the platform could replicate complex 3D printed structures, but also to demonstrate that the moulded needles were able to pierce the skin without sustaining any damage. Chapter 5 was published as "Bio-inspired microneedle design for efficient drug/vaccine coating" in *Biomedical Microdevices*. This journal focuses on diagnostic and therapeutic applications of micro-electro-mechanical systems, microfabrication, and nanotechnology and it is ranked in the 69th percentile in its field.

In Chapter 6, the platform is used to fabricate novel fabric-backed MN electrodes. These electrodes were tested for ECG recording, and compared to standard gel-based technology. This exemplar is a step up in complexity from the needles presented in the previous Chapter, and validates the ability of the platform to merge polymers with commercially available materials and films (in this case, conductive fabric). Chapter 6 was published as "Flexible, Conductive Fabric-Backed, Microneedle Electrodes for Electrophysiological Monitoring" in *Advanced Materials Technologies*. This is a multidisciplinary journal that straddles materials science, innovative technologies, and real-world applications, and ranked in the 92nd percentile in its field.

A final example is given in Chapter 7. Here, multi-electrode MN arrays were functionalised and used to detect lactate. These arrays were produced by combining many of the different modules of the platform including moulding, metallisation, passivation and system integration, thereby showcasing its full capabilities. More specifically, different electrodes were precisely patterned on each array using an optimised metallization process. They were then passivated and functionalised for lactate detection. This is the most complex array to date fabricated with the platform. Chapter 7 was published as "Detection of Lactate via Amperometric Sensors Modified With Direct Electron Transfer Enzyme Containing PEDOT:PSS and Hydrogel Inks" in *IEEE Sensors Letters*. This journal, covering different aspects of sensors and integrated sensor-actuators, it is ranked in the 52nd percentile in its field.

Finally, Chapter 8 summarises the key results achieved in this thesis, together with a reflection on the remaining issues, and some recommendations for potential future work. This work would further improve the platform, advancing MN technology and helping potential mass adoption.

A number of Appendices summarise the publications associated with this work, along with details of patent filings and awards received.

Acknowledgements

Per prima cosa, vorrei ringraziare la mia famiglia che, con i suoi sforzi, mi ha regalato la possibilita' di arrivare in Irlanda ormai 10 anni fa. Voglio che sappiate che la cosa piu' difficile che abbia dovuto affrontare in questi anni non e' stato il lavoro, il dottorato, le giornate super impegnate, e neanche il tempo grigio e piovoso. E' stato il fatto che fossi distante da voi! Ora che questo capitolo finisce per uno nuovo, vi prometto che faro' di tutto per far si che questo sacrificio non sia stato in vano. Premero' il piede sull'acceleratore non solo per assicurare il futuro sia mio che della famiglia che voglio formare, ma anche per rendervi orgogliosi di me e per potervi riabbracciare il prima possibile. Voglio godere al massimo dei momenti che passeremo insieme, delle cose che faremo, e, piu' semplicemente, di poter condividere la mia vita con voi.

Vorrei poi ringraziare la mia Vaninha, che, soprattutto da quando viviamo insieme, mi e' sempe stata vicina, ed ha fatto del suo meglio per cercare di aiutarmi come poteva. Accettando (senza farmelo pesare) che non avessi tutto il tempo che avresti voluto per fare cose insieme, occupandoti della casa quando dovevo lavorare piu' del dovuto, e regalandomi un sorriso radioso tutte le mattine che ti svegliavi al mio fianco. Con i fatti (e non con vuote parole) mi hai dimostrato che, quasi un anno fa, quando ti avevo chiesto se volessi venire a vivere con me, non solo avessi fatto la scelta giusta, ma che fossi anche stato molto fortunato a sentirmi rispondere "Si"!

Ho incontrato un sacco di persone speciali che mi hanno accompagnato durante questi anni e, quindi, non potrei nominarvi tutti senza scrivere un poema (ed una tesi e' gia' piu' che sufficiente). Per questo, spero che possano perdonarmi se saro' un po' piu' breve. Ringrazio tutti gli amici, sia a lavoro che non, per le risate, gli allenamenti, l'ascoltare

tutti i miei (molti) sfoghi, e per prendermi in giro quando servisse, alleggerendo le mie giornate.

Un ricordo nostalgico va anche alla Ghettohouse ed a tutti i fratelli/sorelle che ci hanno vissuto con me: la famiglia acquisita che portero' sempre nel cuore. Abbiamo vissuto da Peter Pan per quanto possibile, senza voler crescere, ma, alla fine, abbiamo spiccato tutti il volo.

Vorrei anche ringraziare il mio supervisor, Conor O'Mahony, per le possibilita' che mi ha dato, per esserci sempre stato quando serviva, e per non avermi insultato quando gli mandavo email e messaggi alle ore piu' improponibili del giorno. Infine, un ringraziamento anche a Paul Galvin, per avermi supportato e co-supevisionato durante questo viaggio.

A tutti voi, grazie mille!!!

First, I'd like to thank my family which, with their efforts, gifted me the chance to arrive to Ireland, almost 10 years ago. I want you to know that the hardest thing I had to face these years was not related to work, or the PhD, or the super busy days, or not even to the grey and rainy days. It was the fact that I was away from you! Now that this chapter is over, and a new one is about to start, I promise you I will do all in my power to ensure this sacrifice was not in vain. I will push on the gas pedal not only to secure my future and the future of the family I want to build, but also to both make you proud, and to be able to hug you as soon as possible. I want to enjoy as much as I can all the moments we will spend together, all the things we will do and, simply, be able to share my life with you.

I would then like to thank my Vaninha, who, especially since we started living together, always stayed by my side, doing her best to help me however she could. You accepted (without complaining) that I could not share with you all the time you would have loved me to, you took care of the house whenever I was busier than usual and had to work overtime, and you blessed me with a beautiful smile every morning you woke up by my side. With your actions (rather than empty words) you demonstrated to me that, almost a year ago, when I asked you to move in with me, not only I made the right choice, but that I was also super lucky you answered “Yes”!

I have met a lot of special people that walked with me during these years, and because of this, I can’t name you all without writing a poem (and a thesis is already enough). Therefore, I hope you will forgive me if I cut it a bit shorter here. I thank all my friends, both from work and outside work, for all the laughs, for all the training sessions, for listening to my (many) rants, and taking the piss whenever needed, which all made my days a lot lighter.

A nostalgic thought also goes to the Ghettohouse, and to all the brothers/sisters who shared those walls with me: my acquired family that I will always cherish within my heart. We lived like Peter Pans as long as we could, refusing to grow up, but in the end, we all started flying with our own wings.

I would love to thank my supervisor, Conor O’Mahony, for the opportunities he offered me, for being there whenever needed, and for not insulting me whenever I was emailing/messaging him at the most inconvenient times of the day. Finally, I also want to thank Paul Galvin, for all the support and for co-supervising me during this journey.

To all of you, my deepest Thank You!!!

Abbreviations and Acronyms

2D	Two Dimensional
2PP	Two-Photon Polymerization
3D	Three Dimensional
AA	Additional Area
A_b	Base area
A_{ex}	Additional exposed area
A_l	Lateral surface area
A_{pp}^{noise}	Peak-to-peak ADC counts of noise in the isoelectric region
A_{pp}^{signal}	Peak-to-peak ADC counts of QRS wave
AC	Alternating Current
Ag	Silver
AgCl	Silver Chloride
AIT	Austrian Institute of Technology
Au	Gold
AuZn	Gold-Zinc alloy
BMF	Boston Micro Fabrication
BSA	Bovine Serum Albumin
C	Bulk concentration of analyte
°C	Celsius (degree)
C	Capacitor
CAD	Computer-Aided Design
cc	Cubic centimetres
CD	Compact Disc
CE	Counter Electrode

CF	Conductive Fabric
CF-MN	Conductive Fabric Microneedle
Cl	Chlorine
cm	Centimetre
CMC	Carboxymethylcellulose
CMRF	Curable Magnetorheological Fluid
COC	Cyclic Olefin Copolymer
COP	Cyclic Olefin Polymer
cPs	Centipoise
Cr	Chrome/Chromium
CREC	Clinical Research Ethics Committee
CV	Cyclic Voltammetry
CVD	Chemical Vapour Deposition
D	Diffusion coefficient of oxidised analyte
dB	Decibel
DC	Direct Current
DEGVE	Diethyleneglycol vinylether
DET	Direct Electron Transfer
DLP	Digital Light Processing
DMA	Dimethacrylate
DMN	Dissolvable Microneedle
DVD	Digital Versatile Disc
σ	Empirical standard deviation
ΔI	Total current
E	Epidermis
ECG	Electrocardiogram

EDM	Electrically Discharged Machined
EEG	Electroencephalogram
EMG	Electromyography
EOG	Electrooculography
ESA	Electrochemical Surface Area
ESI	Electrode-Skin Impedance
ET	Exposure Time
EU	Europe
FcCOOH	Ferrocenemonocarboxylic Acid
FDM	Fused Deposition Modeling
FITC	Fluorescein Isothiocyanate
FPL	Flexor Pollicis Longus
fs	Femtosecond
g	Gram
GS	Glass Substrate
Gy	Gray
h	Height
H	Height
h	Hour
H_2O	Water
H_2O_2	Hydrogen Peroxide
HPLC	High Performance Liquid Chromatography
Hz	Hertz
I_p^{ox}	Oxidation peak current
I_p^{red}	Reduction peak current
ISA	Ideal Surface Area

ISF	Interstitial Fluid
ISO	International Organization for Standardization
J	Joule
JKU	Johannes Kepler University Linz
JPG	Joint Photographic Experts Group (or JPEG)
kSQI	Kurtosis as signal quality index
kDa	Kilodalton
kg	Kilogram
kGy	Kilo-Gray
km	Kilometre
kΩ	Kiloohm
KOH	Potassium Hydroxide
l	Slant height
l	Liter
LAP	Lithium-phenyl-2,4,6-trimethylbenzoyl-phosphinate
LDW	Laser-Direct Writing
LOD	Limit Of Detection
LPCVD	Low-Pressure Chemical Vapour Deposition
LR	Lower Region
MNs	Number of microneedles on array
MeHA	Methacrylated Hyaluronic Acid
mg	Milligram
min	Minute
ml	Millilitre
mL	Millilitre
mm	Millimetre

mM	Millimolar
MN	Microneedle
MRDL	Magnetorheological Drawing Lithography
mTorr	Millitorr
MTS	Microstructured Transdermal System
mV	Millivolt
mW	Milliwatt
MWCNT	Multi-Walled Carbon Nanotubes
μ_x	Empirical mean of x
µA	Microampere
µl	Microlitre
µm	Micrometre
µs	Microsecond
µSL	Microstereolithography
µSLA	Microstereolithography
n	Number of electrons (Chapter 3)
n	Number (Chapter 7)
n	Number
N	Newton
nA	Nanoampere
NFC	Near Field Communication
ng	Nanogram
NH_4Cl	Ammonium Chloride
Ni	Nickel
nm	Nanometre
nl	Nanolitre

Ω	Ohm
OCT	Optical Coherence Tomography
p	P-value
PB	Phosphate Buffer
PBS	Phosphate Buffered Saline
PCB	Printed Circuit Board
PCL	Polycaprolactone
PDMS	Polydimethylsiloxane
PECVD	Plasma-Enhanced Chemical Vapour Deposition
PEDOT:PSS	Poly(3,4-ethylenedioxythiophene) polystyrene sulfonate
PEG	Polyethylene Glycol
PEG-DMA	Poly(ethylene glycol) dimethacrylate
PET	Polyethylene Terephthalate
PI	Polyimide
pL	Picolitre
pl	Picolitre
PLA	Polylactic Acid
PLGA	Poly Lactic-co-Glycolic Acid
PMMA	Polymethyl Methacrylate
PMVE/MA	Poly(methyl vinyl ether-alt-maleic anhydride) – with Gantrez S-97
PMVE/MAH	Poly(methyl vinyl ether-alt-maleic anhydride) – with Gantrez AN-139
PRINT	Particle Replication In Non-wetting Templates
Ps	Poise
PSA	Pressure-Sensitive Adhesive
Pt	Platinum
PTFE	Polytetrafluoroethylene

PVA	Polyvinyl Alcohol
PVC	Polyvinyl Chloride
PVD	Physical Vapour Deposition
PVP	Polyvinylpyrrolidone
r	Radius (Chapter 3)
r	Pearsons' correlation coefficient (Chapter 6)
RMS_{noise}	Root mean square of noise region
RMS_{signal}	Root mean square of signal
R	Resistor
RE	Reference Electrode
RMS	Root Mean Square
ROI	Region Of Interest
rpm	Revolutions per minute
RWM	Round Window Membrane
s	Second
SAM	Self-Assembly Monolayer
SC	Stratum Corneum
SD	Standard Deviation
SE	Skin-Electrode
SEM	Scanning Electron Microscope
SiO_2	Silicon Oxide
SLA	Stereolithography
SNR	Signal-to-Noise Ratio
sps	Samples per second
sq	Square
SUC	Sucrose

T	Thickness (Chapter 3)
TDDS	Transdermal Drug Delivery Systems
Ti	Titanium
TPP	Two-Photon Polymerization
TPU	Thermoplastic Polyurethane
TRA	Trehalose Anhydrous
TSA	Theoretically exposed Surface Area
UHF	Ultra-High Frequency
USP	United States Pharmacopeia
UV	Ultraviolet
v	Scan rate
v	Volume
V	Volt
VMC	Vertical Machining Centers
vol	Volume
VT	Vacuum Table
w	Weight
W	Watt
WE	Working Electrode
wt%	Weight percent

To my family

Table of Contents

Chapter 1 **31**

Introduction **31**

1.1 Skin 31

1.2 Microneedles 32

1.2.1 Fabrication methods 40

1.2.2 Additional modules 45

1.3 Thesis organization 50

1.4 Key novelties 52

1.5 References 53

Chapter 2 **67**

A Multifunctional Platform for the Production and Customization of Polymer-based Microneedle Devices **67**

2.1 Abstract 70

2.2 Introduction 70

2.3 Platform Design 75

2.3.1 Micromoulding Process 77

2.3.2 Geometry 81

2.3.3 Metallization 85

2.3.4 Materials 91

2.3.5 Passivation and Coating 94

2.4 Exemplars 95

2.4.1 ELSAH Biosensor 95

2.4.2 Fabric-based ECG Electrodes 100

2.4.3 Transdermal Delivery 102

2.5 Conclusions 106

2.6 Supplementary Material 106
2.7 References 107
Chapter 3 ..... **120**
Strategies for Passivating Microneedles-based Sensors: Development, Characterization and Comparison **120**
3.1 Abstract 123
3.2 Introduction 124
3.3 Materials and Methods 130
3.3.1 Microneedle Array Production 130
3.3.2 Microneedle Array Passivation 132
3.3.3 Microneedle Testing 136
3.4 Results 138
3.5 Discussion and Conclusions 156
3.6 Supplementary Material 159
3.7 References 159
Chapter 4 ..... **169**
Piezoelectric inkjet coating of injection moulded, reservoir-tipped microneedle arrays for transdermal delivery **169**
4.1 Abstract 171
4.2 Introduction 171
4.2.1 Low-cost transdermal drug delivery (TDD) device 172
4.3 Experimental details 175
4.3.1 Microneedle master – design and fabrication 175
4.3.2 Injection moulding 177
4.3.3 Piezoelectric dispensing 178
4.3.4 Skin preparation and array applications 179

4.3.5 Inspection and classification 180
4.4 Results and discussion 181
4.4.1 Microneedle fabrication using µSL and injection moulding 181
4.4.2 Filling of needle reservoir 183
4.4.3 Skin penetration and delivery 183
4.4.4 Reliability 188
4.5 Conclusion 188
4.6 References 189
Chapter 5 **..... 197**
Bio-inspired microneedle design for efficient drug/vaccine coating 197
5.1 Abstract 199
5.2 Introduction 199
5.3 Materials and methods 203
5.3.1 Computer aided design 203
5.3.2 Two-photon lithography setups 205
5.3.3 Photoresists 206
5.3.4 Wetting tests and fluorescence microscopy imaging 206
5.3.5 Replication 207
5.3.6 Skin penetration 208
5.4 Results and discussion 209
5.5 Conclusion 218
5.6 Supplementary Material 219
5.7 References 219
Chapter 6 **..... 227**
Flexible, Conductive Fabric-Backed, Microneedle Electrodes for Electrophysiological Monitoring 227

6.1 Abstract 229
6.2 Introduction 229
6.3 Experimental Section 233
6.3.1 Mechanical Characterization 233
6.3.2 Skin Insertion Test 234
6.3.3 *In Vivo* Electrode-Skin Impedance Characteristics 234
6.3.4 Skin Compatibility Test 235
6.3.5 ECG Recording: Hardware and Signal Analysis 235
6.3.6 EMG Recording: Hardware and Signal Analysis 237
6.3.7 Electrode Construction 238
6.4 Results and Discussion 241
6.4.1 Materials, Structural, and Fabrication Approach 241
6.4.2 Mechanical Characterization 243
6.4.3 Skin Insertion Test 245
6.4.4 Electrical Characterization 246
6.4.5 Electrophysiological Signal Measurement 249
6.5 Conclusion 257
6.6 Supplementary Material 258
6.7 References 258
Chapter 7 **..... 267**
Detection of Lactate via Amperometric Sensors Modified With Direct Electron Transfer Enzyme Containing PEDOT:PSS and Hydrogel Inks 267
7.1 Abstract 269
7.2 Introduction 270
7.3 Materials and Methods 271
7.3.1 Materials 271

7.3.2 Sensors 271
7.3.3 Ink Preparation 272
7.3.4 Sensor Preparation 273
7.3.5 Electrochemical Lactate Measurement 274
7.4 Results 275
7.4.1 Screen-Printed Sensors: Ink Formulation and Optimization 275
7.4.2 Measurement of Lactate in Blood 277
7.4.3 Microneedle Sensor Modification 277
7.4.4 *In Vitro* Measurements of the Locally Functionalized 279
7.5 Conclusions 280
7.6 References 280
Chapter 8 ..... **283**
Conclusions & Future Work **283**
8.1 Summary of key contributions 283
8.2 Critical review and future work 287
8.3 Conclusion 293
8.4 References 294
Appendices **297**
A.1 Journal Papers 299
A.2 Reviewed Conferences (Oral Presentation) 319
A.3 Invention Disclosure Forms 321
A.4 Patents and Licenses 321
A.5 Awards 322
A.6 Posters (Oral Presentation) 323
A.7 Posters before PhD (Oral Presentation) 326

Chapter 1

Introduction

1.1 Skin

The skin is the largest organ of the human body, and the first line of defence against foreign bodies, ultraviolet (UV) light and pathogens [1]. The skin is organised into three main layers: the hypodermis, the dermis and the epidermis. The hypodermis and dermis are the deepest layers and are rich in blood vessels, neurons, interstitial fluid (ISF) and hair follicles. Above the dermis sits the epidermis, which is composed of five sub-layers, namely the *stratum basale* (basement membrane in Figure 1), *spinosum*, *granulosum*, *lucidum* and *corneum* (Figure 1).

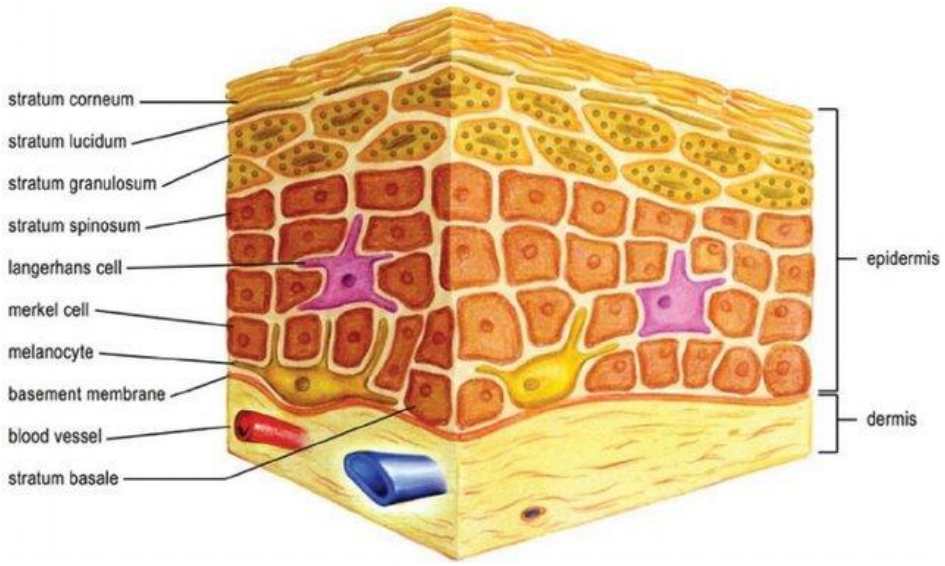


Figure 1. Skin cross section. Reproduced with permission from [2]. Copyright 2007 Taylor & Francis.

Of these strata, the initial four constitutes the viable epidermis while the *stratum corneum* (SC) is in direct contact with the external environment and is the main barrier of the body. This barrier is composed of 20 to 30 layers of dead keratinocytes, called corneocytes, and has a high electrical impedance ($> 10^5$ Ω). Because it is made up of brick-like cells, with no nucleus and cytoplasmic organelles, embedded in a dense lipid matrix, it prevents the passive delivery of all but a few compounds to the body [1], [3], [4]. Because of this, only substances with low molecular weight, lipophilicity, and high potency may be delivered across the SC barrier, therefore requiring low doses to be effective. These drugs include, for example, nicotine, rivastigmine, fentanyl, and some hormones – all delivered using patches. Conversely, ionised, hydrophilic, and hydro-soluble compounds are rarely formulated for percutaneous absorption [4].

1.2 Microneedles

Over the last few decades, microneedles (MNs) have attracted more and more interest because they offer a painless, convenient and easy to apply means to bypass the SC, reaching the viable epidermis and the uppermost part of the dermis [5]. Thanks to this, MNs are widely investigated for several medical applications such as transdermal drug and vaccine delivery, electrochemical sensing and biopotential monitoring [6], [7].

Depending on their working principle, microneedles are generally divided into five categories: solid, coated, dissolving, hollow and hydrogel-forming MNs [8].

Solid MNs are the simplest type of needles: they are used to pierce the skin, creating micro-holes, and they are subsequently removed. This stimulates collagen and elastin expression, improving skin appearance [9]. Alternatively, these channels can be exploited to improve the permeability of the skin, making topical application viable for large molecules [5]. If solid MNs are formed using metals or electrically conductive materials,

they can also be left embedded in the skin and used as electrodes for recording electrophysiological signals [10].

Coated needles are usually solid MNs which are covered with at least one layer of a different material. Depending on the coating, these MNs can be used for different applications. The simplest coating is a metal layer, generally used to make a needle array conductive. Metallized MNs, similarly to electrically conductive solid needles, could serve as electrodes for biopotential capturing [11]. A drug could also be trapped within a degradable coating and be deposited on the needles for transdermal delivery [12]. Finally, the surface of a MN could be functionalised to serve as an electrochemical device, detecting biomarkers or specific medications, pH, or antibodies within the ISF [13].

Dissolving MNs are solid needles that, when in contact with the ISF, start degrading and releasing whatever compound is trapped within the body of the needles inside the skin [14]. These are generally implemented for drug delivery applications.

Hollow microneedles are solid needles designed with a narrow bore exiting close to or at the needle tip, similarly to a conventional needle.

Finally, hydrogel-forming MNs are composed by a hydrophilic polymer which, when in contact with specific environmental conditions, can swell [15].

Both hollow and hydrogel-forming needles are used for two main applications: either to release a drug below the SC or to extract/absorb ISF from the surrounding environment for diagnostic purposes [15], [16].

A representation of the different types of microneedles, focussing on their use for transdermal delivery, is depicted in Figure 2.

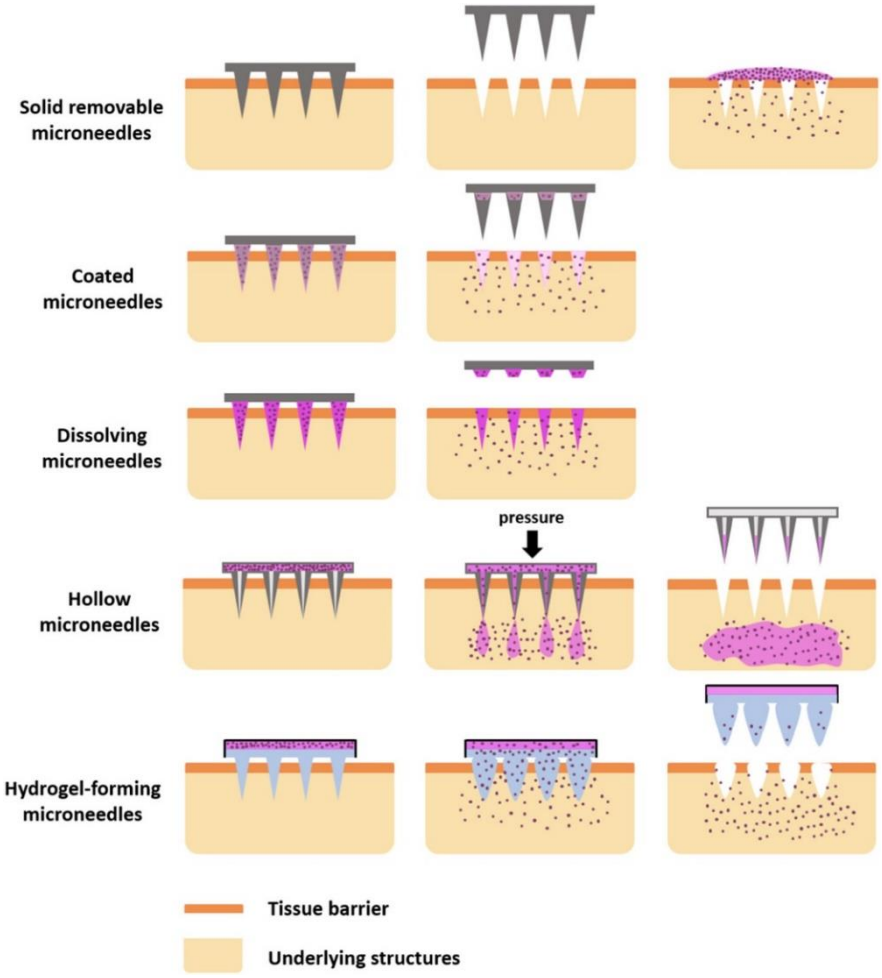


Figure 2. Different type of microneedles. Adapted with permission from [8]. Copyright 2018 Elsevier.

MNs are produced using a wide range of materials, including polymers, hydrogels, sugars, metals, silicon, ceramics, and silk [17], [18]. Examples of different microneedles, showing how diverse they can appear, are reported in Figure 3.

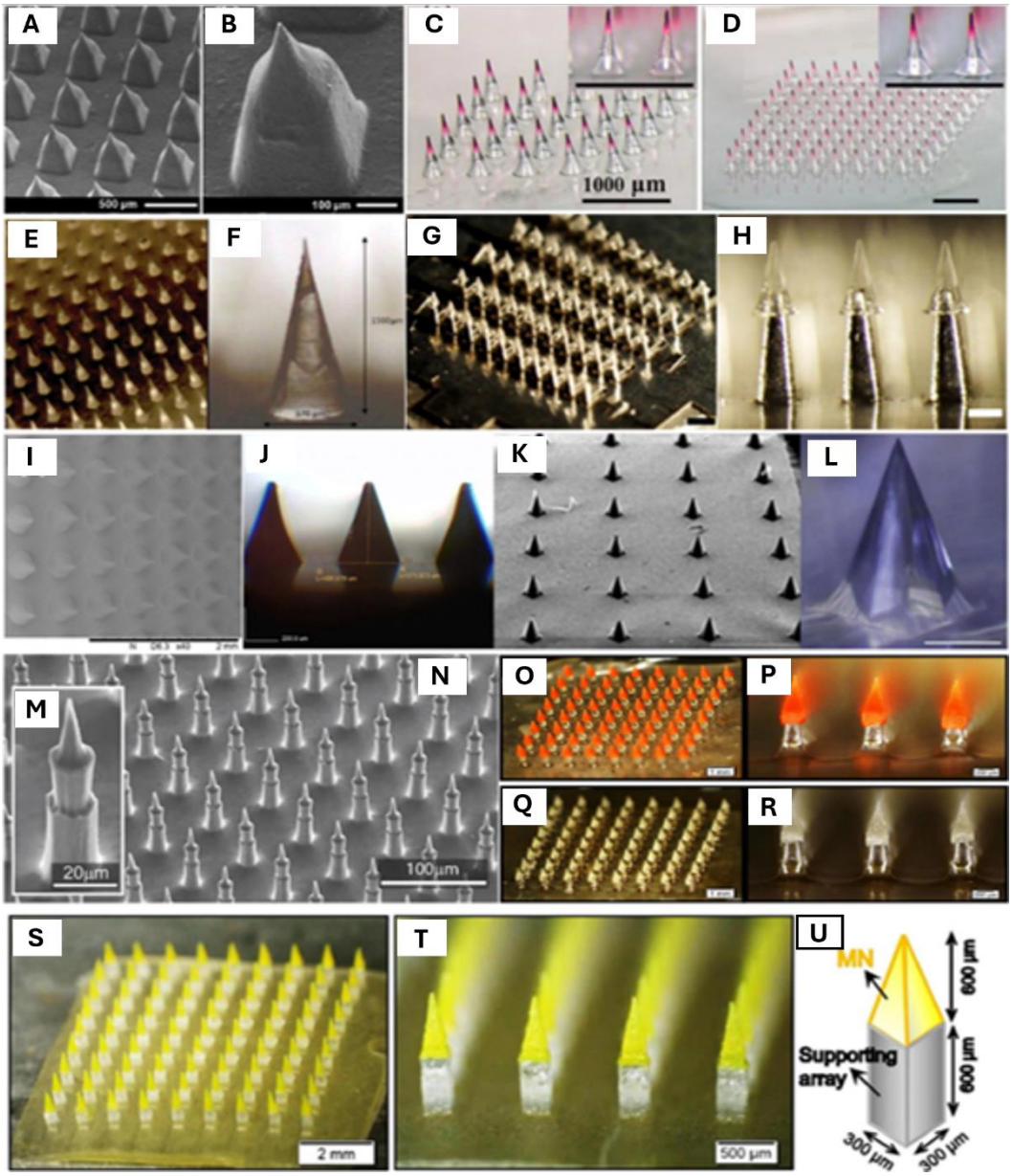


Figure 3. Various type of MNs made using different materials and techniques. Specifically, drawing lithography of maltose (A, B), sodium carboxymethylcellulose (CMC) produced with TheraJect's VaxMat technology (E, F), casting of polysaccharide in aluminium mould (I, J), casting of CMC in polydimethylsiloxane (PDMS) mould (M, N), moulded chitosan MNs on a polyvinyl alcohol/polyvinyl pyrrolidone (PVA/PVP) support (S, T, U), bubble and traditional (C and D respectively) PVA/sucrose MNs casted in engraved PDMS moulds, metal shafts capped with PVA/sucrose arrowheads (G, H), sugar glass formed by vacuum deposition (K, L), and chitosan MNs on polylactic acid

(PLA) support loaded with different compounds (O, P, Q, R). B, F, H, J, L, M, P, R, T are magnifications of A, F, G, I, K, N, O, Q, S respectively. C and D have their own magnification in the top right corner. U is a drawing describing the geometry of the needles shown in S and T. Adapted with permission from [19]. Copyright 2019 Springer Nature.

Due to the large number of possible materials, fabrication techniques span from moulding to lithography, from additive manufacturing to etching, from laser ablation and micro-machining to milling and hot embossing [18].

Amongst these materials, polymers have grown more and more popular for MNs fabrication due to the wide range of properties they exhibit. Polymers can be medical grade, biodegradable, rigid, flexible, swellable, absorptive, conductive and 3D printable [20], [21] - all very desirable qualities for transdermal delivery and diagnostic purposes.

Examples of different uses of polymer microneedles, together with manufacturing methods and key features, are reported in Table 1.

Table 1. Summary of different polymer MNs used for different applications. The production process and the additional features/exhibited properties are also reported.

Production	Application	Materials	Features/notes
Moulding (PDMS - from etched Si master)	Monitoring (pH)	OrmoComp	Metallized (sputter), multi-electrodes [22]
Moulding (PDMS from acrylic machined master)	Biopotential recording (ECG/EMG)	1201AB-3 hard epoxy MNs + 607AB-5 soft epoxy back	Metallized, flexible back, multi-materials [23]
3D printing (stereolithography)	Drug delivery (anticancer therapy)	Unspecified biocompatible resin	Coated, biocompatible [24]
3D printing (FDM) + etching sharpening	Drug delivery	PLA	Coated, biodegradable, loaded [25]
Moulding (PDMS from steel MNs on PCB)	Biopotential recording (ECG/EMG/EOG)	Polyimide	Metallized (sputter), flexible [26]
Magnetorheological drawing lithography	Drug delivery	Epoxy-based curable magnetorheological fluid	Metallized, flexible, patterned [27]
Injection moulding	Monitoring (lactate)	Polycarbonate	Metallized, functionalised [28]
Magnetorheological drawing lithography	Biopotential recording (ECG/EMG/EEG)	Epoxy-based curable magnetorheological fluid	Flexible, metallized (sputter), patterned (LDW) [29]
Moulding (PDMS from steel master)	ISF extraction	Methacrylated acid	Swellable, loaded, sensor integration [30]
Centrifuge moulding	Drug delivery	PEG	Swellable [31]
Moulding (UV-curing in PDMS from EDM aluminium master)	Monitoring (glucose)	SU-8 50 photoresist	Metallized (conformal sputter), functionalised [32]
Moulding (spray deposition in PDMS)	Drug delivery (bi-phasic)	Layered PVP-PLGA	Biodegradable, loaded, implantable, multi-materials [33]
Moulding (centrifuge assisted)	Drug delivery (contraceptive)	PLA + PLGA	Biodegradable, implantable, loaded, bubbles, multi-materials [34]

Moulding (UV-polymerization in laser written PDMS)	Drug delivery (cosmetic)	PVP	Biodegradable, loaded [35]
Moulding (PVA from electroplated lithography-formed PMMA master)	Drug delivery	Poly Methyl Methacrylate (PMMA)	Hollow [36]
Injection moulding	Monitoring (antibiotic)	Polycarbonate	Metallized (e-beam), functionalised, passivated (deposition of varnish) [37]
Moulding (PDMS from parylene-coated PDMS master)	Biopotential recording	SU-8 photoresist	Biocompatible, metallized (vapour deposited), passivated (PVD on mould) [38]
Moulding (PDMS from silicon master)	Monitoring (glucose)	PMMA (NOA 68)	Metallized (thermal evaporation), passivated (spin-coating PMMA), functionalised [39]
Casting (silicon etched master)	Neural interfacing	Polyimide	Metallized (sputter), passivated (spin-coating polyimide), flexible [40]
Moulding (PDMS from silicon master)	Detection (lactate)	Epotek 353ND	Metallized (e-beam), functionalised, passivated (patterned medical tape) [41]
Vacuum casting (in silicone template)	Detection (pH)	Carbon loaded polystyrene	Loaded, functionalised, passivated (enamel coating), metallized (electrochemical deposition) [42]
Moulding (UV-curing in PDMS from PDMS master mould)	Detection (pH)	OrmoComp	Metallized (sputter), functionalised, passivated (spin coated OrmoComp) [43]
Casting (laser ablated PMMA master)	Drug delivery	PDMS	Soft, loadable [44]
Moulding (double PDMS from direct laser written PMMA master)	Drug delivery	PLGA	Loadable, biodegradable [45]
Injection moulding	Drug delivery	Gantrez S-97 + PEG mixture	Swelling [46]
Electro-drawing	Drug delivery	PLGA	Biodegradable [47]

Centrifugal lithography	Drug delivery	Hyaluronic acid	Degradable, loaded [48]
Moving x-ray lithography	Drug delivery	PMMA	Hollow [49]
Particle Replication In Non-wetting Templates (PRINT)	Drug delivery	PVP + PVP/PVA solution for substrate	Degradable, loaded, flexible [50]
Inclined/rotated UV lithography	Solid MNs applications	KMPR photopolymer (SU-8-negative epoxy resist) on glass substrate	Biocompatible [51]
Drawing lithography	Drug delivery	Maltose	Loaded, degradable [52]
Drawing lithography	Drug delivery	Hyaluronic acid	Degradable, loaded [53]
Two-photon polymerization	Drug delivery, ISF extraction	OrmoComp + Ciba IRGACURE 2959	Micro-patterned surface, biomimetic [54]

From Table 1, it is evident that polymers have been used for many different microneedle applications, and that these microneedles have been produced using a wide spread of techniques. Some applications also required the integration of different polymers with varying mechanical or material properties, which is something not easily achievable with all manufacturing methods or materials. Moreover, different applications may require additional features or properties not inherently provided by the core structural materials. Examples are electrical conductivity, the need for a passivation layer, or the ability to react to a certain environment or biomarker. To facilitate rapid development of these devices, a multifunctional manufacturing process, easily adaptable to a range of different materials and use cases, would be highly beneficial for research and prototyping purposes.

This work aims at filling this gap, by developing a platform which could be easily tailored to suit the needs of all the main MN applications. Specifically, an ideal platform should have a core production method able to process a wide variety of polymeric materials. This process should also be able to merge materials of different properties and form

multifunctional arrays, and to be compatible with commercially available materials such as textiles and films. To be fully customisable for many use cases, the platform should also allow the inclusion of optional modules, designed to provide additional functionalities to accommodate the implementation of the previously summarised features. Most notably, electrical functionalities are vital to allow interface with biological signals and electronics. Secondly, the ability to pattern the surface of the arrays with conductive or dielectric materials is necessary to form multi-electrodes sensors or to precisely define sensing or delivery areas. Finally, both the core process and the additional modules of the platform should be compatible with scaling at industrial level.

1.2.1 Fabrication methods

In order to select a core manufacturing method, a review of primary fabrication techniques was carried out. From the summary shown in Table 1, the most commonly used manufacturing methods are additive manufacturing techniques (such as 3D printing), either drawing or moving lithography, direct casting into etched, milled or laser ablated master templates, or vacuum assisted micromoulding (generally into PDMS moulds).

Additive manufacturing techniques use a layer-by-layer approach, adding material one layer at the time to build a part. Examples are stereolithography (SLA), two-photon polymerization (2PP) and fused deposition modelling (FDM) [55]. SLA and 2PP start from a vat of liquid photopolymer, cured one layer at the time using a laser. Depending on the photopolymer and the technology used, radiation from different areas of the electromagnetic spectrum can be utilized for the process. The type of laser, the dimension of the focal point and the type of resin determine the precision of the built part, reaching resolutions as low as a few µm [56]. FDM instead melts a filament of material, and

deposits it on a platform one layer at the time. The filaments used for FDM processes are usually cheaper than the resins utilised for 2PP and SLA technologies. However, FDM cannot compete with the precision achieved by stereolithography and photo polymerization [57].

Additive manufacturing allows full customization over the shape of the produced MN arrays. However, the production process itself is usually slow, costly and, critically, not scalable. Moreover, to achieve good levels of precision and tip sharpness, high-quality 3D printers are needed, which are very expensive [58].

Similarly to additive manufacturing, photolithography exposes a material, known as a photosensitive resist, to a light to either cure or degrade it. Usually, UV radiation is used for this purpose. The interaction between the light source and the photoresist is determined by the type of resist: a positive photoresist is one in which the exposed regions becomes soluble to a solvent known as a resist developer, while the opposite happens for negative resists [59]. Generally, a mask is placed between the light source and the resist, enabling selective exposure of the photoresist to the incoming radiation. After exposure, the resist may be removed using a chemical known as a developer. In this way, the substrate, the mask and the light source can be used to form complex patterns and 3D structures [49].

Lithographic methods such as drawing lithography or other lithographic processes with moving parts (inclined/rotated [51] or moving-mask [60] lithography), can quickly produce MNs and are highly scalable.

Drawing lithography starts from a layer of viscous polymer, and utilizes a drawing plate to shape it. Specifically, the plate is dipped inside the polymer, and slowly withdrawn. This way, the polymer is stretched to a desired length/shape. When this is reached, the

polymer is cured. To form MNs, the drawing plate is usually patterned with drawing pillars. Each pillar will pull the polymer, shaping individual needles. Drawing lithography can either stretch a viscous polymer in the glass transition region, or a curable magnetorheological fluid [27], [61]. In the first case, the polymer is cured by bringing it below the glass transition temperature. In the second case, a magnetic field is used to draw the needles, and then the fluid is solidified by exposing it to heat. However, drawn needles are usually characterised by a long body with a narrow cross-section [61], making them very fragile.

Inclined/rotated lithography irradiates a photoresist through a mask with circular openings. By inclining and rotating the light source used to develop the resist, complex patterns can be created, forming cone-shaped MNs. By varying the inclination/rotation, the geometrical characteristics of the cone can be modified [51].

Moving-mask lithography follows a similar principle: by moving the shadow mask, the resist is exposed to different amounts of radiation, forming MN-shaped patterns in the polymer [60].

However, these techniques may lead to both asymmetric results and low tip sharpness (tip diameter > 20 μm) [51], [60].

Casting/moulding of a polymer involves the filling of a mould, which is the negative copy of the MNs, with the polymer of interest. Moulds can be produced through direct replica casting of the master substrate, typically using a PDMS process. Alternatively, they could also be laser ablated [62] or written [63], or produced using lithographic techniques [64]. Once the mould is filled, the polymer is either cured or dried. The filling can be performed by gravitational action, or assisted using an external force. This force is provided by either filling the mould under vacuum, or by applying a mechanical pressure to the filling

material during the curing process. Pure gravitational action may lead to incomplete filling of the mould, or may leave air bubbles trapped within the needle cavities, producing poor tips or preventing reproducible MNs formation [65]. Micromoulding whilst incorporating a force, however, can produce sharp tips, reproduce intricate structures, is easy to implement and does not require expensive equipment or complex processes. It can handle a wide range of polymers, does not suffer from the same problems found with drawing lithography, and it is scalable at industrial level [18].

This work, for the reasons highlighted above, chose replica moulding as the core process at the base of the platform. Specifically, the fabrication steps start from the preparation of two PDMS moulds from two master templates, between which is sandwiched the structural polymer(s) of choice. One mould is the negative copy of the MNs master (Figure 4F) and is needed to define the shape and pitch of the needles on the front side of the array. The replication must be precise, and able to replicate all type of MNs, even complex shapes (Figure 4A and 4B). The second mould (Figure 4G), which is the negative of a custom milled master, is applied to the rear of the rear of the polymer and is used to define the geometry of the MN arrays, to ensure they have a homogeneous thickness, and to introduce additional features, such as alignment marks or front-to-back vias. Partial vacuum is applied to assist the casting process on the needles' mould, guaranteeing proper filling of the micro cavities. The method was then tested, characterised, and further developed to ensure it could replicate masters with precision, and that it was compatible with polymers exhibiting all the properties mentioned in Table 1. Screening criteria for polymer selection included compatibility with the micromoulding process, the ability to form needles able to pierce the skin without breaking, and the possibility of use in *in vivo* studies. Therefore, low viscosity,

mechanical robustness, and compatibility with medical grade standards were necessary prerequisites for all the materials. A particular focus was also placed on the integration of different materials on the same array (Figure 4E), on allowing the formation of multi-electrode substrates with fully customisable geometries (Figure 4H), and on the merging of polymers with commercially available materials such as textiles (Figure 4D) or polymer films (Figure 4C). Enabling this materials flexibility is one of the main features that sets this fabrication method apart from the other commonly used moulding processes, and is a key novelty of the work.

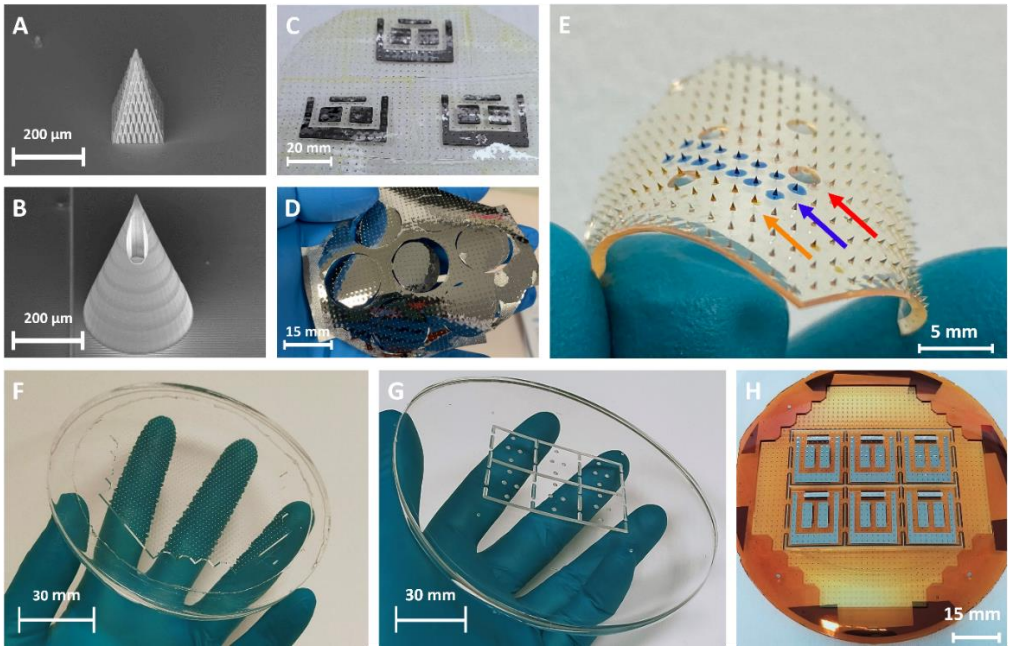


Figure 4. Examples of different microneedles and arrays and moulds produced with the core process. From top left: complex bio-inspired micro-patterned (A) and reservoir equipped (B) MNs; multi-electrode metallized arrays built with medical grade rigid needles integrated on a flexible TPU film (C); conductive fabric with metallized rigid MNs (D); and degradable (blue), UV curing (red), and rigid (orange) MNs merged on a flexible epoxy substrate (E). Finally, pictures of a front (F), and a rear (G) moulds together with the resulting produced wafer (H). Different metals have been deposited to define two

platinum working, one counter, and a silver/silver chloride reference electrode on each of the formed arrays.

This new process represents the most significant contribution of the thesis, and is described in detail in Chapter 2, published as "A Multifunctional Platform for the Production and Customization of Polymer-based Microneedle Devices" in *Sensors and Actuators A: Physical* [66].

1.2.2 Additional modules

After forming the core of the platform, additional process modules were also characterized and developed. In particular, metallization of the array and the addition of a passivation layer were individually considered.

1.2.2.1 Metallization

Metallization is a commonly used practice to provide electrical conductivity to materials that would otherwise be not conductive. This is essential in applications such as biosensing, biopotential monitoring, iontophoresis, or electroporation. There are two main ways normally employed to deposit thin metallic layers: chemical and physical vapour deposition techniques (CVD and PVD respectively). These techniques are vacuum deposition methods that may require or generate heat. Because polymers generally have a low melting point and glass transition temperature, this is the most important parameter to be considered. CVD can be performed either low-pressure (LPCVD) or plasma-enhanced (PECVD). Both processes are thermally induced and require heating up the substrate. To be more precise, LPCVD slowly grows the metal layer using temperatures higher than 600 °C while PECVD films form much faster at lower temperatures (usually in between 200 °C and 400 °C) [67]. Because 200 °C is

generally higher than the melting points and glass transition temperatures of most polymers, CVD processes are not usable. PVD techniques transfer material on a substrate after freeing it from a source. There are three main PVD methods: sputtering [67], e-beam (electron beam) evaporation [68] and thermal evaporation [67], [68]. Thermal evaporation heats up the source, vaporizing it and directing it towards the substrate. This procedure has two main problems: firstly, it could excessively increase the temperature of the substrate and, secondly, it is usually used for low melting point metals [69]. Therefore, it is also not suitable for the platform. As shown by Table 1, both sputtering and e-beam are viable metallization techniques for the MNs: they generally operate at low temperatures, and are compatible with high melting point metals. Sputtering frees atoms from the source by bombarding it with particles [67] while e-beam vaporize metals with high energy beams [70]. Lastly, metals could be deposited on substrates by electroplating. However, electroplating can only coat electrically conductive materials [71] and, typically, polymers are not conductive. Electroplating could therefore only be situationally implemented to either coat a conductive polymer, or overlay a metal on an already deposited metallic layer [69]. Therefore, it is not usable as main metallization technique. After restricting the choice to two suitable candidates, both methods were extensively characterised and tested with common metals used for MNs metallization. Examples are gold (Au), platinum (Pt), silver (Ag), titanium (Ti) and chrome (Cr). The process was repeated with and without masks.

A major issue when metallising microneedles with a specific pattern, which generally requires use of a mask, is the need to place the masks above the tips of the microneedles in order to avoid damage to the structures. As a result, the mask is separated from the substrate by a distance of several hundred micrometres, accounting for the height of the needles and the additional space needed to avoid contact. Therefore, unwanted

'spreading' of the deposited metal may take place underneath the edges of this mask [72]. This effect is similar to photolithographic diffraction when exposing in proximity [66], and can lead to the unwanted metallisation of additional areas of a MN array. The immediate issue is a loss of precision when transferring a desired pattern, hindering the very first reason a mask was used for. However, depending on the severity of the spreading, associated problems, such as formation of short circuits between metal patterns, can arise.

This work has analysed the issue for both sputtering and e-beam evaporation, the main techniques implemented for MNs metallization. Different solutions were proposed to counter undesired spreading. Specifically, new masks were designed by either re-dimensioning the openings in order to compensate for the spreading or by including features on the mask to prevent the phenomenon from happening. The first option drastically improved the precision of the patterned layers, reducing the oversizing caused by the spreading by up to 80%. The second option resulted in an almost exact replication of the pattern. Specifically, the spreading was completely avoided with the inclusion of these additional mask features, and only mild shadowing effects for small features not directly under the metal source was observed. Overall, the replication was near perfect, with a maximum variation from the features' nominal size of less than 5%. This masking method represents the second major contribution of the thesis to the state of the art. More details can be found in Chapter 2, published as "A Multifunctional Platform for the Production and Customization of Polymer-based Microneedle Devices" in *Sensors and Actuators A: Physical* [66].

1.2.2.2 Passivation

Table 1 shows that, when MNs are used for diagnostic purposes, in particular to detect a biomarker or a compound, the needles have to be electrically conductive. The reason for doing this is that, in order to act as a sensor, target-specific chemistries must be bonded to the needles. This functionalization will react with the target biomarker and the result can be electrically measured. However, normally the substrate is metallized together with the MNs, and therefore a passivation layer is generally applied to the substrate around the needles to prevent substrate functionalization and to avoid unwanted responses from interferents outside the SC, such as sweat on the surface of the skin. Different passivation techniques, as summarised in Table 1, include the manual casting of enamel or varnish [37], [42], [73] and the spin-coating of various materials [39], [40], [43]. In addition, a substrate can be passivated through vapour deposition of parylene [74], [75] or by formation of oxide [76].

Although passivation layers are commonly implemented, there is no detailed characterization of their application or performance in the literature.

This work filled this gap. Specifically, different passivation methods were identified, investigated, and compared [77]. More specifically, sputtering of silicon oxide (Figure 6A), application of a patterned medical grade tape (Figure 6B), chemical vapour deposition of parylene with subsequent selective plasma oxygen (Figure 6C), spin coating using two different types of thermally curing polymers (Figure 6D and 6E), and direct application of varnish (Figure 6F) were tested. Both an optical microscope and SEM-assisted visual characterizations were initially carried out to assess the precision and reproducibility of the passivation layer. A second analysis, electrochemical in nature, was

also performed to both validate the previously found results, and to provide new insight on layers that were difficult to visually evaluate. Contact angle measurements were carried out, evaluating the hydrophobic/hydrophilic nature of the surfaces, and discussing how this variation could influence the electrochemical behaviour. Finally, the work also tried to pinpoint the ideal traits a passivation layer for MN-based sensors should have, providing a base for further optimization and development of this key layer.

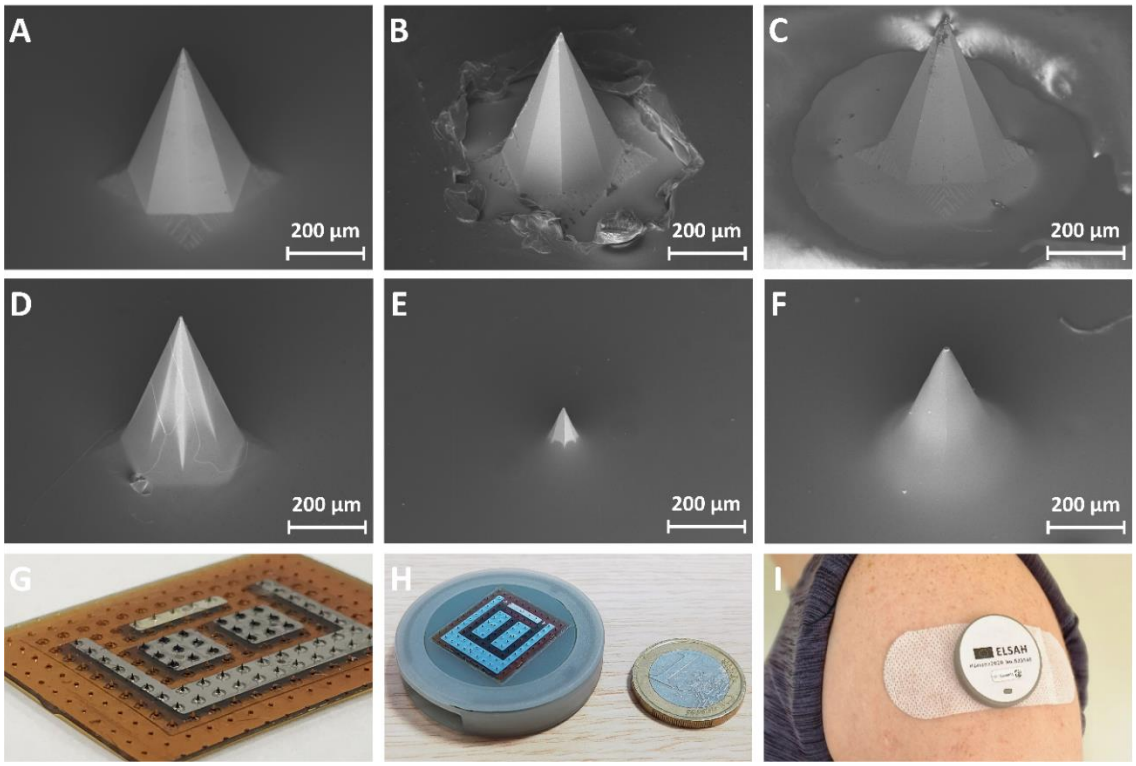


Figure 5. Different passivation applied to MNs: silicon oxide (A), medical grade tape (B), etched parylene (C), sputtering of PMMA (D) and epoxy (E), and brushing of varnish (F). Early iteration of a passivated ELSAH biosensor (G) together with a not passivated final version of the same integrated in a smart device (H). The tested prototype can be seen attached to the arm of a volunteer in the last picture (I).

This characterisation is the most in-depth study of passivation materials performed to date, and constitutes Chapter 3 of this thesis. This work has been published as “Strategies

for Passivating Microneedle-based Sensors: Development, Characterization and Comparison" in *Sensors and Actuators Reports* [78]. One of the characterised layers was also used to passivate a microneedle-based glucose and lactate sensor developed within the Horizon 2020 funded ELSAH project (Figure 5G, 5H and 5I), and was tested on thirty volunteers in a clinical trial performed at the Medical University of Graz. Part of this work has been published as "Detection of Lactate via Amperometric Sensors Modified With Direct Electron Transfer Enzyme Containing PEDOT:PSS and Hydrogel Inks", in *IEEE Sensors Letters* [41].

1.3 Thesis organization

Numerous papers have been published as part of this work, including 10 journal papers (1 more currently under review), and 4 reviewed conference contributions. Moreover, 17 posters were presented and 2 oral talks were given at international conferences, 3 awards were obtained and the work won one of the Wrixon Research Excellence bursaries in 2024. Intellectual property was generated in the form of 1 Invention Disclosure Form and 1 patent application. The most relevant journal publications are included as Chapters 2, 3, 6 and 7. The thesis is organised as follow:

- Chapter 2 presents the platform in detail: the developed moulding process is described, together with new masking techniques used to precisely metallize MN arrays. Exemplars were also provided to show the ability of the platform to contribute to many of the key applications that microneedle devices are used in, such as drug delivery, biomarker monitoring and biopotential signal recording;
- Chapter 3 presents different methods developed to passivate MN sensors. The layers were characterised and compared both visually and electrochemically, providing insight in which one could be best for different use cases;

- Chapter 4 demonstrates the scalability of the moulding core process at industrial level through injection moulding. Reservoir-tipped MNs were built, filled with a fluorescent dye, and tested on *ex vivo* skin samples. The results showed successful skin penetration and no structural damage of the needles was apparent;
- Chapter 5 presents novel bio-inspired micro-patterned MNs used to directionally drive fluids either up or town the sidewalls of a needle. The original 3D printed samples were copied through micromoulding, and tested on *ex vivo* skin samples. This process could be used for applications including precise microneedle coating, drug delivery and interstitial fluid withdrawal;
- Chapter 6 presents novel fabric-backed dry MN electrodes for electrophysiological signal capturing. Following mechanical characterisation, they were electrically tested versus conventional gel-based electrodes. Finally, the electrodes were worn by a volunteer, and the signal quality recorded was compared to that of a conventional wet electrodes both in static and dynamic conditions;
- Chapter 7 presents the most complex use of the developed platform, in which multi-electrode sensors for lactate detection were produced. The sensors were moulded, metallised, chlorinated, passivated, and functionalised. The sensors then underwent testing to prove their efficacy and precision in detecting lactate in an *in vitro* setting;
- After fully developing the platform and its individual modules, final considerations have also been drawn in Chapter 8, including remarks on how to continue this work, and which gaps could be addressed by exploiting the presented process. These recommendations include further development of the platform to ensure scalability of every module at industrial level and to overcome the current

limitations in terms of usable polymers and number of possible material integrations, and to carry out further research on metallization and passivation in order to reach a high level of control over metallic patterns and electrochemically active areas. In addition, initial thoughts on the development of a penetration sensor, intended to ensure that the needles are properly embedded within the skin, are also presented.

1.4 Key novelties

Overall, this work provides several fundamental contributions to the current state of the art, including:

- ✓ A novel laboratory-scale process which enables the rapid prototyping of different type of MNs for applications in transdermal delivery, diagnostics and biopotential monitoring. The process enables use and merger of different materials, including the integration of biomedical-grade polymers, textiles, and commercially available films within the same array, forming multifunctional devices [66];
- ✓ New masking techniques that have improved dimensional accuracy of metal patterns by up to 95% when compared to conventional masks [66];
- ✓ A first comparison of passivation methods for MN sensors. Specifically, spin coating of polymers, direct brushing of varnish, application of patterned tape, sputtering of silicon oxide, and deposition followed by selective etching of parylene were used as passivation techniques. These layers were applied to MNs sensors, and both visually and electrochemically characterised. Not only this is, to my knowledge, the first fully dedicated work characterizing and comparing passivation layers for MNs applications, but it also provides an invaluable reference to help with the selection of a passivation layer for a specific use case.

This work constitutes a base for future development and optimization of such layers, necessary to help scaling at industrial level [78];

- ✓ Numerous published exemplars illustrating the use of novel MN arrays, produced using the platform, for medical applications. More precisely, these included bio-inspired needles both for drug delivery and interstitial fluid extraction, fabric-backed electrodes employed to monitor electrophysiological signals, and biosensors detecting different biomarkers and usable for the development of continuous monitoring devices [41], [54], [79].

1.5 References

[1] H. Yousef, M. Alhajj, A. O. Fakoya, and S. Sharma, 'Anatomy, Skin (Integument), Epidermis', in *StatPearls*, Treasure Island (FL): StatPearls Publishing, 2024. Accessed: Sep. 19, 2024. [Online]. Available: http://www.ncbi.nlm.nih.gov/books/NBK470464/

[2] M. A. Farage, K. W. Miller, P. Elsner, and H. I. Maibach, 'Structural Characteristics of the Aging Skin: A Review', *Cutan. Ocul. Toxicol.*, vol. 26, no. 4, pp. 343–357, Jan. 2007, doi: 10.1080/15569520701622951.

[3] F. Lu *et al.*, 'Review of Stratum Corneum Impedance Measurement in Non-Invasive Penetration Application', *Biosensors*, vol. 8, no. 2, p. 31, Mar. 2018, doi: 10.3390/bios8020031.

[4] S. Demartis *et al.*, 'Delivering hydrosoluble compounds through the skin: what are the chances?', *Int. J. Pharm.*, vol. 646, p. 123457, Nov. 2023, doi: 10.1016/j.ijpharm.2023.123457.

[5] T. Waghule *et al.*, 'Microneedles: A smart approach and increasing potential for transdermal drug delivery system', *Biomed. Pharmacother.*, vol. 109, pp. 1249–1258, Jan. 2019, doi: 10.1016/j.biopha.2018.10.078.

[6] J. Yang *et al.*, 'Recent Progress in Microneedles-Mediated Diagnosis, Therapy, and Theranostic Systems', *Adv. Healthc. Mater.*, vol. 11, no. 10, p. 2102547, 2022, doi: 10.1002/adhm.202102547.

[7] X. Tang *et al.*, 'Using microneedle array electrodes for non-invasive electrophysiological signal acquisition and sensory feedback evoking', *Front. Bioeng. Biotechnol.*, vol. 11, Aug. 2023, doi: 10.3389/fbioe.2023.1238210.

[8] A. S. Rzhevskiy, T. R. R. Singh, R. F. Donnelly, and Y. G. Anissimov, 'Microneedles as the technique of drug delivery enhancement in diverse organs and tissues', *J. Controlled Release*, vol. 270, pp. 184–202, Jan. 2018, doi: 10.1016/j.jconrel.2017.11.048.

[9] M. T. C. McCrudden, E. McAlister, A. J. Courtenay, P. González-Vázquez, T. R. Raj Singh, and R. F. Donnelly, 'Microneedle applications in improving skin appearance', *Exp. Dermatol.*, vol. 24, no. 8, pp. 561–566, 2015, doi: 10.1111/exd.12723.

[10] Z. Liu *et al.*, 'Multichannel microneedle dry electrode patches for minimally invasive transdermal recording of electrophysiological signals', *Microsyst. Nanoeng.*, vol. 10, no. 1, pp. 1–18, May 2024, doi: 10.1038/s41378-024-00702-8.

[11] C. O'Mahony, R. Houlihan, K. Grygoryev, Z. Ning, J. Williams, and T. Moore, 'Design, modelling and preliminary characterisation of microneedle-based electrodes for tissue electroporation in vivo', *J. Phys. Conf. Ser.*, vol. 757, no. 1, p. 012040, Oct. 2016, doi: 10.1088/1742-6596/757/1/012040.

[12] Y. Chen, B. Z. Chen, Q. L. Wang, X. Jin, and X. D. Guo, 'Fabrication of coated polymer microneedles for transdermal drug delivery', *J. Controlled Release*, vol. 265, pp. 14–21, Nov. 2017, doi: 10.1016/j.jconrel.2017.03.383.

[13] F. Tasca, C. Tortolini, P. Bollella, and R. Antiochia, 'Microneedle-based electrochemical devices for transdermal biosensing: a review', *Curr. Opin. Electrochem.*, vol. 16, pp. 42–49, Aug. 2019, doi: 10.1016/j.coelec.2019.04.003.

[14] K. Ita, 'Dissolving microneedles for transdermal drug delivery: Advances and challenges', *Biomed. Pharmacother.*, vol. 93, pp. 1116–1127, Sep. 2017, doi: 10.1016/j.biopha.2017.07.019.

[15] J. G. Turner, L. R. White, P. Estrela, and H. S. Leese, 'Hydrogel-Forming Microneedles: Current Advancements and Future Trends', *Macromol. Biosci.*, vol. 21, no. 2, p. 2000307, Feb. 2021, doi: 10.1002/mabi.202000307.

[16] P. R. Miller *et al.*, 'Extraction and biomolecular analysis of dermal interstitial fluid collected with hollow microneedles', *Commun. Biol.*, vol. 1, no. 1, pp. 1–11, Oct. 2018, doi: 10.1038/s42003-018-0170-z.

[17] M. Chiaranairungroj, A. Pimpin, and W. Srituravanich, 'Fabrication of high-density microneedle masters towards the commercialisation of dissolving microneedles', *Micro Nano Lett.*, vol. 13, no. 3, pp. 284–288, 2018, doi: 10.1049/mnl.2017.0596.

[18] F. K. Aldawood, A. Andar, and S. Desai, 'A Comprehensive Review of Microneedles: Types, Materials, Processes, Characterizations and Applications', *Polymers*, vol. 13, no. 16, p. 2815, Aug. 2021, doi: 10.3390/polym13162815.

[19] R. D. Koyani, 'Biopolymers for microneedle synthesis: from then to now', *Biomanufacturing Rev.*, vol. 4, no. 1, p. 1, Sep. 2019, doi: 10.1007/s40898-019-0006-8.

[20] T. D. Nguyen, T.-H. Nguyen, V. T. Vo, and T.-Q. Nguyen, ‘Panoramic review on polymeric microneedle arrays for clinical applications’, *Biomed. Microdevices*, vol. 26, no. 4, p. 41, Sep. 2024, doi: 10.1007/s10544-024-00724-z.

[21] J.-M. Moon, N. Thapliyal, K. K. Hussain, R. N. Goyal, and Y.-B. Shim, ‘Conducting polymer-based electrochemical biosensors for neurotransmitters: A review’, *Biosens. Bioelectron.*, vol. 102, pp. 540–552, Apr. 2018, doi: 10.1016/j.bios.2017.11.069.

[22] M. Wang, L. Hu, and C. Xu, ‘Recent advances in the design of polymeric microneedles for transdermal drug delivery and biosensing’, *Lab. Chip*, vol. 17, no. 8, pp. 1373–1387, 2017, doi: 10.1039/C7LC00016B.

[23] Y. Hou, Z. Li, Z. Wang, and H. Yu, ‘Miura-ori structured flexible microneedle array electrode for biosignal recording’, *Microsyst. Nanoeng.*, vol. 7, no. 1, Art. no. 1, Jul. 2021, doi: 10.1038/s41378-021-00259-w.

[24] M. J. Uddin *et al.*, ‘3D printed microneedles for anticancer therapy of skin tumours’, *Mater. Sci. Eng. C*, vol. 107, p. 110248, Feb. 2020, doi: 10.1016/j.msec.2019.110248.

[25] M. A. Luzuriaga, D. R. Berry, J. C. Reagan, R. A. Smaldone, and J. J. Gassensmith, ‘Biodegradable 3D printed polymer microneedles for transdermal drug delivery’, *Lab. Chip*, vol. 18, no. 8, pp. 1223–1230, Apr. 2018, doi: 10.1039/C8LC00098K.

[26] J. Li *et al.*, ‘Low-Cost, Low-Impedance Polyimide Based Micro-Needle Array (PI-MNA): A Minimally Invasive Flexible Dry Electrode for Surface Bio-Potential Monitoring’, in *2019 IEEE 32nd International Conference on Micro Electro Mechanical Systems (MEMS)*, Jan. 2019, pp. 28–31. doi: 10.1109/MEMSYS.2019.8870653.

[27] Z. Chen *et al.*, 'Rapid fabrication of microneedles using magnetorheological drawing lithography', *Acta Biomater.*, vol. 65, pp. 283–291, Jan. 2018, doi: 10.1016/j.actbio.2017.10.030.

[28] P. Bollella, S. Sharma, A. E. G. Cass, and R. Antiochia, 'Microneedle-based biosensor for minimally-invasive lactate detection', *Biosens. Bioelectron.*, vol. 123, pp. 152–159, Jan. 2019, doi: 10.1016/j.bios.2018.08.010.

[29] L. Ren *et al.*, 'Fabrication of Flexible Microneedle Array Electrodes for Wearable Bio-Signal Recording', *Sensors*, vol. 18, no. 4, Art. no. 4, Apr. 2018, doi: 10.3390/s18041191.

[30] M. Zheng *et al.*, 'Osmosis-Powered Hydrogel Microneedles for Microliters of Skin Interstitial Fluid Extraction within Minutes', *Adv. Healthc. Mater.*, vol. 9, no. 10, p. 1901683, May 2020, doi: 10.1002/adhm.201901683.

[31] R. F. Donnelly *et al.*, 'Hydrogel-Forming Microneedles Prepared from "Super Swelling" Polymers Combined with Lyophilised Wafers for Transdermal Drug Delivery', *PLoS ONE*, vol. 9, no. 10, p. e111547, Oct. 2014, doi: 10.1371/journal.pone.0111547.

[32] S. Sharma, Z. Huang, M. Rogers, M. Boutelle, and A. E. G. Cass, 'Evaluation of a minimally invasive glucose biosensor for continuous tissue monitoring', *Anal. Bioanal. Chem.*, vol. 408, no. 29, pp. 8427–8435, 2016, doi: 10.1007/s00216-016-9961-6.

[33] S. C. Park, M. J. Kim, S.-K. Baek, J.-H. Park, and S.-O. Choi, 'Spray-Formed Layered Polymer Microneedles for Controlled Biphasic Drug Delivery', *Polymers*, vol. 11, no. 2, Art. no. 2, Feb. 2019, doi: 10.3390/polym11020369.

[34] W. Li, R. N. Terry, J. Tang, M. R. Feng, S. P. Schwendeman, and M. R. Prausnitz, 'Rapidly separable microneedle patch for the sustained release of a contraceptive', *Nat. Biomed. Eng.*, vol. 3, no. 3, Art. no. 3, Mar. 2019, doi: 10.1038/s41551-018-0337-4.

[35] Y. Park, J. Park, G. S. Chu, K. S. Kim, J. H. Sung, and B. Kim, 'Transdermal delivery of cosmetic ingredients using dissolving polymer microneedle arrays', *Biotechnol. Bioprocess Eng.*, vol. 20, no. 3, pp. 543–549, Jun. 2015, doi: 10.1007/s12257-014-0775-0.

[36] F. Pérennès, B. Marmiroli, M. Matteucci, M. Tormen, L. Vaccari, and E. D. Fabrizio, 'Sharp beveled tip hollow microneedle arrays fabricated by LIGA and 3D soft lithography with polyvinyl alcohol', *J. Micromechanics Microengineering*, vol. 16, no. 3, p. 473, Jan. 2006, doi: 10.1088/0960-1317/16/3/001.

[37] S. A. N. Gowers *et al.*, 'Development of a Minimally Invasive Microneedle-Based Sensor for Continuous Monitoring of β-Lactam Antibiotic Concentrations in Vivo', *ACS Sens.*, vol. 4, no. 4, pp. 1072–1080, Apr. 2019, doi: 10.1021/acssensors.9b00288.

[38] Y. Nishinaka, R. Jun, G. S. Prihandana, and N. Miki, 'Fabrication of polymeric dry microneedle electrodes coated with nanoporous parylene', in *2013 Transducers & Eurosensors XXVII: The 17th International Conference on Solid-State Sensors, Actuators and Microsystems (TRANSDUCERS & EUROSENSORS XXVII)*, Jun. 2013, pp. 1326–1327. doi: 10.1109/Transducers.2013.6627021.

[39] C. Barrett, K. Dawson, C. O'Mahony, and A. O'Riordan, 'Development of Low Cost Rapid Fabrication of Sharp Polymer Microneedles for In Vivo Glucose

Biosensing Applications', *ECS J. Solid State Sci. Technol.*, vol. 4, no. 10, p. S3053, Aug. 2015, doi: 10.1149/2.0141510jss.

[40] S. Metz, M. O. Heuschkel, B. Valencia Avila, R. Holzer, D. Bertrand, and Ph. Renaud, 'Microelectrodes with three-dimensional structures for improved neural interfacing', in *2001 Conference Proceedings of the 23rd Annual International Conference of the IEEE Engineering in Medicine and Biology Society*, Istanbul, Turkey: IEEE, 2001, pp. 765–768. doi: 10.1109/IEMBS.2001.1019053.

[41] S. Kurzhals *et al.*, 'Detection of Lactate via Amperometric Sensors Modified With Direct Electron Transfer Enzyme Containing PEDOT:PSS and Hydrogel Inks', *IEEE Sens. Lett.*, vol. 7, no. 9, pp. 1–4, Sep. 2023, doi: 10.1109/LSENS.2023.3307066.

[42] C. Hegarty, A. McConville, R. J. McGlynn, D. Mariotti, and J. Davis, 'Design of composite microneedle sensor systems for the measurement of transdermal pH', *Mater. Chem. Phys.*, vol. 227, pp. 340–346, Apr. 2019, doi: 10.1016/j.matchemphys.2019.01.052.

[43] M. Dervisevic, E. Dervisevic, L. Esser, C. D. Easton, V. J. Cadarso, and N. H. Voelcker, 'Wearable microneedle array-based sensor for transdermal monitoring of pH levels in interstitial fluid', *Biosens. Bioelectron.*, vol. 222, p. 114955, Feb. 2023, doi: 10.1016/j.bios.2022.114955.

[44] F. K. Aldawood, A. Andar, and S. Desai, 'Investigating Laser Ablation Process Parameters for the Fabrication of Customized Microneedle Arrays for Therapeutic Applications', *Pharmaceutics*, vol. 16, no. 7, Art. no. 7, Jul. 2024, doi: 10.3390/pharmaceutics16070885.

[45] K.-T. Tu and C.-K. Chung, ‘Fabrication of biodegradable polymer microneedle array via CO2 laser ablation’, in *10th IEEE International Conference on Nano/Micro Engineered and Molecular Systems*, Apr. 2015, pp. 494–497. doi: 10.1109/NEMS.2015.7147476.

[46] R. E. M. Lutton, E. Larrañeta, M.-C. Kearney, P. Boyd, A. D. Woolfson, and R. F. Donnelly, ‘A novel scalable manufacturing process for the production of hydrogel-forming microneedle arrays’, *Int. J. Pharm.*, vol. 494, no. 1, pp. 417–429, Oct. 2015, doi: 10.1016/j.ijpharm.2015.08.049.

[47] R. Vecchione *et al.*, ‘Electro-Drawn Drug-Loaded Biodegradable Polymer Microneedles as a Viable Route to Hypodermic Injection’, *Adv. Funct. Mater.*, vol. 24, no. 23, pp. 3515–3523, Jun. 2014, doi: 10.1002/adfm.201303679.

[48] S. Lee, S. Fakhraei Lahiji, J. Jang, M. Jang, and H. Jung, ‘Micro-Pillar Integrated Dissolving Microneedles for Enhanced Transdermal Drug Delivery’, *Pharmaceutics*, vol. 11, no. 8, Art. no. 8, Aug. 2019, doi: 10.3390/pharmaceutics11080402.

[49] J. Wang, H. Wang, L. Lai, and Y. Li, ‘Preparation of Microneedle Array Mold Based on MEMS Lithography Technology’, *Micromachines*, vol. 12, no. 1, p. 23, Dec. 2020, doi: 10.3390/mi12010023.

[50] K. A. Moga *et al.*, ‘Rapidly–Dissolvable Microneedle Patches Via a Highly Scalable and Reproducible Soft Lithography Approach’, *Adv. Mater. Deerfield Beach Fla*, vol. 25, no. 36, p. 5060, Jul. 2013, doi: 10.1002/adma.201300526.

[51] H. Takahashi *et al.*, ‘Scalable fabrication of microneedle arrays via spatially controlled UV exposure’, *Microsyst. Nanoeng.*, vol. 2, no. 1, pp. 1–9, Oct. 2016, doi: 10.1038/micronano.2016.49.

[52] K. Lee, C. Y. Lee, and H. Jung, ‘Dissolving microneedles for transdermal drug administration prepared by stepwise controlled drawing of maltose’, *Biomaterials*, vol. 32, no. 11, pp. 3134–3140, Apr. 2011, doi: 10.1016/j.biomaterials.2011.01.014.

[53] M. Dangol *et al.*, ‘Anti-obesity effect of a novel caffeine-loaded dissolving microneedle patch in high-fat diet-induced obese C57BL/6J mice’, *J. Controlled Release*, vol. 265, pp. 41–47, Nov. 2017, doi: 10.1016/j.jconrel.2017.03.400.

[54] C. Plamadeala *et al.*, ‘Bio-inspired microneedle design for efficient drug/vaccine coating’, *Biomed. Microdevices*, vol. 22, no. 1, p. 8, Dec. 2019, doi: 10.1007/s10544-019-0456-z.

[55] R. Nadda, P. K. Singh, and D. B. Das, ‘Revolutionizing microneedle array fabrication using additive manufacturing technologies: Potential applications and clinical translation’, *J. Drug Deliv. Sci. Technol.*, vol. 101, p. 106288, Nov. 2024, doi: 10.1016/j.jddst.2024.106288.

[56] T. Woodfield, K. Lim, P. Morouço, R. Levato, J. Malda, and F. Melchels, ‘5.14 Biofabrication in Tissue Engineering☆’, in *Comprehensive Biomaterials II*, P. Ducheyne, Ed., Oxford: Elsevier, 2017, pp. 236–266. doi: 10.1016/B978-0-12-803581-8.10221-8.

[57] A. Borók, L. M. Kővágó, and A. Bonyár, ‘Comparison of Two 3D Printing Technologies for Microfluidic Applications’, in *2023 46th International Spring Seminar on Electronics Technology (ISSE)*, May 2023, pp. 1–4. doi: 10.1109/ISSE57496.2023.10168389.

[58] M. Olowe, S. K. Parupelli, and S. Desai, ‘A Review of 3D-Printing of Microneedles’, *Pharmaceutics*, vol. 14, no. 12, Art. no. 12, Dec. 2022, doi: 10.3390/pharmaceutics14122693.

[59] J. M. Quero, F. Perdigones, and C. Aracil, ‘11 - Microfabrication technologies used for creating smart devices for industrial applications’, in *Smart Sensors and MEMs (Second Edition)*, S. Nihtianov and A. Luque, Eds., in Woodhead Publishing Series in Electronic and Optical Materials. , Woodhead Publishing, 2018, pp. 291–311. doi: 10.1016/B978-0-08-102055-5.00011-5.

[60] T. Kai, S. Mori, and N. Kato, ‘Development of a Rapid Prototyping System for Microneedles Using Moving-mask Lithography with Backside Exposure’, *Adv. Biomed. Eng.*, vol. 5, no. 0, pp. 63–67, 2016, doi: 10.14326/abe.5.63.

[61] K. Lee and H. Jung, ‘Drawing lithography for microneedles: A review of fundamentals and biomedical applications’, *Biomaterials*, vol. 33, no. 30, pp. 7309–7326, Oct. 2012, doi: 10.1016/j.biomaterials.2012.06.065.

[62] H. R. Nejad, A. Sadeqi, G. Kiaee, and S. Sonkusale, ‘Low-cost and cleanroom-free fabrication of microneedles’, *Microsyst. Nanoeng.*, vol. 4, no. 1, pp. 1–7, Jan. 2018, doi: 10.1038/micronano.2017.73.

[63] B.-J. Kim, H.-J. Kim, S. M. Jung, J.-K. Sung, and H. H. Lee, ‘Fabrication of microneedle using laser written PDMS mold for molecule transport into plant skin’, *Biochip J.*, vol. 3, pp. 281–286, Jan. 2009.

[64] N. R. Mogusala, V. Devadasu, and R. K. Venisetty, ‘Fabrication of Microneedle Molds and Polymer Based Biodegradable Microneedle Patches: A Novel Method’, *J. Drug Deliv. Ther.*, May 2015, Accessed: Dec. 09, 2024. [Online]. Available: https://www.semanticscholar.org/paper/Fabrication-of-Microneedle-Molds-and-Polymer-Based-Mogusala-Devadasu/721e3f8b811516519c97bd2048ca955ddeb066dc

[65] E. Smith, W. M. Lau, T. M. Abdelghany, D. Vukajlovic, K. Novakovic, and K. W. Ng, ‘Vac-and-fill: A micromoulding technique for fabricating microneedle arrays with vacuum-activated, hands-free mould-filling’, *Int. J. Pharm.*, vol. 650, p. 123706, Jan. 2024, doi: 10.1016/j.ijpharm.2023.123706.

[66] A. Bocchino *et al.*, ‘A multifunctional platform for the production and customization of polymer-based microneedle devices’, *Sens. Actuators Phys.*, vol. 388, p. 116491, Jul. 2025, doi: 10.1016/j.sna.2025.116491.

[67] D. Kulkarni *et al.*, ‘Recent Advancements in Microneedle Technology for Multifaceted Biomedical Applications’, *Pharmaceutics*, vol. 14, no. 5, Art. no. 5, May 2022, doi: 10.3390/pharmaceutics14051097.

[68] R. J. Martín-Palma and A. Lakhtakia, ‘Chapter 15 - Vapor-Deposition Techniques’, in *Engineered Biomimicry*, A. Lakhtakia and R. J. Martín-Palma, Eds., Boston: Elsevier, 2013, pp. 383–398. doi: 10.1016/B978-0-12-415995-2.00015-5.

[69] A. Tamayo-Dominguez, P. Sanchez-Olivares, A. Camacho-Hernandez, and J.-M. Fernandez-Gonzalez, ‘Guidelines for Accurate in-House Electroplating and 3-D-Printing Processes Applied to mm-Wave Devices’, *IEEE Microw. Wirel. Compon. Lett.*, vol. 32, no. 11, pp. 1267–1270, Nov. 2022, doi: 10.1109/LMWC.2022.3182868.

[70] C. J. Martin, C. J. Allender, K. R. Brain, A. Morrissey, and J. C. Birchall, ‘Low temperature fabrication of biodegradable sugar glass microneedles for transdermal drug delivery applications’, *J. Controlled Release*, vol. 158, no. 1, pp. 93–101, Feb. 2012, doi: 10.1016/j.jconrel.2011.10.024.

[71] A. S. Hamdy Makhlouf and R. Rodriguez, ‘Chapter 15 - Bioinspired smart coatings and engineering materials for industrial and biomedical applications’, in *Advances*

in Smart Coatings and Thin Films for Future Industrial and Biomedical Engineering Applications, A. S. H. Makhlouf and N. Y. Abu-Thabit, Eds., Elsevier, 2020, pp. 407–427. doi: 10.1016/B978-0-12-849870-5.00018-5.

[72] R. K. Kummamuru, L. Hu, L. Cook, M. Y. Efremov, E. A. Olson, and L. H. Allen, 'A close proximity self-aligned shadow mask for sputter deposition onto a membrane or cavity', *J. Micromechanics Microengineering*, vol. 18, no. 9, p. 095027, Aug. 2008, doi: 10.1088/0960-1317/18/9/095027.

[73] T. M. Rawson *et al.*, 'Microneedle biosensors for real-time, minimally invasive drug monitoring of phenoxymethylpenicillin: a first-in-human evaluation in healthy volunteers', *Lancet Digit. Health*, vol. 1, no. 7, pp. e335–e343, Nov. 2019, doi: 10.1016/S2589-7500(19)30131-1.

[74] A. T. Satti, J. Park, J. Park, H. Kim, and S. Cho, 'Fabrication of Parylene-Coated Microneedle Array Electrode for Wearable ECG Device', *Sensors*, vol. 20, no. 18, Art. no. 18, Jan. 2020, doi: 10.3390/s20185183.

[75] R. Wang, W. Zhao, W. Wang, and Z. Li, 'A Flexible Microneedle Electrode Array With Solid Silicon Needles', *J. Microelectromechanical Syst.*, vol. 21, no. 5, pp. 1084–1089, Oct. 2012, doi: 10.1109/JMEMS.2012.2203790.

[76] W.-C. Lee, N. G. Gurudatt, D.-S. Park, K. B. Kim, C. S. Choi, and Y.-B. Shim, 'Microneedle array sensor for monitoring glucose in single cell using glucose oxidase-bonded polyterthiophene coated on AuZn oxide layer', *Sens. Actuators B Chem.*, vol. 320, p. 128416, Oct. 2020, doi: 10.1016/j.snb.2020.128416.

[77] A. Bocchino *et al.*, 'Development and Characterization of Passivation Methods for Microneedle-based Biosensors', in *2022 44th Annual International Conference of*

the IEEE Engineering in Medicine & Biology Society (EMBC), Jul. 2022, pp. 1275–1278. doi: 10.1109/EMBC48229.2022.9871005.

[78] A. Bocchino *et al.*, 'Strategies for passivating microneedle-based sensors: development, characterization and comparison', *Sens. Actuators Rep.*, vol. 9, p. 100328, Jun. 2025, doi: 10.1016/j.snr.2025.100328.

[79] O. P. Singh, A. Bocchino, T. Guillerm, Y. Hu, F. Stam, and C. O'Mahony, 'Flexible, Conductive Fabric-Backed, Microneedle Electrodes for Electrophysiological Monitoring', *Adv. Mater. Technol.*, vol. 9, no. 3, p. 2301606, 2024, doi: 10.1002/admt.202301606.

Chapter 2

A Multifunctional Platform for the Production and Customization of Polymer-based Microneedle Devices

Authors: Andrea Bocchino, Carlota Marquez-Grana, Om Prakash Singh, Eva Melnik, Steffen Kurzhals, Giorgio C. Mutinati, Sion Coulman, Christopher Martin, Keng Wooi Ng, Mariane Massufero Vergilio, James Birchall, Paul Donovan, Paul Galvin, and Conor O'Mahony.

Journal: *Sensors and Actuators A: Physical*, volume 388, article 116491.

Publication Date: 01st July 2025.

DOI: 10.1016/j.sna.2025.116491

Contribution: As lead author, I was responsible for writing the paper and for the development of the platform itself. In particular, I developed the core production process for the customization and fabrication of polymer-based microneedle devices. I have also increased the production throughput by designing a modular vacuum table. I developed the different features necessary for wafer and geometry customization, characterized and optimised masked metallization techniques for electrode formation, demonstrated the compatibility of the process for different materials, and demonstrated direct implementation of the platform in several microneedles' applications. For the first exemplar, I was directly involved in the development and optimization of the sensor

design, chlorination optimization, passivation development and integration of the final 3D printed wearable device with enzymes and readout electronics developed by co-authors (Section 2.4.1, Figure 9 and 10B). Additional detail on these specific biosensors is presented in Chapter 7. For ECG capturing, I was responsible for the conceptualization of the integration between the polymer and the substrate material together with the development of the first prototype for simultaneous double ECG capturing. This prototype was the base for the development of the recording device used in the exemplar (more details in Chapter 6) and characterised by co-authors. The core process was used by the co-authors to produce the needles presented within the transdermal delivery exemplar. The co-authors were also responsible for the testing of the needles. These contributions are contained within Section 2.4.3 (Figure 12, 13 and 14 by co-authors).

CRediT Authors Statement:

Andrea Bocchino: Conceptualization, Data curation, Formal analysis, Investigation, Methodology, Validation, Writing – original draft, Writing – review & editing.

Carlota Marquez-Grana: Data curation, Investigation, Methodology, Validation, Writing – review & editing.

Om Prakash Singh: Data curation, Investigation, Methodology, Writing – review & editing.

Eva Melnik: Data curation, Investigation, Methodology, Writing – review & editing.

Steffen Kurzhals: Data curation, Investigation, Methodology, Writing – review & editing.

Giorgio C. Mutinati: Funding acquisition, Investigation, Project administration, Resources, Writing – review & editing.

Sion Coulman: Data curation, Investigation, Methodology, Writing – review & editing.

Christopher Martin: Data curation, Investigation, Methodology, Writing – review & editing.

Keng Wooi Ng: Data curation, Investigation, Methodology, Writing – review & editing.

Mariane Massufero Vergilio: Data curation, Investigation, Methodology, Writing – review & editing.

James Birchall: Funding acquisition, Investigation, Writing – review & editing.

Paul Donovan: Methodology, Visualization, Writing – review & editing.

Paul Galvin: Project administration, Resources, Supervision, Writing – review & editing.

Conor O'Mahony: Conceptualization, Funding acquisition, Investigation, Methodology, Project administration, Resources, Supervision, Writing – review & editing.

Chapter adapted from below link under the Creative Commons license 4.0 (CC BY 4.0).
The Section numbers, Figures/Tables/References style has been adapted to conform to the style and numbering of the thesis.

Additional changes:

- Section 2.3.3: "calliper" changed to "caliper".
- Figure 4D: scale bar modified.

https://www.sciencedirect.com/science/article/pii/S0924424725002973

Link to license:

https://creativecommons.org/licenses/by/4.0/

2.1 Abstract

Polymer microneedles (MNs) have significant potential for use in transdermal delivery and diagnostics applications due to their low cost, versatility, and compatibility with medical grade materials and industrial manufacturing processes. These polymers can also have a wide range of different and desirable properties such as biocompatibility, degradability, and flexibility.

To facilitate rapid development of these devices, a multifunctional manufacturing process, easily adaptable to a range of different materials and use cases, would be highly beneficial for research and prototyping purposes. With that in mind, we have developed a multifunctional platform that may be used to produce sharp-tipped microneedle arrays with a variety of substrate materials, mechanical characteristics, electrical properties, and diagnostic functionalities. The paper first presents an outline of the platform concept and the double-sided moulding process that lies at its core, followed by a description of the various add-on steps that are used to customise the geometrical, mechanical, electrical, and functional aspects of the arrays.

Finally, we illustrate the versatility of the platform with three exemplars, namely a solid, electrochemically active MN sensor for biomarker diagnostics, a fabric-backed, flexible MN electrode for biopotential monitoring, and a biodegradable array for transdermal drug delivery.

2.2 Introduction

Microneedles are sharp needle-like structures, typically no more than a millimetre in length, and that are capable of painlessly piercing the outermost layer of the epidermis, known as the *stratum corneum* (SC) [1]. The *stratum corneum* typically ranges from 10 µm to 30 µm in thickness [2], and is comprised of densely packed corneocytes embedded

in a lipid bilayer matrix [3]. This presents a considerable barrier to the transdermal delivery of drugs and vaccines, prevents the sampling of diagnostic materials, and hinders the passage of electrical and optical signals into and out of the body. Arrays of microneedles may be used to penetrate this barrier and reach the viable epidermis and the uppermost layer of the dermis that lie beneath. Both layers are rich in interstitial fluid-borne biomarkers and immune-responsive cells, and lie close to the capillary network, making them an ideal target for bloodless diagnostics and for the transdermal delivery of drugs and vaccines. Moreover, because of their short length, MNs do not strike the nerve endings nor the capillary vessels that lie deeper in the skin; their use is therefore perceived as painless and bloodless by the user. MN arrays are easy to both apply and dispose of, and reduce any risk of needle-phobia that could lead to patient non-adherence [4], [5]. Due to these properties, MNs have been widely investigated for many applications including delivery of drugs [6], [7] and vaccines [8], biomarker diagnostics [9], detection of biopotentials such as ECG, EEG and EMG signals [10], [11], [12], enhancement of optical transmission through skin [13], and electroporation/iontophoresis [14].

Considering the numerous different applications MNs can be used for, they have been fabricated using a wide variety of materials and techniques. Typical examples include silicon, metals, resins, polymers, silk, ceramics and sugars produced by techniques such as etching, laser cutting, electro-polishing, 3D printing and micromoulding [15], [16].

Because of their low cost, medical grade and compatibility with high-volume manufacturing techniques such as injection moulding, polymer materials have the potential to reduce the cost of the MN devices together with the complexity of the production process [17], [18]. Moreover, polymers exhibit a large variety of properties that are appealing for MNs production. Biocompatible, degradable, swellable, flexible

and rigid MNs may all be fabricated by simply choosing the appropriate polymer [19]. Examples of these needles are shown in Table 1.

Table 1. Review of different polymer MNs arrays.

Materials	Application	Production Process	Features	Ref.
OrmoComp	pH monitoring	UV-cured Polydimethylsiloxane (PDMS) mould, Si master	Metallized (sputter), multi-electrodes	[20]
1201AB-3 hard epoxy, 607AB-5 soft substrate	ECG, EMG recording	Moulding in PDMS, acrylic machined master	Metallized, flexible arrays	[21]
Unspecified "Class I biocompatible resin"	Anticancer therapy	Stereolithography	Biocompatible, inkjet coating	[22]
Polylactic acid (PLA)	Drug delivery	FDM 3D printing and etching sharpening	Coated, biodegradable, loaded	[23]
Polyimide	ECG, EMG, EOG recording	Moulding in PDMS, steel MNs on printed circuit board (PCB) master	Metallized (sputter), flexible arrays	[24]
Curable magnetorheological fluid (CMRF), epoxy-based	Drug delivery	Magnetorheological drawing lithography (MRDL)	Metallized, flexible, micro-patterned arrays	[25]
Polycarbonate	Lactate detection	Injection moulding	Metallized, functionalised sensors	[26]
CMRF	ECG, EMG, EEG recording	MRDL	Flexible, metallized (sputter), laser-direct writing (LDW) patterning	[27]
Methacrylated hyaluronic acid (MeHA)	Interstitial fluid (ISF) extraction	Moulding in PDMS, steel master	Swellable, loaded, MNS for sensor integration	[28]

Polyethylene glycol (PEG)	Drug delivery	Centrifuge assisted moulding	Swellable, controllable cross-linking	[29]
SU-8 50 photoresist	Glucose monitoring	UV-curing in spinning PMDS mould, electrically discharged machined (EDM) aluminium master	Metallized (conformal sputter), functionalized	[30]
Layered Polyvinylpyrrolidone (PVP) and Poly lactic-co-glycolic acid (PLGA)	Bi-phasic drug delivery	Spray deposition in PDMS mould	Biodegradable, implantable, drug loaded matrix	[31]
PLA and PLGA	Contraceptive delivery	Centrifuge assisted moulding	Biodegradable, implantable, drug loaded matrix, bubbles	[32]
PVP	Cosmetic delivery	UV polymerization in laser written PDMS mould	Biodegradable, drug loaded matrix	[33]
Polymethyl methacrylate (PMMA)	Drug delivery	Moulding in sacrificial PVA, lithography formed electroplated PMMA master	Hollow, formed from a sacrificial intermediate mould	[34]
Polycarbonate	Antibiotic monitoring	Injection moulding	Functionalised, metallized (e-beam), passivated	[35]
SU-8 photoresist	Biopotential measurement	Moulding from PDMS, parylene-coated PDMS master	Biocompatible, passivated, metallized (vapour-deposition)	[36]
Silk fibroin	Wound healing, monitoring/sensing	Moulding from PDMS, laser engraved mould	Origami structure, patterned microfluidic, biocompatible	[37]

Polyethylene glycol diacrylate-sodium alginate and dopamine-gelatin	Drug delivery	Moulding	Nature-inspired structures for enhanced adhesion, biocompatible, swellable	[37]

From this brief summary, it is evident that polymers have been widely used for many different microneedle applications, and all devices and materials referred to in Table 1 are available in grades that comply with biocompatibility testing standards such as ISO 10993-1 and USP Class VI. To facilitate rapid development of these devices, a multifunctional manufacturing process, easily adaptable to a range of different materials and use cases, would be highly beneficial for research and prototyping purposes. With that in mind, we have previously developed a wafer-level micromoulding process for the manufacture of sharp-tipped microneedle arrays for biosensing applications [38]. In this work, we extend that process to develop a multifunctional platform that may be used to produce arrays with a variety of substrate materials, mechanical characteristics, electrical properties, and diagnostic functionalities. The platform represents a significant evolution of the original process, not only because it allows the use of degradable and swellable polymers, but also because it can accommodate the merging of several materials within the same device. Moreover, the use of a modular vacuum table, shown in Section 2.3.1, increases the production throughput, thereby scaling up the process from the original work and enabling batch production capabilities.

An outline of the platform concept and the double-sided moulding process that lies at its core is provided in Section 2.3, followed by a description of the various add-ons that are used to customise the geometrical, mechanical, electrical, and functional aspects of the arrays. Finally, we illustrate adaptability of the platform by showing its application in

three different applications, namely biomarker diagnostics, biopotential monitoring and transdermal delivery.

2.3 Platform Design

The aim of this work is to develop a multifunctional process that could easily be used to quickly prototype MN arrays for different applications. To arrive at such a one-fits-all platform, a core technique to fabricate a wide range of array types is an essential element of the entire concept. The foundation of our platform is a double-sided, vacuum casting micromoulding process, which has been adapted to the batch fabrication of polymeric wafer substrates.

Starting from this core, different 'building blocks' have been developed and may be used as required to fully customize the MN arrays. Firstly, the mould templates are tailored to the intended use case in terms of array size and shape, electrical vias, needle height, and surface topology. Then, based on the required properties of the final application, the structural polymers are selected. These different materials will provide the necessary biomechanical (such as flexibility), or functional (such as biocompatibility, degradability or optical) properties. While the process is generally implemented using a single material to form monolithic needles, in some cases the substrate and microneedles may require different properties and therefore two separate materials will be used.

If electrical functions are required, metal deposition techniques such as evaporation or sputtering may be used to define electrodes, tracks, interconnect, and functional areas. These layers typically use vias created during the initial moulding stage to establish front to rear connection without the need for a separate via formation step.

For many applications, particularly in biosensing, it is desirable to ensure that only the surfaces of the microneedles themselves are in contact with the skin [39]. Therefore,

passivation layers may also be added to the platform to block unwanted interference arising from the contact between the array substrate and the skin.

Lastly, a coating step is often required in both drug delivery and diagnostics [40]. For transdermal delivery of drugs and vaccines, arrays may be coated using a range of spraying, dipping, dropping and immersion processes with therapeutic agents that subsequently dissolve in the skin [41]. In electrochemical diagnostics, needle tips may be functionalised with electroactive analytes, such as enzymes or antibodies, that react with a specific target [42].

A summary of this multifunctional process is represented in Figure 1.

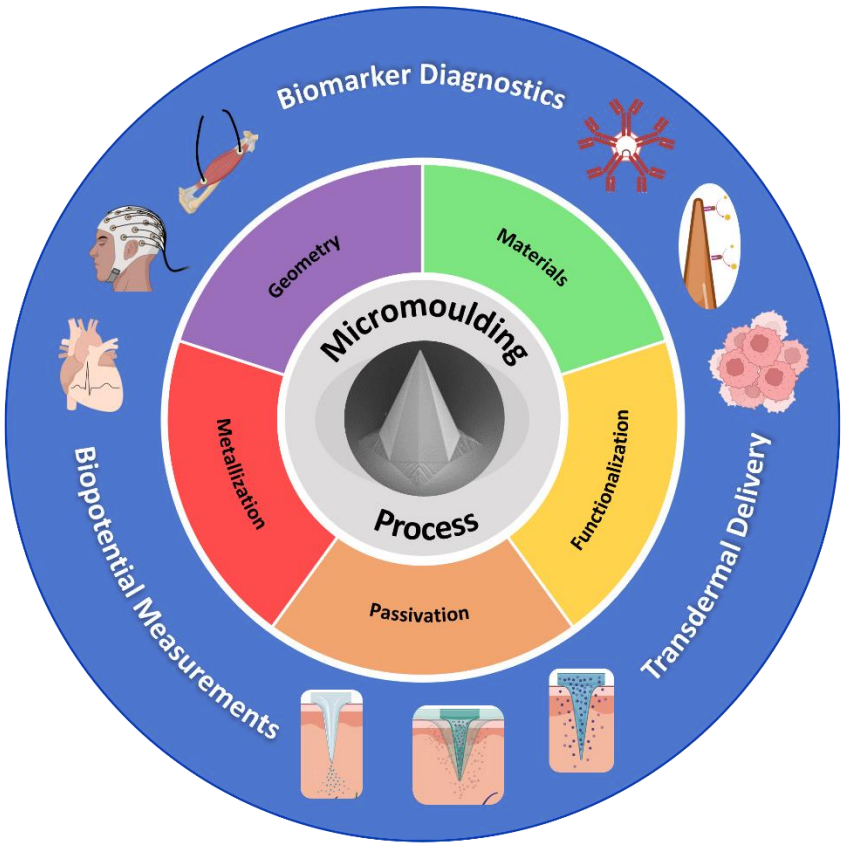


Figure 1. Schematic representation of the platform design. In the centre: SEM picture of a 500 µm tall microneedle. Adapted from image created with BioRender.com.

In the next section, the core production process will be presented, followed by a description of the additional steps that can be used to customise the platform.

2.3.1 Micromoulding Process

The micromoulding process, an early version of which was described in a previous publication [38], used two flexible, PDMS moulds to form a polymeric MN wafer. The front mould was the negative copy of a silicon master template on which 500 µm tall MNs were etched, while the rear mould was formed from a milled glass template and used to define the outline of circular, detachable arrays. This fabrication approach already simplified and sped up the manufacturing of the arrays, pre-forming them on the wafer and enabling through-wafer electrical connectivity without the need for additional wafer dicing and interconnect steps.

In this paper, the technique has been expanded to accommodate the use and combination of different materials and master templates, Figure 2.

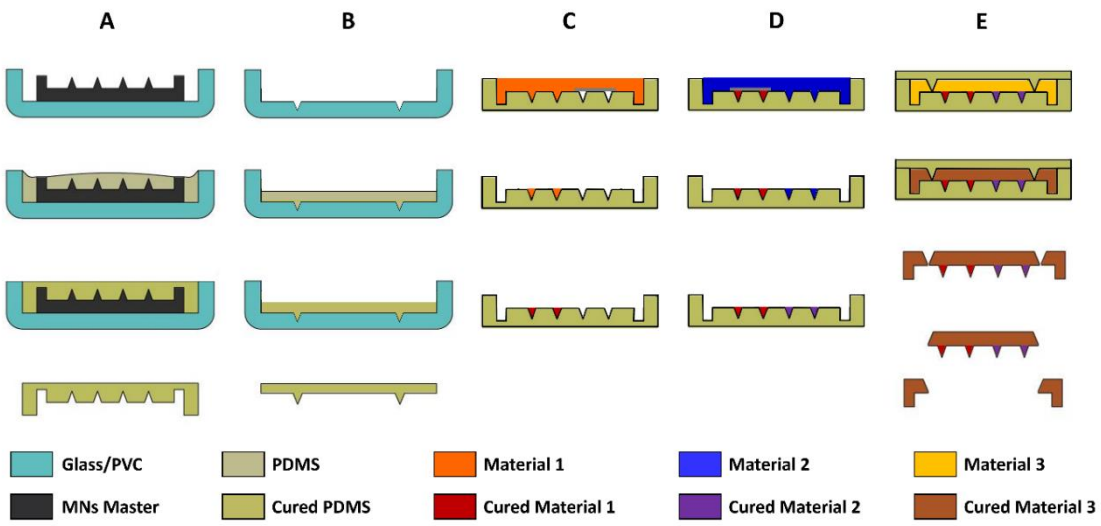


Figure 2. Schematic of the core production process used to form MN arrays. In this example, microneedles are moulded from two different materials on a substrate of a third material. After preparing the front and rear moulds (A and B, respectively), the MNs (C and D) and the substrate (E) are formed using the desired materials. The shape of the arrays is dictated by the rear mould design while the materials are selected based on the desired properties of the device. To populate the array with different type of needles, tape is used to selectively protect areas of the front mould (C and D) as needed.

Similarly to the original process, two moulds are made by mixing PDMS (Sylgard 184 Silicon Elastomer Kit, Dow Chemical Company, MI, USA) according to the manufacturer's instructions and pouring it over the front and rear master templates, which may be formed from any desirable process or material. The front template defines needle geometry, pitch, and surface topology, while the rear template defines array shape and size, through-wafer vias, and, when needed (see Section 2.3.3), marks for mask alignment. After cooling, the PDMS moulds are removed from the templates (Figure 2A and Figure 2B). The polymer of choice is then poured on the front mould which is placed on a customised vacuum table (VT), shown in Figure 3.

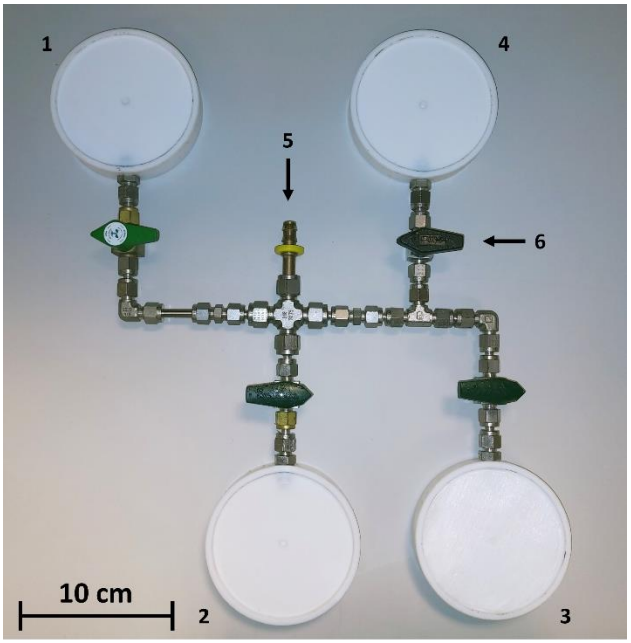


Figure 3. Modular vacuum table equipped with four polytetrafluoroethylene (PTFE) vacuuming stations (numbered 1 to 4). A vacuum can be applied to the entire table via the general inlet (5). Each station can be individually disconnected from the vacuum simply closing the corresponding valve (6).

Since PDMS is permeable to gases [43], application of negative pressure to the rear of the PDMS layer can aid in drawing the material into the mould, thereby aiding in filling of the cavity tips and improving microneedle sharpness. In this case, the VT is connected to a negative pressure source of approximately 1 bar, which is usually maintained for a minimum of 20 minutes. The VT was designed using a modular format to easily scale up the production throughput at laboratory level, together with enabling parallel testing of different material formulations or production conditions. This is an improvement over the previously used process, which could handle the preparation of a single wafer per iteration [38]. At present, the production of a batch of up to 4 x 100 mm diameter substrates is possible, although this could be extended as required by connecting additional stations to the VT. If needed, less than four wafers may be processed simply closing the valves of

the unused stations. The production of a batch of four wafers can be used as a practical example to highlight the advantages of the modular VT over the previous process. In the previous single-wafer production, the polymer of choice was prepared, sandwiched in between the PDMS moulds, positioned on the VT, and then cured. This process was carried out one wafer at the time. Excluding curing, each wafer took a total of 25 minutes to mould: 5 minutes preparation time, and a further minimum time of 20 minutes on the VT. When using the modular VT, a proportionately larger quantity of polymer was prepared and subsequently divided over the four different front moulds. Similarly, by having 4 vacuuming stations, all wafers were simultaneously exposed to low pressure for 20 minutes. Therefore, only 25-30 minutes were required for the production of the four-wafer batch, resulting in significant time savings over the singular approach.

If a monolithic device is required, the rear mould may be placed over the uncured polymer at this point. A metallic cylinder, weighting 500 g, was applied to the rear of the mould-polymer-mould stack aids in ensuring that the two moulds come into intimate contact over the entire area. The arrays are finally hardened by either curing or drying the polymer as required before removal of the moulds.

If a bilayer construction is preferred, excess material is removed with a spatula (Figure 2C) whilst the mould is on the vacuum table, as the negative pressure helps to retain polymer within the MN pockets during the removal process. The needles are then cured or dried before the application of the substrate material (Figure 2E). This deposition and removal step can be repeated several times to fabricate needles from a variety of different materials on the same array. In this case, a temporary layer, such as Kapton tape, is applied to either block off selected areas of the front mould (Figure 2C) or to protect the previously formed MNs while casting and removing the second polymer (Figure 2D). Depending on material requirements, the needles are either UV/heat cured or dried at

room temperature, and the substrate layer is then applied (Figure 2E). If needed, materials such as pre-formed films, components or fabrics may be used as a substrate instead of a mouldable polymer. In this case, these materials are pressed against the polymer needles before curing. A video, included as supporting information, provides a visual representation of the process, showing the different steps in detail.

2.3.2 Geometry

It is essential that the platform allows full control over the geometrical design of the moulded MNs. This may be done in two ways: by changing the master templates used in the core process and, if any electrical functionality is needed, by defining appropriate masks for the metallization (see Section 2.3.3).

The front master template defines the shape, pitch, and height of the MNs. In addition to conventional microfabrication techniques such as silicon etching, the development of additive manufacturing technologies has enabled the precise fabrication of microscopic structures. Several groups have used this approach to print MNs that are either too expensive or too difficult to produce using tradition silicon-based processes [6], [44], [45], [46]. It is of paramount importance that the core moulding process is capable of precisely replicating these complex structures. Therefore, a total of four different designs have been used to fully evaluate the moulding capabilities of the fabrication procedure: 1) Tyndall's silicon MNs, wet-etched from a 100 mm diameter wafer to form 500 µm tall octagonal pyramids with a pitch of 1750 µm [47]; 2) 3D printed conical MNs also with a height of 500 µm and a pitch of 1750 µm, but with a 60 µm reservoir designed close to the tip. These arrays were produced by Upnano (Vienna, Austria) using an NanoOne printer with a 10x objective and UpPhoto resin; 3) 3D printed needles slanted at an angle of 60° to the horizontal, at a pitch of 615 µm between needles, 1050 µm between MN

rows, and designed with 4 different heights (165, 345, 555 and 775 µm respectively). These arrays were produced by Boston Micro Fabrication (BMF, Maynard, USA), using a 2 µm resolution S130 printer and HTL-Y resin; 4) microneedles designed by Johannes Kepler University Linz (JKU) in the shape of 210 µm tall square pyramids incorporating a surface pattern of biomimetic features as small as 2 µm, intended to aid the transport of liquids over the needle surface for coating purposes. A 515 nm laser with a 290 fs pulse and 1 MHz repetition rate was used to produce the patterned MNs in OrmoComp resist [46].

All designs were glued to a support that was printed using a Formlab 3+ printer (Solid Print3D Ltd, UK) and white resin (F2GPWH04 from Solid Print3D Ltd, UK), and attached inside a petri dish to form the master template. A medical grade epoxy (Epotek 353ND from Epoxy Technology Europe GmbH, Augsburg, Germany) was used to mould the needles. SEM pictures of the results can be seen in Figure 4. The moulding process copied all features of the masters with a high degree of fidelity, proving its usability with different types of templates.

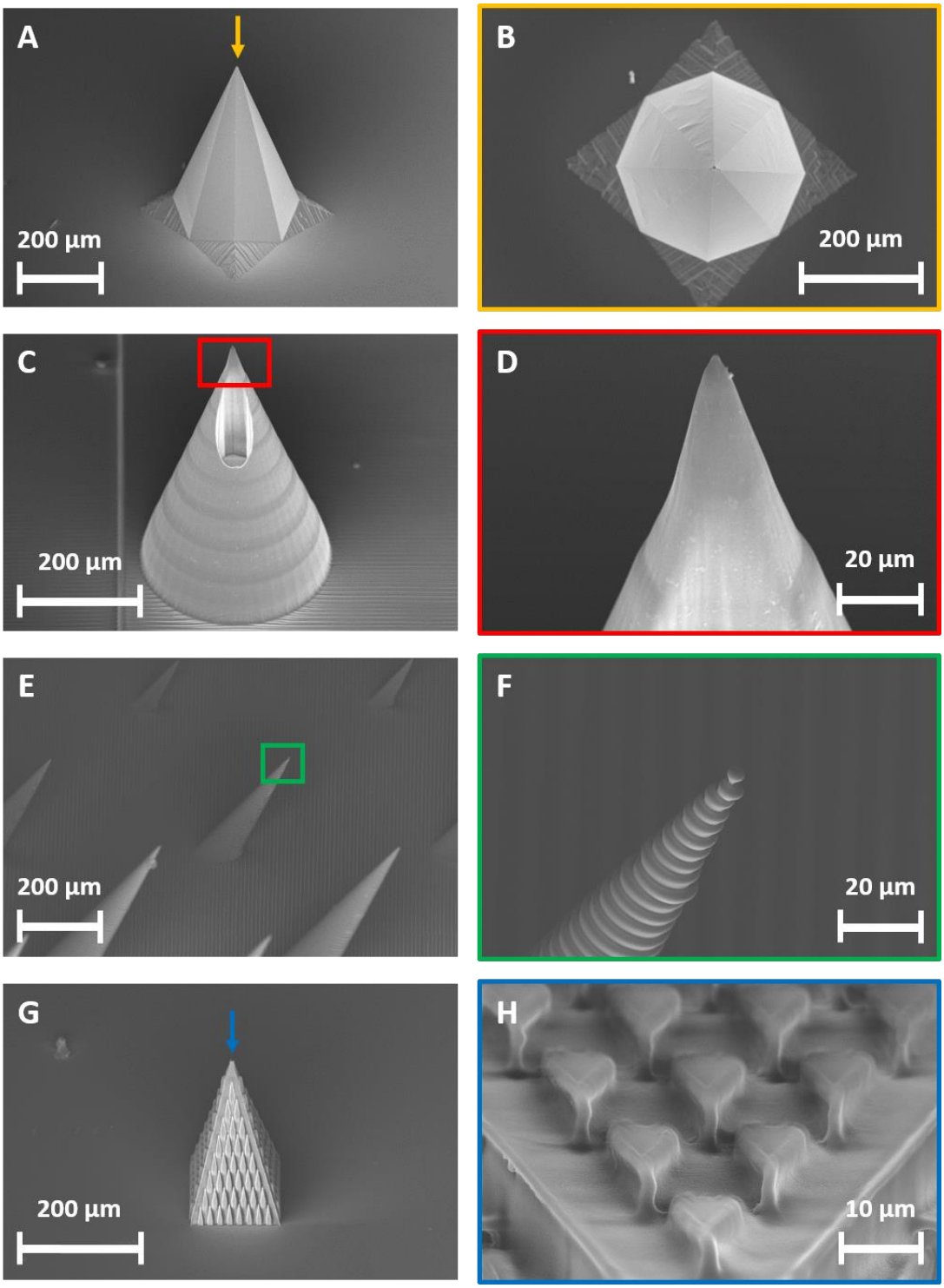


Figure 4. Different type of moulded MNs: Tyndall's MNs (front, A, and top view, B), Upnano-printed MNs (front side, C, and magnification of the tip, D), BMF-printed MNs (front side, E, and magnification of a tip, F) and JKU's MNs (front side, G, and top magnified view of the pattern, H).

Figure 5 shows examples of both a front and a rear mould, together with close ups of some of the key features. While any suitable process or material can be used to form the rear master template, in this example the desired profile is milled inside a polyvinyl chloride (PVC) Petri dish. To facilitate front-to-rear electrical connection using holes or vias moulded through the polymer, 45°-angled conical cavities were milled on the rear master, Figure 5C. To help achieve optimal via formation on the wafer, the resulting PDMS cone should be designed to be 25% higher than the rest of the profile; the PDMS compresses slightly once the two moulds are brought into contact, ensuring intimate contact between the surfaces, and alleviating the risk of unwanted polymer blocking the via channel. Electrical links between the faces of the arrays can then be achieved by simply metallizing both sides of the substrate and vias. Similarly, additional features, such as alignment marks (Figure 5D), can be milled into the master if required.

The rear master also defines the shape of the arrays using ridge-like features, and short gaps in these ridges, Figure 5E and Figure 5F, are used to form tabs that hold the moulded array to the carrier frame of the wafer. Light finger pressure or pick-and-place tools may subsequently be used to detach the arrays from the frame.

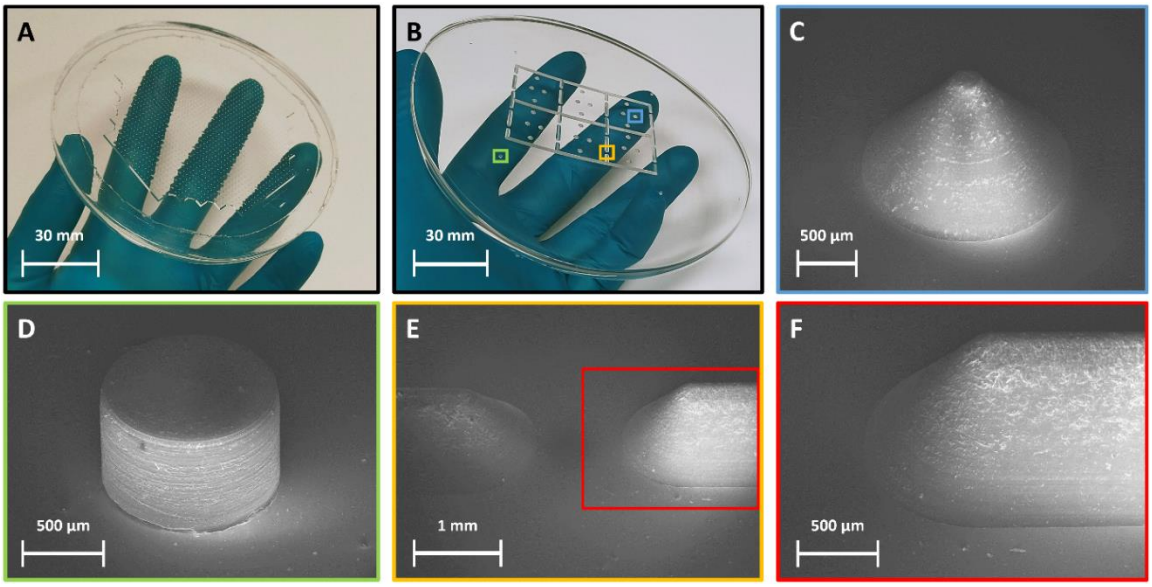


Figure 5. PDMS moulds produced from the front (A) and the rear (B) master. SEM pictures of the distinctive features present on the rear mould: cones for front-to-rear via formation (C); cylindrical alignment marks (D); ridges with gaps (E, F) to define the shape of the array and the tabs that hold the arrays to the wafer frame.

2.3.3 Metallization

A metallization step is necessary to make electrically functional MNs for use in applications such as biosensing, biopotential monitoring, iontophoresis, or electroporation. Different metals can be used for different purposes. For example, gold (Au), platinum (Pt) and silver (Ag) are commonly used for sensor development, while titanium (Ti) and chrome (Cr) are usually implemented as adhesion layers to strengthen the bond between other metals and the substrate. Two main techniques can be used to deposit a thin metallic layer over the arrays: chemical vapour deposition (CVD) and physical vapour deposition (PVD).

CVD processes chemically drive a reaction on a substrate. There are two main CVD technologies: low-pressure CVD (LPCVD) and plasma-enhanced CVD (PECVD). The

deposition is thermally induced, and therefore, it heats up the substrate itself. LPCVD uses temperatures higher than 600 °C to slowly grow homogeneous layers on the material. On the other hand, PECVD operates at lower temperature, typically between 200 °C and 400 °C, but the film growth is faster and therefore less precise [48]. Our platform uses polymers to form the MNs. Polymers generally have low glass transition temperatures and melting points. Therefore, CVD processes are not suitable as main metallization technique.

PVD processes aim at freeing material from a metal source and transferring it directly on the substrate. Typical PVD techniques include thermal evaporation [48], [49], electron beam (e-beam) evaporation [49] and sputtering [48]. Thermal evaporation heats up the source material and generates a vapour flux from the source to the substrate. Since this method is generally used for low melting point metals and it is not ideal for the fabrication of thin layers [50], it is not a suitable option for use with this platform. E-beam uses high energy electron beams to vaporize even high-melting point metals [49], while sputtering bombards the source with particles to free atoms or molecules that can condense on the substrate [48]. E-beam evaporation and sputtering are both viable options for polymer MNs metallization and this is clearly visible from Table 1.

Finally, metals can be deposited using electroplating. Electroplating is an electrochemical deposition technique that produces a metal coating on an electrically conductive material [50]. However, polymers are generally not electrically conductive and therefore would require a preliminary metal coating in order to be electroplated [51]. Therefore, this method will not be considered as a primary metallisation step in this work.

Both e-beam and sputtering were investigated for MNs metallization. The systems used in this study were a Quorum Q300TD (Quorum, UK) sputterer and a Temescal EUFC4900 (Ferrotec, USA) e-beam evaporator. Both techniques can be used to

completely cover the substrates with a metal layer. However, when a specific metallic pattern has to be deposited on the MN arrays, a mask must be used. To avoid damaging the needles, no mask can be place in contact with the tips. Therefore, any metallization must be carried out using the mask in close proximity with the substrate, potentially exposing the wafer to deposition of the metal beyond the desired masked area and leading to a spreading or blurring of the intended feature [52]. This effect is similar to photolithographic diffraction when exposing in proximity. Polymer MN wafers were produced and metallised with patterned aluminium masks to test the severity of this effect with both techniques. Tyndall's 500 µm tall silicon MN wafers were used as a front master template. The rear master template was formed as described in Section 2.3.2 and was designed to divide the wafer into four rectangular arrays, each provided with four through-vias to enable multiple front-to-rear electrical connections. The masks were formed by milling test patterns, Figure 6A, in 100 mm aluminium disks. The original thickness of the disks was 1.1 mm, into which a 100 µm deep central recess was milled to avoid physical contact between the mask and the tips of the MNs. Therefore, when the mask is pressed against the wafer, it is 100 µm and 600 µm away from the tip of the needles and from the substrate, respectively. Two masks were used to metallise each wafer: one positioned in hard contact with the rear of the substrate while the second, exploiting the recess, was positioned over the front side of the MNs. The masks were aligned with the wafer and affixed to it using Kapton tape (Farnell, Ireland). Ti and Pt were deposited as test materials, in thicknesses of 20 nm and 100 nm respectively. No significant difference between the mask designs and deposited patterns was observed either for the masks in hard contact with the rear of the wafer, or for the e-beam proximity-masked deposition on the front. However, as shown in Figure 6B, sputtered patterns showed a high degree of spreading, leading to a significant loss of precision.

To quantify this loss, the resulting test pattern dimensions were measured with a Vernier caliper and compared with the designed mask dimensions. The deposited pattern had dimensions that were (0.8 ± 0.2) mm greater than those of the mask, i.e. a metal spreading of 0.4 mm on each edge was observed. This is an issue both because of the lack of precision and because of the potential for unwanted electrical connections between interconnects or electrodes. The length or the direction of the feature did not seem to affect the magnitude of the spreading. Therefore, smaller features will be proportionally less precise than bigger ones.

To solve this problem, the mask can be undersized to compensate for the metal spreading. Based on the previous analysis, a new metal mask was designed, reducing the size of each dimension by 1 mm. This new mask was intended to form a biosensor on the MN arrays, incorporating one rectangular reference electrode (RE), two square working electrodes (WE) and a counter electrode (CE) wrapping around the other three. The fabricated mask and the resulting sputtered metallization patterns can be seen in Figure 6C and Figure 6D respectively.

The smaller openings produced electrode dimensions closer to the target designs; the metallised pattern had dimensions (0.3 ± 0.1) mm smaller than intended. Further iterations are likely to reduce this remaining error further. The sensors were then tested using a multimeter both to check the quality of the front-to-rear electrical path and to assess unwanted inter-electrode connections. The resistance of the front-to-rear connection established by the through via was consistently below 25 Ω. However, undesired inter-electrode connections, with electrical resistances ranging from tens of kΩ to a few MΩ, were observed. Although this may not be a problem when electrodes are distant from each other, it could become an issue when the form factor of a sensor has to be minimised and the electrodes are, like in this case, closely packed. This effect is also assumed to be due

to spreading of the metal in the gap underneath the mask and was not observed when e-beam evaporation was used as a deposition technique.

As an additional measure to physically prevent any undesired metal spreading, pattern blurring and unwanted electrical connections during the sputtering process, wall-like features were incorporated at the edges of the mask openings. These protrusions must come into hard contact with the substrate in between the MNs without touching the needles themselves. An iterative process for sizing the walls has led to walled features of 600 µm deep, accounting for both the recess and the needle height, and a thickness not higher than half the base-to-base distance between MNs. Using a walled mask (Figure 6E), the resulting sensor (Figure 6F) showed no inter-electrode electrical connections.

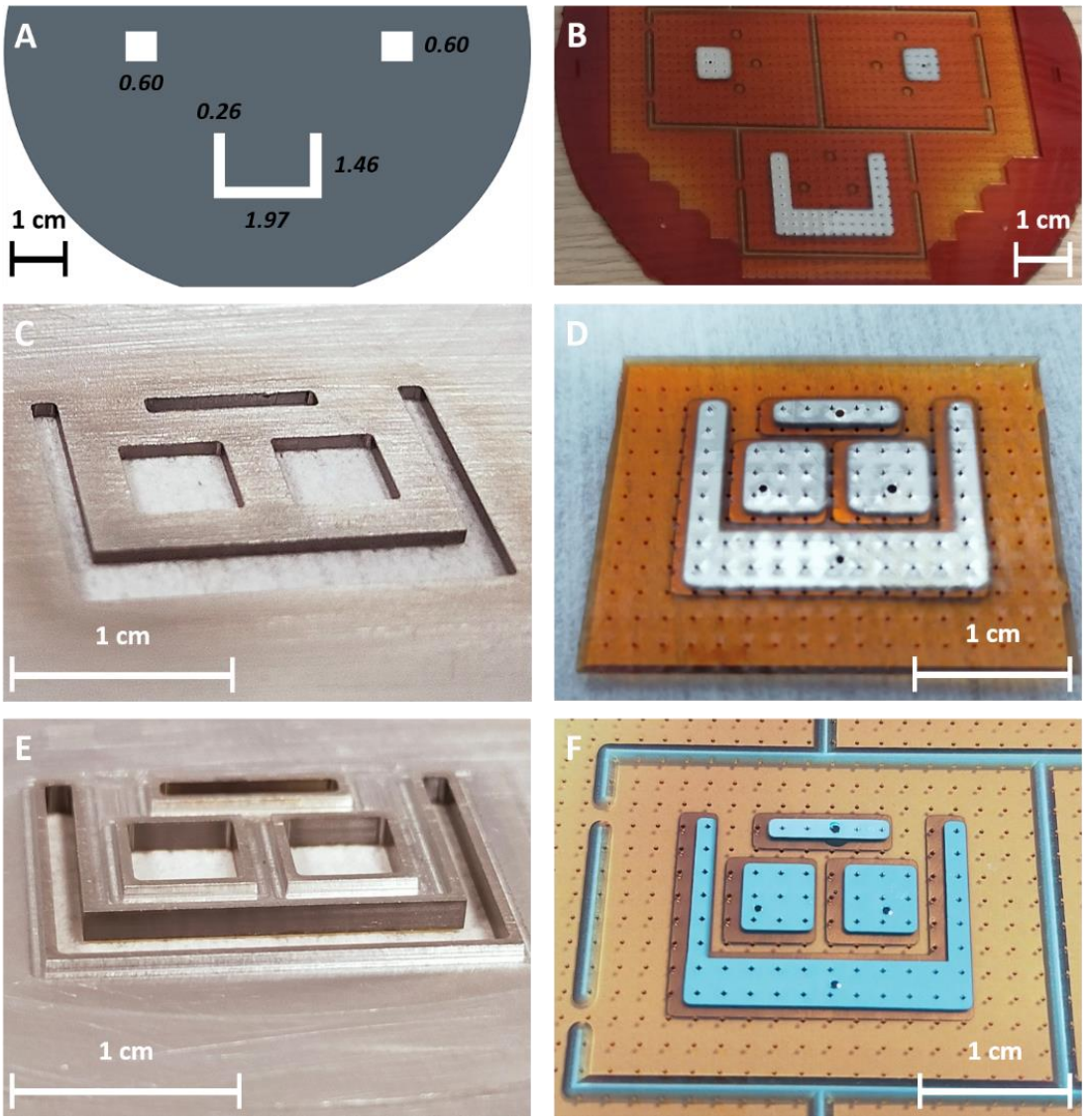


Figure 6. (A, B) Initial test mask design (features dimensioned in cm), together with resulting sputtered metal pattern – note the blurred patterns due to spreading of the metal under the mask. (C, D) An undersized metal mask with associated metal pattern – some blurring is still visible although the dimension accuracy has improved. (E, F) Undersized mask incorporating protruding walls intended to prevent unwanted metal spreading, along with resultant biosensor electrode pattern.

In summary, e-beam is the preferred metallization technique due to its high precision and lack of metal spreading underneath the mask. Sputtering may also be used, although the high level of metal spreading may lead to dimensional inaccuracies and limit its use for densely packed features. The implementation of wall-like structures on the masks may be used to prevent this problem but increases the complexity and, consequentially, the cost of the masks.

2.3.4 Materials

Although the platform may be used to simply form monolithic wafers, different substrate and/or microneedle materials may be combined as required. The MNs themselves must be made with a mouldable material and be robust enough to pierce the skin without breaking. For the purposes of this work, a polymer was considered mouldable if its viscosity was not more than approximately 5000 cPs at room temperature. Additional properties that may be of interest for the MNs are biocompatibility, biodegradability, and absorption capabilities. To date, a range of polymers have successfully been used at the core of the platform, including a medical grade epoxy (Epotek 353ND from Epoxy Technology Europe Ltd, UK) [53], a UV curable medical grade photopolymer (NOA 68 from Edmund Optics, UK) [54], several degradable polymers including polyvinylpyrrolidone (PVP), polyvinyl alcohol (PVA), PVP-PVA mixtures, polycaprolactone (PCL), poly(lactic-co-glycolic acid) (PLGA), PCL/PLGA mixtures, sugars including trehalose anhydrous (TRA) and sucrose (SUC), and swellable hydrogels including Gantrez S-97 and Gantrez AN-139 cross-linked with PEG – PMVE/MA and PMVE/MAH respectively. Following the core process outlined in Section 2.3.1, all materials were firstly prepared as required, poured on the front mould, and then positioned on the VT. The excess material was removed, the needles were either cured or dried, and

then coupled with a substrate polymer and rear mould. Alternatively, the substrate material was pressed against the MNs after excess removal and the stack subsequently cured (see below).

Desirable properties for the substrate include biocompatibility and flexibility. Biocompatible polymers have been already demonstrated in the implementation of the core process [35]. Regardless of the polymer of choice, accredited testing should be undertaken to certify that the combination of materials used in the final device is biocompatible according to ISO 10993 standards for cytotoxicity, irritation, and skin sensitization. Flexibility can be implemented using a mouldable polymer, a flexible film or textile. The only constraint for the choice of the substrate material is that it must bond to the MN material. Three main materials were successfully used as flexible backing substrates: a low viscosity epoxy (Epotek 310M from Epoxy Technology Europe Ltd, UK), a conductive fabric (NCS95R-CR from Marktek Inc, Chesterfield, USA) [10] and a thermoplastic polyurethane (TPU) sheet (ST604, Bemis Associates Inc, Shirley, USA) [55].

As mentioned during the description of the core moulding process, the epoxy was poured on the rear of the needles, the rear mould added and then the material was cured to form the hybrid wafer. Non-adhesive materials such as films or fabric must be applied to the mould before the microneedle material is cured or dried.

To demonstrate the capabilities of the platform to produce multi-materials arrays, a patch combining three different types of MNs was produce as shown in Figure 7.

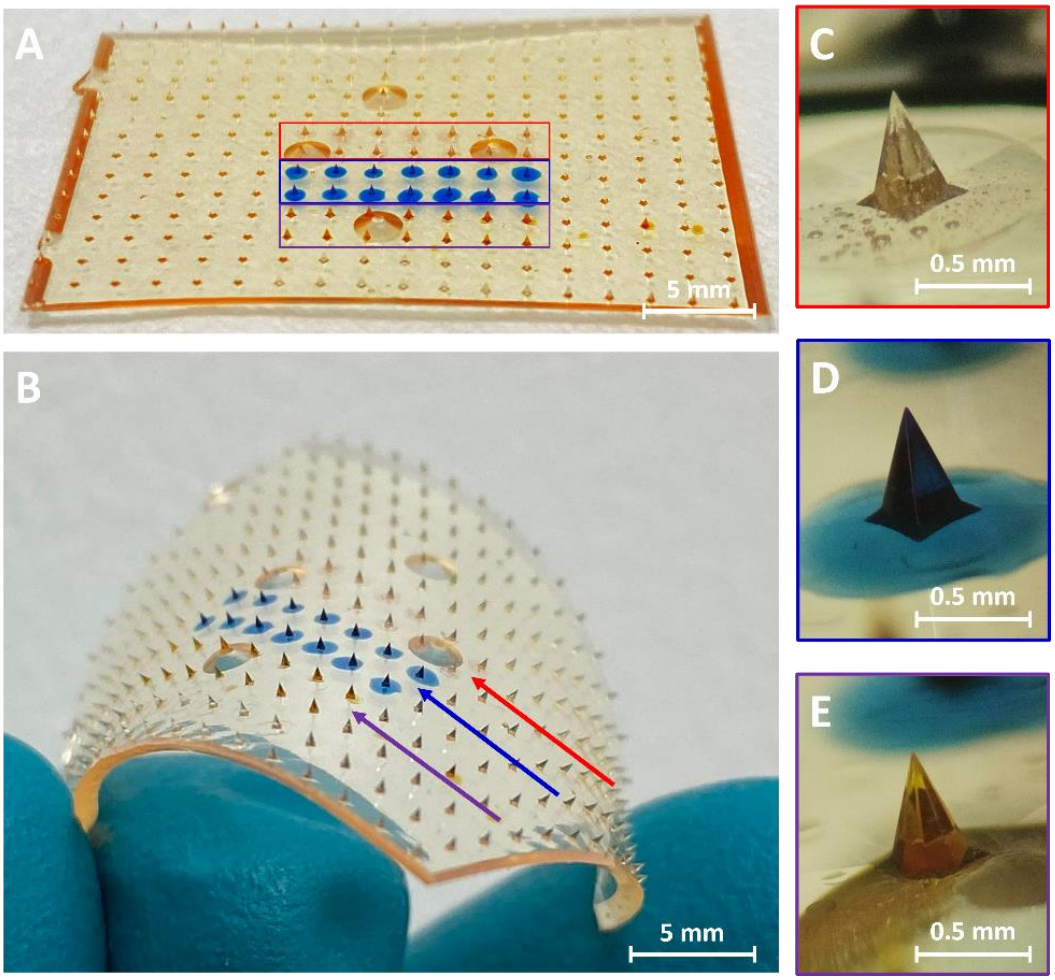


Figure 7. MNs array (A and B) produced merging together different materials: a UV-curable polymer (NOA 68 - C), a methylene blue loaded PVP-PVA degradable mixture, and a medical grade epoxy (Epotek 353ND) were integrated on a flexible epoxy substrate (Epotek 310M). The different MNs are highlighted using red, blue, and purple arrows, respectively.

The array combines medical grade (Epotek 353ND, Figure 7E), degradable (PVP-PVA loaded with methylene blue, Figure 7D), and UV-curable (NOA 68 coloured with a red dye to highlight the different material, Figure 7C) MNs. Two rows of seven needles were formed for each material, also proving the spatial selectivity achievable with the platform. These needles were bonded to a flexible backing formed with Epotek 310M.

2.3.5 Passivation and Coating

In addition to all the aspects shown so far, some extra features, such as passivation of the array, functionalization of the needles, chlorination of the metal or sterilization of the patch may be needed for the intended application.

Passivation may be desirable for multiple purposes on MN-based devices: it is often used to geometrically define the areas of the electrodes [56], remove interferences coming from the array substrate or non-targeted body fluids [20], or selectively expose only part of the needle body [57]. MNs can be passivated using a variety of different techniques and materials, including spin-coating of different polymers such as OrmoComp [20] or polyimide [58], chemical vapour deposition (CVD) of parylene [57], or direct casting of varnish [35] or SU-8 [58]. We have further investigated, characterized and compared different passivation techniques in a previous work [39].

MNs can be coated for transdermal drug delivery [40], [41], or be functionalised in a variety of different ways to detect specific biomarkers [9], antibodies [59], drugs [35], or characteristics such as skin pH [20]. Functionalization is the key to producing MN-based biosensors, which provides unique advantages due to their minimally invasive nature [42], [60]. An electrochemical sensor is usually comprised of one or more working electrodes (WEs), responsible for the detection of the desired biomarker, a counter electrode (CE) and a reference electrode (RE). The CE is used to apply the input potential to the WE [61] while the RE is needed to provide a constant potential to be used, as the name suggest, as a reference for the measurement [62]. Silver/silver-chloride (Ag/AgCl) is commonly used as a RE material, achieved by depositing Ag in various ways and then chlorinating it with Cl-based solutions [53], [63], [64], [65].

Because of the nature of their applications, sterility is an important consideration for MN devices. Several methods can be used as sterilization techniques, divided into those that require high temperatures, low temperatures or are based on the use of liquid chemicals. High temperature techniques can either use steam or dry heat while low temperature procedures use gasses, ozone, pulsed light or radiation [66]. Considering that our platform is based on polymer materials, usually vulnerable to high temperatures, the use of low temperature techniques is advised, and the effects of sterilisation procedures on the structural properties of the microneedles, as well as on the efficacy of the coating layers, should be thoroughly characterised.

2.4 Exemplars

The capabilities of the platform were demonstrated using three exemplars, each targeting one of the main medical application areas for MNs.

2.4.1 ELSAH Biosensor

MNs have the potential to enable the next generation of wearable systems for minimally invasive continuous glucose monitoring [9]. The ELSAH project (funded from the European Union's Horizon 2020 research and innovation program under grant agreement No 825549) developed a MN-based, integrated wearable sensor system for simultaneous glucose and lactate detection in ISF. MN wafers based on Tyndall's MN template were produced using 7 g of Epotek 353ND; each wafer was divided into six 19 x 21 mm^2 rectangular biosensors. Custom metal masks were used to form two working electrodes (WEs), one counter electrode (CE) and one reference electrode (RE) on each sensor. Front-to-rear electrical connection was achieved by exploiting the conical through-wafer vias described earlier. Both WEs, the CE and the rear metallization were formed by depositing 20 nm of Ti and 100 nm of Pt whilst 30 nm of Ti, 60 nm of nickel (Ni) and

150 nm of silver (Ag) were used for the RE. The metal layers were all deposited using a Temescal EUFC4900 (Temescal, USA) e-beam evaporator. The RE was then chlorinated by exposing the Ag to a 15% solution of sodium hypochlorite for 10 seconds. The solution was then washed away with ultrapure water and the sensor dried using a nitrogen gun. A fully metallized and chlorinated ELSAH biosensor wafer is shown in Figure 8.

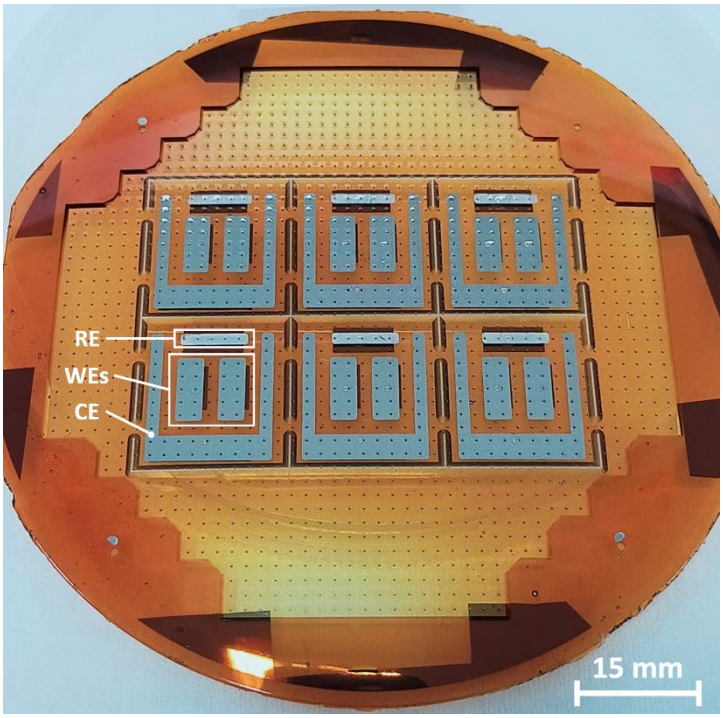


Figure 8. An epoxy ELSAH wafer. All 6 biosensors have been metallized and the REs chlorinated.

On each of the six sensors, a 5 x 1 MN RE is visible above two rectangular 5 x 2 MN WEs. A U-shaped CE is wrapped around them. Loctite EDAG 7019 (Henkel, Düsseldorf, Germany), a conductive Ag/AgCl ink, was used to fill the through-vias, ensuring a reliable front-to-rear electrical connection. The WEs were treated with a cysteamine hydrochloride solution (104 mg in a mixture of 7.6 ml physiological phosphate-buffered saline – PBS – solution and 2.4 ml glycerol) to improve the adhesion of the subsequent enzyme-based functionalization. For the passivation of the non-sensing areas, a medical

grade tape (ARcare 7759, Adhesives Research, Limerick, Ireland), was cut to size and patterned with circular holes of diameter (760.4 ± 0.6 µm, n = 5) to match the MN pitch. A Speedy 360 laser cutter from Trotec (Marchtrenk, Austria) was used for cutting the tape. After manually applying the passivation, the sensors were ready for modification. Direct electron transfer (DET) enzymes Glucozyme and Lactazyme (developed and supplied by DirectSens GmbH Vienna, Austria) react with glucose and lactate respectively, and were added to two different poly(3,4-ethylenedioxythiophene) polystyrene sulfonate (PEDOT:PSS) inks formulated and deposited by AIT Austrian Institute of Technology GmbH (AIT, Vienna, Austria). A BioDOT AD1520 dispenser (BioDot Limited, Chichester, UK) was used to locally deposit the inks directly on the individual MNs. The deposited volume per WE was 150 nl for glucose detection (ink formulation: 38.3 µl water with 0.6 mg bovine serum albumin (BSA) and 4 mg Glucozyme, 89.4 µl PEDOT 1.1% (w/w)) and 600 nl for lactate detection (ink formulation: 17 µl water, 13.2 µl PEDOT 1.1% (w/w), 51.8 µl Lactazyme 7.9 mg ml^{-1} in water). Finally, a protective poly(ethylene glycol) dimethacrylate (PEG-DMA) based hydrogel layer [53] was dispensed on the needles using the BioDOT AD1520. This layer acted as a protective layer for the functionalization underneath [67]. 3 x 50 nl and 2 x 250 nl of hydrogel ink per needle were used for glucose and lactate modified WEs, respectively. After deposition, the ink was crosslinked using a UVP CL-1000 UV crosslinker (Analytic Jena US LLC, Upland, Canada), washed with PBS and dried under vacuum conditions. After the drying process, the hydrogel layer forms a stiff, thin (µm-range) layer on the microneedles, which swells when it comes in contact with ISF.

To be used on humans, the sensors must be sterilised, and the impact of sterilization was evaluated by preparing a batch of sensors, eight functionalised (both WEs) for glucose detection and eleven for lactate detection. Four sensors per type were then individually

sealed inside an aluminium-coated bag together with a silica gel bag (1 g). The sensors were e-beam sterilized at 25 kGy by Mediscan GmbH (Seibersdorf, Austria). Before and after sterilization, the sensors were stored at 4 °C. The remaining control sensors were sealed in similar fashion and also stored at 4 °C. *In vitro* chronoamperometric measurements were performed on both sterilized and unsterilized biosensors. Solutions of glucose and lactate in PBS were used with concentrations varying between 0 and 30 mM, Figure 9. A reduction in the maximum current of -49% and -68% after sterilisation can be observed for glucose and lactate biosensors respectively. Furthermore, a reduced current resolution compared to the unsterilized biosensors was detected. However, the final resolution of the glucose biosensors in the concentration range of 2.5 - 10 mM with 8 nA mM^{-1} and the final resolution of lactate biosensors in the range of 0 - 2.5 mM of 599 nA mM^{-1} will be sufficient to test ISF concentrations [68], [69] in healthy volunteers during a planned *in vivo* study.

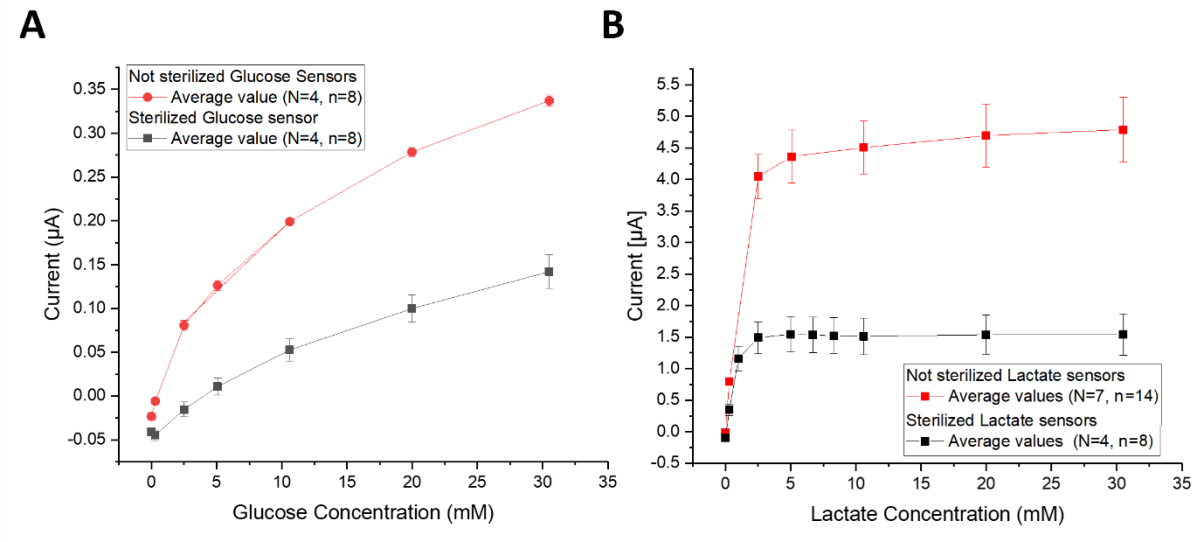


Figure 9. Calibration curves of unsterilized and sterilized biosensors in the 0 - 30 mM glucose (A) and lactate (B) range in PBS solution. N represents the number of sensors used for testing and n the total number of modified WEs.

The difference between sterilized and non-sterilized sensors is caused by a reduction in enzyme activity. This has already been reported for microneedle-based biosensors with glucose oxidase sterilised by gamma irradiation with a dose of 25 kGy [70]. More recently, enzyme activity tests combined with circular dichroism showed that gamma irradiation induces a loss in enzyme activity in both glucose oxidase and cellobiose dehydrogenase (CDH) enzymes [71], used in this work. Also, it has been demonstrated that a very low irradiation flow rate (25 kGy applied at 260 Gy h^{-1} for 96 h instead of the standard 1670 Gy h^{-1} for 15h) can help preserve the sensor performances [71]. Therefore, in preliminary tests, we compared the impact of 25kGy e-beam and gamma irradiation at standard irradiation flow rates on the sensor performance/enzyme activity. E-beam irradiation had less impact, and it was consequentially chosen for this work.

Sensors were prepared for the volunteer study following the same protocol and glued with medical grade adhesive (Loctite 4011, Henkel, Düsseldorf, Germany) to a 3D printed disk, functionalised, and e-beam sterilised. The sensors were then inserted inside a 3D printed enclosure, interfaced with a printed circuit board for sensor readout and wireless communication, and tested for glucose and lactate detection on 30 healthy volunteers by the Medical University of Graz (MUG, Graz, Austria). Pictures of the system are shown in Figure 10. The 3D printed disks and enclosures were produced by Sanmina (Fermoy, Ireland) using a Tough 1500 resin and a Form 3B printer (both from FormLabs GmbH, Berlin, Germany). A PCB, equipped with a potentiostat on chip, near field and ultra-high frequency communication (NFC and UHF respectively), was built by Infineon Technologies Austria (Villach, Austria) [72]. Full details of the study and associated data will be reported in a future publication.

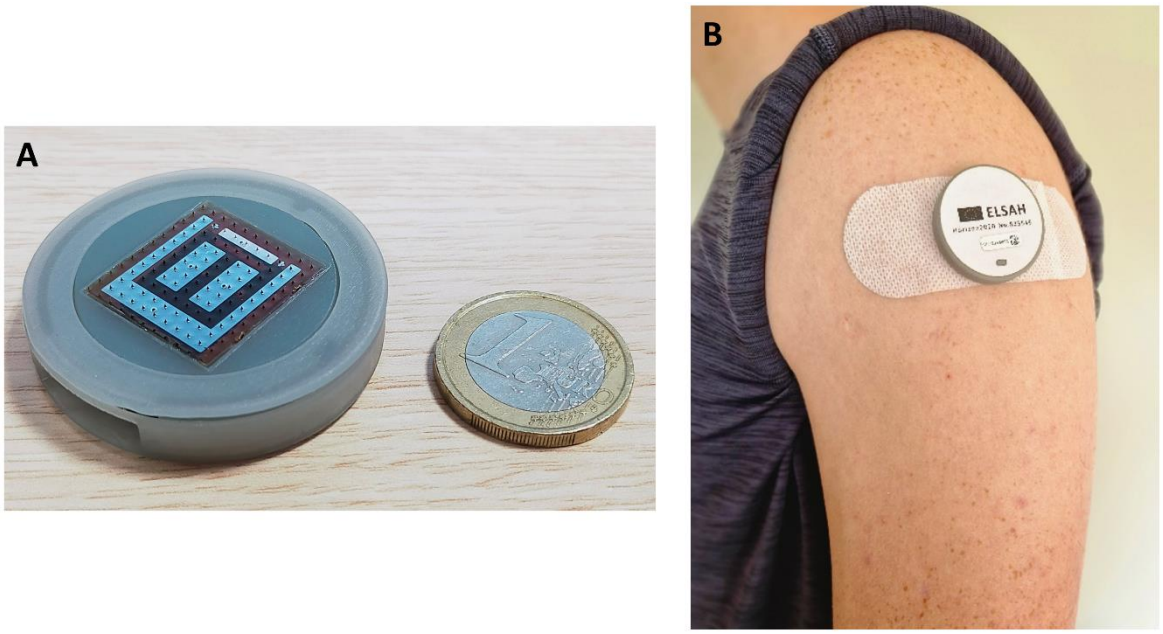


Figure 10. ELSAH system used for *in vitro* testing (A) and final device affixed to the arm of a volunteer (B). There is no size difference between the testing device and the final device.

2.4.2 Fabric-based ECG Electrodes

Microneedle-based 'dry' electrodes have significant potential for use in biopotential recording applications because of their ability to create a low impedance interface with the skin and bypass some of the problems, such as the need for skin abrasion, shaving and the use of a wet gel, that are associated with conventional gel-based electrodes [21]. Using the platform outlined earlier, we developed and characterised a flexible MN-based dry electrode for electrocardiogram (ECG) recording. Epotek 353ND was used to form the needles. As explained in Section 2.3.1, the front mould was placed on a VT and the excess material removed. A conductive fabric was patterned into 18 mm diameter circular electrodes and cut to shape to fit the needle mould. A Cricut Maker (from Cricut, South Jordan, USA) cutting machine was used for this operation. The fabric substrate was then pressed against the MNs mould, and the epoxy was cured at 80 °C for 1 hour. Once peeled

away from the mould, flexible electrodes with rigid MNs bonded to the conductive fabric were formed (Figure 11A). 20 nm of Ti and 150 nm of Au were used to metallise the MN side of the newly formed arrays, while front-to-rear electrical connection was self-realised around the sides of the electrodes. For characterisation purposes, commercially available Red Dot 2239 electrodes (3M, Ireland) were stripped of their gel pads and used to build the dry electrodes: the circular arrays were detached from the wafer and glued to the modified Red Dot with a medical grade conductive glue (Epotek Med-H20E from Epoxy Technology Inc, USA). The glue was cured according to manufacturer's instructions and the electrodes sterilised with a ProCleaner Plus (Bioforce Nanoscience, USA) ozone cleaner. To compare electrode performance with commercially available options, simultaneous recordings of ECG traces from commercial wet (Red Dot) and dry electrodes were acquired from healthy volunteers. This study was approved by the Clinical Research Ethics Committee of the Cork Teaching Hospitals (ref ECM 3 (ZZ) 10/11/20) and all participants provided written informed consent. A dual-channel ECG recording system was used to capture both signals in different static and walking conditions. An example of the two traces can be seen in Figure 11B.

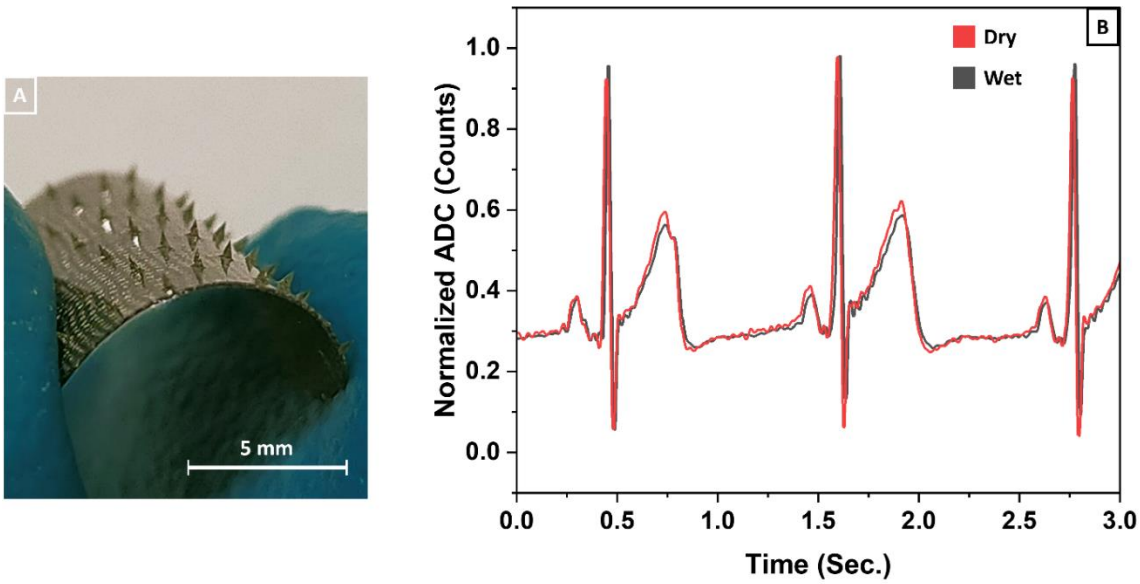


Figure 61. Conductive cloth-epoxy hybrid electrode (A) together with simultaneous ECG recordings from wet and dry electrodes (B).

It is clear that the dry electrodes capture ECG signals with a similar level of fidelity to the commercial wet electrodes. Signal-to-noise ratios were in excess of 20 dB while sitting, and the P wave, QRS complex, and T wave of the ECG signal are clearly identifiable from both sets of electrodes. However, the dry electrodes do not require skin preparation or a wet gel, whilst providing a comparable level of signal quality and low electrode-skin impedance. Additional information and detailed analysis can be found in a previous work [10].

2.4.3 Transdermal Delivery

Biodegradable or dissolvable microneedles (DMN) are the subject of intense research interest for applications in drug and vaccine delivery [8], and numerous DMNs moulded from the Tyndall template have been described in previous works [73], [74]. These dissolvable materials and microneedles could also be used to protect labile medicants, thereby increasing their stability over a prolonged period. To test this hypothesis together

with an evaluation of their delivery capabilities, different dissolvable MNs were produced following the process described in Section 2.3.1. In particular, TRA/SUC sugar needles, PVP/PVA polymer needles and PCL/PLGA polymer needles were fabricated.

The sugar needles, Figure 12A and Figure 12B, were used to test the stability of a macromolecule loaded inside the sugar glasses. To do that, a β-galactosidase enzyme was loaded inside a TRA/SUC dehydrated matrix and stored under vacuum desiccation conditions at 20 ± 2 °C and under refrigerated desiccation conditions at 4 ± 2 °C. The same enzyme was also loaded in dehydrated sodium phosphate buffer (PB) and used as a control. The residual enzyme activity was quantified at time points by a 2-nitrophenyl β-D-Galactopyranoside assay. The results, represented as means measured over 3 samples, are shown in Figure 12C.

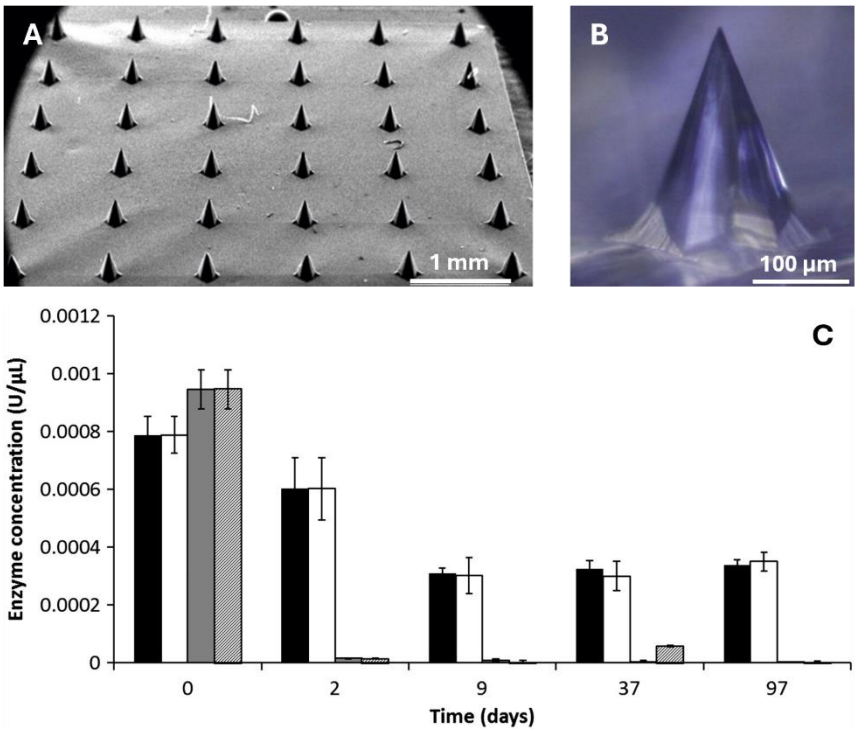


Figure 72. Scanning electron micrograph of an entire sugar glass microneedle array (a) together with a light photomicrograph of an individual sugar glass microneedle (B).

Assessment of enhanced biomolecule stability within sugar glasses as a function of different storage conditions (C). The β-galactosidase enzyme was incorporated either within solid sugar glass (black and white bars) or in a lyophilised phosphate buffer (dark grey and light grey striped bars). Samples were stored under vacuum desiccation at 20 ± 2 °C (white and stripped bars) or desiccation at 4 ± 2 °C (black and grey bars) for a period of 3 months. All images in Figure 12 (A-C) are reproduced with permission [75]. Copyright 2011, Elsevier B.V.

The testing demonstrated that, when loaded inside a sugar glass, more than 40% of the enzyme activity was retained over a period of 3 months. On the other hand, the enzyme loaded inside the PB almost entirely denatured after dehydration. Additional information can be found in a previous work [75].

The PVP and PVA needles were produced using an Epotek 353ND circular MN array as a master (Figure 13). The master itself was produced with the previously described moulding process, using a silicon wafer as a starting point. The mould was prefilled with a hyaluronic acid and niacinamide formulation before adding either the PVP, PVA or PVP/PVA, trapping the formulation inside the forming needles. These actives are used in the management of dermatological conditions such as acne or atopic dermatitis [76], [77]. These needles were tested on full thickness porcine skin and were able to successfully deliver over 150 μg cm^{-2} of drug over a 24-hour period [78].

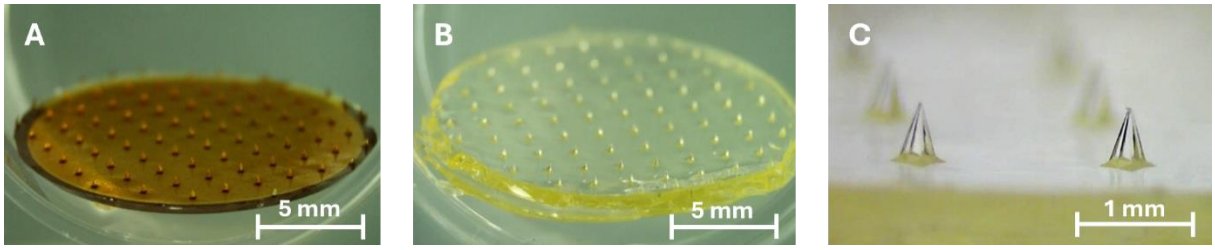


Figure 13. Epoxy master (A) together with resulting PVP array (B), and a close up picture of two similarly prepared PVA microneedles (C).

Both the sugar and the PVP/PVA needles were fast dissolving needles. To demonstrate the ability of the platform to produce slow dissolving MNs, PCL, PLGA and PCL/PLGA needles were also produced and tested on skin samples to prove their ability to penetrate the skin. PCL/PLGA MNs are reported in Figure 14 together with an image showing penetration marks on a skin sample.

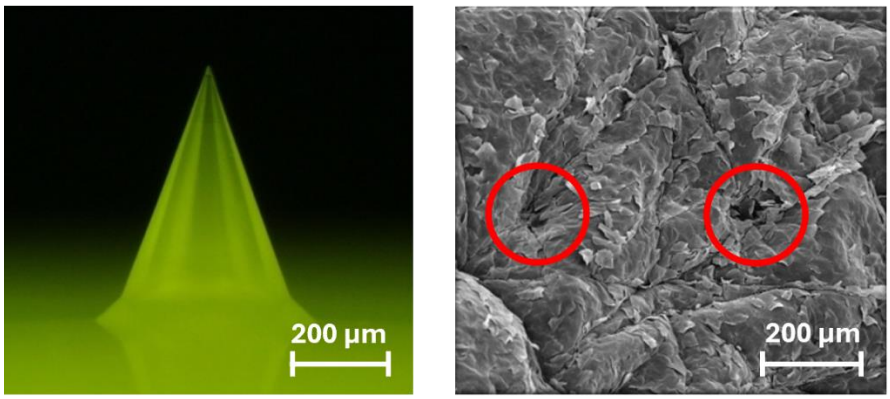


Figure 14. Microneedles prepared from a blend of PCL and PLGA (A) together with a SEM picture showing penetration marks (red circles) produced by MNs application (B).

Human factors studies also indicate that microneedle-based treatments such as these would be well received by patients, who value its convenience, minimally invasive nature and the potential for self-administration [79], [80].

2.5 Conclusions

A multifunctional platform for the rapid prototyping and production of polymer microneedle arrays was established and characterized. The shape, dimension and number of arrays can be varied simply by designing the front and rear master templates accordingly. In this double-sided process, the front template is used to define the geometry, pitch and height of the microneedles themselves, while the rear template shapes the arrays as well as additional features, such as electrical through-wafer vias and alignment marks. The polymer is chosen according to the properties required for the final application. One or more materials may be used to form the MNs and the substrate, or even integrated to combine different properties on single arrays. The moulded MNs can be customised for various sensing applications by using different techniques to deposit metal, passivation and electrochemical layers as required. Sputtering and e-beam evaporation have been characterized and employed to produce patterned electrodes and sensors, and shadow masking techniques have been developed to accurately deposit electrically active regions while preventing the undesirable 'spreading' of metal beneath the masks. Three different exemplars were described, including an electrochemical biosensor for transdermal diagnostics, a flexible ECG sensor, and a biodegradable drug delivery array. These examples illustrate how easily the process may be adapted to a wide range of use cases, making it highly valuable for prototyping and research purposes.

2.6 Supplementary Material

Supplementary video available here:
https://www.sciencedirect.com/science/article/pii/S0924424725002973 .

Alternatively, the same video can be found at:

https://zenodo.org/records/15835760 (DOI: 10.5281/zenodo.15835760) .

2.7 References

[1] F. K. Aldawood, A. Andar, and S. Desai, 'A Comprehensive Review of Microneedles: Types, Materials, Processes, Characterizations and Applications', *Polymers*, vol. 13, no. 16, p. 2815, Aug. 2021, doi: 10.3390/polym13162815.

[2] C. Czekalla, K. H. Schönborn, J. Lademann, and M. C. Meinke, 'Noninvasive Determination of Epidermal and Stratum Corneum Thickness in vivo Using Two-Photon Microscopy and Optical Coherence Tomography: Impact of Body Area, Age, and Gender', *Skin Pharmacol. Physiol.*, vol. 32, no. 3, pp. 142–150, Mar. 2019, doi: 10.1159/000497475.

[3] Histology, Stratum Corneum, StatPearls. 〈http://www.ncbi.nlm.nih.gov/books/NBK513299/〉, 2023 (accessed 8 January 2024).

[4] J. Wang *et al.*, 'Microneedle-based transdermal detection and sensing devices', *Lab. Chip*, vol. 23, no. 5, pp. 869–887, Mar. 2023, doi: 10.1039/D2LC00790H.

[5] M. Zheng, T. Sheng, J. Yu, Z. Gu, and C. Xu, 'Microneedle biomedical devices', *Nat. Rev. Bioeng.*, vol. 2, no. 4, pp. 324–342, Apr. 2024, doi: 10.1038/s44222-023-00141-6.

[6] R. Parhi and D. S. N, 'Review of Microneedle based Transdermal Drug Delivery Systems', *Int. J. Pharm. Sci. Nanotechnol.*, vol. 12, no. 3, pp. 4511–4523, May 2019, doi: 10.37285/ijpsn.2019.12.3.1.

[7] T. Waghule *et al.*, 'Microneedles: A smart approach and increasing potential for transdermal drug delivery system', *Biomed. Pharmacother.*, vol. 109, pp. 1249–1258, Jan. 2019, doi: 10.1016/j.biopha.2018.10.078.

[8] I. Menon *et al.*, 'Microneedles: A New Generation Vaccine Delivery System', *Micromachines*, vol. 12, no. 4, p. 435, Apr. 2021, doi: 10.3390/mi12040435.

[9] J. Madden, C. O'Mahony, M. Thompson, A. O'Riordan, and P. Galvin, 'Biosensing in dermal interstitial fluid using microneedle based electrochemical devices', *Sens. Bio-Sens. Res.*, vol. 29, p. 100348, Aug. 2020, doi: 10.1016/j.sbsr.2020.100348.

[10] O. P. Singh, A. Bocchino, T. Guillerm, Y. Hu, F. Stam, and C. O'Mahony, 'Flexible, Conductive Fabric-Backed, Microneedle Electrodes for Electrophysiological Monitoring', *Adv. Mater. Technol.*, vol. 9, no. 3, p. 2301606, 2024, doi: 10.1002/admt.202301606.

[11] M. O'Sullivan, A. Temko, A. Bocchino, C. O'Mahony, G. Boylan, and E. Popovici, 'Analysis of a Low-Cost EEG Monitoring System and Dry Electrodes toward Clinical Use in the Neonatal ICU', *Sensors*, vol. 19, no. 11, Art. no. 11, Jan. 2019, doi: 10.3390/s19112637.

[12] A. T. Satti, J. Park, J. Park, H. Kim, and S. Cho, 'Fabrication of Parylene-Coated Microneedle Array Electrode for Wearable ECG Device', *Sensors*, vol. 20, no. 18, Art. no. 18, Jan. 2020, doi: 10.3390/s20185183.

[13] H. Zhang *et al.*, 'Biocompatible Light Guide-Assisted Wearable Devices for Enhanced UV Light Delivery in Deep Skin', *Adv. Funct. Mater.*, vol. 31, Mar. 2021, doi: 10.1002/adfm.202100576.

[14] C. O'Mahony, R. Houlihan, K. Grygoryev, Z. Ning, J. Williams, and T. Moore, 'Design, modelling and preliminary characterisation of microneedle-based electrodes for tissue electroporation in vivo', *J. Phys. Conf. Ser.*, vol. 757, no. 1, p. 012040, Oct. 2016, doi: 10.1088/1742-6596/757/1/012040.

[15] A. Tucak *et al.*, 'Microneedles: Characteristics, Materials, Production Methods and Commercial Development', *Micromachines*, vol. 11, no. 11, p. 961, Oct. 2020, doi: 10.3390/mi11110961.

[16] N. Gan, M. Wei, Q. Zhou, K. Dong, and B. Gao, 'Silk Fibroin-Based Triboelectric Nanogenerators for Energy Harvesting and Biomedical Applications', *ACS Appl. Nano Mater.*, vol. 7, no. 8, pp. 8407–8423, Apr. 2024, doi: 10.1021/acsanm.4c00335.

[17] C. O'Mahony *et al.*, 'Characterisation of Microneedle-Based ECG Electrodes Fabricated Using an Industrial Injection-Moulding Process', in *2019 IEEE 32nd International Conference on Micro Electro Mechanical Systems (MEMS)*, Jan. 2019, pp. 557–560. doi: 10.1109/MEMSYS.2019.8870721.

[18] K. Schossleitner *et al.*, 'Differences in biocompatibility of microneedles from cyclic olefin polymers with human endothelial and epithelial skin cells', *J. Biomed. Mater. Res. A*, vol. 107, no. 3, pp. 505–512, Mar. 2019, doi: 10.1002/jbm.a.36565.

[19] M. Wang, L. Hu, and C. Xu, 'Recent advances in the design of polymeric microneedles for transdermal drug delivery and biosensing', *Lab. Chip*, vol. 17, no. 8, pp. 1373–1387, 2017, doi: 10.1039/C7LC00016B.

[20] M. Dervisevic, E. Dervisevic, L. Esser, C. D. Easton, V. J. Cadarso, and N. H. Voelcker, 'Wearable microneedle array-based sensor for transdermal monitoring of pH levels in interstitial fluid', *Biosens. Bioelectron.*, vol. 222, p. 114955, Feb. 2023, doi: 10.1016/j.bios.2022.114955.

[21] Y. Hou, Z. Li, Z. Wang, and H. Yu, 'Miura-ori structured flexible microneedle array electrode for biosignal recording', *Microsyst. Nanoeng.*, vol. 7, no. 1, Art. no. 1, Jul. 2021, doi: 10.1038/s41378-021-00259-w.

[22] M. J. Uddin *et al.*, '3D printed microneedles for anticancer therapy of skin tumours', *Mater. Sci. Eng. C*, vol. 107, p. 110248, Feb. 2020, doi: 10.1016/j.msec.2019.110248.

[23] M. A. Luzuriaga, D. R. Berry, J. C. Reagan, R. A. Smaldone, and J. J. Gassensmith, 'Biodegradable 3D printed polymer microneedles for transdermal drug delivery', *Lab. Chip*, vol. 18, no. 8, pp. 1223–1230, Apr. 2018, doi: 10.1039/C8LC00098K.

[24] J. Li *et al.*, 'Low-Cost, Low-Impedance Polyimide Based Micro-Needle Array (PI-MNA): A Minimally Invasive Flexible Dry Electrode for Surface Bio-Potential Monitoring', in *2019 IEEE 32nd International Conference on Micro Electro Mechanical Systems (MEMS)*, Jan. 2019, pp. 28–31. doi: 10.1109/MEMSYS.2019.8870653.

[25] Z. Chen *et al.*, 'Rapid fabrication of microneedles using magnetorheological drawing lithography', *Acta Biomater.*, vol. 65, pp. 283–291, Jan. 2018, doi: 10.1016/j.actbio.2017.10.030.

[26] P. Bollella, S. Sharma, A. E. G. Cass, and R. Antiochia, 'Microneedle-based biosensor for minimally-invasive lactate detection', *Biosens. Bioelectron.*, vol. 123, pp. 152–159, Jan. 2019, doi: 10.1016/j.bios.2018.08.010.

[27] L. Ren, K. Yu, and Y. Tan, 'Monitoring and Assessing the Degradation Rate of Magnesium-Based Artificial Bone In Vitro Using a Wireless Magnetoelastic Sensor', *Sensors*, vol. 18, no. 9, p. 3066, Sep. 2018, doi: 10.3390/s18093066.

[28] M. Zheng *et al.*, 'Osmosis-Powered Hydrogel Microneedles for Microliters of Skin Interstitial Fluid Extraction within Minutes', *Adv. Healthc. Mater.*, vol. 9, no. 10, p. 1901683, May 2020, doi: 10.1002/adhm.201901683.

[29] R. F. Donnelly *et al.*, 'Hydrogel-Forming Microneedles Prepared from "Super Swelling" Polymers Combined with Lyophilised Wafers for Transdermal Drug Delivery', *PLoS ONE*, vol. 9, no. 10, p. e111547, Oct. 2014, doi: 10.1371/journal.pone.0111547.

[30] S. Sharma, Z. Huang, M. Rogers, M. Boutelle, and A. E. G. Cass, 'Evaluation of a minimally invasive glucose biosensor for continuous tissue monitoring', *Anal. Bioanal. Chem.*, vol. 408, no. 29, pp. 8427–8435, 2016, doi: 10.1007/s00216-016-9961-6.

[31] S. C. Park, M. J. Kim, S.-K. Baek, J.-H. Park, and S.-O. Choi, 'Spray-Formed Layered Polymer Microneedles for Controlled Biphasic Drug Delivery', *Polymers*, vol. 11, no. 2, Art. no. 2, Feb. 2019, doi: 10.3390/polym11020369.

[32] W. Li, R. N. Terry, J. Tang, M. R. Feng, S. P. Schwendeman, and M. R. Prausnitz, 'Rapidly separable microneedle patch for the sustained release of a contraceptive', *Nat. Biomed. Eng.*, vol. 3, no. 3, Art. no. 3, Mar. 2019, doi: 10.1038/s41551-018-0337-4.

[33] Y. Park, J. Park, G. S. Chu, K. S. Kim, J. H. Sung, and B. Kim, 'Transdermal delivery of cosmetic ingredients using dissolving polymer microneedle arrays', *Biotechnol. Bioprocess Eng.*, vol. 20, no. 3, pp. 543–549, Jun. 2015, doi: 10.1007/s12257-014-0775-0.

[34] F. Pérennès, B. Marmiroli, M. Matteucci, M. Tormen, L. Vaccari, and E. D. Fabrizio, 'Sharp beveled tip hollow microneedle arrays fabricated by LIGA and 3D soft lithography with polyvinyl alcohol', *J. Micromechanics Microengineering*, vol. 16, no. 3, p. 473, Jan. 2006, doi: 10.1088/0960-1317/16/3/001.

[35] S. A. N. Gowers *et al.*, 'Development of a Minimally Invasive Microneedle-Based Sensor for Continuous Monitoring of β-Lactam Antibiotic Concentrations in Vivo', *ACS Sens.*, vol. 4, no. 4, pp. 1072–1080, Apr. 2019, doi: 10.1021/acssensors.9b00288.

[36] Y. Nishinaka, R. Jun, G. S. Prihandana, and N. Miki, 'Fabrication of polymeric dry microneedle electrodes coated with nanoporous parylene', in *2013 Transducers & Eurosensors XXVII: The 17th International Conference on Solid-State Sensors, Actuators and Microsystems (TRANSDUCERS & EUROSENSORS XXVII)*, Jun. 2013, pp. 1326–1327. doi: 10.1109/Transducers.2013.6627021.

[37] M. Wei, Q. Zhou, X. Ma, and B. Gao, 'Review of biomimetic ordered microstructures in advancing synergistic integration of adhesion and microfluidics', *RSC Adv.*, vol. 14, no. 17, pp. 11643–11658, Apr. 2024, doi: 10.1039/D3RA07698A.

[38] C. O'Mahony, K. Grygoryev, A. Ciarlone, G. Giannoni, A. Kenthao, and P. Galvin, 'Design, fabrication and skin-electrode contact analysis of polymer microneedle-based ECG electrodes', *J. Micromechanics Microengineering*, vol. 26, no. 8, p. 084005, Jul. 2016, doi: 10.1088/0960-1317/26/8/084005.

[39] A. Bocchino *et al.*, 'Development and Characterization of Passivation Methods for Microneedle-based Biosensors', in *2022 44th Annual International Conference of the IEEE Engineering in Medicine & Biology Society (EMBC)*, Jul. 2022, pp. 1275–1278. doi: 10.1109/EMBC48229.2022.9871005.

[40] K. Ahmed Saeed AL-Japairai *et al.*, 'Current trends in polymer microneedle for transdermal drug delivery', *Int. J. Pharm.*, vol. 587, p. 119673, Sep. 2020, doi: 10.1016/j.ijpharm.2020.119673.

[41] R. S. J. Ingrole and H. S. Gill, ‘Microneedle Coating Methods: A Review with a Perspective’, *J. Pharmacol. Exp. Ther.*, vol. 370, no. 3, pp. 555–569, Sep. 2019, doi: 10.1124/jpet.119.258707.

[42] P. Dardano, I. Rea, and L. De Stefano, ‘Microneedles-based electrochemical sensors: New tools for advanced biosensing’, *Curr. Opin. Electrochem.*, vol. 17, pp. 121–127, Oct. 2019, doi: 10.1016/j.coelec.2019.05.012.

[43] O. Ojuroye, R. Torah, and S. Beeby, ‘Modified PDMS packaging of sensory e-textile circuit microsystems for improved robustness with washing’, *Microsyst. Technol.*, vol. 28, no. 6, pp. 1467–1484, Jun. 2022, doi: 10.1007/s00542-019-04455-7.

[44] R. V. Dixon *et al.*, ‘Microneedle-based devices for point-of-care infectious disease diagnostics’, *Acta Pharm. Sin. B*, vol. 11, no. 8, pp. 2344–2361, Aug. 2021, doi: 10.1016/j.apsb.2021.02.010.

[45] A. S. Cordeiro *et al.*, ‘Two-Photon Polymerisation 3D Printing of Microneedle Array Templates with Versatile Designs: Application in the Development of Polymeric Drug Delivery Systems’, *Pharm. Res.*, vol. 37, no. 9, p. 174, Aug. 2020, doi: 10.1007/s11095-020-02887-9.

[46] C. Plamadeala *et al.*, ‘Bio-inspired microneedle design for efficient drug/vaccine coating’, *Biomed. Microdevices*, vol. 22, no. 1, p. 8, Dec. 2019, doi: 10.1007/s10544-019-0456-z.

[47] C. O’Mahony, ‘Structural characterization and in-vivo reliability evaluation of silicon microneedles’, *Biomed. Microdevices*, vol. 16, no. 3, pp. 333–343, Jun. 2014, doi: 10.1007/s10544-014-9836-6.

[48] D. Kulkarni *et al.*, ‘Recent Advancements in Microneedle Technology for Multifaceted Biomedical Applications’, *Pharmaceutics*, vol. 14, no. 5, Art. no. 5, May 2022, doi: 10.3390/pharmaceutics14051097.

[49] R. J. Martín-Palma and A. Lakhtakia, ‘Chapter 15 - Vapor-Deposition Techniques’, in *Engineered Biomimicry*, A. Lakhtakia and R. J. Martín-Palma, Eds., Boston: Elsevier, 2013, pp. 383–398. doi: 10.1016/B978-0-12-415995-2.00015-5.

[50] A. Tamayo-Dominguez, P. Sanchez-Olivares, A. Camacho-Hernandez, and J.-M. Fernandez-Gonzalez, ‘Guidelines for Accurate in-House Electroplating and 3-D-Printing Processes Applied to mm-Wave Devices’, *IEEE Microw. Wirel. Compon. Lett.*, vol. 32, no. 11, pp. 1267–1270, Nov. 2022, doi: 10.1109/LMWC.2022.3182868.

[51] A. S. Hamdy Makhlouf and R. Rodriguez, ‘Chapter 15 - Bioinspired smart coatings and engineering materials for industrial and biomedical applications’, in *Advances in Smart Coatings and Thin Films for Future Industrial and Biomedical Engineering Applications*, A. S. H. Makhlouf and N. Y. Abu-Thabit, Eds., Elsevier, 2020, pp. 407–427. doi: 10.1016/B978-0-12-849870-5.00018-5.

[52] R. K. Kummamuru, L. Hu, L. Cook, M. Y. Efremov, E. A. Olson, and L. H. Allen, ‘A close proximity self-aligned shadow mask for sputter deposition onto a membrane or cavity’, *J. Micromechanics Microengineering*, vol. 18, no. 9, p. 095027, Aug. 2008, doi: 10.1088/0960-1317/18/9/095027.

[53] S. Kurzhals *et al.*, ‘Detection of Lactate via Amperometric Sensors Modified With Direct Electron Transfer Enzyme Containing PEDOT:PSS and Hydrogel Inks’, *IEEE Sens. Lett.*, vol. 7, no. 9, pp. 1–4, Sep. 2023, doi: 10.1109/LSENS.2023.3307066.

[54] C. Barrett, K. Dawson, C. O'Mahony, and A. O'Riordan, 'Development of Low Cost Rapid Fabrication of Sharp Polymer Microneedles for In Vivo Glucose Biosensing Applications', *ECS J. Solid State Sci. Technol.*, vol. 4, no. 10, p. S3053, Aug. 2015, doi: 10.1149/2.0141510jss.

[55] O. P. Singh, A. Bocchino, T. Guillerm, and C. O'Mahony, 'Design, Fabrication and Performance Assessment of Flexible, Microneedle–Based Electrodes For ECG Signal Monitoring', in *2022 44th Annual International Conference of the IEEE Engineering in Medicine & Biology Society (EMBC)*, Jul. 2022, pp. 846–849. doi: 10.1109/EMBC48229.2022.9871073.

[56] C. Hegarty, A. McConville, R. J. McGlynn, D. Mariotti, and J. Davis, 'Design of composite microneedle sensor systems for the measurement of transdermal pH', *Mater. Chem. Phys.*, vol. 227, pp. 340–346, Apr. 2019, doi: 10.1016/j.matchemphys.2019.01.052.

[57] D. Terutsuki, S. Yamaguchi, Y. Abe, H. Abe, and M. Nishizawa, 'Porous Microneedle-Based Potentiometric Sensor for Intradermal Electrolyte Monitoring', *Electrochemistry*, vol. 91, no. 4, pp. 047007–047007, 2023, doi: 10.5796/electrochemistry.23-00027.

[58] S. Metz, M. O. Heuschkel, B. Valencia Avila, R. Holzer, D. Bertrand, and Ph. Renaud, 'Microelectrodes with three-dimensional structures for improved neural interfacing', in *2001 Conference Proceedings of the 23rd Annual International Conference of the IEEE Engineering in Medicine and Biology Society*, Istanbul, Turkey: IEEE, 2001, pp. 765–768. doi: 10.1109/IEMBS.2001.1019053.

[59] 'Microneedle-based device for biological analysis', Frontiers. 〈 https://www.frontiersin.org/articles/10.3389/fbioe.2022.851134〉, 2022 (accessed 16 January 2023).

[60] H. Abdullah, T. Phairatana, and I. Jeerapan, 'Tackling the challenges of developing microneedle-based electrochemical sensors', *Microchim. Acta*, vol. 189, no. 11, p. 440, Nov. 2022, doi: 10.1007/s00604-022-05510-3.

[61] K. C. Honeychurch, '13 - Printed thick-film biosensors', in *Printed Films*, M. Prudenziati and J. Hormadaly, Eds., in Woodhead Publishing Series in Electronic and Optical Materials. , Woodhead Publishing, 2012, pp. 366–409. doi: 10.1533/9780857096210.2.366.

[62] P. Kurzweil, 'Electrochemical Terminology | Electrochemical Cell Nomenclature', in *Encyclopedia of Electrochemical Power Sources (Second Edition)*, J. Garche, Ed., Oxford: Elsevier, 2025, pp. 449–464. doi: 10.1016/B978-0-323-96022-9.00035-9.

[63] X. Huang *et al.*, '3D-assembled microneedle ion sensor-based wearable system for the transdermal monitoring of physiological ion fluctuations', *Microsyst. Nanoeng.*, vol. 9, no. 1, pp. 1–16, Mar. 2023, doi: 10.1038/s41378-023-00497-0.

[64] J. Ju, L. Li, S. Regmi, X. Zhang, and S. Tang, 'Microneedle-Based Glucose Sensor Platform: From Vitro to Wearable Point-of-Care Testing Systems', *Biosensors*, vol. 12, no. 8, Art. no. 8, Aug. 2022, doi: 10.3390/bios12080606.

[65] D. S. Macedo *et al.*, 'An unusually stable solid state Ag|AgCl reference electrode for long term continuous measurements based on a crosslinked poly(vinyl acetate)/KCl composite', *Electrochimica Acta*, vol. 368, p. 137636, Feb. 2021, doi: 10.1016/j.electacta.2020.137636.

[66] S. Mohapatra, ‘Chapter 59 - Sterilization and Disinfection’, in *Essentials of Neuroanesthesia*, H. Prabhakar, Ed., Academic Press, 2017, pp. 929–944. doi: 10.1016/B978-0-12-805299-0.00059-2.

[67] E. Cihan *et al.*, ‘Novel Approach for the Immobilization of Cellobiose Dehydrogenase in PEDOT:PSS Conductive Layer on Planar Gold Electrodes’, *Chemosensors*, vol. 12, no. 3, Art. no. 3, Mar. 2024, doi: 10.3390/chemosensors12030036.

[68] D. K. Ming *et al.*, ‘Real-time continuous measurement of lactate through a minimally invasive microneedle patch: a phase I clinical study’, *BMJ Innov.*, vol. 8, no. 2, Apr. 2022, doi: 10.1136/bmjinnov-2021-000864.

[69] D. M. E. Freeman *et al.*, ‘Continuous Measurement of Lactate Concentration in Human Subjects through Direct Electron Transfer from Enzymes to Microneedle Electrodes’, *ACS Sens.*, vol. 8, no. 4, pp. 1639–1647, Apr. 2023, doi: 10.1021/acssensors.2c02780.

[70] S. Sharma, Z. Huang, M. Rogers, M. Boutelle, and A. E. G. Cass, ‘Evaluation of a minimally invasive glucose biosensor for continuous tissue monitoring’, *Anal. Bioanal. Chem.*, vol. 408, no. 29, pp. 8427–8435, 2016, doi: 10.1007/s00216-016-9961-6.

[71] R. Bennett *et al.*, ‘Effects of Sterilization on Cellobiose Dehydrogenase and Glucose Oxidase Based Glucose Biosensors’, *Adv. Sens. Res.*, vol. 3, no. 11, p. 2400056, 2024, doi: 10.1002/adsr.202400056.

[72] M. Haberler *et al.*, ‘A Self-Contained, Single-Chip Amperometric Measurement Platform for Biomedical Applications’, in *2021 16th International Conference on*

Telecommunications (Con^{TEL}), Jun. 2021, pp. 105–109. doi: 10.23919/Con^{TEL}52528.2021.9495989.

[73] Y. Tian *et al.*, 'Intradermal Administration of Influenza Vaccine with Trehalose and Pullulan-Based Dissolving Microneedle Arrays', *J. Pharm. Sci.*, vol. 111, no. 4, pp. 1070–1080, Apr. 2022, doi: 10.1016/j.xphs.2022.01.033.

[74] J. Lee *et al.*, 'Efficient fabrication of thermo-stable dissolving microneedle arrays for intradermal delivery of influenza whole inactivated virus vaccine', *Biomater. Sci.*, vol. 11, no. 20, pp. 6790–6800, Oct. 2023, doi: 10.1039/D3BM00377A.

[75] C. J. Martin, C. J. Allender, K. R. Brain, A. Morrissey, and J. C. Birchall, 'Low temperature fabrication of biodegradable sugar glass microneedles for transdermal drug delivery applications', *J. Controlled Release*, vol. 158, no. 1, pp. 93–101, Feb. 2012, doi: 10.1016/j.jconrel.2011.10.024.

[76] J. Mehrabi, W. Shehadeh, E. S. Gallo, O. Artzi, and T. Horovitz, 'Comparison of 2 Hyaluronic Acid-based Fillers for the Treatment of Acne Scars: Structural Lifting Versus Biostimulatory Effect', *Dermatol. Surg. Off. Publ. Am. Soc. Dermatol. Surg. Al*, vol. 49, no. 6, pp. 581–586, Jun. 2023, doi: 10.1097/DSS.0000000000003789.

[77] J. Zhu, J. Wang, and S. Wang, 'A single-center, randomized, controlled study on the efficacy of niacinamide-containing body emollients combined with cleansing gel in the treatment of mild atopic dermatitis', *Skin Res. Technol.*, vol. 29, no. 9, p. e13475, Sep. 2023, doi: 10.1111/srt.13475.

[78] M. Massufero-Vergilio, G.R. Leonardi, J.C. Birchall, 'Dissolvable microneedle array for enhanced niacinamide application for skin disorders', Submitted to: *J. Drug. Deliv. Sci. Technol.*, January 2025..

[79] J. C. Birchall, R. Clemo, A. Anstey, and D. N. John, ‘Microneedles in clinical practice--an exploratory study into the opinions of healthcare professionals and the public’, *Pharm. Res.*, vol. 28, no. 1, pp. 95–106, Jan. 2011, doi: 10.1007/s11095-010-0101-2.

[80] B. Gualeni *et al.*, ‘Human-centred design of a new microneedle-based hormonal contraceptive delivery system’, *Gates Open Res.*, vol. 5, p. 96, Dec. 2021, doi: 10.12688/gatesopenres.13233.3.

Chapter 3

Strategies for Passivating Microneedles-based Sensors: Development, Characterization and Comparison

Authors: Andrea Bocchino, Sofia Rodrigues Teixeira, Fiona Barry, Chinmay Thatte, Adam Ryan, Fahima Rahman, Yuan Hu, Simone Iadanza, Paul Galvin, Steffen Kurzhals, Eva Melnik, Giorgio Mutinati, Conor O'Mahony.

Journal: *Sensors and Actuators Reports*, volume 9, article 100328.

Publication Date: June 2025.

DOI: 10.1016/j.snr.2025.100328

Contribution: Passivation (together with metallization) was the second most relevant module of the platform and one of the main contributions of this work. Here, it was thoroughly analysed. As lead author, I was responsible for writing the paper and developing the procedures which I used to apply the different layers to the MNs. I produced and metallised all the MNs using the platform presented in the previous chapter. I have also designed the 3D printed holders with electrical interconnects, necessary for testing, and mounted the arrays on them. This was vital to electrochemically characterize the different layers. I have also entirely performed the visual characterization of the layers, effectively providing a first comparison tool to pair with the electrochemical

testing that was subsequently performed by co-authors (electrochemical testing presented within Section 3.3.3, Section 3.4 – Figure 9 and 10 produced by co-authors).

CRediT Authors Statement:

Andrea Bocchino: Conceptualization, Data curation, Formal analysis, Investigation, Methodology, Validation, Visualization, Writing – original draft, Writing – review & editing.

Sofia Teixeira: Data curation, Formal analysis, Investigation, Validation, Writing – original draft, Supervision, Visualization, Writing – original draft, Writing – review & editing.

Fiona Barry: Data curation, Investigation, Validation, Writing – review & editing.

Chinmay Thatte: Data curation, Investigation, Validation, Writing – review & editing.

Adam Ryan: Data curation, Investigation, Validation, Writing – review & editing.

Fahima Rahman: Data curation, Investigation, Validation, Writing – review & editing.

Yuan Hu: Visualization, Writing – review & editing.

Simone Iadanza: Investigation, Resources, Validation, Writing – review & editing.

Paul Galvin: Project administration, Resources, Supervision, Writing – review & editing.

Steffen Kurzhals: Methodology, Writing – review & editing.

Eva Melnik: Methodology, Writing – review & editing.

Giorgio C. Mutinati: Funding acquisition, Project administration, Resources, Writing – review & editing.

Conor O'Mahony: Funding acquisition, Methodology, Project administration, Resources, Supervision, Writing – review & editing.

Chapter adapted from below link under the Creative Commons license 4.0 (CC BY 4.0).

The Section numbers, Figures/Tables/References style has been adapted to conform to the style and numbering of the thesis.

Additional changes:

- Section 3.2: "focussed" changed to "focused".
- Section 3.1: "SiO2" changed to "SiO_2".

https://www.sciencedirect.com/science/article/pii/S2666053925000463

Link to license:

https://creativecommons.org/licenses/by/4.0/

3.1 Abstract

Microneedles (MNs) are sharp, pillar-like structures shorter than 1 mm. They can painlessly pierce the stratum corneum (SC), the outermost layer of the skin, and interface with the underlying dermal interstitial fluid, rich in biomarkers. Due to these properties, MNs have been widely investigated for several diagnostic applications. In particular, MN-based biosensors could enable the development of the new generation of minimally invasive continuous monitoring systems. To become a biosensor, the body or the tip of the needles must be functionalized. In addition, the area surrounding the MNs is usually passivated to prevent substrate interferences. Although passivation layers are widely used, there is a lack of characterization of such layers. This work aims at filling this gap, by developing, characterizing, and comparing six different passivation techniques. These include the application of polymethyl methacrylate (PMMA), Epotek 353ND, silicon oxide (SiO_2), parylene, varnish and an adhesive film to microneedle arrays. The performance of each method was then assessed using electrochemical measurements, optical and SEM imaging, and contact angle analysis.

Significant variability was observed across the various methods and materials. When assessed in terms of the electrochemically active area available after passivation, the tape and parylene were the most promising layers, while varnish and epoxy were the worst performing materials. The PMMA performed better than the other liquid passivations, but still requires refinement due to the high degree of unwanted coverage of the needles. Finally, the SiO_2 layer seemed to be a viable option, but also remains in need of additional optimization.

3.2 Introduction

Interstitial fluid (ISF) is an extracellular fluid that surrounds blood vessels and cells, and that comprises 15-25% of body weight [1]. This fluid filters from the capillaries and is then removed through the lymphatic system [2]. Thanks to this circulatory mechanism, ISF is rich in biomarkers, ions and compounds. Their concentrations are in near equilibrium with those found in blood. For these reasons, together with the high amount of ISF present in the body, interstitial fluid has been widely investigated as a means of disease detection, healthcare diagnostics and monitoring of athletic performances [3], [4], [5].

A number of methods may be used to sample ISF, including the use of suction blisters, biopsies, reverse iontophoresis, microdialysis or implantable sensors [6]. However, each of these techniques has limitations such as the need for minor surgery, clinical expertise, and patient discomfort.

An emerging alternative involves the use of microneedle-based devices [7] – arrays of short, sharp structures that painlessly penetrate the skins outermost *stratum corneum* layer. They are too short to stimulate the underlying nerve endings or strike the capillary network that lies deeper in the epidermis [8], [9].

Microneedles were initially developed for use in drug and vaccine delivery [10], but have also been demonstrated for ISF sampling and analysis [7]. Since microneedles provide a direct interface with ISF [11], hollow MNs can be used to withdraw fluid for out-of-the-body analysis [12]. Electrochemically modified solid needles may also be applied to the skin for continuous monitoring [13]. Typical examples of MN-based sensor applications include detection of biomarkers such as lactate [14] and glucose [15], pH measurement [16], or analysis of different electrolytes [17].

To act as an ISF sensor, the needles need to be electrically conductive and are usually metallised using different techniques, such as thermal evaporation, e-beam deposition or electroplating. Target-specific chemistries are then bonded to the structures. However, in many cases the substrate is metallised along with the needles themselves. Therefore, the substrate must be passivated to block any functionalisation in those areas. Failure to do so may lead to unwanted responses from interferents on the skin outside of the SC. This substrate passivation limits reactions to those which take place on the body of the needle and, therefore, improves selectivity and sensitivity to the target analyte.

An ideal passivation layer should firstly have a high and uniform electrical resistance, avoiding any type of undesired interference between substrate metallisation and electrochemical layers. Secondly, the layer should be relatively thin in comparison to the needle height, as the material thickness obviously reduces the height available for skin penetration.

To be as effective as possible, the layer should entirely cover the substrate around the MNs. Moreover, after application, MNs are usually not fully embedded into the skin [18]. In this case, the lower region of the needles may then come into contact with other external media, such as sweat. These media could potentially influence the readout of the sensor. Therefore, an ideal passivation should also cover this lower region. Here, the passivation should be conformal to the MNs themselves, and should avoid reducing their usable height. It should also be precisely controllable, i.e. capable of being accurately deposited and patterned or etched, to leave the desired portion of the MNs available for functionalization. To be used *in vivo*, the passivation material should be biocompatible with standards such as ISO 10993-5 and -10 for cytotoxicity and skin sensitization. Finally, it should also be compatible with mass manufacturing techniques.

Figure 1 depicts two different passivation layers: one is representation of an 'ideal' passivation layer (A), while the second presents several issues (B). Firstly, the thickness of the ideal passivation layer (T) is much smaller than the height of the MNs (H). The passivation also covers the lower region (LR) of the needles in a conformal fashion, limiting the reduction in usable height to the thickness of the layer (T). In contrast, the second, suboptimal example is much thicker (T') and not conformal to the needles, strongly reducing the height available for skin penetration (H-T').

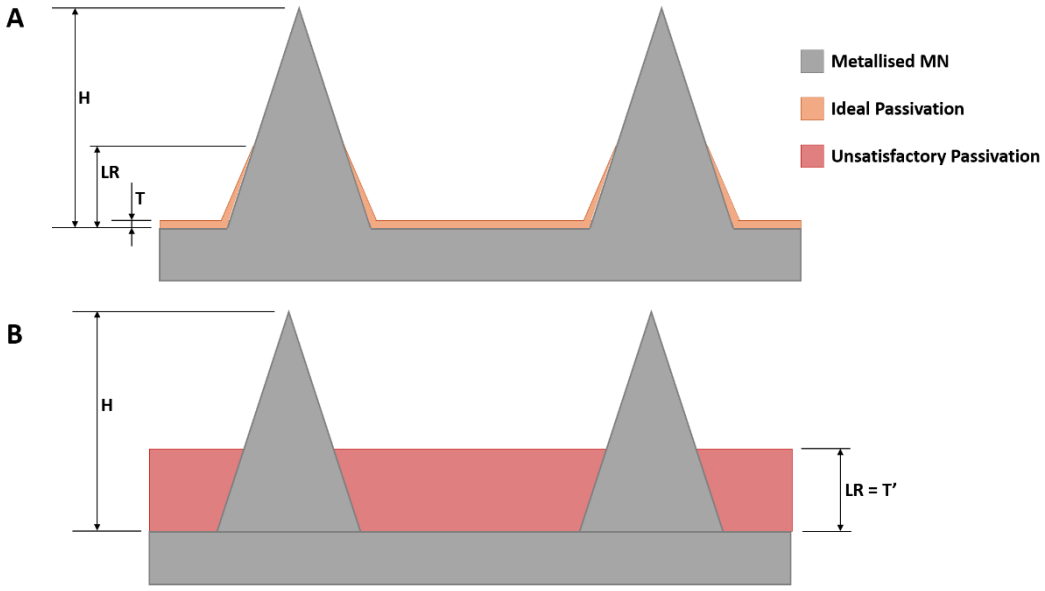


Figure 1. Visual representation of an ideal (A) and an unsatisfactory (B) passivation layer.

Table 1 reports examples of metallised and passivated MNs devices used for diagnostic applications. Different passivation techniques include spin-coating [19], [20], [21], oxide formation [22], application of varnish or enamel [23], [24], [25] and chemical vapour deposition (CVD) [26], [27].

Table 1. MN type, production method, metallization, passivation, and application for several MN-based diagnostic devices .

MNs	Production	Metallization	Passivation	Application
280µm PMMA (NOA 68)	Replica moulding	Thermally evaporated Au	Spin-coated PMMA (NOA 68)	Glucose sensing [19], [28]
600µm stainless steel	Wet etching	Electroplated Au and electrodeposited Pt-black	5µm parylene coating	Glucose sensing [29]
500µm stainless steel (SUS304)	Not specified	Electroplated Au	Electrochemical formation of AuZn oxide	Glucose sensing [22]
1mm poly(carbonate)	Injection moulding	E-beamed Au and Ag	Syringe-deposited insulating varnish	B-Lactam antibiotic continuous concentration monitoring [23], [24]
550µm stainless steel (316L)	Etching steel and punching	Electroplated Au	Chemical vapour deposition of	ECG monitoring [26]

	out the MNs		5µm of parylene	
70µm polyimide	Casting in silicon etched master	Sputtered Pt	4-10µm spin coated polyimide (PI-2732)	Neural interfacing [20]
60µm glass	Wet etching	Deposited Pt	5µm deposited SU-8	Neural interfacing [20]
320µm silicon	Wet etching	Sputtered Au	8µm parylene coating	EEG monitoring [30]
80µm silicon	Deep reactive ion etching	Sputtered Au/Pt	5µm parylene coating	Invasive neural electrical stimulation and recording [27]
500µm Epotek 353ND	Replica moulding	E-beamed Ti/Pt and Ti/Ni/Ag	55µm thick medical tape	Lactate amperometric detection [14]
700µm carbon-loaded polystyrene	Micro-moulding	Electrochemically deposited Ag (only on reference MNs)	Enamel coating	pH measurement [25]

250µm OrmoComp	Moulding	AC/DC sputtered Au	Spin coated OrmoComp (2 µl)	pH monitoring	[21]

Although passivation layers are increasingly used for ISF diagnostics, relatively little data related to the characterization of such layers has been reported. We have previously developed a platform for the rapid prototyping of microneedle-based devices – a process that includes application of passivation layers for diagnostic purposes [31]. Preliminary data relating to passivation materials and techniques have also been reported in a previous work [32]. In this paper, we provide a more extensive analysis of existing and new passivation layers, including varnish, parylene, silicon oxide (SiO_2), polymers (PMMA and Epotek 353ND, a USP class VI epoxy) and a medical grade adhesive film (ARcare 7759). The processes used to apply these coatings are also reviewed to provide additional insight regarding advantages and disadvantages of the different techniques and materials. Visual and electrochemical analyses were used to compare the layers in terms of reproducibility, uniformity and electrochemically active area. It is intended that this screening work will form a basis from which future research will continue optimizing the most promising passivation methods. This research should be focused on maximising performance, scalability, and reproducibility.

Significant variability was observed across the various methods and materials, highlighting the need for further research and process development in this area. When assessed in terms of the electrochemically active area available after passivation, the tape and parylene were the most promising layers, while varnish, epoxy and PMMA were the

worst performing materials. Finally, SiO_2 seemed to be a viable option, but it remains in need of additional optimization.

3.3 Materials and Methods

3.3.1 Microneedle Array Production

A 100 mm diameter silicon MN wafer was produced through wet KOH etching [33] and glued (NOA68 from Norland Products NJ, USA) to a glass petri dish to form a front side master template. The needles were in the shape of ultra-sharp, 500 µm tall octagonal pyramids with a tip-to-tip distance of 1750 µm. The octagonal shape of the needles is determined by the orientation of the crystalline planes, and their interaction with the KOH etchant and the surface masks [33]. The height and pitch were selected based on prior experience and *in vivo* experimental work, such as [34], where the 500 µm tall needles showed good skin penetration, biomechanical robustness and quick skin recovery, as well as a painless and bloodless sensation for the user. To form a rear side master, a PVC petri dish was also milled with a custom geometry.

A replica moulding process (Figure 2) [34] was used to copy these master templates and to manufacture PDMS (Sylgard 184, Dow Corning, MI, USA) moulds: the two components of the PDMS kit were mixed in a 10:1 ratio, poured on the masters, degassed and finally peeled away. The front mould formed the negative copy of the MNs (Figure 2A). The rear mould divided the resulting wafer into individual arrays (Figure 2B), detachable by finger pressure. For this work, the arrays were designed as circles with a diameter of 9 mm.

Similarly, the two components of a medical grade epoxy (Epotek 353ND from Epoxy Technology, MA, USA) were mixed in a 10:1 ratio, poured on the front mould, spread to

cover the entire surface, and degassed inside a vacuum chamber. The rear mould was then placed on the front mould and used to sandwich the epoxy in between. To ensure proper filling of the MNs holes, the stack was placed on a vacuum table for one hour and then oven cured at 80° C. Finally, the wafer was left to cool down to reach room temperature and the moulds peeled away (Figure 2C).

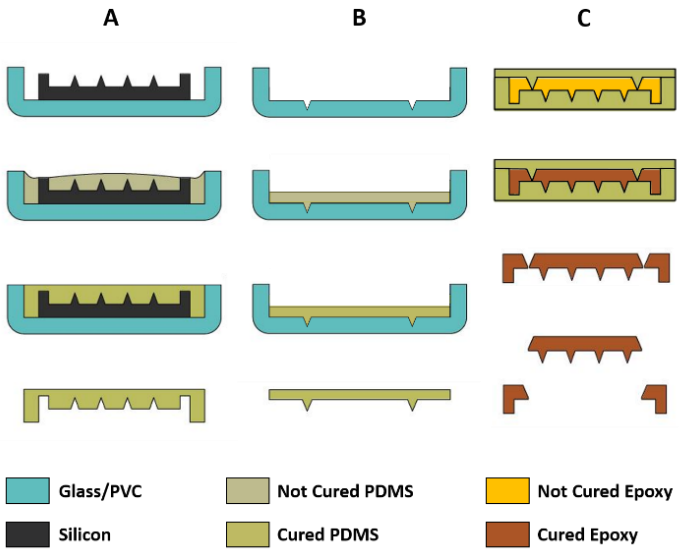


Figure 2. MNs production process schematic: front (A) and back (B) moulds are fabricated from the master templates. The moulds are then used to produce a polymer MNs wafer (C). Reproduced under the terms of the CC-BY 4.0 license from ref [32], Copyright 2022, the Authors, published by IEEE.

The polymeric wafer was then metallized front and back with 20 nm of titanium (Ti), functioning as an adhesion layer, and 100 nm of platinum (Pt). A Temescal EUFC4900 (Ferrotec, USA) e-beam deposition tool was used for the metallization. The geometry of the back mould enabled through-wafer electrical connection and divided the wafer into 17 circular electrodes, each with a diameter of 9 mm. Figure 3 shows one of these metallized circular arrays.

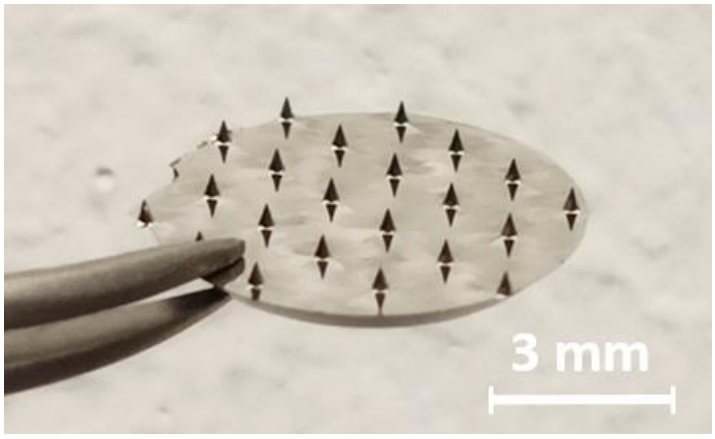


Figure 38. 9 mm metallized circular MN array.

3.3.2 Microneedle Array Passivation

In this study, layer thicknesses as well as deposition and patterning methods were based on literature reviews and commonly available microfabrication techniques.

The arrays were passivated using six different materials: Maybelline 130 varnish (Maybelline, New York, USA), 600 nm silicon oxide, A15 PMMA (from EM Resist, Manchester, England), Epotek 353ND (from Epoxy Technology Europe GmbH, Augsburg, Germany), a 55 µm thick medical-grade tape (ARcare 7759 from Adhesives Research, Limerick, Ireland) and a 2 µm thick parylene layer.

The varnish was directly brushed over the MN array. The tips of the needles were exposed due to gravity as the wet varnish flowed back towards the substrate. Once the first layer of varnish was dry, a second layer was applied in the same manner. This method is expected to create a coating with a thickness greater on the substrate than on the lower body of the needle.

SiO_2 was deposited and patterned at wafer level using an existing double masked sputtering process. An aluminum shadow mask was machined using a VMC (Vertical Machining Centers) tool. This mask was a 100 mm disk composed of 1 mm wide metal

bars separated by 0.75 mm wide openings. The mask was positioned on the wafer so that the bars were aligned with and covering all MN rows (Figure 4A and 4B). A 300 nm oxide layer was then deposited on the wafer (Figure 4C). The mask was then separated from the wafer, rotated 90° (Figure 4D) and the sputtering repeated once more (Figure 4E). Theoretically, the double deposition passivated the entire surface except for 1 x 1 mm^2 squares centered on each needle (Figure 4F). Sputtering should allow the deposition of very thin and conformal layers, potentially maximizing the amount of usable height.

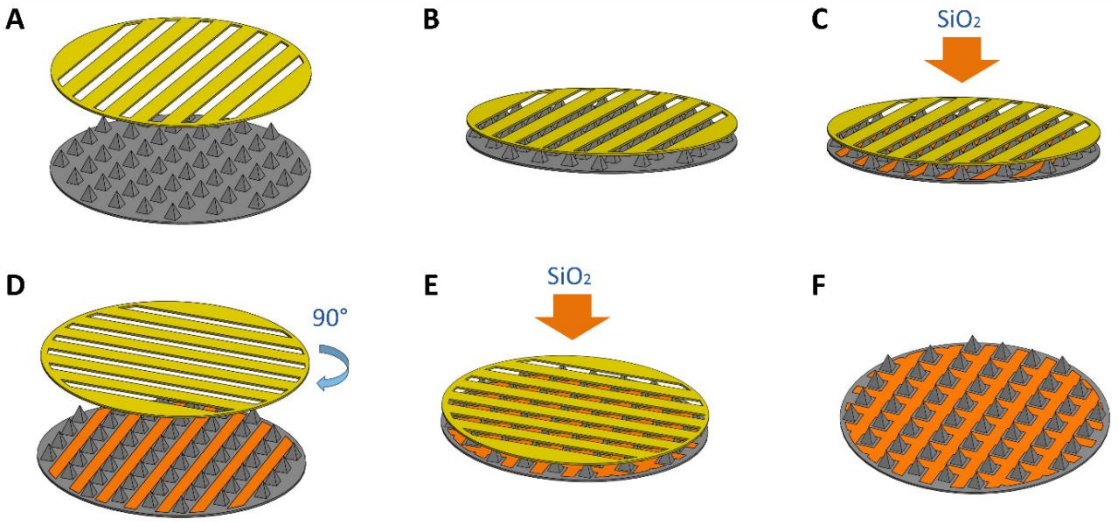


Figure 4. Schematic of the SiO_2 deposition process: the MN wafer was coupled with the metal mask (A) so that the needles were protected (B). SiO_2 was then sputtered on the wafer (C). The mask was rotated 90 degrees (D) and the process repeated (E), passivating the wafer except for 1 x 1 mm^2 squares around centred on the MNs (F).

SiO_2 is also commonly implemented in various microelectronics applications, and it is known to be a very stable passivation layer. It resists several chemical and thermal processes, it is a good electrical insulator, and it is a great barrier against impurities [35]. It is resistant to corrosion and abrasion, it is resistant to microorganisms colonization, and

thin layers of SiO_2 are very flexible [36]. All these characteristics make sputtering of SiO_2 very appealing as a potential candidate material for MN passivation.

Both PMMA and Epotek were spin-coated on the arrays using an OPTIcoat ST30 coater from ATMvision (Singen, Germany). In both cases, the arrays were washed with acetone and blown dry with nitrogen prior to coating. The spin-coating profile for PMMA was 100 rpm for 2 s, followed by 500 rpm for 2 s and 1400 rpm for 45 s. The material was then baked at 150° C for 3 min on a hotplate. The Epotek was pre-heated at 50° C to decrease the viscosity and spun at 500 rpm for 2 s followed by 1000 rpm for 2 s and 2500 rpm for 45 s. Finally, the epoxy was baked for 2 min at 150° C. Spin coating should help to improve the uniformity of the coating over more manual techniques such as brushing (as used for varnish). However, the MNs are 3D structures. Therefore, they could interact with the coating process in a manner that may lead to different thicknesses on opposite sides of each needle. The spin coating recipes have been selected following testing of different spinning parameters. These tests have been included as supplementary information. Both PMMA and epoxies have good stability [37], [38], and ISO certified medical-grade options, making them promising candidates for passivating biosensors.

ARcare 7759 is a single-sided acrylic pressure-sensitive adhesive (PSA) on a clear polyester backing. After removal of the release liner, the backing/adhesive layers have a combined nominal thickness of 55 µm (25 µm for the backing and 30 µm for the AS-110 medical grade acrylic adhesive). The tape was cut to shape and patterned with 500 µm circular holes using a Graphtec CE7000-40 vinyl cutter. The holes were centered over each MN. The adhesive layer was manually applied to each array and pressed down with tweezers to properly attach it to the substrate. ARcare is the thickest passivation layer and will not cover the lower region of the MNs. However, it should be durable and mechanically very stable. The adhesive layer is a certified medical grade material, and

this tape has already been used for *in vivo* studies [31], proving its biocompatibility. As demonstrated by the production of perforated tapes for products such as wound dressings, patterning of tape is also scalable at industrial level. These qualities make this passivation technique very appealing for use on MN-based biosensors.

Prior to parylene coating, the back of the wafer was protected by applying Kapton polyimide tape (Farnell, Ireland) (Figure 5A and 5B). The front of the wafer was passivated with a 2 µm thick layer of parylene (Figure 5C) using a Labcoater 3 Parylene Deposition System (PDS 2010 from Specialty Coating Systems, Indianapolis, USA). The protective tape was then removed from the back of the wafer (Figure 5D), and the individual arrays detached from the wafer frame. Using the vinyl cutter, a Kapton sheet (Farnell, Ireland) was perforated with 500 µm circular openings positioned to correspond with the MNs. Individual pieces were cut to match the shape of the arrays. The Kapton sheet was then placed on the arrays (Figure 5E and 5F). The metal masks described earlier were used to function both as heatsinks and as a clamping mechanism, firmly locking this sheet against the array (Figure 5G). The parylene was finally etched from the exposed needles and surrounding circular areas with 4 cycles of plasma oxygen (Figure 5H), exposing the Pt (Figure 5I). The plasma was generated using 285 W power, 23 ml/min of oxygen and delivered by a March Plasmod plasma asher (March Instruments Incorporated, acquired by Nordson, Ohio, USA). The first 3 cycles were 5 minutes long while the last plasma cycle was 3 minutes long. At the end of each one of them, the samples were blown with nitrogen and left to cool down at room temperature to minimize thermal stresses. In a manner similar to SiO_2, parylene should form a thin, precise, and conformal layer. Hence, the available height usable for penetration should be maximized. Also, it is widely used for medical devices due to its excellent biocompatibility, corrosion resistance, and long-term stability [39], [40]. Therefore, parylene would be more

appealing than SiO_2. However, the additional etching step makes the process more complex. Still, both plasma etching [41] and chemical vapor deposition [42] are used at industrial level, making this technique fully scalable.

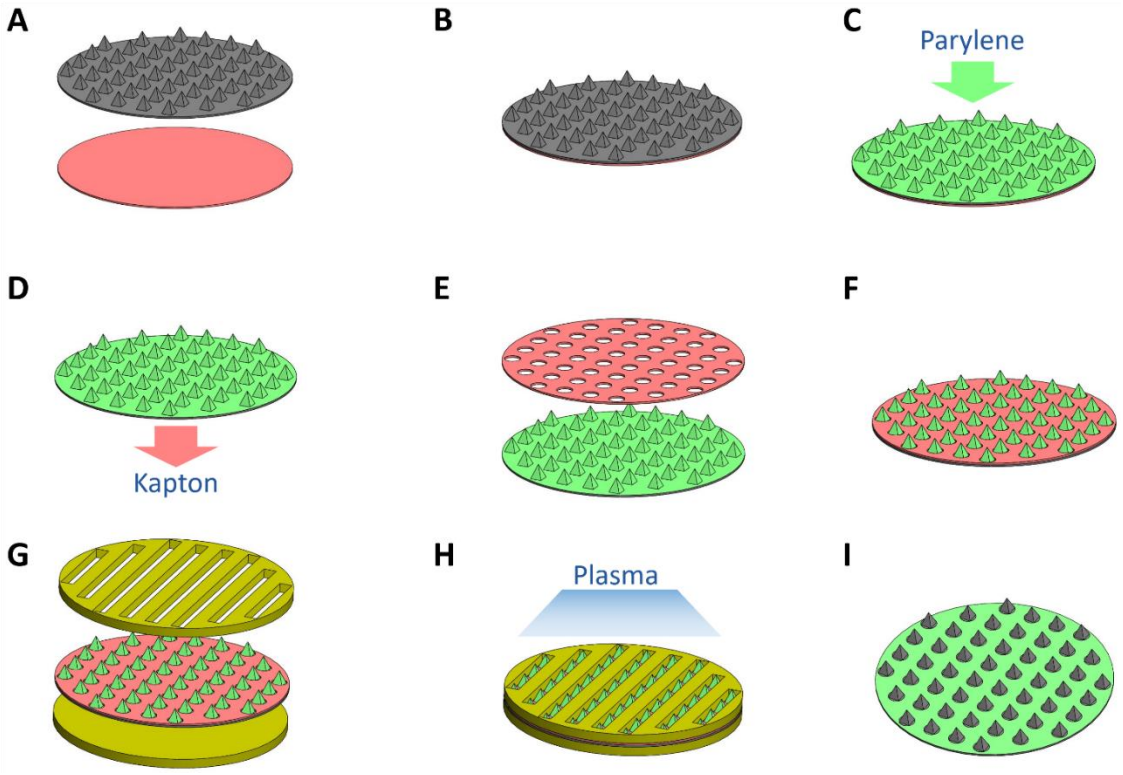


Figure 5. Schematic of the parylene passivation: Kapton tape was used to protect the back of the wafer (A and B) and parylene was then deposited on the front (C). The tape was removed (D) and a Kapton sheet was cut, placed on the MN arrays (E and F) and sandwiched in between metal masks (G). The parylene was then plasma etched (H) to expose the needles and circular areas around them (I).

3.3.3 Microneedle Testing

All arrays were visually inspected using both an optical microscope and a Zeiss Supra 40 scanning electron microscope (SEM). Using data combined from both techniques, the average exposed area was calculated for each passivation method.

To electrochemically evaluate and compare all samples, the arrays were mounted on 3D printed supports equipped with electrical connection (Figure 6).

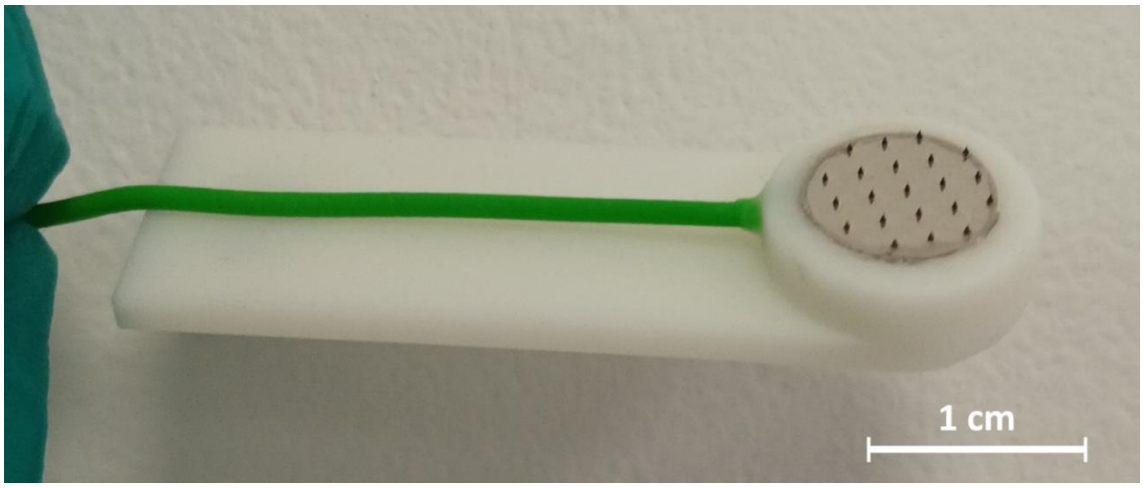


Figure 6. MN array mounted on a 3D printed support with electrical connectivity.

The supports were printed with a Formlab 3+ printer (Solid Print3D Ltd, UK) and white resin (F2GPWH04 from Solid Print3D Ltd, UK). The arrays were attached to the supports using 8330S conductive glue (MG Chemicals, Manchester, UK). All gaps in between the two parts were completely sealed using Loctite Power Flex superglue (Henkel Corp., OH, USA).

Cyclic voltammetry (CV) was employed to characterize the samples: the arrays were used as a working electrode (WE) together with an external Ag/AgCl reference electrode (RE - Gamry, Warminster, PA 18974, USA) and a Pt wire (Gamry Instruments, PA, USA), functioning as counter electrode (CE). The measurements were performed at room temperature with an Autolab MAC90389 electrochemical workstation (Metrohm, Cheshire, UK) using a NOVA 2.1 software and a Faraday cage (Metrohm).

The CV scans were performed in a 10mM PBS solution (pH = 7.4) containing 1mM FcCOOH, sweeping between 0 and 0.6 V with a 0.05 V/s scan rate. The arrays were

cleaned prior to characterization with CV scans executed in a H_2O: NH_4Cl: H_2O_2 solution (5:1:1 ratio). The potential of the cleaning CV was cycled between -0.5 V to 0.5 V using a scan rate of 0.05 V/s versus the Ag/AgCl Re and the Pt CE.

Ammonium chloride (NH_4Cl), ferrocenemonocarboxylic acid (FcCOOH) and phosphate buffered saline (PBS) were all acquired from Merck (Sigma Aldrich, Arklow, Ireland). Milli-Q water (H_2O; resistivity 18.2 MΩ.cm) was use as solvent for all solutions.

The surface properties of passivation layers, particularly hydrophobicity, play a critical role in influencing biomolecule adhesion and subsequent electrochemical performance. To evaluate this, contact angle measurements were performed for each passivation layer. They were carried out using an OCA20 wetting angle kit by DataPhysics Instruments GmbH (Filderstadt, Germany). Three samples were used for each layer.

3.4 Results

A primary objective of adding a passivation layer is to isolate the substrate area while allowing as much of the needle body as possible to remain in contact with the epidermal layers. Therefore, both SEM and optical microscopy images were analysed to calculate the total exposed area of the arrays after application of the various layers. ImageJ [43] was used to perform the analysis of the pictures. The optical microscope images were used to check for defects in the passivation layers covering the substrate and, if present, to determine the exposed area around the needles. On the other hand, SEM was essential to accurately evaluate the non-passivated percentage of the lateral surface of the MNs. Six MNs for each passivation technique were used to calculate an average unprotected area. This value was used to estimate the total exposed area for each array passivated with the same method. Figure 7 shows an example of the passivated MNs compared with a bare needle. The MNs shown in the pictures are 500 µm tall. An image of the SiO_2 sample

was not included in Figure 7 because no evident visual differences with the control were observed.

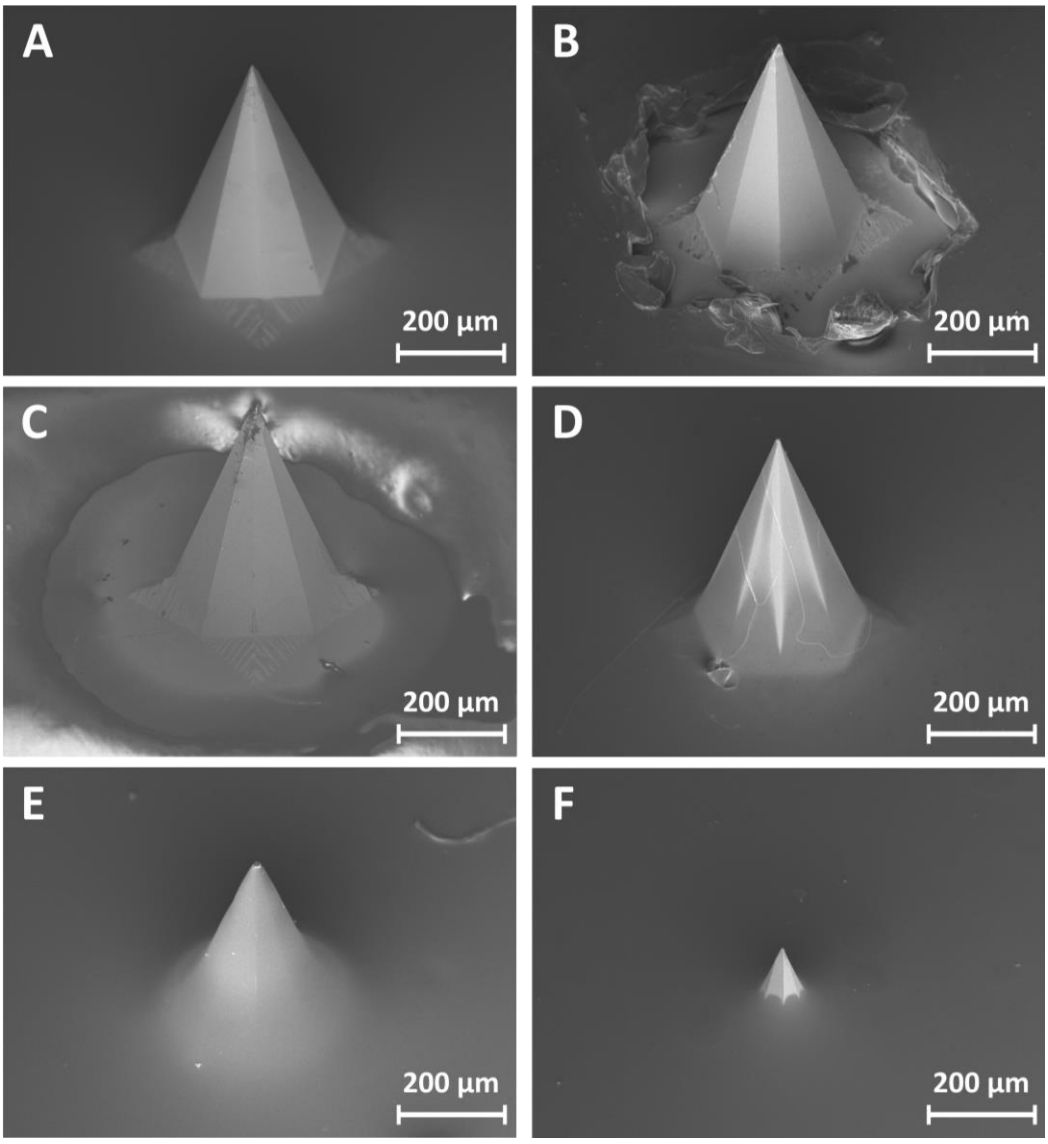


Figure 7. SEM images of a bare MN (A) together with all passivated needles. The passivation captured are ARcare 7759 (B), parylene (C), PMMA (D), varnish (E) and Epotek (F) respectively. No evident difference was observed between SEM pictures of control and SiO_2 passivated MNs.

The MNs are shaped as octagonal pyramids. Therefore, the lateral surface area, A_l and the base area A_b, can be calculated using the following formulas:

$$A_l = 2s\sqrt{4h^2 + s^2 cot^2\left(\frac{\pi}{8}\right)} \qquad (1)$$

$$A_b = 2s^2 cot\left(\frac{\pi}{8}\right) \qquad (2)$$

where s is the base edge length and h is the pyramid height.

Considering Figure 7, the MNs covered with varnish exhibited a shape more similar to a cone. Therefore, for this specific passivation, A_l was calculated using:

$$A_l = \pi r l \qquad (3)$$

where r is the base radius of the cone and l is its slant height.

The average values found for h and s together with the corresponding calculated lateral areas are reported below in Table 2. The values reported for varnish are l instead of h and r instead of s (highlighted in the table itself close to the number).

Six arrays were analyzed and tested for each passivation method. Due to the circular nature of the MN samples and the positioning of the rear mould, the number of needles on each array may vary from sensor to sensor. The average number of MNs on each array was 18 ± 3. The theoretically exposed surface area (*TSA*) was calculated for each

electrode. Varnish, PMMA and Epotek only used the lateral unprotected area (A_l) and multiplied it by the number of needles on the array. ARcare 7759 and parylene followed the same procedure. However, before multiplying by the number of MNs, the exposed substrate area (A_{ex}) minus the base area of the octagonal pyramids (A_b) was added to A_l. A_{ex} was calculated once again by analyzing six SEM pictures with ImageJ and averaging the results. The circular exposed substrate areas were 0.46 ± 0.02 mm^2 and 0.17 ± 0.01 mm^2 for the parylene and ARcare 7759 respectively. The same steps were followed for the SiO_2. However, it was difficult to clearly see the pattern of the deposited oxide because of the thin and transparent nature of the material. Therefore, for this passivation, A_{ex} was calculated starting from the 1 mm^2 square theoretically produced by the double sputtering process. Because the sputtering was performed with the mask not in hard contact with the substrate, the oxide was likely to spread underneath the mask [44], covering more area than intended (Figure 8).

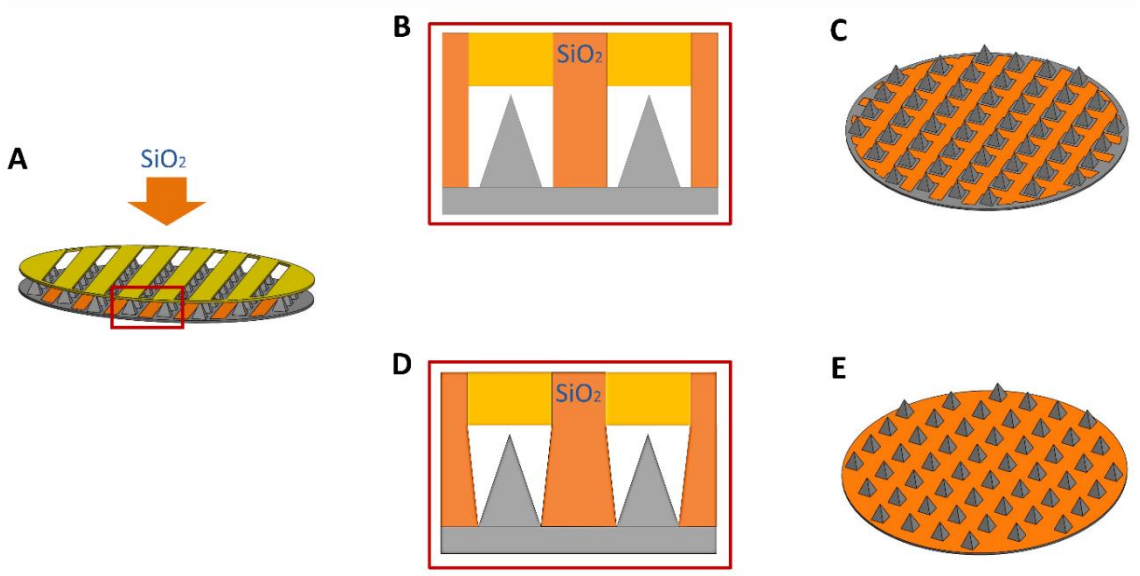


Figure 8. Schematic representing the undesired spreading of the SiO_2 underneath the mask. This phenomenon has also been reported by other authors [44]. Once the sample was ready for sputtering, a gap was present between the tip of the MNs and the mask (A). Ideally, the oxide should have covered only the exposed area (B and C), however, it spread underneath the mask (D), covering more surface (E).

From our previous experience with sputtering metals on masked MN wafers [31], the side of the exposed square could be reduced from a nominal value of 1 mm to as little as 0.5 mm. The spreading would form a layer decreasing in thickness with distance under the mask. This would also explain the difficulties encountered while trying to visually identify a clear distinction between the sputtered and the unprotected area. Considering the possible side reduction, A_{ex} could vary between 1 mm^2 and 0.25 mm^2. Therefore, A_{ex} was considered as 0.625 ± 0.375 mm^2.

After finding all A_l and A_{ex}, six different arrays were prepared for every passivation. The average exposed area was then calculated for each different type of array as explained. If

any defect was spotted in the passivation, this additional area (*AA*) was averaged and added to the total unprotected area. Therefore, *TSA* was calculated as follows:

$$TSA = (A_l + A_{ex} - A_b)MNs + AA \qquad (4)$$

where *MNs* is the number of needles on the array.

As stated, for PMMA, varnish and Epotek, A_{ex} and A_b were not used.

Possible sources of errors were taken into consideration for all dimensions. For the MNs where the passivation is not covering any part of the needles, the uncertainty in *h* and *s* is caused exclusively by the moulding process (control, SiO_2, parylene and ARcare 7759). If the MNs are partially covered, the standard deviation found while averaging the values taken from the SEM images was used instead (PMMA, varnish, Epotek). These errors were also propagated to calculate the possible variation for A_l. A_{ex} inaccuracy was either taken from the possible imprecision introduced by the passivation process (SiO_2) or from the standard deviation found from image analysis. The propagation of the error was also used to find the *TSA* uncertainty for each passivation. All data is summarized in Table 2.

Table 2. Average values for h, s, A_l and A_{ex} are calculated for each passivation technique (n = 6 for each cases). For the varnish, l and r are reported instead. The theoretical surface area (*TSA*) of the exposed portion of the differently passivated arrays is reported in the last column.

Passivation	***h* (µm)**	***s* (µm)**	A_l **(mm^2)**	A_{ex} **(mm^2)**	***TSA*** **(mm^2)**
Control	500 ± 5	124 ± 2	0.259 ± 0.007	All exposed	55.2 ± 0.8
SiO_2	500 ± 5	124 ± 2	0.259 ± 0.007	0.625 ± 0.375	18 ± 12
Parylene	500 ± 5	124 ± 2	0.259 ± 0.007	0.45 ± 0.02	9.5 ± 0.5
ARcare 7759	500 ± 5	124 ± 2	0.259 ± 0.007	0.17 ± 0.01	6.4 ± 0.4
PMMA	359 ± 16	92 ± 4	0.14 ± 0.01	0	2.4 ± 0.3
Varnish	191 ± 33, *l*	60 ± 10, *r*	0.05 ± 0.02	0	0.8 ± 0.3
Epotek 353ND	131 ± 14	32 ± 12	0.017 ± 0.009	0	0.3 ± 0.2

In the context of passivated microneedles, electrochemical correlation can be important in understanding how the passivation layer affects the electrochemical properties of the microneedles.

Therefore, cyclic voltammetry was carried out on the six previously prepared sensors. This was done to evaluate the electrical isolation provided by the different passivation layers: the lower the observed currents are, the higher electrochemical isolation the passivation provides. Average electron transfer behavior results are reported in Figure 9.

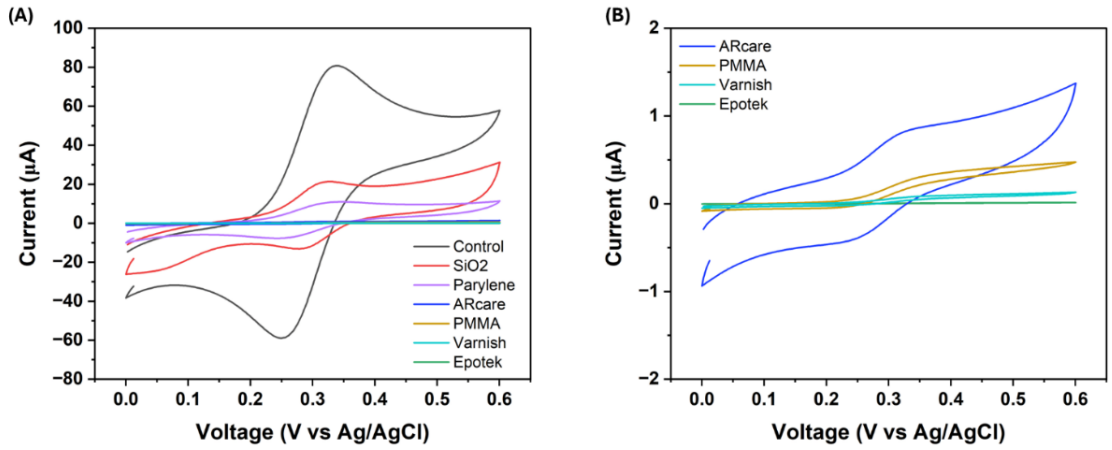


Figure 9. CV scans in 1 mM FcCOOH in 10 mM PBS for each passivation method (A) together with magnification on the ARcare 7759, PMMA, varnish and Epotek curves (B).

Understanding the electrochemical properties of passivated microneedles is important for optimizing their performance in various applications. Passivation layers significantly affect electron transport properties, especially in enzyme-modified sensors. As demonstrated by different studies [45], [46], comparing different passivation methods provides valuable insights and offers a more thorough understanding of their impact. Oxidation and reduction peak currents, namely I_p^{ox} and I_p^{red}, total current variation (ΔI) and Electrochemical Surface Area (*ESA*) were extracted from the curves and are reported in Table 3.

Table 3. Peak currents (I_p^{ox} and I_p^{red}) and total current (ΔI) extracted from the graphs in Figure 9. The ESA calculated from equation (6) is also reported.

	Peak Current (x 10^{-7} A)			
Passivation	I_p^{ox}	I_p^{red}	**ΔI (μA)**	***ESA* (mm^2)**
Control	808 ± 113	-590 ± 84	140 ± 20	57.8 ± 0.8
SiO_2	214 ± 23	-131 ± 38	35 ± 6	15.3 ± 0.2
Parylene	172 ± 18	-133 ± 21	30 ± 4	12.3 ± 0.1
ARcare 7759	110 ± 10	-77 ± 11	19 ± 2	7.9 ± 0.1
PMMA	3.0 ±0.5	-0.3 ± 0.2	0.33 ± 0.07	0.210 ± 0.004
Varnish	0.8 ± 0.1	-0.16 ± 0.05	0.10 ± 0.02	0.060 ± 0.001
Epotek	0.081 ± 0.02	-0.0003 ± 0.006	0.008 ± 0.003	0.0060 ± 0.0002

The *ESA* was calculated starting from the following relation for I_p^{ox} [47]:

$$I_p^{ox} = (2.69 \cdot 10^5) \cdot n^{\frac{3}{2}} \cdot ESA \cdot C \cdot D^{\frac{1}{2}} \cdot v^{\frac{1}{2}}, \qquad (5)$$

where n is the number of electrons transferred in the redox, D is the diffusion coefficient of the oxidised analyte, C is the bulk concentration of the analyte and v is the used scan rate. For our system, $C = 10^{-3}$ mol/cm^3, $v = 0.05$ V/s, $n = 1$, $D = 5.4 \times 10^{-6}$ cm^2/s.

Therefore, the electrochemical surface area can be calculated as:

$$ESA = \frac{I_p^{ox} \cdot n^{-\frac{3}{2}} \cdot D^{-\frac{1}{2}} \cdot v^{-\frac{1}{2}}}{(2.69 \cdot 10^5) \cdot C}, \qquad (6)$$

The imprecision for the *ESA* was calculated only considering the standard deviation of I_p^{ox}. In a perfect scenario, the *ESA* should correspond with the *TSA* recorded in Table 2. Therefore, the *ESA* was then compared with the previously calculated *TSA*. The values are reported in Table 4, along with the Ideal Surface Area (*ISA*). This is the product of the lateral surface area A_l multiplied by the number of needles per array. It represents the surface area that would result from application of an ideal passivation layer. This layer would cover the entire substrate area whilst allowing the total surface area of the needle to remain exposed.

Table 4. Comparison *TSA* calculated from the images analysis with the experimentally measured *ESA*. In addition, the average number of MNs is reported for each sample together with the total lateral MNs area on the samples (*ISA*).

Passivation	**# MNs per array**	***ISA* (mm^2)**	***TSA* (mm^2)**	***ESA* (mm^2)**
Control	22	5.7 ± 0.2	55.2 ± 0.8	57.8 ± 0.8
SiO_2	17 ± 1	4.4 ± 0.1	18 ± 12	15.3 ± 0.2
Parylene	15 ± 1	3.9 ± 0.1	9.5 ± 0.5	12.3 ± 0.1
ARcare 7759	18 ± 1	4.7 ± 0.1	6.4 ± 0.4	7.9 ± 0.1
PMMA	17 ± 1	4.4 ± 0.1	2.4 ± 0.3	0.210 ± 0.004
Varnish	21 ± 1	5.4 ± 0.2	0.8 ± 0.3	0.060 ± 0.001
Epotek	19 ± 1	4.9 ± 0.1	0.3 ± 0.2	0.0060 ± 0.0002

These results were also plotted and are visually represented in Figure 10.

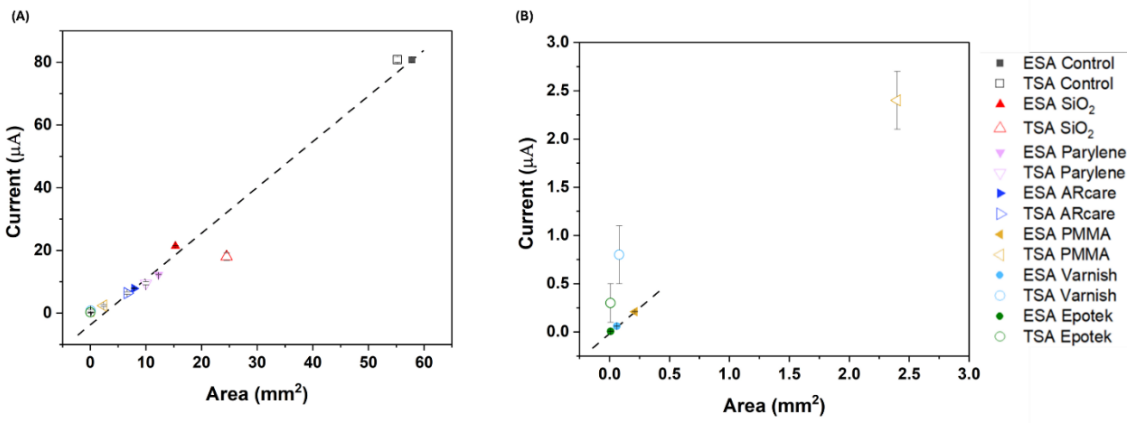


Figure 10. Scatter plots of current vs area showing differences between the electrochemically found *ESA* (full marker) and visually measured *TSA* (empty marker). A dashed line was traced starting from the control to highlight the linear correlation between area and observed current (*ESA*). The second plot (B) focuses on the smaller values not clearly visible in the first one (A).

It is immediately clear from Table 4 that the *TSA*/*ESA* varies strongly with passivation type. ARcare 7759 was the closest to its *ISA*. In addition, in some cases, significant differences were also observed between the *ESA* and *TSA* measurements. Therefore, each samples' group was individually inspected to find the cause of these variations.

Starting from the control, the *ESA* was slightly larger than what was initially estimated. From Figure 11, it is evident that the superglue used to seal the mounted electrodes formed an irregular shape at the edges of the array. This made a precise assessment of the area more difficult while processing the images. Moreover, cyanoacrylate has the tendency to bloom [48], the effect of which will further increase any visual underestimation of the exposed area.

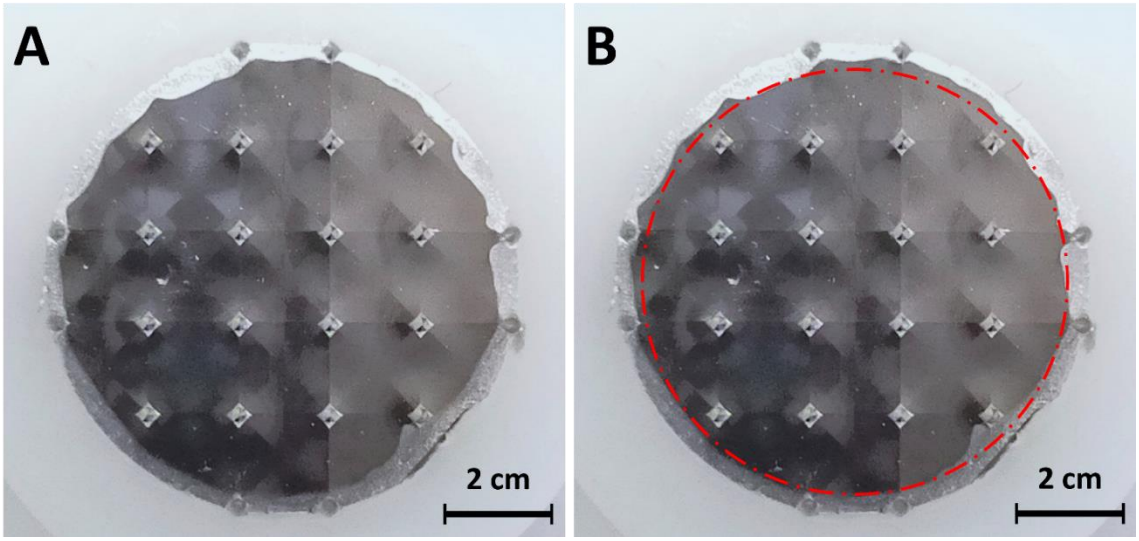


Figure 11. Top view of a bare microneedle array assembled for electrochemical characterization (A). The red dashed circle has been included to highlight the irregularity of the superglue used to insulate the front of the electrode from the back (B).

Overall, these phenomena easily explain the < 3% difference found in between the *TSA* and *ESA* measured on control samples. Changing the adhesive or improving control over dispensing/environmental factors, could reduce this discrepancy even further [48].

SiO_2's *TSA* had a large uncertainty due to the potential spreading of the oxide below the mask. However, the measured *ESA* was also within this range and could be used to experimentally calculate the dimensions of the exposed area around the MNs. Firstly, for each needle, A_l was removed from the *ESA* and A_b re-added. Then *AA* was subtracted, and the remaining surface divided by the number of MNs. The number of needles for the SiO_2 samples was 17 ± 1. Considering this variability, the real A_{ex} for the SiO_2 process was calculated to be 0.47 ± 0.03 mm^2.

Both ARcare 7759 and parylene showed an *ESA* higher than the *TSA* and *ISA*, indicating a larger exposed area. Analyzing ARcare 7759 first, two possible causes were highlighted

by the SEM analysis. Because of the relatively low resolution provided by the mechanical cutting process, the edges of the openings are not sharply defined (Figure 12). Therefore, the standard deviation calculated for A_{ex} was probably an underestimation of the real variability of the hole size. Secondly, because the tape was placed on the arrays by hand, it was difficult to reliably ensure intimate contact between the passivation and the substrate (Figure 12A). Partial lifting of the tape would expose more electroactive area, explaining the higher *ESA*.

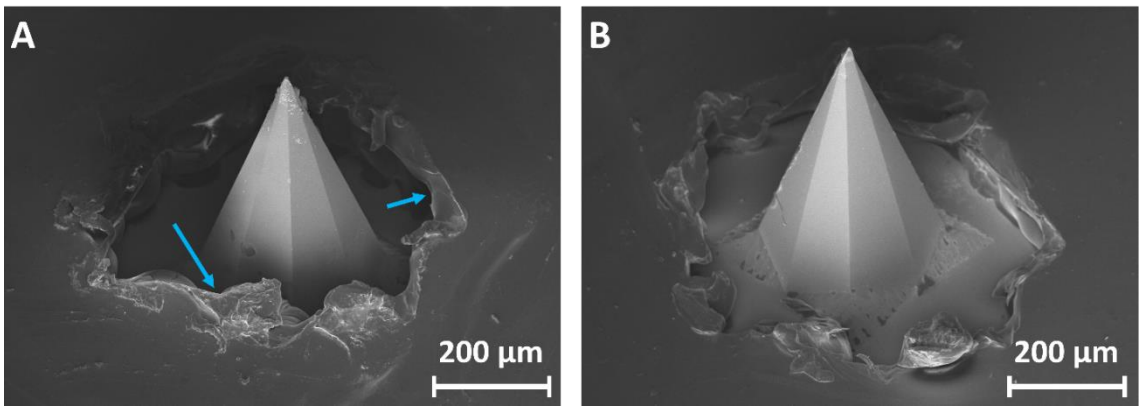


Figure 12. SEM images of two ARcare 7759 passivated MNs. The first image (A) is showing the tape lifting (blue arrows) while, in the second case (B) the tape is in intimate contact with the substrate.

Using a laser cutter instead of a vinyl cutter [14] would increase the reproducibility and precision of the layer. This would guarantee a more homogenous result, avoiding the irregular edges shown in Figure 12. However, considering the possible risk of the lifting of the tape, this passivation may not be the best option for densely packed MN arrays.

The parylene passivated sensors were inspected next. Defects, highlighted by blue arrows on Figure 13, were occasionally found alongside the rim of the passivation layer. These imperfections increased A_{ex}, explaining the original *TSA* underestimation. Considering

they were all placed in similar positions over the parylene edges, this was more likely caused by the removal of the Kapton mask, which was peeled away from the array in the direction in which defects were subsequently found. Interestingly, the area calculated during the initial analysis reported in Table 2 was already showing parylene etching over a surface bigger than what the Kapton mask was leaving exposed. The parylene appeared to be removed over circles with a diameter of 754 µm (± 15 µm, n = 6) rather than the originally designed 500 µm, which we assume is due to under-etching below the Kapton mask.

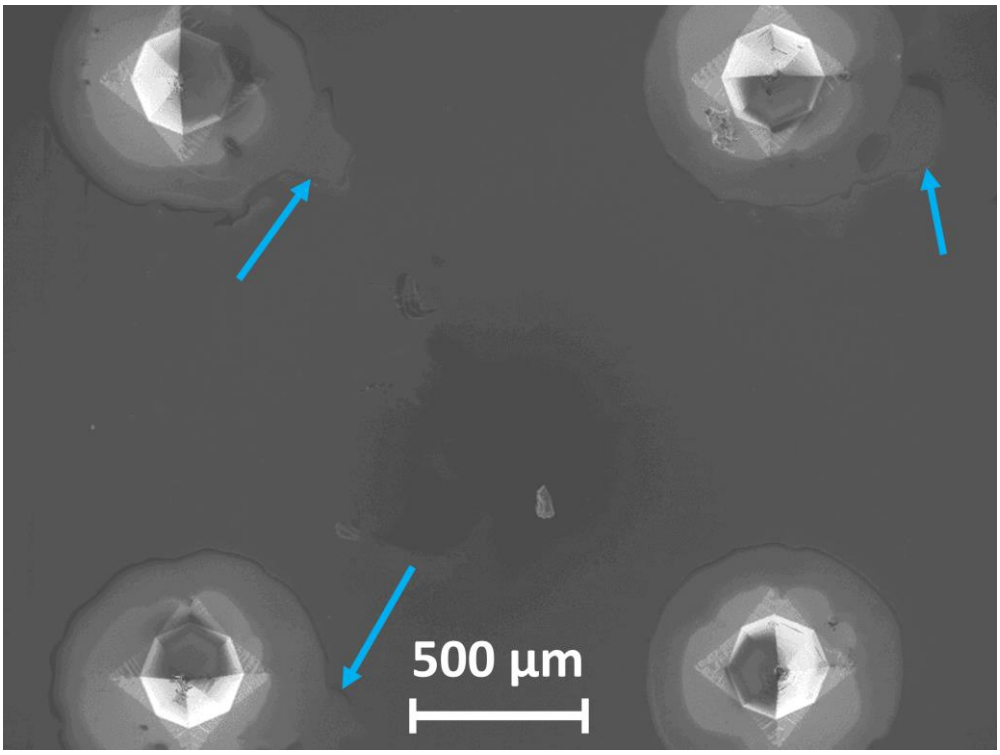


Figure 13. Parylene passivated MNs after oxygen etching. Blue arrows are highlighting examples of defects that may occur at the edges of the parylene layer.

The three liquid layers (PMMA, vanish and Epotek) showed exposed areas that were significantly smaller than those measured using the other methods. For varnish and Epotek, this area was near zero. The experimentally measured *ESA* of the Epotek

passivated arrays was 55 times smaller than the expected *TSA*. Similarly, both PMMA and varnish also had very large differences between *ESA* and *TSA*. For Epotek passivation, it was immediately evident from the SEM and optical miscroscope images (Figure 14) that the needle coverage was highly variable. Secondly, the polymer was not conformal to the MNs. It rather formed a thick layer over the entirety of the space in between needles, greatly reducing the height available for skin penetration. The *ESA* result showed that the exposed area was near zero. This indicates that the spin coating process may also result in a thin layer coating the entire needle, that was difficult to visually detect during *TSA* calculation.

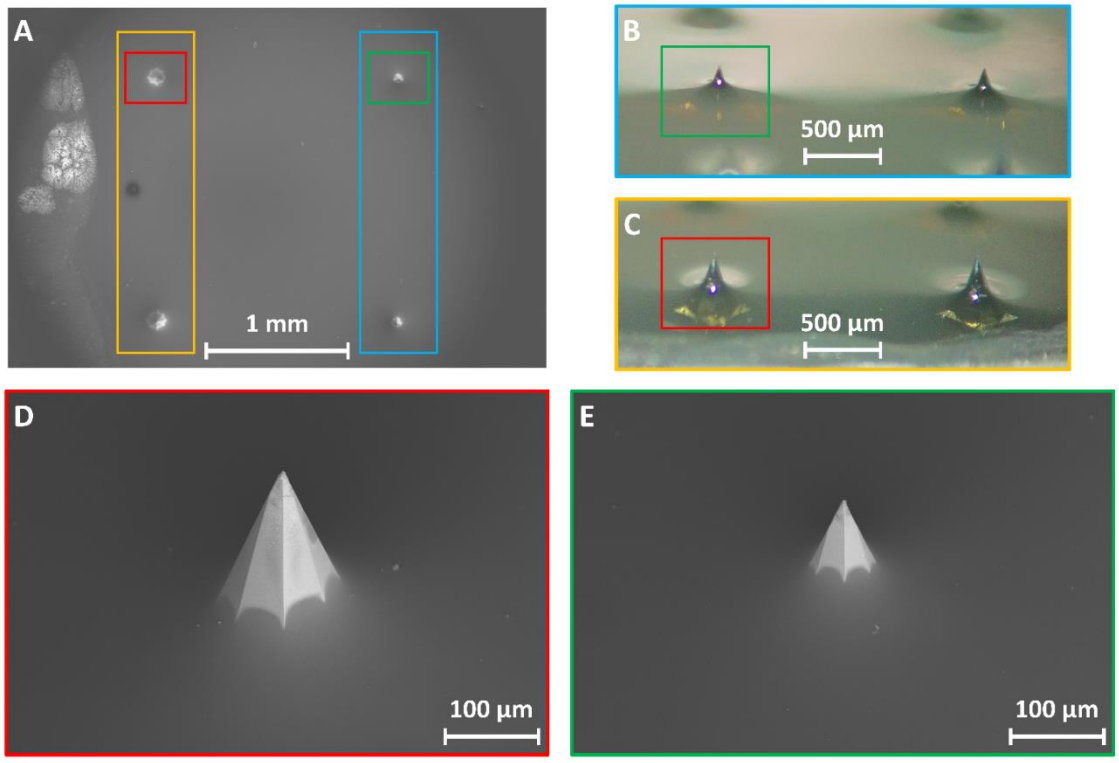


Figure 14. SEM images of an Epotek passivated array (A) together with close up views of 2 MNs (D and E). Optic microscope images of the same needles are reported as well (B and C). Colour coding was used to better show correlations between different images.

The result could indicate the need to refine the spin coating profile. It could also mean that a thermal curing polymer, whose viscosity highly varies with temperature changes, may not be ideal for spin coating.

As shown in Figure 15, the spincoated PMMA polymer layer was thinner and more conformal to the needles, allowing more of the structure to protrude above the passivation. However, considering the high discrepancy in between *TSA* and *ESA*, it is likely that a thin and visually undetectable layer of PMMA is covering a significant portion of the MNs.

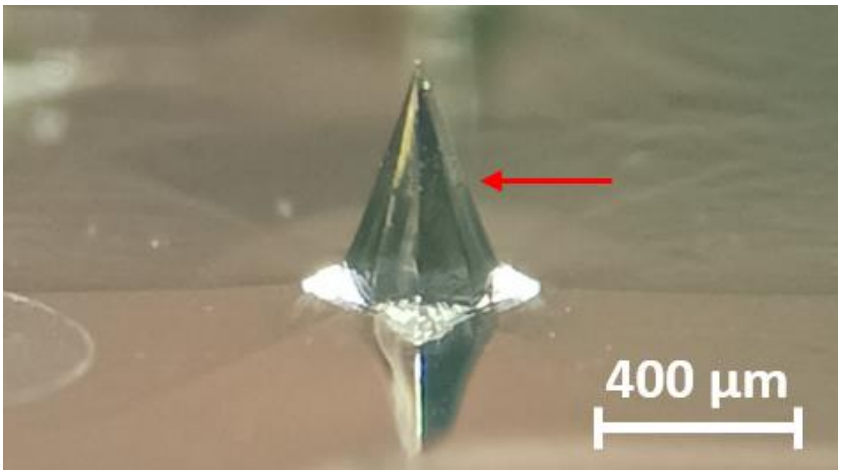


Figure 15. Optic microscope image of a PMMA passivated MN. The red arrow is showing the possible edge of the passivation on the side of the needle. However, the difference is not clearly detectable.

The last remaining electrodes which needed deeper investigation were the varnish-passivated arrays. The SEM pictures showed a shape more similar to a cone than to a pyramid, already suggesting the presence of varnish high on the needles. High resolution optical microscopy was used to better assess the coverage of the needles. Varnish is clearly visible on the sides of the needles almost for the entirety of its height (Figure 16).

Contrarily to what was assumed using the SEM, the only evidently exposed areas seemed to be the tip and the intersections between the lateral faces of the octagonal pyramid. This reduced area is likely to be the reason of the overestimation in *TSA* compared to *ESA*. Like PMMA, varnish was conformal to the shape of the needles.

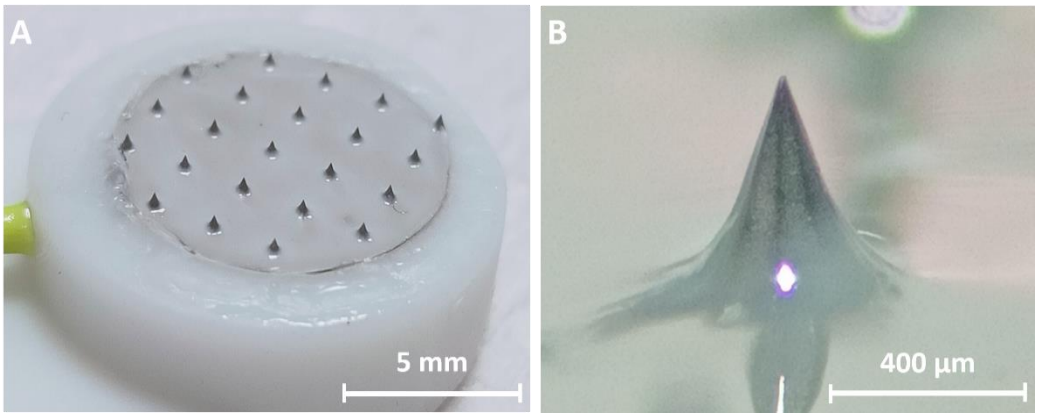


Figure 16. Picture of a varnish passivated array (A) and 75° angled optical microscope magnification of an individual needle (B).

The results of the contact angle measurements are reported in Table 5.

Table 5. Contact angled measured for the different passivation layers.

Passivation	Contact angle (°)
Control	45.0 ± 2.8
ARcare 7759	29.8 ± 1.8
Parylene	39.4 ± 1.1
PMMA	45.1 ± 2.4
Epotek	52.2 ± 2.8
Varnish	64.3 ± 1.1
SiO_2	65.3 ± 1.2

Hydrophobicity reduces biomolecule adhesion. This was shown by Yan et al. which demonstrated that hydrophobic self-assembled monolayers (SAMs) can enhance direct electron transfer by minimizing undesired surface interactions [49]. Conversely, more hydrophilic surfaces demonstrate increased biomolecule adhesion [50]. As shown by Heydari-Bafrooei and Ensafi, this can enhance electron transfer efficiency by promoting effective biomolecule immobilization [51]. However, this increased adhesion may also lead to non-specific adsorption of unwanted species, causing higher background noise and reduced signal reproducibility [52].

3.5 Discussion and Conclusions

Passivation layers are an essential component of microneedle-based biosensor devices, and are used to block responses arising from the unwanted functionalisation of the

substrate around the needles. In this paper, we have firstly provided a definition of an ideal passivation layer, and then carried out a preliminary study of six potential passivation materials.

Three liquid layers - PMMA, varnish and Epotek 353ND - were found to result in coatings difficult to control. These led to low or near-zero exposed areas in all three cases. Uniformity of the coverage, together with high difference between *ESA* and expected *TSA*, was also a concern. Significant additional work is required to optimise the coating procedures and to render these materials a viable option for passivation. Direct brushing is relatively uncontrollable and, critically, not scalable. This makes it an inferior option to spin coating. Finally, spinning of Epotek resulted in a dramatic reduction of the height available for skin penetration, making this particular passivation process unusable. Therefore, the choice of the spin coating material is also critical to achieve more controllable results.

While sputtered silicon oxide may be used to passivate the substrate area, this method is prone to spreading of the material beneath the mask, covering more area than intended. This led to a significant difference between *ESA* and *ISA*. Further refinement, by either finding a way to control this spreading effect or by avoiding it altogether, would greatly improve the resolution of the deposited pattern. SiO_2 is highly stable, and sputtering is an industrially viable deposition option. Therefore, a solution to this problem could potentially make the sputtering of this oxide one of the best techniques for biosensor passivation. We have recently reported early progress in this regard, developing wall-like features which could potentially help in solving this issue [31]. Also, although some studies have shown promising results for SiO_2 use in *in vivo* applications, detailed biocompatibility studies should also be conducted to further reinforce their usability [36].

Parylene and Arcare 7759 seemed to be the best performing passivation materials, with experimentally measured and theoretical exposed areas of similar size. Parylene deposition resulted in a thin, reliable and controllable covering. However, its use would still benefit from a deeper understanding of the etching process, together with a refinement of the masking mechanism. This could also enable a more accurate covering of the substrate, resulting in an *ESA* closer to the *ISA*. Whilst medical tape is relatively thick, reducing the height of the needle available for penetration, it can be mechanically applied without the need for specialised deposition or etching tools. Laser cutting could be used to greatly improve the fidelity of the pattern on the tape in a scalable manner. The hole size could also be increased to facilitate a better contact between substrate and passivation, but this would come at a higher difference in between *ESA* and *ISA*. Finally, the single faced tape used in this work could be replaced with a double-sided tape, thereby providing a method of ensuring skin adhesion as well as sensor passivation. To be fully industrially viable, a custom machine should be used to reliably apply the tape to the arrays in a repeatable and automatic fashion.

Surfaces of increased hydrophobicity reduce biomolecule adhesion, which may result in improved signal stability and reduced surface fouling during electrochemical measurements. However, hydrophilic surfaces enhance biomolecule adhesion, improving electron transfer efficiency. Therefore, optimizing the hydrophobicity of passivation layers is essential to balance effective biomolecule adhesion with favourable electron transport properties. For enzyme-modified sensors, moderate hydrophobicity may provide an optimal compromise between enhancing electron transfer efficiency whilst minimizing interference from non-specific adsorption. Integrating this approach with advanced surface modification techniques may offer promising solutions for improving sensor performance in various biosensing applications.

While a number of teams have reported various materials and techniques, no commonly accepted standard for MN biosensor passivation exists, and so this work performed a preliminary study of use-case driven passivating materials and methods. In this manner, we hope to provide a basis for accelerating research in this important topic. Although a number of promising options have been developed, the high variability observed across the various methods and materials investigated here highlights the need for further research and process development in this area.

3.6 Supplementary Material

Supplementary material available in Appendix A.1.

3.7 References

[1] C. Kolluru, M. Williams, J. Chae, and M. R. Prausnitz, 'Recruitment and Collection of Dermal Interstitial Fluid Using a Microneedle Patch', *Adv. Healthc. Mater.*, vol. 8, no. 3, p. 1801262, 2019, doi: 10.1002/adhm.201801262.

[2] R. H. Stewart, 'A Modern View of the Interstitial Space in Health and Disease', *Front. Vet. Sci.*, vol. 7, 2020, doi: 10.3389/fvets.2020.609583.

[3] Y. Marunaka, 'The Proposal of Molecular Mechanisms of Weak Organic Acids Intake-Induced Improvement of Insulin Resistance in Diabetes Mellitus via Elevation of Interstitial Fluid pH', *Int. J. Mol. Sci.*, vol. 19, no. 10, Art. no. 10, Oct. 2018, doi: 10.3390/ijms19103244.

[4] W. Pan *et al.*, 'An Integrated Stretchable Sensing Patch for Simultaneously Monitoring of Physiological and Biochemical Parameters', in *2021 IEEE 16th International Conference on Nano/Micro Engineered and Molecular Systems (NEMS)*, Apr. 2021, pp. 762–767. doi: 10.1109/NEMS51815.2021.9451353.

[5] S. A. Byrnes and B. H. Weigl, ‘Selecting analytical biomarkers for developing diagnostic technologies for global health applications: Conference topics — Healthcare (medical technology)’, in *2017 IEEE Global Humanitarian Technology Conference (GHTC)*, Oct. 2017, pp. 1–1. doi: 10.1109/GHTC.2017.8239264.

[6] P. P. Samant *et al.*, ‘Sampling interstitial fluid from human skin using a microneedle patch’, *Sci. Transl. Med.*, vol. 12, no. 571, p. eaaw0285, Nov. 2020, doi: 10.1126/scitranslmed.aaw0285.

[7] K. M. Saifullah and Z. Faraji Rad, ‘Sampling Dermal Interstitial Fluid Using Microneedles: A Review of Recent Developments in Sampling Methods and Microneedle-Based Biosensors’, *Adv. Mater. Interfaces*, vol. 10, no. 10, p. 2201763, 2023, doi: 10.1002/admi.202201763.

[8] F. K. Aldawood, A. Andar, and S. Desai, ‘A Comprehensive Review of Microneedles: Types, Materials, Processes, Characterizations and Applications’, *Polymers*, vol. 13, no. 16, p. 2815, Aug. 2021, doi: 10.3390/polym13162815.

[9] X. Zhang, Y. Wang, J. Chi, and Y. Zhao, ‘Smart Microneedles for Therapy and Diagnosis’, *Research*, vol. 2020, pp. 1–26, Dec. 2020, doi: 10.34133/2020/7462915.

[10] S. Dharadhar, A. Majumdar, S. Dhoble, and V. Patravale, ‘Microneedles for transdermal drug delivery: a systematic review’, *Drug Dev. Ind. Pharm.*, vol. 45, no. 2, pp. 188–201, Feb. 2019, doi: 10.1080/03639045.2018.1539497.

[11] J. Yang *et al.*, ‘Recent Progress in Microneedles-Mediated Diagnosis, Therapy, and Theranostic Systems’, *Adv. Healthc. Mater.*, vol. 11, no. 10, p. 2102547, 2022, doi: 10.1002/adhm.202102547.

[12] R. Amarnani and P. Shende, ‘Microneedles in diagnostic, treatment and theranostics: An advancement in minimally-invasive delivery system’, *Biomed. Microdevices*, vol. 24, no. 1, p. 4, 2022, doi: 10.1007/s10544-021-00604-w.

[13] J. Madden, C. O’Mahony, M. Thompson, A. O’Riordan, and P. Galvin, ‘Biosensing in dermal interstitial fluid using microneedle based electrochemical devices’, *Sens. Bio-Sens. Res.*, vol. 29, p. 100348, Aug. 2020, doi: 10.1016/j.sbsr.2020.100348.

[14] S. Kurzhals *et al.*, ‘Detection of Lactate via Amperometric Sensors Modified With Direct Electron Transfer Enzyme Containing PEDOT:PSS and Hydrogel Inks’, *IEEE Sens. Lett.*, vol. 7, no. 9, pp. 1–4, Sep. 2023, doi: 10.1109/LSENS.2023.3307066.

[15] M.-N. Chien, Y.-J. Chen, C.-H. Bai, and J.-T. Huang, ‘Continuous Glucose Monitoring System Based on Percutaneous Microneedle Array’, *Micromachines*, vol. 13, no. 3, p. 478, Mar. 2022, doi: 10.3390/mi13030478.

[16] J. J. García-Guzmán, C. Pérez-Ràfols, M. Cuartero, and G. A. Crespo, ‘Toward In Vivo Transdermal pH Sensing with a Validated Microneedle Membrane Electrode’, *ACS Sens.*, vol. 6, no. 3, pp. 1129–1137, Mar. 2021, doi: 10.1021/acssensors.0c02397.

[17] D. Terutsuki, S. Yamaguchi, Y. Abe, H. Abe, and M. Nishizawa, ‘Porous Microneedle-Based Potentiometric Sensor for Intradermal Electrolyte Monitoring’, *Electrochemistry*, vol. 91, no. 4, pp. 047007–047007, 2023, doi: 10.5796/electrochemistry.23-00027.

[18] A. Ripolin, J. Quinn, E. Larrañeta, E. M. Vicente-Perez, J. Barry, and R. F. Donnelly, ‘Successful application of large microneedle patches by human

volunteers', *Int. J. Pharm.*, vol. 521, no. 1–2, pp. 92–101, Apr. 2017, doi: 10.1016/j.ijpharm.2017.02.011.

[19] C. Barrett, K. Dawson, C. O'Mahony, and A. O'Riordan, 'Development of Low Cost Rapid Fabrication of Sharp Polymer Microneedles for In Vivo Glucose Biosensing Applications', *ECS J. Solid State Sci. Technol.*, vol. 4, no. 10, p. S3053, Aug. 2015, doi: 10.1149/2.0141510jss.

[20] S. Metz, M. O. Heuschkel, B. Valencia Avila, R. Holzer, D. Bertrand, and Ph. Renaud, 'Microelectrodes with three-dimensional structures for improved neural interfacing', in *2001 Conference Proceedings of the 23rd Annual International Conference of the IEEE Engineering in Medicine and Biology Society*, Istanbul, Turkey: IEEE, 2001, pp. 765–768. doi: 10.1109/IEMBS.2001.1019053.

[21] M. Dervisevic, E. Dervisevic, L. Esser, C. D. Easton, V. J. Cadarso, and N. H. Voelcker, 'Wearable microneedle array-based sensor for transdermal monitoring of pH levels in interstitial fluid', *Biosens. Bioelectron.*, vol. 222, p. 114955, Feb. 2023, doi: 10.1016/j.bios.2022.114955.

[22] W.-C. Lee, N. G. Gurudatt, D.-S. Park, K. B. Kim, C. S. Choi, and Y.-B. Shim, 'Microneedle array sensor for monitoring glucose in single cell using glucose oxidase-bonded polyterthiophene coated on AuZn oxide layer', *Sens. Actuators B Chem.*, vol. 320, p. 128416, Oct. 2020, doi: 10.1016/j.snb.2020.128416.

[23] S. A. N. Gowers *et al.*, 'Development of a Minimally Invasive Microneedle-Based Sensor for Continuous Monitoring of β-Lactam Antibiotic Concentrations in Vivo', *ACS Sens.*, vol. 4, no. 4, pp. 1072–1080, Apr. 2019, doi: 10.1021/acssensors.9b00288.

[24] T. M. Rawson *et al.*, 'Microneedle biosensors for real-time, minimally invasive drug monitoring of phenoxymethylpenicillin: a first-in-human evaluation in healthy volunteers', *Lancet Digit. Health*, vol. 1, no. 7, pp. e335–e343, Nov. 2019, doi: 10.1016/S2589-7500(19)30131-1.

[25] C. Hegarty, A. McConville, R. J. McGlynn, D. Mariotti, and J. Davis, 'Design of composite microneedle sensor systems for the measurement of transdermal pH', *Mater. Chem. Phys.*, vol. 227, pp. 340–346, Apr. 2019, doi: 10.1016/j.matchemphys.2019.01.052.

[26] A. T. Satti, J. Park, J. Park, H. Kim, and S. Cho, 'Fabrication of Parylene-Coated Microneedle Array Electrode for Wearable ECG Device', *Sensors*, vol. 20, no. 18, Art. no. 18, Jan. 2020, doi: 10.3390/s20185183.

[27] R. Wang, W. Zhao, W. Wang, and Z. Li, 'A Flexible Microneedle Electrode Array With Solid Silicon Needles', *J. Microelectromechanical Syst.*, vol. 21, no. 5, pp. 1084–1089, Oct. 2012, doi: 10.1109/JMEMS.2012.2203790.

[28] C. Robinson, 'Development of on-farm diagnostic devices', Doctoral thesis, University College Cork, 2020. Accessed: Jan. 30, 2023. [Online]. Available: https://cora.ucc.ie/handle/10468/10886

[29] S. R. Chinnadayyala and S. Cho, 'Porous Platinum Black-Coated Minimally Invasive Microneedles for Non-Enzymatic Continuous Glucose Monitoring in Interstitial Fluid', *Nanomaterials*, vol. 11, no. 1, p. 37, Dec. 2020, doi: 10.3390/nano11010037.

[30] R. Wang, X. Jiang, W. Wang, and Z. Li, 'A microneedle electrode array on flexible substrate for long-term EEG monitoring', *Sens. Actuators B Chem.*, vol. 244, pp. 750–758, Jun. 2017, doi: 10.1016/j.snb.2017.01.052.

[31] A. Bocchino *et al.*, ‘A multifunctional platform for the production and customization of polymer-based microneedle devices’, *Sens. Actuators Phys.*, vol. 388, p. 116491, Jul. 2025, doi: 10.1016/j.sna.2025.116491.

[32] A. Bocchino *et al.*, ‘Development and Characterization of Passivation Methods for Microneedle-based Biosensors’, in *2022 44th Annual International Conference of the IEEE Engineering in Medicine & Biology Society (EMBC)*, Jul. 2022, pp. 1275–1278. doi: 10.1109/EMBC48229.2022.9871005.

[33] C. O’Mahony, ‘Structural characterization and in-vivo reliability evaluation of silicon microneedles’, *Biomed. Microdevices*, vol. 16, no. 3, pp. 333–343, Jun. 2014, doi: 10.1007/s10544-014-9836-6.

[34] C. O’Mahony, K. Grygoryev, A. Ciarlone, G. Giannoni, A. Kenthao, and P. Galvin, ‘Design, fabrication and skin-electrode contact analysis of polymer microneedle-based ECG electrodes’, *J. Micromechanics Microengineering*, vol. 26, no. 8, p. 084005, Jul. 2016, doi: 10.1088/0960-1317/26/8/084005.

[35] S. F. Bent, ‘Chapter 5 - Semiconductor Surface Chemistry’, in *Chemical Bonding at Surfaces and Interfaces*, A. Nilsson, L. G. M. Pettersson, and J. K. Nørskov, Eds., Amsterdam: Elsevier, 2008, pp. 323–395. doi: 10.1016/B978-044452837-7.50006-X.

[36] R. Lacerda-Santos *et al.*, ‘In vivo biocompatibility of silicon dioxide nanofilm used as antimicrobial agent on acrylic surface’, *An. Acad. Bras. Ciênc.*, vol. 92, p. e20181120, Apr. 2020, doi: https://doi.org/10.1590/0001-3765202020181120.

[37] A. Fernández, A. Redondo, J. Martín-de-León, and D. Cantero, ‘PMMA stability under hydrothermal conditions’, *J. Supercrit. Fluids*, vol. 198, p. 105938, Jul. 2023, doi: 10.1016/j.supflu.2023.105938.

[38] Y. Minami, T. Tsuyuki, H. Ishikawa, Y. Shimoyama, K. Sato, and M. Yoshida, 'Degradation of stable thermosetting epoxy resins mediated by bases in amide solvents', *Polym. J.*, vol. 57, no. 2, pp. 149–162, Feb. 2025, doi: 10.1038/s41428-024-00979-6.

[39] M. A. Surmeneva *et al.*, 'Effect of parylene C coating on the antibiocorrosive and mechanical properties of different magnesium alloys', *Appl. Surf. Sci.*, vol. 427, pp. 617–627, Jan. 2018, doi: 10.1016/j.apsusc.2017.08.066.

[40] M. Cieślik, K. Engvall, J. Pan, and A. Kotarba, 'Silane–parylene coating for improving corrosion resistance of stainless steel 316L implant material', *Corros. Sci.*, vol. 53, no. 1, pp. 296–301, Jan. 2011, doi: 10.1016/j.corsci.2010.09.034.

[41] B. He, Y. Yang, M. F. Yuen, X. F. Chen, C. S. Lee, and W. J. Zhang, 'Vertical nanostructure arrays by plasma etching for applications in biology, energy, and electronics', *Nano Today*, vol. 8, no. 3, pp. 265–289, Jun. 2013, doi: 10.1016/j.nantod.2013.04.008.

[42] K.-H. Dahmen, 'Chemical Vapor Deposition', in *Encyclopedia of Physical Science and Technology (Third Edition)*, R. A. Meyers, Ed., New York: Academic Press, 2003, pp. 787–808. doi: 10.1016/B0-12-227410-5/00102-2.

[43] C. A. Schneider, W. S. Rasband, and K. W. Eliceiri, 'NIH Image to ImageJ: 25 years of image analysis', *Nat. Methods*, vol. 9, no. 7, pp. 671–675, Jul. 2012, doi: 10.1038/nmeth.2089.

[44] R. K. Kummamuru, L. Hu, L. Cook, M. Y. Efremov, E. A. Olson, and L. H. Allen, 'A close proximity self-aligned shadow mask for sputter deposition onto a membrane or cavity', *J. Micromechanics Microengineering*, vol. 18, no. 9, p. 095027, Aug. 2008, doi: 10.1088/0960-1317/18/9/095027.

[45] Y. Xie, T. Liu, Z. Chu, and W. Jin, ‘Recent advances in electrochemical enzymatic biosensors based on regular nanostructured materials’, *J. Electroanal. Chem.*, vol. 893, p. 115328, Jul. 2021, doi: 10.1016/j.jelechem.2021.115328.

[46] X. Liu, B. Yin, C. Yang, and S. Wu, ‘Passivation strategies for enhancing sensitivity and repeatability of microelectrode electrochemical sensors’, *Talanta*, vol. 273, p. 125946, Jun. 2024, doi: 10.1016/j.talanta.2024.125946.

[47] ‘Study of Electrode Reactions and Interfacial Properties’, in *Analytical Electrochemistry*, John Wiley & Sons, Ltd, 2006, pp. 29–66. doi: 10.1002/0471790303.ch2.

[48] iain656, ‘Managing blooming in an adhesives process’, What’s New in Electronics. Accessed: Jun. 21, 2024. [Online]. Available: https://www.wnie.online/managing-blooming-in-an-adhesives-process-2/

[49] X. Yan, J. Tang, D. Tanner, J. Ulstrup, and X. Xiao, ‘Direct Electrochemical Enzyme Electron Transfer on Electrodes Modified by Self-Assembled Molecular Monolayers’, *Catalysts*, vol. 10, no. 12, Art. no. 12, Dec. 2020, doi: 10.3390/catal10121458.

[50] P. M. Tsimbouri, L. E. McNamara, E. V. Alakpa, M. J. Dalby, and L.-A. Turner, ‘Chapter 7 - Cell–Material Interactions’, in *Tissue Engineering (Second Edition)*, C. A. V. Blitterswijk and J. De Boer, Eds., Oxford: Academic Press, 2014, pp. 217–251. doi: 10.1016/B978-0-12-420145-3.00007-9.

[51] E. Heydari-Bafrooei and A. A. Ensafi, ‘Nanomaterials-based biosensing strategies for biomarkers diagnosis, a review’, *Biosens. Bioelectron. X*, vol. 13, p. 100245, May 2023, doi: 10.1016/j.biosx.2022.100245.

[52] J. Y. Lichtenberg, Y. Ling, and S. Kim, ‘Non-Specific Adsorption Reduction Methods in Biosensing’, *Sensors*, vol. 19, no. 11, Art. no. 11, Jan. 2019, doi: 10.3390/s19112488.

Chapter 4

Piezoelectric inkjet coating of injection moulded, reservoir-tipped microneedle arrays for transdermal delivery

Authors: Conor O'Mahony, Andrea Bocchino, Michael J. Haslinger, Stefan Brandstätter, Helene Außerhuber, Klaudia Schossleitner, A. James P. Clover, Daniel Fechtig.

Journal: *Journal of Micromechanics and Microengineering*, volume 29, article 8.

Publication Date: 4th June 2019.

DOI: 10.1088/1361-6439/ab222b

Contribution: I was responsible for the testing of the injection moulded microneedles (produced by Austrian collaborators) on *ex vivo* skin samples (Section 4.3.4). I prepared both the skin testing setup and the samples, developing skin model and needle characterization procedures (analysis before and after application of the needles, evaluation of penetration and delivery – Section 4.3.5, Section 4.4.2 and Figure 4, Section 4.4.3 and Figure 6, and Section 4.4.4) used in the rest of the thesis. I have also analysed the skin after application. I took the images, processed them, and quantified the intensity of the fluorescence (Section 4.4.3 and Figure 5, 7, and 8). This proved skin penetration and effective delivery, observing dye diffusion within the entire cross section of the tissue samples.

I have also contributed to the writing and the reviewing of the paper.

Chapter shared from below link (author-created, un-copyedited version of an article accepted for publication in *Journal of Micromechanics and Microengineering*) under the Creative Commons license 3.0 (CC BY-NC-ND 3.0). The Section numbers, Figures/Tables/References style has been adapted to conform to the style and numbering of the thesis.

Additional changes:

- Section 4.2: “flowrates” changed to “flow rates”.
- Reference [44]: access date added.

https://cora.ucc.ie/items/a493b549-f61d-4c08-84ac-2ee241a63680

Link to license:

https://creativecommons.org/licenses/by-nc-nd/3.0/

The Version of Record is available online at https://doi.org/10.1088/1361-6439/ab222b
(© 2019 IOP Publishing Ltd).

4.1 Abstract

Coated microneedles have significant potential for use in transdermal delivery applications. In this paper, we describe the fabrication of microneedle master templates using microstereolithography techniques and subsequently use a commercial injection moulding process to replicate these microneedles in biocompatible cyclic olefin polymer (COP) materials. Notably, the 475 μm-tall needle designs feature a shallow pit or reservoir at the tip, thereby providing both a target and holder for incoming droplets that are deposited using a piezoelectric inkjet printer. Using this design, no tilting or rotation of the needle array is required during the filling process. In the preliminary tests reported here, the reservoir is filled with a FITC-labelled dye that acts as a model drug, and *ex vivo* skin tests are used to verify skin penetration, the transfer of this model drug to the skin and to measure the reliability of the needles themselves. To our knowledge, this is the first time that such an inkjet-filled, reservoir-tipped microneedle has been demonstrated.

4.2 Introduction

Patch-based transdermal drug delivery is highly attractive due to its needle-free nature and potential for self-administration, with corresponding benefits in increased patient compliance, reduced clinical time, elimination of needle-stick injuries and sharps waste. However, the outermost layer of the skin poses a formidable barrier to the transdermal delivery of drugs and vaccines. Despite being relatively thin (typically 10–20 μm thick), the *stratum corneum* prevents the passage of all but a small number of low molecular weight drugs, currently estimated at fewer than 20 products [1], [2], [3]. However, this specialized and constantly renewing layer of cornified and keratin-rich cell bodies is not the only hurdle to overcome. The skin barrier is further fortified by a high number of cell–cell junctions in the epidermal layers beneath [4]. To efficiently deliver drugs across these

multiple barriers in the epidermis of mammalian skin new transdermal drug delivery technologies are needed.

Microneedle technologies have been proposed as a potential solution to this issue. Consisting of short, sharp structures generally measuring less than 1 mm in length and provided in arrays of anything up to several thousand per square centimetre, microneedle patches can be used to penetrate the *stratum corneum* and deliver drugs or vaccines to the viable epidermis immediately below in a painless and minimally invasive manner [5], [6].

These arrays can be deployed in four primary delivery mechanisms. Firstly, simple solid microneedles can be used to painlessly perforate the skin before the subsequent application of a topical formulation or patch [7]. Secondly, drugs and vaccines can be infused in small volumes and at low flow rates through hollow microneedles in much the same manner as with conventional hypodermic needles [8]. Thirdly, a number of techniques such as brushing, dipping, inkjet printing or spraying can be used to coat microneedles with a formulation that is dried and later dissolved in the skin [9]. Lastly, dissolvable microneedles (DMNs) are moulded from a biodegradable polymer into which a drug or vaccine is mixed and which dissolves once in contact with the moist epidermal layers beneath the *stratum corneum* [10].

4.2.1 Low-cost transdermal drug delivery (TDD) device fabrication

Microneedles have traditionally been fabricated using techniques borrowed from the semiconductor industry, such as photolithography, thin-film deposition, wet and dry etching, and wafer dicing [11], [12]. Although precise and in some cases capable of producing complex and ultrasharp devices that integrate additional functionality such as

fluidics and electronics, semiconductor-based processing is expensive, often slow, and tends to use materials that may not be accepted as standard in the medical devices industry. Therefore, there is growing interest in the low-cost, rapid fabrication of transdermal drug delivery systems (TDDS), using a combination of one or more techniques for fabrication, replication and/or functionalization [13]. Micromoulding has attracted wide interest for low-cost microneedle fabrication, using both solid [14] and biodegradable [15] materials. In particular, biodegradable microneedles have the advantage that the drug or vaccine of interest may be mixed with the structural material. This provides a single-step fabrication process and a low-cost delivery route with the potential for relatively high dose loading [16], and significant progress is being made in addressing issues such as polymer processing temperatures, biomechanical strength and long-term stability during storage [17]. Alternative processes that may provide low-temperature fabrication, such as droplet air blowing [18] and drawing lithography [19], are also emerging as candidates for low-cost needle manufacture.

Among more commercially established technologies, injection moulding is commonly used for the manufacture of biomedical components [20], [21], and has been shown to be capable of replicating the small features and sharp tips usually associated with microneedles, in low cost, high-throughput facilities. 3M Corporation have demonstrated transdermal drug delivery using both solid [22], [23], [24] and hollow [25] injection moulded microneedles, fabricated from medical-grade, liquid crystalline polymer materials under their microstructured transdermal system (MTS) brand. Others have used injection moulding techniques to create microneedles in materials such as polycarbonate, polyethylene terephthalate (PET), cyclic olefin copolymer (COC), and polyoxymethylene [26], [27], [28], [29].

3D printing approaches such as two-photon polymerization (2PP), microstereolithography (μSL) or digital light processing (DLP) are also emerging as a new way of making microneedles, and can now achieve very precise geometries [30]. Ultra-sharp polymer microneedles specifically designed to perforate the round window membrane (RWM) of the inner ear with a view to precisely delivering therapeutics across that membrane were fabricated using 2PP [31], achieving a tip radius of 500 nm. 2PP was also employed to fabricate 630 nm-diameter microneedles for use in single call analysis from a drop cast resist material [32], while μSL was used to develop 700 μm tall biodegradable microneedles for chemotherapeutic drug delivery [33]. 3D printing has also been used to fabricate a curved microneedle array for treatment of trigger finger, and to subsequently deliver diclofenac gel using the 'poke and patch' approach [34].

These low-cost 3D printing approaches can be merged with non-contact coating techniques, particularly piezoelectric inkjet deposition [35], [36], to form fully functional transdermal drug delivery patches. The team at University of North Carolina and North Carolina State University, have combined μSL and elastomeric vacuum casting to create microneedles from Gantrez polymers, which were then coated with various formulations using piezoelectric printing [37], [38], [39]. Later, that group used a combination of injection moulding, drawing lithography and piezoelectric printing to demonstrate poly(glycolic) acid microneedles that were coated with itraconazole and voriconazole formulations [40], [41]. In all cases, deposition was facilitated by carefully arranging the needles so that a flat face of the needle was positioned at 90° to the incoming droplet path, and in [41], loading was maximised by rotating the needle midway through the process in order to coat both sides. In [42], μSL printing and inkjet disposition were combined for applications in insulin delivery.

Clearly, in studies performed to date, multiple coating steps or careful positioning of the microneedle array substrate is required in order to obtain sufficiently high dose loading. An alternative method of increasing dose loading, without using substrate orientation or multiple deposition passes, could be by modifying the structure of the microneedle tip itself to receive and to hold larger volumes of formulation. In this paper, we therefore describe the fabrication of microneedle master templates using μSL techniques and show that it is possible to use a commercial injection moulding process to replicate these microneedles in cyclic olefin polymers (COPs), with shape and sharpness approaching that of the original master template. Notably, the microneedles have been designed to incorporate a shallow pit or reservoir at the tip, thereby providing both a target and holder for incoming droplets that are deposited using a piezoelectric inkjet printer. This reservoir retains the formulation close to the tip, and also has the potential to increase loading capacity. In the preliminary tests reported here, the reservoir is filled with a FITC-labelled dye that acts as a model drug, and *ex vivo* skin tests are used to verify the transfer of this model drug to the skin. In addition, we measure the reliability of the needles themselves. To our knowledge, this is the first time that such a reservoir-tipped microneedle has been demonstrated.

4.3 Experimental details

4.3.1 Microneedle master – design and fabrication

Microneedle master templates were produced using microstereolithography (μSL), i.e. the spatially controlled solidification of a liquid resin by direct ultraviolet photo-polymerization in a series of layers. The microneedles were designed as 475 μm tall, cone-like structures with a sidewall angle of 73°, at a pitch of 1.4 mm, and incorporating a 180 μm deep reservoir (volume approximately 59 pL) near the tip, Figure 1. This bevel-

like, offset design positions the drug cargo close to the tip, whilst retaining the tip itself for better skin penetration and needle reliability.

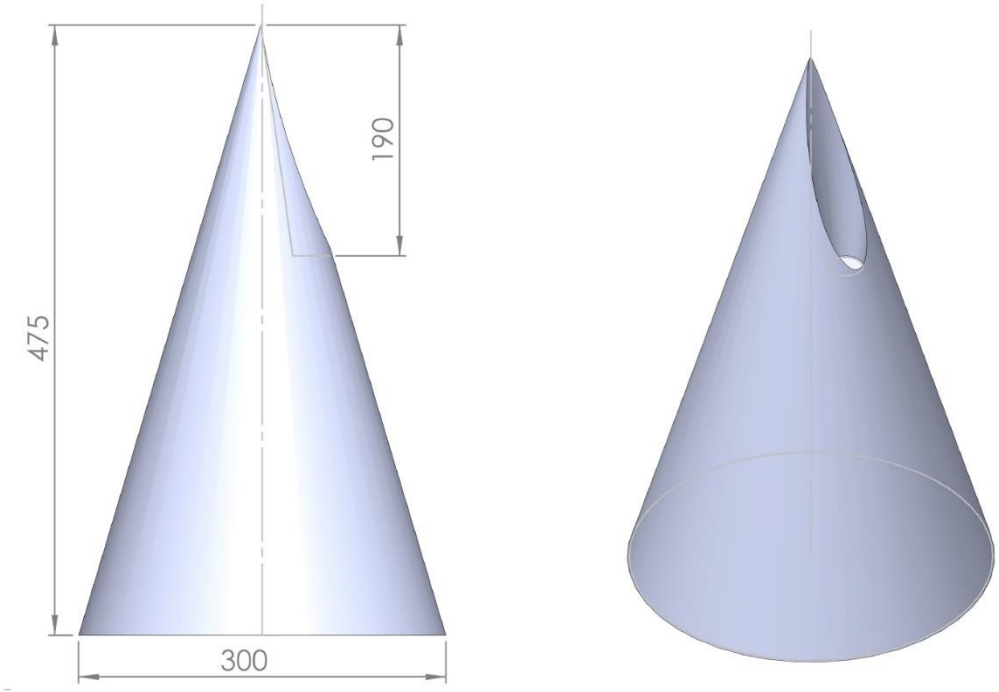


Figure 1. CAD drawing of the microneedle master design.

Needles were printed using a custom-built μSLA system using a 375 nm UV-laser diode and a scanning galvanometer mirror to solidify a UV-curing adhesive (07A22X-8, Sony CID Corp., Tokyo). First, a square base for the arrays was printed using 4 × 100 μm thick layers. Next, 5 μm thick layers were used to create the lower body of the needle, while the layer thickness was reduced to 2 μm for the last 15 layers. This smaller step height results in increased accuracy and tip sharpness. Arrays of 5 × 5 needles were produced, and the printing time for one array was roughly 5 h, depending on the final resolution and chosen layer thickness.

4.3.2 Injection moulding

Using these templates, arrays of sharp polymer microneedle structures were then manufactured at STRATEC Consumables GmbH (Anif, Austria), using a proprietary replication process based on their former CD/DVD production equipment. This involved mounting a customized insert on an existing CD mould, and using an isothermal injection moulding process without compression. A Sumitomo Disc 40E Disc Molding Subsystem (Sumitomo SHI Demag Plastics Machinery North America, Inc., OH, USA) was used for moulding; the mould temperature was 80 °C and the clamping pressure set at 25 tons, Figure 2. The material was Zeonor 1020R cyclic olefin polymer (Zeon Europe GmbH, Dusseldorf, Germany), which we have already shown to be biocompatible according to ISO 10993-5 and USP 87 standards [43], and the process resulted in easy de-moulding as well as sharp needle tips. A milling procedure was then used to partially isolate each electrode from the frame, leaving the array lightly tethered on two thin supports for subsequent easy removal.



Figure 2. Sumitomo Disc 40E disc moulding subsystem. Reproduced with permission from [44].

4.3.3 Piezoelectric dispensing

The injection moulded needles were then filled using a Dimatix DMP 2800 drop-on-demand inkjet printer (FujiFilm Dimatix, Santa Clara, CA). An actuation pulse of amplitude 15 V and duration of 11.5 µs, and a maximum jetting frequency of 5000 Hz was used. Nominal drop volume was 10 pl and the escape velocity of the droplets was between 2–8 m s^{-1}.

The ink was a mixture of 5 wt% fluorescein isothiocyanate (FITC) dye for imaging purposes, 22 wt% water and a 73 wt% mixture of volatile solvents. The dry mass of one drop (FTIC) was 0.536 ng per drop. The ink temperature was set to 50 °C, and the print bed was heated to 30 °C. Ambient laboratory conditions (20 °C and relative humidity of 50%) prevailed. Loaded needles were then dried at 100 °C for 30 min.

For these initial tests and to aid with subsequent visualisation of the dye transfer to skin, just one column of each array (i.e. 5 × 1 needles) was loaded. Initially the array was aligned with one axis of the printer, and the coordinates of the first needle in the target row were selected using the printhead camera and Dimatix internal software. Subsequent needles were coated by moving the nozzle along the row, in steps equal to the microneedle pitch, starting from the location of this first needle. A variety of deposition settings and skin insertion times were used as specified in Table 1 below.

Table 1. Needle loading parameters and skin insertion times for each sample type.

Array number	# drops	Nominal volume (pl)	Total dry mass (ng)	Insertion time (min)
1	2	20	1072	10
2	4	40	2144	10
3	4	40	2144	5
4	6	60	3216	5
5	6	60	3216	1

4.3.4 Skin preparation and array applications

Following protocols approved by the Clinical Research Ethics Committee of the Cork Teaching Hospitals (CREC), human skin was excised following plastic surgical operations and stored at −80 °C until needed. It was then defrosted, trimmed of excess fat, cut into squares of approximately 3 cm × 3 cm, and mounted on an artificial tissue substrate (Wound Closure Pad, Limbs & Things, Bristol, UK) to mimic the mechanical properties of underlying tissue.

Spring-loaded applicators are often used to apply microneedle devices to the skin in a consistent manner [45]. In this case, a custom-built applicator was used to ensure repeatable and reliable skin penetration. This applicator uses a spring constant of 274 N m^{-1}, and generated impact energy of (0.4 ± 0.01) J cm^{-2}.

Methylene blue staining is a technique routinely used to assess microneedle penetration [46], and was also used here to confirm skin breach. During this procedure, uncoated arrays (i.e. with empty tip reservoirs) were applied to the skin with the applicator and left in place for 20 min. After removal, the impact area was stained with a 1% solution (w/vol) of methylene blue (Sigma-Aldrich, Dublin, Ireland) for 90 min. Excess dye was removed with tissue, the skin was cleaned with water and 70% ethanol, before being tape stripped ten times (9040 Paper Tape, 3M Corp., St Paul, MN) in order to ensure than any remaining dye was present under the *stratum corneum* and not on its surface.

To test the fluorescent dye-loaded microneedle arrays, the applicator maintained a force of (5.90 ± 0.54) N on the needle array for a specific time after impact. Six arrays were tested at varying insertion times, see Table 1.

4.3.5 Inspection and classification

Optical microscope images of the methylene blue-stained impact area after insertion and skin washing/stripping were recorded using a digital camera. A thorough inspection of the fluorescent dye-loaded needles was also performed. Each of the 6 injection moulded arrays featured 21 needles—a total of 126 needles. Of these, one column (five needles) on each array was filled. Each needle, whether filled or not, was individually inspected both before and after skin insertion, from a variety of angles and orientations, using microscopes including stereozoom (SZX12, Olympus Corp., Tokyo, Japan), digital (VHX-200, Keyence Ltd, Milton Keynes, UK) and fluorescent (Olympus BX51). The purpose of this exercise was to visually confirm delivery of the dye and to assess any damage that occurred during the insertion process.

Following application to *ex vivo* tissue as outlined above, fluorescent microscopy was used to examine the transfer of material from filled needles to skin. Pictures of the surface

of the skin were taken with the fluorescent microscope at exposure times (ETs) of 50 ms, 100 ms and 200 ms.

Finally, the skin samples were cut using a scalpel along the line of the holes left by the loaded needles. Images of the cross section of the skin were taken with the fluorescent microscope to assess the diffusion of the dye underneath the *stratum corneum*.

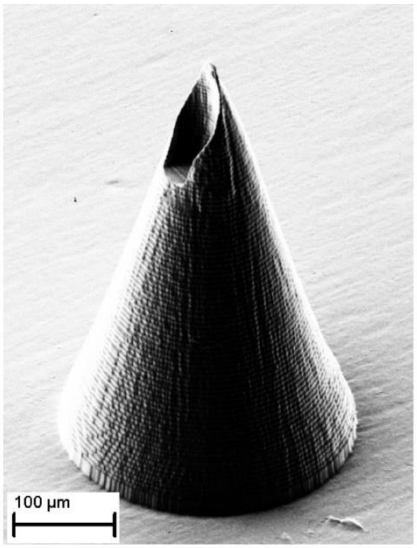
In order to quantify the intensity of the fluorescence as a function of array insertion time, an image analysis was performed using the software ImageJ [47]. A region of interest (ROI) was defined by firstly selecting an initial pixel at the boundary of the fluorescent area, and then using the software's 'Wand' tool to identify a contiguous area based on the condition that all the boundary pixel values must be in the range initial pixel value ± tolerance, where the tolerance value was set to 22 and kept constant for each image analysis.

To remove the influence of the background signal, the mean intensity per pixel of the region outside of the ROI was calculated for each image, and subtracted from each pixel within the ROI. The total intensity was calculated by summing this net fluorescence per pixel over all pixels within the ROI.

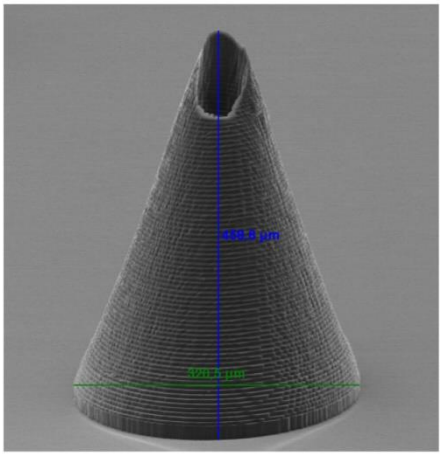
4.4 Results and discussion

4.4.1 Microneedle fabrication using µSL and injection moulding

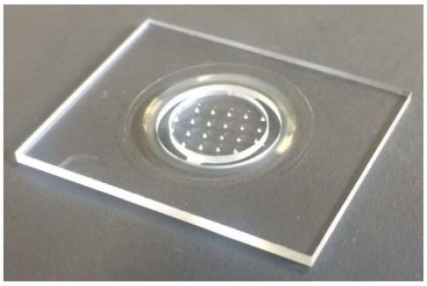
Images of the µSL master structure and injection-moulded needle array are illustrated in Figure 3. Note the milled slot and tethers linking the array to the support frame.



(a)



(b)



(c)

Figure 3. (a) SEM image of µSL master structure, (b) SEM of injection moulded microneedle, and (c) injection moulded array prior to removal from support frame.

4.4.2 Filling of needle reservoir

Background fluorescence from the epoxy material itself prevented a thorough analysis of the polymer microneedle coating using fluorescence microscopy, and so droplet location and consistency was assessed using optical microscopy, Figure 4. In general all of the incoming material was positioned in the reservoir and little or no splashing was observed on or around the needle.



Figure 4. (Left) Example of reservoir-tipped microneedles after the filling procedure. (Right) Top-down perspective of filled microneedles.

4.4.3 Skin penetration and delivery

Penetration markings remaining after the staining procedure described in Section 4.3.4 are shown in Figure 5.

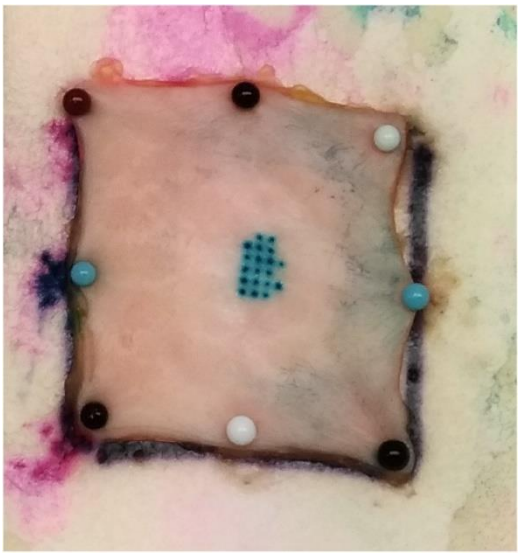


Figure 5. *Ex vivo* skin sample stained with methylene blue dye following microneedle array insertion. The needle pitch is 1.4 mm.

Methylene blue is hydrophilic with a low molecular weight, and the intact, hydrophobic *stratum corneum* cannot take up the stain. Once the *stratum corneum* barrier is disrupted, the dye diffuses through the newly created pores to the underlying epidermis, where it binds to the tissue due to its high affinity for proteins. Therefore, the presence of blue markings after microneedle application is generally regarded as definitive proof of successful insertion. Note that 19 marks are present, while there are 21 needles on the array, and a closer inspection revealed that two needles on the right-hand side of the array were damaged during handling, resulting in no penetration at these locations.

To establish if the fluorescent dye was delivered inside the skin, analysis of both the microneedle arrays and skin samples was performed as outlined in Section 4.3.5. Figure 6 illustrates the needle already shown in Figure 4 after skin insertion for 10 min.

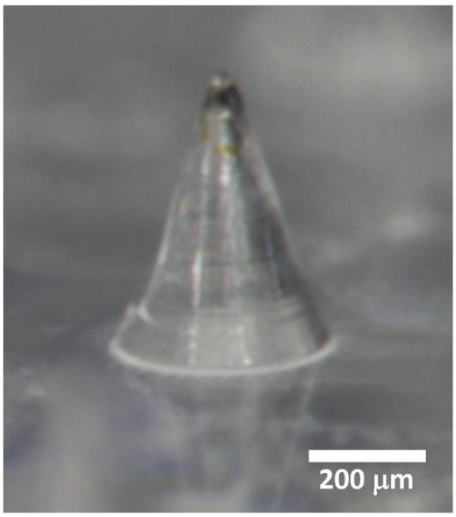


Figure 6. Microneedle of Figure 3 (left) shown after skin insertion.

The dye almost completely disappeared from the tip of the microneedle, indicating that it was transferred to the skin. Further evidence of transdermal delivery is evident from the fluorescent photos of the skin samples. As shown in Figures 7 and 8, the points where the skin was pierced by the needles are clearly visible and the fluorescent dye has diffused beneath the *stratum corneum*.

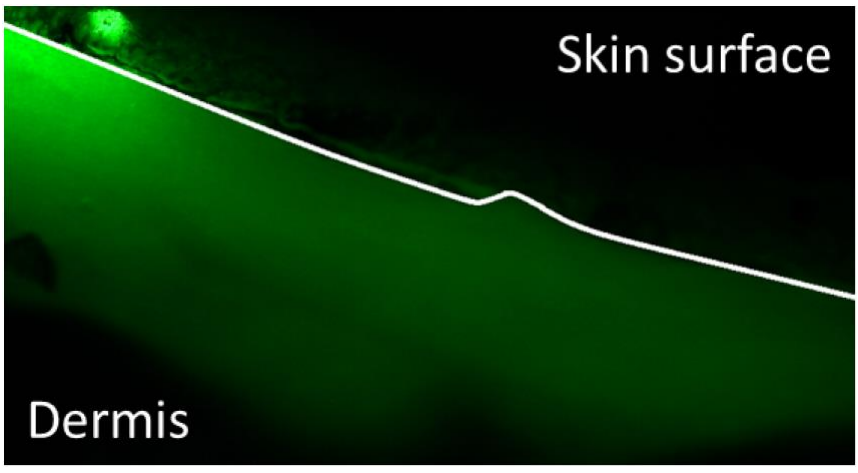


Figure 7. Cross-section of skin sample. The point of needle insertion and diffusion of dye beneath the surface is clearly visible.

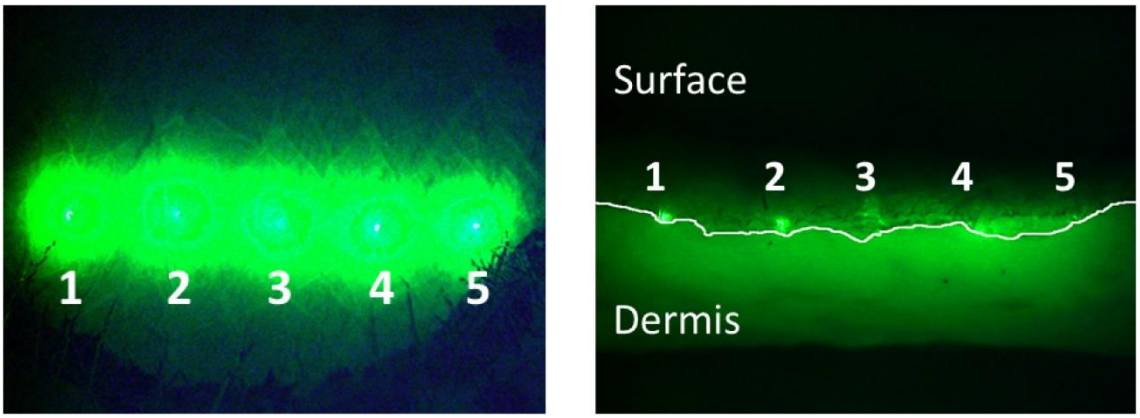


Figure 8. Delivery to skin. (Left) En-face image. (Right) Cross-section of the same skin sample; the boundary between skin surface and underlying tissue is marked. Images taken after 10 min insertion at 50 ms exposure time. The needle pitch is 1.4 mm.

To quantify the dye delivery process as outlined in Section 4.3.5, the background contribution was removed and the value of the fluorescence recalculated for the entire row of dye-loaded needles, Figure 8. Exposure time for all of this analysis was 50 ms (as longer exposures tended to exhibit saturation) and the resultant intensity data is shown in Figure 9. Two independent variables are present, i.e. droplet quantity and skin insertion time. In general, the results are as expected, i.e. increasing either the number of droplets or the skin insertion time results in an increase in fluorescent intensity.

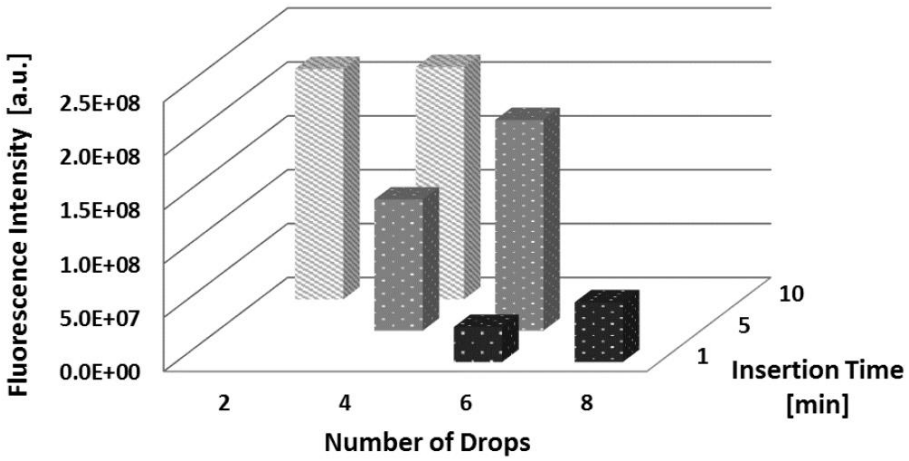


Figure 9. Fluorescence intensity as a function of skin insertion time and needle loading.

The only exception to this trend is for 10 min insertion times, where the fluorescence intensities are much higher than for 1 or 5 min insertion times, but do not vary significantly as a function of loading volume. This may be caused by the skin becoming saturated after that period, meaning that additional dye delivery does not alter the fluorescence readings.

This is the first demonstration of an injection-moulded, reservoir-tipped microneedle. However, this preliminary proof-of-concept work is limited in scope and additional tests of larger sample sets are required in order to draw definitive statistical conclusions. Secondly, while useful for initial device validation during process development, this fluorescence method is somewhat limited due to its projection of a 3D diffusion pattern onto a 2D image. Future development will require more accurate quantification of drug loading and release profiles through the use of assays such as HPLC analysis and *in vitro/in vivo* models. However, these results verify transdermal delivery of the model drug from reservoir-tipped needles. Delivery trends are as expected, and show that this novel needle design offers a promising method of transdermal delivery.

4.4.4 Reliability

During post-insertion inspection, it was noted that a significant number of needles suffered minor tip damage during the skin delivery tests. One array was damaged after removal due to manual handling, and, of the other five arrays that competed a full inspection, 33% of all needles indicated some degree of tip damage. This was always confined to the tip region and no major structural failures of the body of the microneedles were observed. Needle tips seemed to be flattened or crushed, i.e. no breakage or brittle fracture was seen. It is therefore unlikely that any material remained in the skin after use, and, as these are single-use devices, this tip blunting should not pose a major issue. It is nevertheless undesirable and other polymers and/or tip designs should be investigated.

4.5 Conclusion

This paper has shown that two low-cost techniques—injection moulding and inkjet printing—may be combined to produce coated microneedles for transdermal drug and vaccine delivery. Initially, μSL was used to produce 475 μm tall microneedles, which featured a flat-bottomed pit or reservoir located close to the needle tip. This reservoir increases loading capacity and removes the need to tilt samples in order to present a flat surface to the incoming droplet.

These designs were then replicated at a commercial injection-moulding facility, using a modified process based on former CD/DVD production equipment. An inkjet printer was used to deposit a model drug (FITC) into the reservoir, and needle arrays were inserted into *ex vivo* human skin using an applicator. Subsequent fluorescence analysis showed the results were largely in line with expectations, i.e. intensity increased with needle loading and skin insertion time. This work shows that it is feasible to rapidly produce

large quantities of coated microneedle arrays, using automated processes, in medical-grade material and at low cost.

4.6 References

[1] A. C. Watkinson, 'A commentary on transdermal drug delivery systems in clinical trials', *J. Pharm. Sci.*, vol. 102, no. 9, pp. 3082–3088, Sep. 2013, doi: 10.1002/jps.23490.

[2] M. R. Prausnitz and R. Langer, 'Transdermal drug delivery', *Nat. Biotechnol.*, vol. 26, no. 11, pp. 1261–1268, Nov. 2008, doi: 10.1038/nbt.1504.

[3] M. Amjadi, S. Sheykhansari, B. J. Nelson, and M. Sitti, 'Recent Advances in Wearable Transdermal Delivery Systems', *Adv. Mater. Deerfield Beach Fla*, vol. 30, no. 7, Feb. 2018, doi: 10.1002/adma.201704530.

[4] C. M. Niessen, 'Tight Junctions/Adherens Junctions: Basic Structure and Function', *J. Invest. Dermatol.*, vol. 127, no. 11, pp. 2525–2532, Nov. 2007, doi: 10.1038/sj.jid.5700865.

[5] M. R. Prausnitz, 'Engineering Microneedle Patches for Vaccination and Drug Delivery to Skin', *Annu. Rev. Chem. Biomol. Eng.*, vol. 8, no. 1, pp. 177–200, Jun. 2017, doi: 10.1146/annurev-chembioeng-060816-101514.

[6] K. Ita, 'Transdermal Delivery of Drugs with Microneedles—Potential and Challenges', *Pharmaceutics*, vol. 7, no. 3, pp. 90–105, Jun. 2015, doi: 10.3390/pharmaceutics7030090.

[7] J. B. Carey *et al.*, 'Microneedle Array Design Determines the Induction of Protective Memory CD8+ T Cell Responses Induced by a Recombinant Live Malaria Vaccine

in Mice', *PLOS ONE*, vol. 6, no. 7, p. e22442, Jul. 2011, doi: 10.1371/journal.pone.0022442.

[8] M. Dul *et al.*, 'Hydrodynamic gene delivery in human skin using a hollow microneedle device', *J. Control. Release Off. J. Control. Release Soc.*, vol. 265, pp. 120–131, Nov. 2017, doi: 10.1016/j.jconrel.2017.02.028.

[9] R. Haj-Ahmad *et al.*, 'Microneedle Coating Techniques for Transdermal Drug Delivery', *Pharmaceutics*, vol. 7, no. 4, pp. 486–502, Nov. 2015, doi: 10.3390/pharmaceutics7040486.

[10] M. Leone, J. Mönkäre, J. A. Bouwstra, and G. Kersten, 'Dissolving Microneedle Patches for Dermal Vaccination', *Pharm. Res.*, vol. 34, no. 11, pp. 2223–2240, Nov. 2017, doi: 10.1007/s11095-017-2223-2.

[11] S. Henry, D. V. McAllister, M. G. Allen, and M. R. Prausnitz, 'Microfabricated Microneedles: A Novel Approach to Transdermal Drug Delivery', *J. Pharm. Sci.*, vol. 87, no. 8, pp. 922–925, Aug. 1998, doi: 10.1021/js980042+.

[12] C. O'Mahony, 'Structural characterization and in-vivo reliability evaluation of silicon microneedles', *Biomed. Microdevices*, vol. 16, no. 3, pp. 333–343, Jun. 2014, doi: 10.1007/s10544-014-9836-6.

[13] S. Indermun *et al.*, 'Current advances in the fabrication of microneedles for transdermal delivery', *J. Control. Release Off. J. Control. Release Soc.*, vol. 185, pp. 130–138, Jul. 2014, doi: 10.1016/j.jconrel.2014.04.052.

[14] C. O'Mahony, K. Grygoryev, A. Ciarlone, G. Giannoni, A. Kenthao, and P. Galvin, 'Design, fabrication and skin-electrode contact analysis of polymer microneedle-based ECG electrodes', *J. Micromechanics Microengineering*, vol. 26, no. 8, p. 084005, Jul. 2016, doi: 10.1088/0960-1317/26/8/084005.

[15] E. A. Allen, C. O'Mahony, M. Cronin, T. O'Mahony, A. C. Moore, and A. M. Crean, 'Dissolvable microneedle fabrication using piezoelectric dispensing technology', *Int. J. Pharm.*, vol. 500, no. 1–2, pp. 1–10, Mar. 2016, doi: 10.1016/j.ijpharm.2015.12.052.

[16] X. Hong *et al.*, 'Dissolving and biodegradable microneedle technologies for transdermal sustained delivery of drug and vaccine', *Drug Des. Devel. Ther.*, vol. 7, pp. 945–952, 2013, doi: 10.2147/DDDT.S44401.

[17] K. Ita, 'Dissolving microneedles for transdermal drug delivery: Advances and challenges', *Biomed. Pharmacother.*, vol. 93, pp. 1116–1127, Sep. 2017, doi: 10.1016/j.biopha.2017.07.019.

[18] J. D. Kim, M. Kim, H. Yang, K. Lee, and H. Jung, 'Droplet-born air blowing: Novel dissolving microneedle fabrication', *J. Controlled Release*, vol. 170, no. 3, pp. 430–436, 2013, doi: 10.1016/j.jconrel.2013.05.026.

[19] K. Lee and H. Jung, 'Drawing lithography for microneedles: A review of fundamentals and biomedical applications', *Biomaterials*, vol. 33, no. 30, pp. 7309–7326, Oct. 2012, doi: 10.1016/j.biomaterials.2012.06.065.

[20] L. Zema, G. Loreti, A. Melocchi, A. Maroni, and A. Gazzaniga, 'Injection Molding and its application to drug delivery', *J. Control. Release Off. J. Control. Release Soc.*, vol. 159, no. 3, pp. 324–331, May 2012, doi: 10.1016/j.jconrel.2012.01.001.

[21] U. M. Attia, S. Marson, and J. R. Alcock, 'Micro-injection moulding of polymer microfluidic devices', *Microfluid. Nanofluidics*, vol. 7, no. 1, pp. 1–28, Jul. 2009, doi: 10.1007/s10404-009-0421-x.

[22] D. Duan *et al.*, ‘Enhanced delivery of topically-applied formulations following skin pre-treatment with a hand-applied, plastic microneedle array’, *Curr. Drug Deliv.*, vol. 8, no. 5, pp. 557–565, Sep. 2011, doi: 10.2174/156720111796642318.

[23] S. Kommareddy *et al.*, ‘Influenza subunit vaccine coated microneedle patches elicit comparable immune responses to intramuscular injection in guinea pigs’, *Vaccine*, vol. 31, no. 34, pp. 3435–3441, Jul. 2013, doi: 10.1016/j.vaccine.2013.01.050.

[24] Y. Zhang, K. Brown, K. Siebenaler, A. Determan, D. Dohmeier, and K. Hansen, ‘Development of lidocaine-coated microneedle product for rapid, safe, and prolonged local analgesic action’, *Pharm. Res.*, vol. 29, no. 1, pp. 170–177, Jan. 2012, doi: 10.1007/s11095-011-0524-4.

[25] S. A. Burton *et al.*, ‘Rapid intradermal delivery of liquid formulations using a hollow microstructured array’, *Pharm. Res.*, vol. 28, no. 1, pp. 31–40, Jan. 2011, doi: 10.1007/s11095-010-0177-8.

[26] K. B. Mirza, C. Zuliani, B. Hou, F. S. Ng, N. S. Peters, and C. Toumazou, ‘Injection moulded microneedle sensor for real-time wireless pH monitoring’, *Annu. Int. Conf. IEEE Eng. Med. Biol. Soc. IEEE Eng. Med. Biol. Soc. Annu. Int. Conf.*, vol. 2017, pp. 189–192, Jul. 2017, doi: 10.1109/EMBC.2017.8036794.

[27] K. Nair *et al.*, ‘Investigation of Plasma Treatment on Micro-Injection Moulded Microneedle for Drug Delivery’, *Pharmaceutics*, vol. 7, no. 4, pp. 471–485, Oct. 2015, doi: 10.3390/pharmaceutics7040471.

[28] F. Sammoura, J. Kang, Y.-M. Heo, T. Jung, and L. Lin, ‘Polymeric microneedle fabrication using a microinjection molding technique’, *Microsyst. Technol.*, vol. 13, no. 5–6, pp. 517–522, Jan. 2007, doi: 10.1007/s00542-006-0204-1.

[29] K. L. Yung *et al.*, ‘Sharp tipped plastic hollow microneedle array by microinjection moulding’, *J. Micromechanics Microengineering*, vol. 22, no. 1, p. 015016, Dec. 2011, doi: 10.1088/0960-1317/22/1/015016.

[30] S. H. Lim, H. Kathuria, J. J. Y. Tan, and L. Kang, ‘3D printed drug delivery and testing systems - a passing fad or the future?’, *Adv. Drug Deliv. Rev.*, vol. 132, pp. 139–168, Jul. 2018, doi: 10.1016/j.addr.2018.05.006.

[31] A. Aksit *et al.*, ‘In-vitro perforation of the round window membrane via direct 3-D printed microneedles’, *Biomed. Microdevices*, vol. 20, no. 2, p. 47, Jun. 2018, doi: 10.1007/s10544-018-0287-3.

[32] M. Kavaldzhiev, J. E. Perez, Y. Ivanov, A. Bertoncini, C. Liberale, and J. Kosel, ‘Biocompatible 3D printed magnetic micro needles’, *Biomed. Phys. Eng. Express*, vol. 3, no. 2, p. 025005, Feb. 2017, doi: 10.1088/2057-1976/aa5ccb.

[33] Y. Lu *et al.*, ‘Microstereolithography and characterization of poly(propylene fumarate)-based drug-loaded microneedle arrays’, *Biofabrication*, vol. 7, no. 4, p. 045001, Sep. 2015, doi: 10.1088/1758-5090/7/4/045001.

[34] S. H. Lim, J. Y. Ng, and L. Kang, ‘Three-dimensional printing of a microneedle array on personalized curved surfaces for dual-pronged treatment of trigger finger’, *Biofabrication*, vol. 9, no. 1, p. 015010, Jan. 2017, doi: 10.1088/1758-5090/9/1/015010.

[35] C. O’Mahony *et al.*, ‘Accuracy and feasibility of piezoelectric inkjet coating technology for applications in microneedle-based transdermal delivery’, *Microelectron. Eng.*, vol. 172, pp. 19–25, Mar. 2017, doi: 10.1016/j.mee.2017.02.018.

[36] M. J. Uddin, N. Scoutaris, P. Klepetsanis, B. Chowdhry, M. R. Prausnitz, and D. Douroumis, ‘Inkjet printing of transdermal microneedles for the delivery of anticancer agents’, *Int. J. Pharm.*, vol. 494, no. 2, pp. 593–602, Oct. 2015, doi: 10.1016/j.ijpharm.2015.01.038.

[37] R. D. Boehm, P. R. Miller, S. L. Hayes, N. A. Monteiro-Riviere, and R. J. Narayan, ‘Modification of microneedles using inkjet printing’, *AIP Adv.*, vol. 1, no. 2, p. 22139, Jun. 2011, doi: 10.1063/1.3602461.

[38] R. D. Boehm, P. R. Miller, W. A. Schell, J. R. Perfect, and R. J. Narayan, ‘Inkjet Printing of Amphotericin B onto Biodegradable Microneedles Using Piezoelectric Inkjet Printing’, *JOM*, vol. 65, no. 4, pp. 525–533, Apr. 2013, doi: 10.1007/s11837-013-0574-7.

[39] R. D. Boehm, P. R. Miller, J. Daniels, S. Stafslien, and R. J. Narayan, ‘Inkjet printing for pharmaceutical applications’, *Mater. Today*, vol. 17, no. 5, pp. 247–252, Jun. 2014, doi: 10.1016/j.mattod.2014.04.027.

[40] R. D. Boehm, J. Daniels, S. Stafslien, A. Nasir, J. Lefebvre, and R. J. Narayan, ‘Polyglycolic acid microneedles modified with inkjet-deposited antifungal coatings’, *Biointerphases*, vol. 10, no. 1, p. 011004, Mar. 2015, doi: 10.1116/1.4913378.

[41] R. D. Boehm, P. Jaipan, S. A. Skoog, S. Stafslien, L. VanderWal, and R. J. Narayan, ‘Inkjet deposition of itraconazole onto poly(glycolic acid) microneedle arrays’, *Biointerphases*, vol. 11, no. 1, p. 011008, Mar. 2016, doi: 10.1116/1.4941448.

[42] C. P. P. Pere *et al.*, ‘3D printed microneedles for insulin skin delivery’, *Int. J. Pharm.*, vol. 544, no. 2, pp. 425–432, Jun. 2018, doi: 10.1016/j.ijpharm.2018.03.031.

[43] K. Schossleitner *et al.*, 'Differences in biocompatibility of microneedles from cyclic olefin polymers with human endothelial and epithelial skin cells', *J. Biomed. Mater. Res. A*, vol. 107, no. 3, pp. 505–512, Mar. 2019, doi: 10.1002/jbm.a.36565.

[44] SD40E Disc Molding Subsystem 2019. Accessed: 15 April 2019. Available: www.sumitomo-shi-demag.us/sd40emain.html.

[45] T. R. R. Singh, N. J. Dunne, E. Cunningham, and R. F. Donnelly, 'Review of patents on microneedle applicators', *Recent Pat. Drug Deliv. Formul.*, vol. 5, no. 1, pp. 11–23, Jan. 2011, doi: 10.2174/187221111794109484.

[46] G. Li, A. Badkar, S. Nema, C. S. Kolli, and A. K. Banga, 'In vitro transdermal delivery of therapeutic antibodies using maltose microneedles', *Int. J. Pharm.*, vol. 368, no. 1–2, pp. 109–115, Feb. 2009, doi: 10.1016/j.ijpharm.2008.10.008.

[47] C. T. Rueden *et al.*, 'ImageJ2: ImageJ for the next generation of scientific image data', *BMC Bioinformatics*, vol. 18, no. 1, p. 529, Nov. 2017, doi: 10.1186/s12859-017-1934-z.

Chapter 5

Bio-inspired microneedle design for efficient drug/vaccine coating

Authors: Cristina Plamadeala, Saransh R. Gosain, Florian Hischen, Boris Buchroithner, Sujitha Puthukodan, Jaroslaw Jacak, Andrea Bocchino, Derek Whelan, Conor O'Mahony, Werner Baumgartner, Johannes Heitz.

Journal: *Biomedical Microdevices*, volume 22, article 8.

Publication Date: 16th December 2019.

DOI: 10.1007/s10544-019-0456-z

Contribution: I was responsible for the replication with medical grade polymers of the micro-patterned microneedles used in this study (Section 5.3.5 and Figure 5). This was an important step to both understand if the moulding process was able to precisely replicate highly complex structures, validating the core fabrication method, together with seeing if it was compatible with the replication of 3D printed microneedles. Both qualities were necessary features for the development of a successful platform. Moreover, this initial work was used to test if the moulded needles were able to successfully pierce the skin without sustaining any damages. I have also collaborated with the testing of the MNs on *ex vivo* skin samples, proving successful skin penetration (Section 5.3.6 and Figure 6a).

I have also contributed to the writing and the reviewing of the paper.

Chapter adapted from below link under the Creative Commons license 4.0 (CC BY 4.0). The Section numbers, Figures/Tables/References style has been adapted to conform to the style and numbering of the thesis.

https://link.springer.com/article/10.1007/s10544-019-0456-z

Link to license:

https://creativecommons.org/licenses/by/4.0/

5.1 Abstract

Biomimetics is the interdisciplinary scientific field focused on the study and imitation of biological systems, with the aim of solving complex technological problems. In this paper, we present a new bio-inspired design for microneedles (MNs) and MN arrays, intended for rapidly coating the MNs with drug/vaccine. The biomimetic approach consists in ornamenting the lateral sides of pyramidal MNs with structures inspired by the external scent efferent systems of some European true bugs, which facilitate a directional liquid transport. To realize these MNs, two-photon polymerization (TPP) technique was used. Liquid coating capabilities of structured and non-structured MNs were compared. Moreover, both *in vivo* and *ex vivo* skin tests were performed to prove that MNs pierce the skin. We show that the arrays of MNs can be accurately replicated using a micro-moulding technique. We believe this design will be beneficial for the process of drug/vaccine loading onto the needles' surfaces, by making it more efficient and by reducing the drug/vaccine wastage during MN coating process.

5.2 Introduction

Microneedles (MNs) are sharp, needle-like projections, generally less than 1 mm tall and arranged in arrays covering surfaces ranging from a few square millimetres up to several square centimetres [1]. Due to their short dimensions and correspondingly shallow penetration depths (10–80 % of their length [2]), MNs are able to penetrate into the outermost epidermal layers, without irritating the nerve endings or reaching the blood vessels that lie deeper in the skin. Consequently, MNs are minimally invasive, and do not trigger pain sensations nor induce bleeding [3]. Therefore, it is expected that MNs will find wide-ranging applications in transdermal drug and vaccine delivery [1].

Generally, based on their overall geometry and mechanism of drug delivery, microneedles can be divided into four different types, i.e. solid, coated, dissolving, and hollow MNs [4]. Solid MNs are used for skin pre-treatment, i.e. for creating micro-pores in the skin. Subsequently, a topical formulation is placed onto the pre-treated area and it diffuses through the micro-pores into the skin [5]. Coated MNs are covered with a thin layer of formulation before applying them onto the skin. Upon penetrating the skin, the formulation dissolves and releases the active ingredients [6]. Dissolving MNs are made up of polymeric materials mixed with an active agent. When inserted into the skin, they rapidly degrade, releasing the drug or vaccine cargo [7]. Hollow MNs, similar to hypodermic injections, have an opening through which the liquid formulation is injected into the skin [8].

One of the most common methods used for coating microneedles with a drug formulation is the dip coating technique: the MN patch is immersed in a solution, then withdrawn, and dried. Even though the procedure is simple, it has several disadvantages: the immersion may last a long time; the thickness of the coating layer is not uniform (making it complicated to accurately dose the drug); and finally - due to gravitational force - the liquid drug formulation tends to accumulate at the base of the MNs, resulting in drug loss [9]. These disadvantages determined the development of new coating techniques, such as gas-jet drying [10], spray drying [11], electrohydrodynamic atomisation [12], and ink-jet printing [13]. While these techniques allow a more precise and uniform drug deposition, with reduced drug wastage, they require rather sophisticated equipment and trained personnel.

Biomimetic thinking has brought considerable improvement to the field of microneedle design. Substantial work is being carried out towards understanding the mechanism of female mosquitos' proboscis (mouthparts) insertion into skin. This knowledge was

implemented in MN design and production [14]. It has been shown by different research groups that mosquito bio-inspired MNs need considerably lower insertion forces to penetrate the skin [15]. Similar results were obtained with MNs mimicking the North American porcupine quills [16]. Apart from that, MNs with swellable tips inspired by the proboscis of an endoparasite (Pomphorhynchus laevis) were proven to be efficient in the adhesion to, and interlocking with the soft tissues. These MN patches are much more flexible than conventional polymer-based MNs, therefore they are easily removed from the tissues, without damaging the tissue or the MNs [17].

Biomimetic approaches could also be of significant use in MN drug/vaccine coating. Nature inspired surfaces with special wetting properties range from ultra-hydrophobic self-cleaning applications of the lotus-effect [18] up to hydrophilic polymer anti-fouling coating applications inspired by marine mussels [19]. In the context of MN coating, bio-inspired microfluidic devices and structured surfaces which, coming in contact with different liquids, promote a directional movement of the liquids [20], [21], [22], [23], [24], [25], [26], [27], are of great interest.

In our previous work, we have developed artificial surface structures inspired by the external scent efferent system of some European true bugs [27]. These bugs use oriented microstructures for unidirectional transport of defensive liquids on their body surfaces (from the places where the liquids are secreted to the places where they are evaporated). We have previously shown that technical surfaces (such as polymers or steels) with open capillary channels containing scaled up bug-inspired oriented structures are able to transport liquids (such as soapy solutions or oils) in the direction the tips of the structures point to, while halting the transport in any other direction. We also reported that similar self-organised conical structures inspired by the external scent efferent system of European true bugs obtained on polyimide foil (with dimensions in the range of tens of

micrometres) were able to sustain the directional liquid movement of soap-water solution even when tilted [27]. Similar microstructures, when placed in a closed capillary channel configuration, guide the movement of oily liquids in the direction against the tips of the structures [25].

In this paper, we have combined rapid prototyping techniques and microneedle fabrication technologies towards the specific goal of a MN design capable of being quickly and easily coated with a uniform layer of drugs or vaccines. We accomplished this by ornamenting the lateral faces of pyramidal MNs with bio-inspired microstructures, which facilitate the directional transport of the liquids from the bottom of the MNs towards their tips.

To create the microneedles, two-photon polymerization (TPP) lithography was used – an intrinsically three-dimensional (3D) micro-fabrication technique, which enables production of micro-scale devices with feature sizes below the resolution limit [28]. This method is largely implemented to create MNs and MN arrays, as it offers the advantage of generating structures of user-defined designs, sizes, and distributions [29]. Wetting tests have shown that the bio-inspired structures transport fluid towards the tip of the needle, as intended. A micro-replication technique [30] was used to quickly produce copies that are geometrically indistinguishable from the master templates. The replicas were also used to demonstrate skin penetration through *ex vivo* skin studies. To our knowledge, this work represents the first MN design which makes use of bio-inspired surface structures for passive liquid transportation on its lateral surfaces. This paper is a preliminary engineering study that focusses on the manufacturing challenge of writing microstructures on very steep sidewalls, which lead to a fluid transport to the needle tip, and then carries out preliminary work to assess feasibility.

5.3 Materials and methods

5.3.1 Computer aided design

A complete test sample consists of three parts – a guiding channel, and two different MNs. All the computer-aided designs (CADs) were realized using SketchUp Make 2017 – a freeware for three-dimensional (3D) modelling.

The channel, consisting of periodic bug-inspired microstructures (Figure 1a, b), is intended to guide the fluid to the base of the MNs in a controlled manner (Figure 1c). Each bug-inspired microstructure had a length of 23 μm, a base width of 10 μm and a height of 1 μm (Figure 1a). Length to base width ratio was kept 2.3 to 1, as described in [27]. Distance between the tips of the two consecutive microstructures within one row was set to 25 μm, and the distance between the tips of two microstructures from two consecutive rows was set to 24 μm (Figure 1b). The whole design of the channel resembles the letter T. Each of the two 'arms' had a square gap with an area of about 170×170 μm^2, into which the MNs were fabricated. The microstructures building up the 'arms' of the vertical channel are oriented towards the MNs. The vertical channel measures 900 μm in length, the horizontal channel measures 1500 μm in length, and both channels have a width of 300 μm.

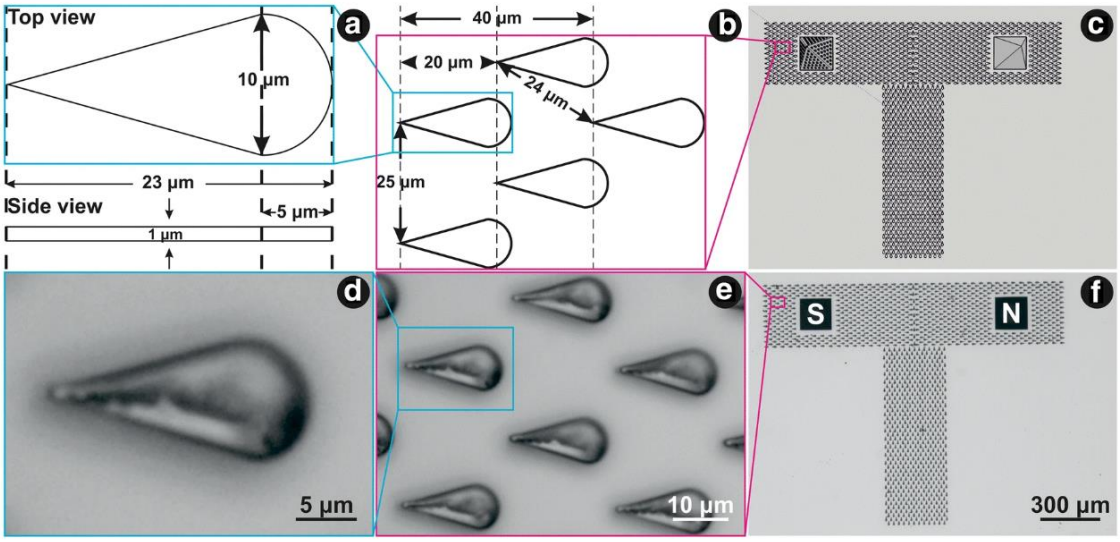


Figure 1. Computer-aided designs of (a) a single microstructure (top and side view); (b) microstructures and the distances between them in different directions; (c) the whole test sample - T channel and two MNs – structured (S) and non-structured (N). Optical microscope images of (d) an individual microstructure; (e) several microstructures, and (f) the whole test sample.

The MNs were designed as 210 µm high pyramids with square bases, 160 µm long sides and 10 µm thick walls (Figure 2a, c). The structured MN had the lateral triangular faces ornamented with bug-inspired microstructures. Each microstructure was 20 µm long (slightly shorter than the microstructures in the guiding channel, due to the expected elongation on z-direction), with a base width of 10 µm and a tip height of 5 µm, keeping the same length: width: height ratio as in [27]. The distance between two consecutive rows was set to 30 µm.

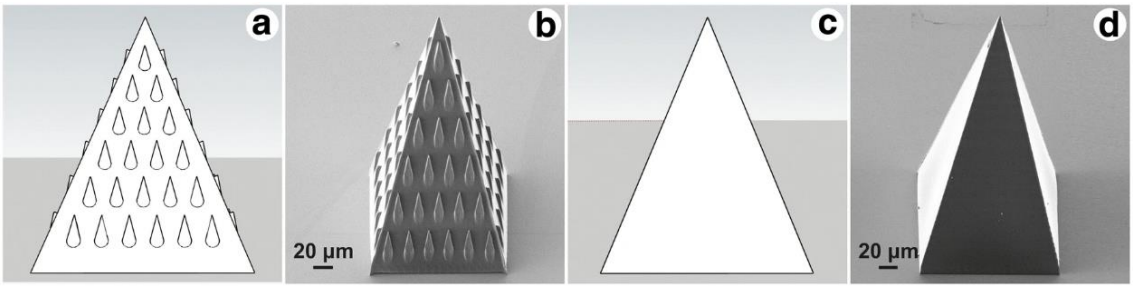


Figure 2. Computer-aided design of (a) the structured MN, and (b) the non-structured MN. The corresponding SEM images of (c) the structured MN, and (d) the non-structured MN.

5.3.2 Two-photon lithography setups

To write the guiding channel, a custom-made setup (Ti-sapphire femtosecond laser (Mai Tai, Spectra Physics), wavelength = 800 nm, pulse length = 150 fs, repetition rate = 80 MHz) was used. The setup is described in more detail in [25]. The channels were written on a #1.5 glass substrate, with an area of 24×50 mm^2, and thickness of 170 ± 30 µm (Menzel-Gläser coverslips) at a speed of 20 µm s^{-1}, with a laser excitation power of 12 mW.

To write the MNs, a commercially available setup, provided by the Workshop of Photonics® was used. The 515 nm laser beam, with a repetition rate of 1 MHz, and 290 fs pulse duration, was focused into the photoresist by an objective lens with 50-fold magnification and 0.42 numerical aperture. The MNs were written layer by layer (layer thickness = 1 µm) in a sandwich sample configuration [31]. For the non-structured MNs, a writing speed of 3 mm s^{-1} and a power of 2.4 mW were used; for the structured MNs, a speed of 1 mm s^{-1} and a power of 1 mW were used, both measured in front of the objective lens.

5.3.3 Photoresists

The photoresist used for the microstructured guiding channels was OrmoComp® (micro resist technology GmbH). The photoresist used for MNs consisted of OrmoComp® and 1 wt% of Ciba® IRGACURE® 2959 (Sigma-Aldrich). In both cases, the unpolymerized photoresist was dissolved in OrmoDev developer (micro resist technology GmbH).

5.3.4 Wetting tests and fluorescence microscopy imaging

Wetting tests were performed to prove the wettability of the lateral sides of the structured MNs. The liquid used for wetting tests and fluorescence microscopy imaging was a mixture of 1 to 10 of an ethanol solution of Alexa Fluor® 555 fluorophore (Invitrogen™, ThermoFisher Scientific Inc.) and distilled water. Furthermore, less than 1% of soap (DAWN liquid dish soap) was added, in order to adjust the liquid contact angle in a range of 40° to 50°, which is a prerequisite for the directional liquid movement [27].

For fluorescence analysis, a Nikon Eclipse Ti-U microscope (Nikon Instruments Inc.), with a Texas Red filter cube, with excitation window at 540–580 nm, and emission window at 600–660 nm (Nikon Instruments Inc.) was used. Before performing the wetting test, the samples were imaged in the red channel, to assess their auto-fluorescence. Afterwards, a small volume of water-fluorophore solution was deposited in the close proximity of the microstructured channel (Figure 3b). After the wetting test, that is, after the complete evaporation of the liquid, the samples were again imaged in the red channel. Fluorescence microscope images were recorded and line intensity profiles were obtained using the ImageJ software.

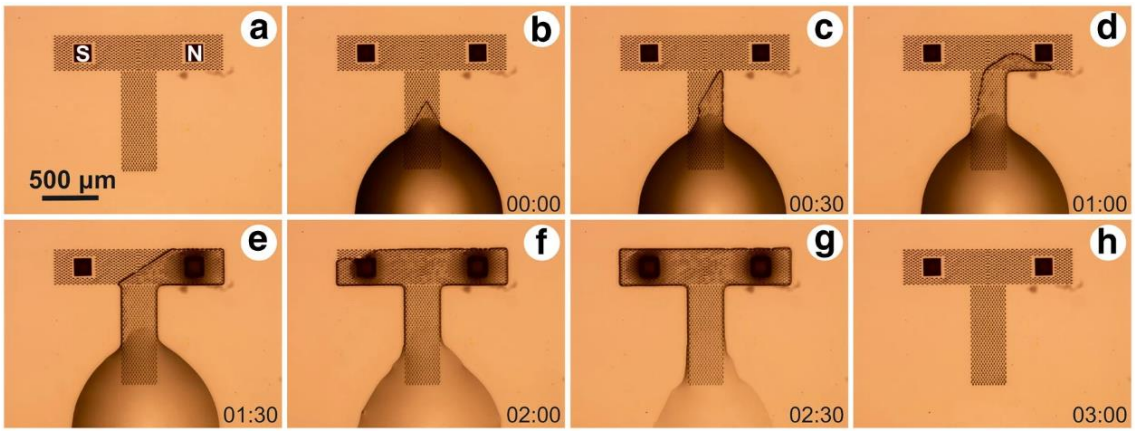


Figure 3. a Microscope image of the sample before the wetting test. b–h Liquid front movement in the guiding channel, captured every 30 s following liquid deposition at the bottom of the guiding channel (b) until complete evaporation of the liquid (H).

5.3.5 Replication

For mass-production of MNs, a micro-replication process, which is fast and cost-efficient, is necessary. To prove that even the features of the structured MNs can be replicated with high accuracy and no damage, arrays of 3 × 3 MNs (spaced 750 µm apart) printed on a glass slide were replicated as described in [30]. The master arrays were gold sputter coated prior to replication, and imaged with a scanning electron microscope (SEM). The gold layer is also helpful for the last step of replication, as it assists the demoulding.

The glass slide containing the MNs was attached to a polystyrene Petri dish using Super Glue (Loctite Superglue). After the glue had dried, a mixture of 10:1 of the two components of polydimethylsiloxane SYLGARD 184 (Neyco) was poured inside the Petri dish, covering the MNs array. The Petri dish was then left overnight on a levelled shelf, and cured in the morning at 80 °C for 1 h.

In a similar way, the two components of EPO-TEK® 353ND (Epoxy Technology, Inc.) were mixed together in a ratio of 10:1, degassed, and used to fill the SYLGARD® 184

mould. A flat disk of PDMS was used as rear mould and the ensemble was put on top of a vacuum table covered by a 500 g weight for 1 h. The EPO-TEK® 353ND was cured at 80 °C for 1 h and left at room temperature for 14 h to cool down. Finally, the two moulds peeled away from the MNs patch.

The master template (the original MNs array), as well as the epoxy replicas, were SEM imaged to assess the fidelity of the replication process. From the SEM images, the MNs' base lengths, tip widths, as well as the heights, widths and lengths of individual microstructures were measured using the ImageJ software.

5.3.6 Skin penetration

To confirm skin penetration, MNs were used for two sets of skin tests. Following protocols approved by the Clinical Research Ethics Committee of the Cork Teaching Hospitals (CREC), human skin was excised following plastic surgical operations and stored at −80 °C until needed. The skin was thawed and incubated in phosphate-buffered saline (PBS) solution (Sigma-Aldrich) for 30 min at 32 °C. Then, the skin samples were trimmed of the excess fat, cut into squares of approximately 3 cm × 3 cm and mounted on am artificial tissue substrate (Wound Closure Pad, Limbs & Things, Bristol, UK), to mimic the mechanical properties of underlying tissues. A custom-built, spring-loaded applicator, with a spring constant of 274 N/m, and impact energy of 0.4 ± 0.01 J/cm^2 was used to apply the epoxy MNs array with a surface of 4×4 mm^2 to the skin in a repeatable and reliable manner. After the impact, the applicator maintained a force of 0.5 N on the MNs array, and retracted after 2 min. The test was repeated three times to confirm the reproducibility of the results. After each test, the impact areas were stained with methylene blue (Sigma-Aldrich) for 10 min, prior to PBS rinsing and tape stripping to

remove the excess dye present on the surface of the skin [32]. Optical microscope images of the impact areas and of the MNs after insertion were recorded.

For a second set of skin tests, an optical coherence tomography (OCT) system was used to observe the penetration depth of the MNs. The MNs array was pressed against the forearm skin of a healthy male volunteer and fixed with tape prior to recording the images. The commercially available TELESTO™ Spectral Domain OCT imaging system (Thorlabs, Inc.) using a super-luminescent diode, with a central wavelength at 1325 nm, with a 150 nm bandwidth was employed. The device offers a lateral resolution of 15 µm and an axial resolution of less than 7.5 µm. After performing several skin tests, the MNs were imaged using a scanning electron microscope.

5.4 Results and discussion

Figures 1a–c show in detail the computer-aided design of the bug-inspired microstructures which make up the guiding channel. Figure 1c shows the guiding channel and two different MNs – the structured MN on the left-hand side and the unstructured MN on the right-hand side (used as negative control sample). Figures 1d–f show the corresponding optical microscope images of the bug-inspired microstructures and the whole T-array, after the developing process. One microstructure of the guiding channel has a length of 21.20 ± 0.47 µm, base width of 9.95 ± 0.46 µm, and a tip width of 1.21 ± 0.22 µm. The difference from the designed length is due to a post-curing shrinkage of up to 7% (OrmoComp® data sheet). Due to the ellipsoidal voxel shape in TPP writing [32], [33], [34], an elongation of the microstructures in the z-direction occurred. Therefore, the average height of the microstructures was 14.65 ± 2.26 µm.

The CAD designs of the structured and non-structured MNs are shown in Figure 2a, c, respectively. The corresponding SEM micrographs are presented in Figure 2b, d,

respectively. Both MNs have tips of about 1 μm in diameter, and base lengths of 150 μm (post-curing shrinkage). The bug inspired microstructures on the lateral surfaces of the structured MN (Figure 2c) are regular and well defined. Post-curing shrinkage and the voxel elongation in z-direction influenced the dimensions of the micro-ornamentation on the MNs lateral sides. Measurements revealed average tip height of 3.94 ± 0.21 μm, tip width of 2.01 ± 0.24 μm, base width of 9.81 ± 0.22 μm, and length of about 31.42 ± 0.61 μm.

An image sequence of the liquid movement in the guiding channel is presented in Figure 3. The droplet was deposited at the lower rim of the vertical channel (Figure 3b), and within the following two minutes the liquid front reached the MNs (Figure 3f, g). As seen in Figure 3d, e, the liquid front had a tendency of moving towards the right-hand side of the T-array. Therefore, the liquid front does not come in contact with both MNs in the same time. This was a systematic error, encountered in every experiment. It was a result of a slightly tilted glass slide during the writing process, causing the microstructures height difference within the array. To counteract this effect, for each sample with a structured MN on the left-hand side and the not-structured MN on the right-hand side, a sample with switched position of the two MNs was tested. In all cases, the fluorescent microscope analysis was consistent with the results shown in Figure 4c.

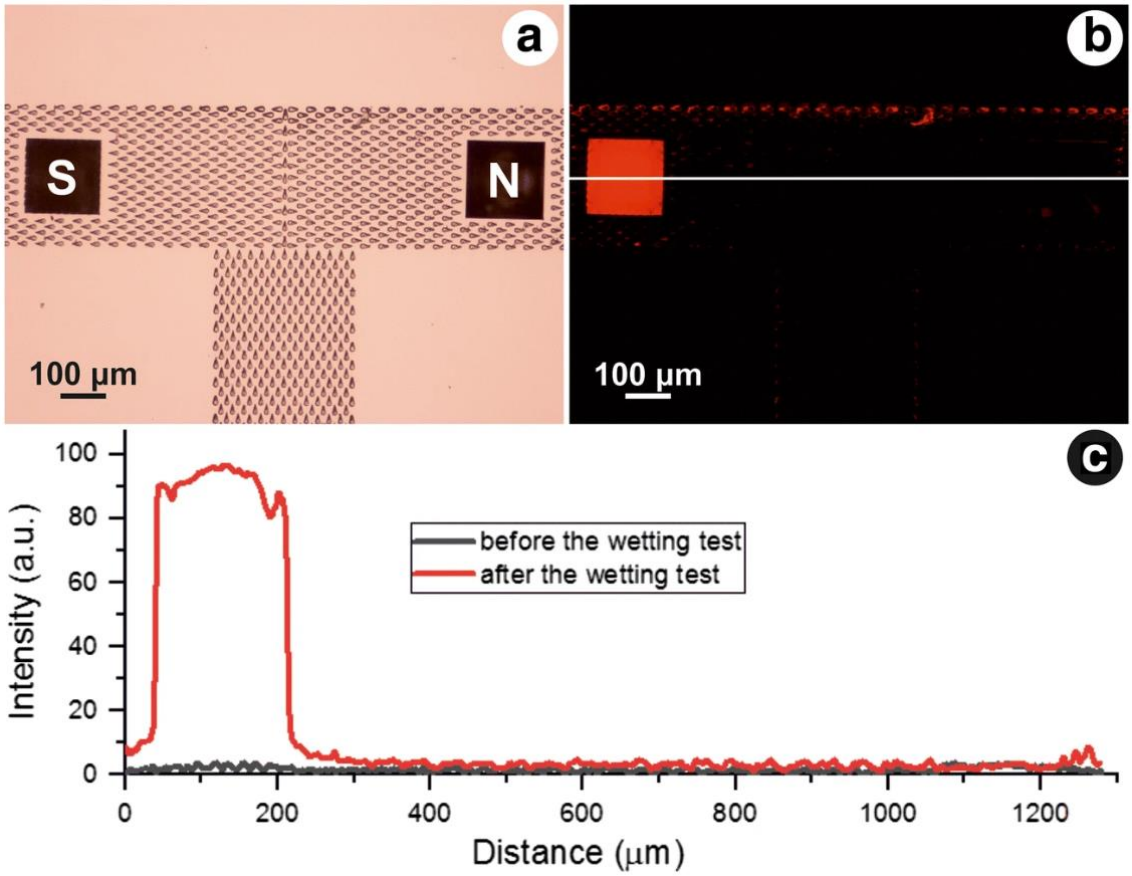


Figure 4. (a) Optical microscope image of the T-shaped channel and the two microneedles after the wetting test. (b) Fluorescent microscope image taken in the red channel after the wetting test performed with a fluorophore-soap-water solution. (c) Intensity profile along the yellow line in Figure 4b (before and after the wetting test).

Figure 4b, c present in summary the results of the wetting tests performed with a soap-liquid solution containing a fluorescent dye. Figure 4b shows an intense fluorescent signal originating from the structured MN (left-hand side), in contrast to the non-structured MN (right-hand side), whose edges are barely observable. Confocal microscope imaging of the non-structured MN after the wetting test (Supplement 1) showed a 30–40 µm high liquid front at the MN's base. This corresponds to the 15 µm high liquid front moving in the structured guiding channel, and additional capillary action manifested by the liquid

front when it encounters the MN's edges. On the other hand, confocal microscope imaging of the structured MN after the wetting test (Supplement 2) showed the fluorescence of the MN on the whole z-axis travel range of 100 µm. These results are consistent with the ones presented in Figure 4b. It is clear that the surface structures on the structured MN aid the liquid front movement on its lateral sides, justified by the intense fluorescence signal on the structured MN, compared to the non-structured one.

Figure 4c shows the intensity profile along the white line shown in Figure 4b, before the wetting test (grey curve) and after the wetting test (red curve). Low auto-fluorescence before the wetting test is observed. The fluorescence detected from the non-structured MN after the wetting test showed intensities in the same range as the structures of the guiding channel (due to comparable height of the liquid front). In contrast, the intensity detected from the structured MN rose up to 100. The wetting tests were repeated several times. The results were consistent – no or very little fluorescence recorded from the non-structured MN, and high signals recorded from the structured MNs.

MNs with the same bug-inspired ornamentation, but pointing downwards, were also tested (Supplement 3). According to [27], the stopping liquid front needs to create a V-shaped front before halting completely. In the case of MNs, the V-shaped liquid front would be formed on the MN itself, and hence the fluorescence signal after the wetting test is comparable to the MN with surface structures pointing upwards. Also according to [27], the velocity of the stopping liquid front (against the tips of the microstructures) is considerably slower than that of the advancing liquid front in the direction of the tips of the microstructures. Therefore, this study focuses only on the MNs with upwards pointing microstructures.

Figure 5 shows scanning electron micrographs of the 3 × 3 array of MNs produced with TPP, imaged after replication (Figure 5a) and its corresponding replica in EPO-TEK®

353ND (Figure 5d). After the replication process, all the MNs on the master template were intact on the glass substrate. A more detailed top and side views of the original MN can be seen in Figure 5b, c, and the equivalent replicated MN in Figure 5e, f, respectively. The MNs in this array had slightly different lengths and distributions of the micro-ornamentations than earlier presented in Figure 2c. Despite being densely packed, the surface structures on the replicated MNs are very well defined.

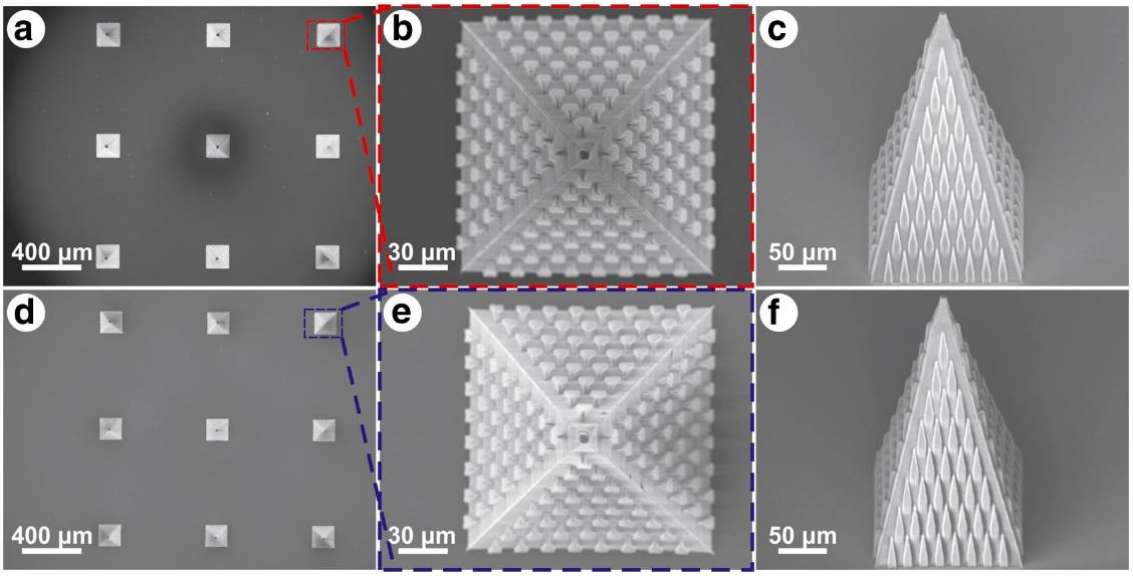


Figure 5. Scanning electron micrographs of the 3 × 3 MNs array of (a) the TPP original, and (d) its corresponding epoxy replica. SEM micrograph of a TPP structured MN from the 3 × 3 array: (b) top view, and (c) side view. SEM micrograph of an epoxy replicated structured MN: (e) top view, and (f) side view.

Measurements of the MNs' base length yielded an average value of 155.01 ± 1.69 µm for the original one, and a value of 150.51 ± 1.38 µm for the replicated MN. The difference is due to post curing shrinkage. The tip diameters for both of MNs were about 6 µm. Microstructures' lengths, base and tip widths mean values and standard deviations (n = 36) are summarised in Table 1. Student t-test revealed no significant difference

between the three sets of data, as the p-values were always greater than 0.1. These results show a successful and exact replication of the MNs array.

Table 1. Mean values and standard deviations of the bug-inspired microstructures lengths, base and tip widths. The parameters were measured on the 36 microstructures, visible on the lateral faces of the original MN (Figure 5c) and its corresponding replicated MN (Figure 5f).

	Length (µm)		**Base width (µm)**		**Tip width (µm)**	
	Original	**Replica**	**Original**	**Replica**	**Original**	**Replica**
Mean value	39.66	39.7	9.72	9.69	2.15	2.24
Std. deviation	0.71	0.89	0.37	0.35	0.33	0.31

Figure 6 shows in summary the results of the skin tests performed on *ex vivo* human skin and on a male volunteer. Each of the skin tests performed with the epoxy MNs array showed five to six penetration marks. Figure 6a shows six methylene blue stained marks. The number of penetration marks and their dimension can be explained by the irregularity and elasticity of the skin surface. Another possible explanation might be the poor penetration of some the needles.

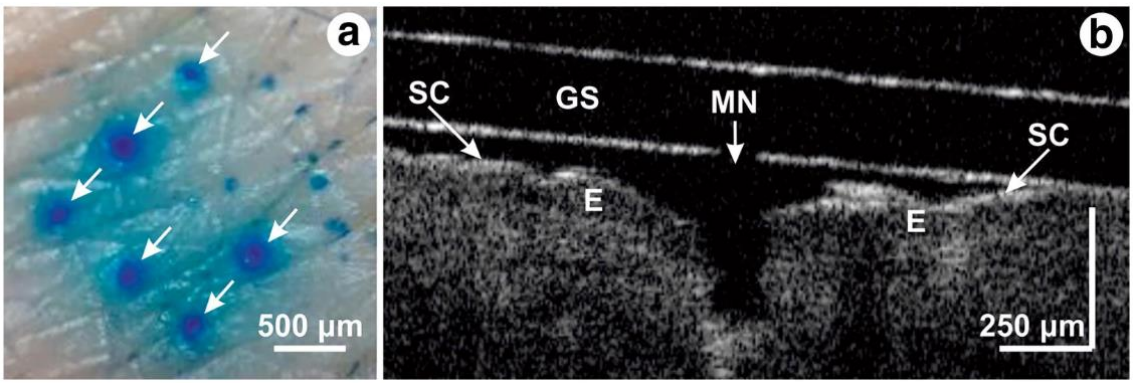


Figure 6. Skin penetration tests. a Methylene blue stained marks after the skin test. b Optical coherence tomography of one MN (SC – stratum corneum, MN – microneedle, GS – glass substrate, E – epidermis).

Optical coherence tomography analysis of the skin (Figure 6b) allowed to discriminate between distinct skin layers and even sublayers [35]. The outermost sublayer, the *stratum corneum* (SC), appears as a thin intense line due to the presence of keratin. The epidermis (E) is located right below the SC, and gives a less intense OCT signal. OCT analysis showed that when being pressed against the skin, the MNs penetrated to a depth of about two thirds of their height, corresponding to similar results presented in [36]. Nonetheless, MNs had sufficient impact energy and sharpness to break the SC barrier and penetrate through to the epidermal layer. OCT images were also recorded after the MN patch was removed (not shown). The penetration marks were much smaller than the MN dimensions, in agreement with the results from Figure 6a, most likely due to skin's elastic properties. No pain sensations were reported by the volunteer.

Optical microscope and scanning electron microscope analysis of the MNs (data not shown), which were subjected to several skin tests, showed no damage caused by the tests. This confirms the mechanical stability of the MNs: the MNs did not break and presented no risk of remaining in the skin.

The wetting tests were performed using a water-based liquid on OrmoComp® MNs. To obtain a directional flow, it is essential that the dimensional parameters (structures heights and curvatures) are set in the correct range, and that the liquid contact angle is adjusted under 45°. As discussed in detail in [27], the microstructures parameters and the contact angle define the shape of the fluid front around each microstructure. When the liquid fronts of neighbouring microstructures touch, a fluid transport in the forward direction occurs. The transport velocity is mainly determined by liquid viscosity, as these velocities allow considering a laminar flow conditions.

A general problem when applying drugs via a MN patch is to correctly dose the administered drug, as the needles loading is a delicate process [9]. Several approaches are discussed to find better solutions [10], [11], [12], [13]. The use of microstructures might reveal a new strategy. As seen in Supplement 2, the fluorescent agent is mainly concentrated at the microstructures rims, at the bottom of the channel and on the MN's lateral faces. This effect is due to solvent evaporation in the capillaries surrounding each microstructure, leaving only the non-volatile ingredients. The liquid volume in each capillary channel around identical microstructures on the MN lateral faces should be approximately the same (at least under idealized conditions [27]), depending on the contact angle and the structure geometry. Thus, the liquid loaded on a MN with a certain number of microstructures can be defined as the total volume of fluid that can be hold within the microstructures capillary network, minus the volatile part of the solvent. This obviously requires a known concentration of the pharmaceutical agent in the solvent and the constriction that the agent is non-volatile. How much of the active agent is in the end transferred into the tissue of the patient during application is an open question, which is the case for several other loading techniques discussed in literature.

Immersion coating (i.e. the entire array is immersed in the formulation) is the simplest of all coating techniques, but it leads to significant wastage of the active ingredient, since coatings are produced on the entire microneedle patch and only a small percentage is actually delivered [37]. Instead, dip coating is a preferable method of coating microneedles that involves the partial immersion of the tip region of the needle into the coating formulation, so that the base is not needlessly coated. However, it generally requires the construction of precise equipment capable of accurately and repeatedly lowering an array into liquid with microscopic precision, and this process may not be scalable to a high-volume manufacturing environment. High-viscosity solutions are typically used during the coating process, as this is an effective method of increasing drug loading, but it may also result in the formation of a large bulb of dried formulation at or near the tip, which leads to reduced tip sharpness and makes skin penetration difficult [38], [39]. In response to those limitations, this work proposes the use of novel microstructures that could lead to uniform coating on the lateral faces of the microneedle, without significantly altering the geometry or tip sharpness of the microneedle and without waste of active ingredient.

As mentioned above, the performance of the structures is dependent on contact angle and the viscosity of the formulation must be adjusted to keep the contact angle under 45°, with sufficient transport velocity. While this early engineering proof-of-concept work has not considered specific drugs or vaccines, we expect that coating of a wide range of formulations should be possible once the contact angle constraints are met. A good review of the active materials that have been coated onto microneedles to date is available in [40].

We do not think that the structures themselves will be critical for drug release and delivery, but will rather aid in uniform loading of the drug cargo onto the needle surfaces.

It is preferable that drug loading is concentrated around the lateral surfaces of the microneedle, and around the upper portions in particular (see Figure 2 of [40]), as a number of works have shown that microneedles do not penetrate to their full height due to skin elasticity and compression, and that penetration depth is generally limited to between half and two-thirds of needle height [36], [41]. Because of this, it is desirable that drug cargo is not located around the lower regions of the needle, as it does not enter the skin and is therefore wasted. Similarly, drug coatings on the base of the needle array (and in this case, in the lateral flow channels) will also be wasted. Because of this, future work will investigate the use of carefully controlled volumes that will travel from the channel to the upper half of the needle with the aim of increasing the percentage of delivered cargo and reducing the level of wasted formulation. We do not envisage the structures themselves affecting drug delivery, as the skins should conform to the relatively low heights of the microstructures. Furthermore, interstitial fluid could even collect around any gaps that may remain, and may even aid dissolution of the coating.

5.5 Conclusion

As microneedles are becoming a more auspicious tool for transdermal drug delivery, a large amount of research is being carried out to optimize MN aspect ratios, fabrication materials and techniques, as well as the methods used for coating their surfaces with drug and vaccine formulations. In this study we describe a novel biomimetic approach towards drug delivery and show proof of principle. We introduced a new MN design - the lateral faces of the MNs were ornamented with bug-inspired microstructures. When compared to the non-structured negative control MN, the structured MN proved to be easily loaded with liquid. We showed that the MN arrays can be rapidly replicated, with high accuracy, in medical-grade epoxy materials. Skin tests proved that the MNs are able to break the *stratum corneum* barrier and reach the epidermis, with no damage to the MNs, and no

pain sensation for the volunteer. However further research is required to better characterise and demonstrate pharmacological loading capabilities of the MN and drug delivery efficiency both *in vitro* and *in vivo* models.

In the future, we envisage an array of hundreds of MNs, interconnected by a net of guiding channels, consisting of bug-inspired structures. The arrays would be easily loaded with necessary drugs/vaccines, without recourse to complicated deposition procedures, and with minimal formulation wastage. To our knowledge, this is the first MN design that makes use of bio-inspired surface structures for passive liquid transportation on its lateral surfaces.

5.6 Supplementary Material

Supplementary material available in Appendix A.2.

5.7 References

[1] E. Larrañeta, M. T. C. McCrudden, A. J. Courtenay, and R. F. Donnelly, 'Microneedles: A New Frontier in Nanomedicine Delivery', *Pharm. Res.*, vol. 33, no. 5, pp. 1055–1073, May 2016, doi: 10.1007/s11095-016-1885-5.

[2] A. M. Römgens, D. L. Bader, J. A. Bouwstra, F. P. T. Baaijens, and C. W. J. Oomens, 'Monitoring the penetration process of single microneedles with varying tip diameters', *J. Mech. Behav. Biomed. Mater.*, vol. 40, pp. 397–405, Dec. 2014, doi: 10.1016/j.jmbbm.2014.09.015.

[3] H.-R. Jeong, H.-S. Lee, I.-J. Choi, and J.-H. Park, 'Considerations in the use of microneedles: pain, convenience, anxiety and safety', *J. Drug Target.*, Jan. 2017,

[4] Y.-C. Kim, J.-H. Park, and M. R. Prausnitz, ‘Microneedles for drug and vaccine delivery’, *Adv. Drug Deliv. Rev.*, vol. 64, no. 14, pp. 1547–1568, Nov. 2012, doi: 10.1016/j.addr.2012.04.005.

[5] J. Nguyen, K. B. Ita, M. J. Morra, and I. E. Popova, ‘The Influence of Solid Microneedles on the Transdermal Delivery of Selected Antiepileptic Drugs’, *Pharmaceutics*, vol. 8, no. 4, Art. no. 4, Dec. 2016, doi: 10.3390/pharmaceutics8040033.

[6] H. S. Gill and M. R. Prausnitz, ‘Coated microneedles for transdermal delivery’, *J. Controlled Release*, vol. 117, no. 2, pp. 227–237, Feb. 2007, doi: 10.1016/j.jconrel.2006.10.017.

[7] M. Leone, J. Mönkäre, J. A. Bouwstra, and G. Kersten, ‘Dissolving Microneedle Patches for Dermal Vaccination’, *Pharm. Res.*, vol. 34, no. 11, pp. 2223–2240, Nov. 2017, doi: 10.1007/s11095-017-2223-2.

[8] K. Ita, ‘Ceramic microneedles and hollow microneedles for transdermal drug delivery: Two decades of research’, *J. Drug Deliv. Sci. Technol.*, vol. 44, pp. 314–322, Apr. 2018, doi: 10.1016/j.jddst.2018.01.004.

[9] R. Haj-Ahmad *et al.*, ‘Microneedle Coating Techniques for Transdermal Drug Delivery’, *Pharmaceutics*, vol. 7, no. 4, pp. 486–502, Nov. 2015, doi: 10.3390/pharmaceutics7040486.

[10] X. Chen *et al.*, ‘Dry-coated microprojection array patches for targeted delivery of immunotherapeutics to the skin’, *J. Controlled Release*, vol. 139, no. 3, pp. 212–220, Nov. 2009, doi: 10.1016/j.jconrel.2009.06.029.

[11] M. G. McGrath, A. Vrdoljak, C. O’Mahony, J. C. Oliveira, A. C. Moore, and A. M. Crean, ‘Determination of parameters for successful spray coating of silicon

microneedle arrays', *Int. J. Pharm.*, vol. 415, no. 1, pp. 140–149, Aug. 2011, doi: 10.1016/j.ijpharm.2011.05.064.

[12] H. Khan, Mehta ,P., Msallam ,H., Armitage ,D., and Z. and Ahmad, 'Smart microneedle coatings for controlled delivery and biomedical analysis', *J. Drug Target.*, vol. 22, no. 9, pp. 790–795, Nov. 2014, doi: 10.3109/1061186X.2014.921926.

[13] R. D. Boehm, P. R. Miller, J. Daniels, S. Stafslien, and R. J. Narayan, 'Inkjet printing for pharmaceutical applications', *Mater. Today*, vol. 17, no. 5, pp. 247–252, Jun. 2014, doi: 10.1016/j.mattod.2014.04.027.

[14] X. Q. Kong and C. W. Wu, 'Mosquito proboscis: An elegant biomicroelectromechanical system', *Phys. Rev. E*, vol. 82, no. 1, p. 011910, Jul. 2010, doi: 10.1103/PhysRevE.82.011910.

[15] S. Aoyagi, H. Izumi, and M. Fukuda, 'Biodegradable polymer needle with various tip angles and consideration on insertion mechanism of mosquito's proboscis', *Sens. Actuators Phys.*, vol. 143, no. 1, pp. 20–28, May 2008, doi: 10.1016/j.sna.2007.06.007.

[16] W. K. Cho *et al.*, 'Microstructured barbs on the North American porcupine quill enable easy tissue penetration and difficult removal', *Proc. Natl. Acad. Sci. U. S. A.*, vol. 109, no. 52, pp. 21289–21294, Dec. 2012, doi: 10.1073/pnas.1216441109.

[17] S. Y. Yang *et al.*, 'A bio-inspired swellable microneedle adhesive for mechanical interlocking with tissue', *Nat. Commun.*, vol. 4, no. 1, p. 1702, Apr. 2013, doi: 10.1038/ncomms2715.

[18] W. Barthlott and C. Neinhuis, ‘Purity of the sacred lotus, or escape from contamination in biological surfaces’, *Planta*, vol. 202, no. 1, pp. 1–8, Apr. 1997, doi: 10.1007/s004250050096.

[19] L. M. Hamming and P. B. Messersmith, ‘Fouling Resistant Biomimetic Poly(Ethylene Glycol) Based Grafted Polymer Coatings’, *Mater. Matters*, vol. 3, no. 52, 2008.

[20] P. Comanns, K. Winands, K. Arntz, F. Klocke, and W. Baumgartner, ‘Laser-based Biomimetic Functionalization Of Surfaces: From Moisture Harvesting Lizards To Specific Fluid Transport Systems’, *Int. J. Des. Nat. Ecodynamics*, vol. 9, no. 3, pp. 206–215, 2014.

[21] G. Buchberger *et al.*, ‘Bio-inspired Microfluidic Devices for Passive, Directional Liquid Transport: Model-based Adaption for Different Materials’, *Procedia Eng.*, vol. 120, pp. 106–111, Jan. 2015, doi: 10.1016/j.proeng.2015.08.576.

[22] P. Comanns *et al.*, ‘Directional, passive liquid transport: the Texas horned lizard as a model for a biomimetic “liquid diode”’, *J. R. Soc. Interface*, vol. 12, no. 109, p. 20150415, Aug. 2015, doi: 10.1098/rsif.2015.0415.

[23] P. Comanns, P. C. Withers, F. J. Esser, and W. Baumgartner, ‘Cutaneous water collection by a moisture-harvesting lizard, the thorny devil (Moloch horridus)’, *J. Exp. Biol.*, vol. 219, no. 21, pp. 3473–3479, Nov. 2016, doi: 10.1242/jeb.148791.

[24] S. V. Kirner *et al.*, ‘Mimicking bug-like surface structures and their fluid transport produced by ultrashort laser pulse irradiation of steel’, *Appl. Phys. A*, vol. 123, no. 12, p. 754, Nov. 2017, doi: 10.1007/s00339-017-1317-3.

[25] C. Plamadeala *et al.*, 'Bioinspired polymer microstructures for directional transport of oily liquids', *R. Soc. Open Sci.*, vol. 4, no. 3, p. 160849, Mar. 2017, doi: 10.1098/rsos.160849.

[26] G. Buchberger *et al.*, '"Fluidic diode" for passive unidirectional liquid transport bioinspired by the spermathecae of fleas', *J. Bionic Eng.*, vol. 15, no. 1, pp. 42–56, Jan. 2018, doi: 10.1007/s42235-017-0003-7.

[27] F. Hischen *et al.*, 'The external scent efferent system of selected European true bugs (Heteroptera): a biomimetic inspiration for passive, unidirectional fluid transport', *J. R. Soc. Interface*, vol. 15, no. 140, p. 20170975, Mar. 2018, doi: 10.1098/rsif.2017.0975.

[28] T. Tanaka, H.-B. Sun, and S. Kawata, 'Rapid sub-diffraction-limit laser micro/nanoprocessing in a threshold material system', *Appl. Phys. Lett.*, vol. 80, no. 2, pp. 312–314, Jan. 2002, doi: 10.1063/1.1432450.

[29] S. D. Gittard, A. Ovsianikov, B. N. Chichkov, A. Doraiswamy, and R. J. Narayan, 'Two-photon polymerization of microneedles for transdermal drug delivery', *Expert Opin. Drug Deliv.*, vol. 7, no. 4, pp. 513–533, Apr. 2010, doi: 10.1517/17425241003628171.

[30] C. O'Mahony, R. Houlihan, K. Grygoryev, Z. Ning, J. Williams, and T. Moore, 'Design, modelling and preliminary characterisation of microneedle-based electrodes for tissue electroporation in vivo', *J. Phys. Conf. Ser.*, vol. 757, no. 1, p. 012040, Oct. 2016, doi: 10.1088/1742-6596/757/1/012040.

[31] J. Serbin, A. Ovsianikov, and B. Chichkov, 'Fabrication of woodpile structures by two-photon polymerization and investigation of their optical properties', *Opt. Express*, vol. 12, no. 21, pp. 5221–5228, Oct. 2004, doi: 10.1364/OPEX.12.005221.

[32] H.-B. Sun, T. Tanaka, and S. Kawata, ‘Three-dimensional focal spots related to two-photon excitation’, *Appl. Phys. Lett.*, vol. 80, no. 20, pp. 3673–3675, May 2002, doi: 10.1063/1.1478128.

[33] R. J. DeVoe, H. W. Kalweit, C. A. Leatherdale, and T. R. Williams, ‘Voxel shapes in two-photon microfabrication’, in *Multiphoton Absorption and Nonlinear Transmission Processes: Materials, Theory, and Applications*, SPIE, Feb. 2003, pp. 310–316. doi: 10.1117/12.459028.

[34] J. Fischer and M. Wegener, ‘Three-dimensional direct laser writing inspired by stimulated-emission-depletion microscopy [Invited]’, *Opt. Mater. Express*, vol. 1, no. 4, pp. 614–624, Aug. 2011, doi: 10.1364/OME.1.000614.

[35] E. C. Sattler, R. Kästle, and J. Welzel, ‘Optical coherence tomography in dermatology’, *J. Biomed. Opt.*, vol. 18, no. 6, p. 061224, Jan. 2013, doi: 10.1117/1.JBO.18.6.061224.

[36] J. Enfield, M.-L. O’Connell, K. Lawlor, E. Jonathan, C. O’Mahony, and M. Leahy, ‘In-vivo dynamic characterization of microneedle skin penetration using optical coherence tomography’, *J. Biomed. Opt.*, vol. 15, no. 4, p. 046001, 2010, doi: 10.1117/1.3463002.

[37] J. A. Matriano *et al.*, ‘Macroflux® Microprojection Array Patch Technology: A New and Efficient Approach for Intracutaneous Immunization’, *Pharm. Res.*, vol. 19, no. 1, pp. 63–70, Jan. 2002, doi: 10.1023/A:1013607400040.

[38] Y. Chen, B. Z. Chen, Q. L. Wang, X. Jin, and X. D. Guo, ‘Fabrication of coated polymer microneedles for transdermal drug delivery’, *J. Controlled Release*, vol. 265, pp. 14–21, Nov. 2017, doi: 10.1016/j.jconrel.2017.03.383.

[39] Y.-C. Kim, F.-S. Quan, D.-G. Yoo, R. W. Compans, S.-M. Kang, and M. R. Prausnitz, ‘Enhanced Memory Responses to Seasonal H1N1 Influenza Vaccination of the Skin with the Use of Vaccine-Coated Microneedles’, *J. Infect. Dis.*, vol. 201, no. 2, pp. 190–198, Jan. 2010, doi: 10.1086/649228.

[40] R. S. J. Ingrole and H. S. Gill, ‘Microneedle Coating Methods: A Review with a Perspective’, *J. Pharmacol. Exp. Ther.*, vol. 370, no. 3, pp. 555–569, Sep. 2019, doi: 10.1124/jpet.119.258707.

[41] A. Ripolin, J. Quinn, E. Larrañeta, E. M. Vicente-Perez, J. Barry, and R. F. Donnelly, ‘Successful application of large microneedle patches by human volunteers’, *Int. J. Pharm.*, vol. 521, no. 1–2, pp. 92–101, Apr. 2017, doi: 10.1016/j.ijpharm.2017.02.011.

Chapter 6

Flexible, Conductive Fabric-Backed, Microneedle Electrodes for Electrophysiological Monitoring

Authors: Om Prakash Singh, Andrea Bocchino, Theo Guillerm, Yuan Hu, Frank Stam, Conor O'Mahony.

Journal: *Advanced Materials Technologies*, volume 9, article 2301606.

Publication Date: 08 December 2023.

DOI: 10.1002/admt.202301606

Contribution: I was responsible for the conceptualization and development of the production process used to merge commercial materials (in this work, conductive fabric) with curable polymers (see Chapter 2). This is presented in Sections 6.3.7.2 and 6.4.1. Similarly, I co-designed the protocol to test the developed electrodes and compare them with the standard gel based counterparts (contributions presented in Sections 6.3.1, 6.3.2, 6.3.3, 6.4.1, and 6.4.5). Finally, I designed the initial prototype the device used to capture the ECGs, enabling simultaneous recording of multiple traces (preliminary prototype to the device built and presented within Section 6.3.5. I had also a Matlab code build to analyse the SNR of the traces, compare them, and automatically detect characteristic features/points of the trace – such as the QRS complex. This helped with the development of the software used for this analysis).

Finally, I have also contributed to the writing and the reviewing of the paper.

Chapter adapted from below link under the Creative Commons license 4.0 (CC BY 4.0). The Section numbers, Figures/Tables/References style has been adapted to conform to the style and numbering of the thesis.

https://advanced.onlinelibrary.wiley.com/doi/full/10.1002/admt.202301606

Link to license:

https://creativecommons.org/licenses/by/4.0/

6.1 Abstract

Microneedle-based electrodes have attracted significant attention due to their potential applications in high-quality, long-term electrophysiological monitoring. In this study, micromoulding technology is used to develop a flexible, conductive fabric microneedle (CF–MN) electrode by bonding a conductive textile to polymeric microneedle arrays. The resulting electrode conforms to the curved surfaces of the body, and the use of a conductive textile backing reduces metallization time and costs by 50% over double-sided dry electrodes. The electrode-skin impedance of the CF–MN electrodes is significantly lower than that of gel electrodes over a wide frequency range, and tests on healthy volunteers, both at rest and under a range of ambulatory conditions, showed that the electrodes are capable of acquiring electrocardiography (ECG) and electromyography (EMG) signals that have a comparable kurtosis and signal-to-noise ratio to those recorded using conventional electrodes, but without the need for skin preparation or the use of a wet gel. The biomechanical properties of the electrode are also characterized. This is the first demonstration of CF–MN electrodes that can ultimately be integrated into clothing, which in turn can facilitate personalized cardiac health management by enabling continuous, long-term ECG/EMG monitoring during daily activities.

6.2 Introduction

Electrophysiological signals obtained from the surface of the body can offer valuable insights into health and well-being [1], [2], [3]. Electrocardiography (ECG) and electromyography (EMG), which measure electrical signals from the heart and skeletal muscles, respectively, are amongst the simplest and most widely used procedures for screening cardiovascular diseases (including arrhythmias, fibrillation, or heart failure), [4] and muscular activity (e.g., for motor disability and neuromuscular disorder detection,

or for prosthesis control). [5] The use of lightweight, wearable devices to acquire these surface biopotential measurements is an attractive solution for applications in health and lifestyle; these monitors usually incorporate electrodes, an electronic acquisition system, signal processing software, and machine learning algorithms. [2]

Electrodes are crucial for obtaining physiological signals by converting ionic current to electronic current. [6] The electrode-skin impedance (ESI) is a key parameter of such electrodes, [1] with undesirably high ESI leading to lower signal quality and signal-to-noise ratio (SNR). Wet gel electrodes are commonly used in clinical and research settings, and use an electrolytic gel to establish a low impedance connection with skin. This gel tends to become dry over time, and the use of wet electrodes also often requires skin preparation such as shaving or abrasion to further reduce the skin-electrode impedance. [7] However, skin preparation can be uncomfortable, time-consuming, and may cause skin irritation or infection. This can be especially problematic for premature babies, people with sensitive skin, and the elderly. [8], [9]

Dry electrodes offer improved comfort, stability, and signal quality compared to wet gel electrodes, making them a promising solution for long-term monitoring, sports and lifestyle applications, and telemedicine. [10], [11] Researchers have proposed several types of dry electrodes, including those made from stiff materials, soft/flexible materials, and textiles. Textile-based electrodes are attractive for sensing physiological parameters due to their accessibility, comfort, and ability to sense parameters such as respiratory rate, ECG, and EMG. [12], [13], [14] Conductive fabrics woven, embroidered, or knitted into clothes may also be used as electrodes. Nonetheless, the issue of stretching and the potential for loose skin-electrode contact during movement represent significant challenges that can result in motion artifacts. [15], [16] These challenges pose a major

obstacle to obtaining electrophysiological signals that are free from artifacts. The CF–MN electrode described here can offer a potential solution to some of these issues.

Microneedles (MN) are sharp, submillimeter, spike-like structures, originally developed for drug and vaccine delivery but now finding applications in diagnostic and biopotential monitoring applications. [17], [18], [19] MN dry electrodes can record electrophysiological signals with low ESI by painlessly penetrating the high impedance (> 105 Ω) *stratum corneum* layer without requiring skin preparation, which is convenient for clinicians and patients alike. [20], [21], [22] Ongoing research aims to improve the biocompatibility and performance of microneedle-based electrodes. [23], [24], [25], [26], [27], [28], [29] Of particular interest is the development of flexible microneedle electrodes, which are more tolerable for long-term applications as they can conform to the curved body surface and lessen the possibility of causing pain or irritation. These electrodes could be integrated into textiles or “smart garments” and their flexible nature could also reduce the risk of needle failure. Figure 1 illustrates the use of equivalent circuit models for these three electrode types, comprising resistors (R) and capacitors (C) arranged in parallel and series combinations to approximate the electrical impedance of the skin. These models aim to capture the effective behaviours of the skin's complex structures and the properties of its different layers in contact with the electrodes.

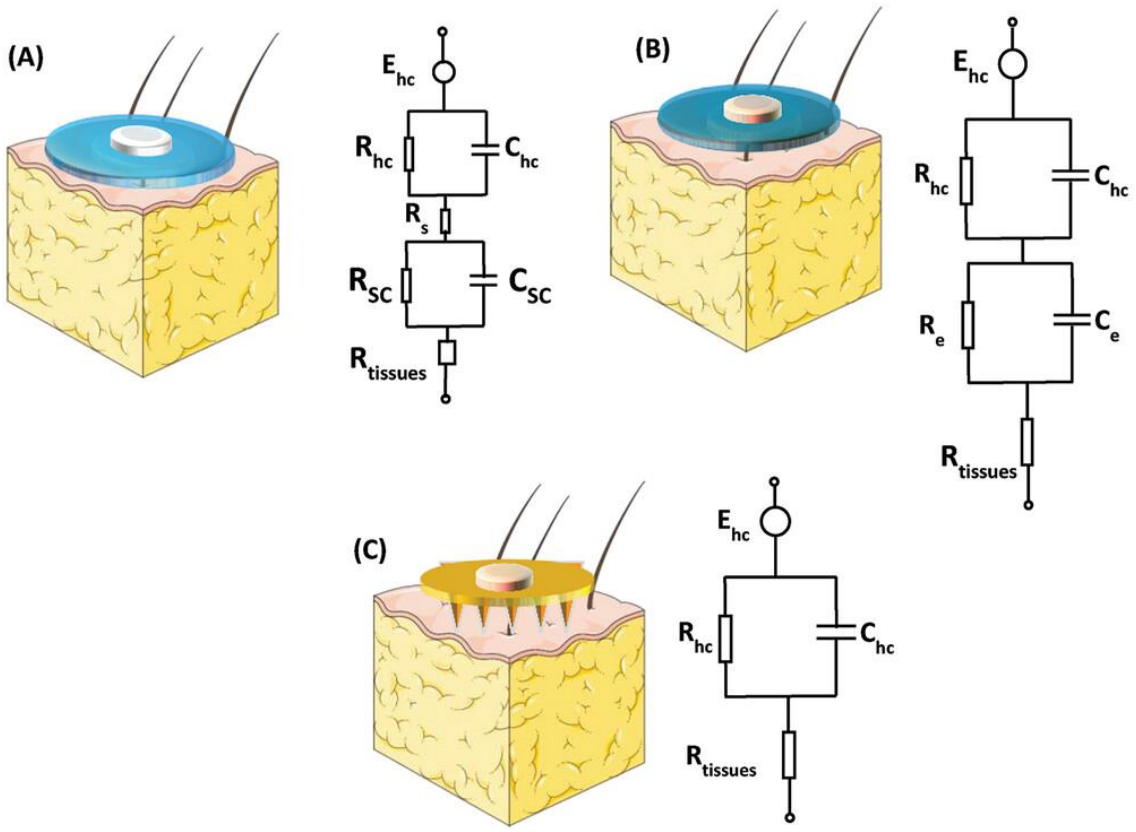


Figure 1. Schematic representation and equivalent electrical model for A) conventional wet electrodes, B) dry electrodes, and C) CF–MN electrodes. E_{hc} is the half-cell potential between electrode and skin; R_{hc} and C_{hc} are the charge transfer resistance and equivalent capacitance; R_s is the series resistance of gel, moisture, and sweat; R_{sc} and C_{sc} are the equivalent resistance and capacitance of epidermis layer; R_{tissue} is the resistance of dermis and underlying tissues.

Many microfabrication technologies used for microneedle manufacture have limitations due to their requirements for expensive equipment and complex infrastructure. [24], [25], [28], [29], [30], [31], [32], [33], [34], [35], [36], [37], [38], [39], [40] Micromoulding technology is a simpler and cost-effective alternative that enables the production of sharp and precise microneedles. We have previously demonstrated a double-sided

micromoulding procedure for the production of sharp-tipped microneedle electrodes that also incorporated through-wafer vias to facilitate metallization at the wafer scale. [41]

In this study, we adapt that micromoulding process to introduce flexible biopotential dry electrodes based on conductive fabric-backed microneedles with a sharp tip, called CF–MN. These electrodes can record high-quality signals from the heart and muscle and are mechanically robust by maintaining good contact. This simple fabrication process is the first-ever report on the fabrication of CF–MN through micromoulding technology for surface electrophysiological monitoring and further has the advantage of only requiring metallization on the front face of the electrode, reducing metallization costs and time by ≈ 50% compared with standard, double-sided electrodes. We combine the CF–MN electrode with specialized ECG and EMG recording systems to enable biopotential recording with high SNR and low motion artifacts. Tests on healthy volunteers, both at rest and under a range of ambulatory conditions, show that the electrodes are capable of acquiring ECG and EMG signals with quality comparable to those recorded using commercial wet electrodes. Our proposed technology is expected to facilitate personalized cardiac health management by enabling continuous, long-term ECG/EMG monitoring during daily activities.

6.3 Experimental Section

6.3.1 Mechanical Characterization

The flexibility and compressibility of CF–MN arrays were assessed utilizing an Instron tensile testing machine (Model 5565, Instron, Buckinghamshire, UK). Three samples with dimensions of 2×6 cm^2 were prepared for machine testing. A setup was developed for stretching and bending tests as described in reference, [27] and data was recorded at 1 mm min^{-1} with five samples per second.

An axial compression test for strength conformance by applying pressure to the array with a probe that moved downward at a speed of 0.01 mm^{-1} s until a maximum force of 35N was reached. The mode of failure of the microneedles was characterized using a scanning electron microscope and force/displacement curve analysis.

6.3.2 Skin Insertion Test

Skin insertion tests were performed using a microneedle array and an impact inserter device. [34] *Ex vivo* human abdominal skin, discarded after cosmetic surgical procedures, was obtained following ethical approval by the Clinical Research Ethics Committee of the Cork Teaching Hospitals (CREC) and informed consent from all patients (approval reference ECM 4 (aa) 06/08/13). This was incubated in PBS before being clamped in a customized 3D-printed jig for controlled stretching. A total of five plastic discs of 1 mm thickness were placed underneath the skin sample to stretch and dome the surface into a shape approximating that of *in vivo* skin. The CF–MN electrode was applied to the skin sample with an impact energy of ≈ 0.38 J cm^{-2} and 5 N residual force. [34], [36].

6.3.3 *In Vivo* Electrode-Skin Impedance Characteristics

In accordance with policies and procedures of the Clinical Research Ethics Committee (CREC) of the Cork Teaching Hospitals, the biomechanical and electrical characteristics of the electrodes were measured in a small cohort of healthy volunteers. The study protocol was approved by CREC (ECM 3 (ZZ) 10/11/20), and all participants provided written consent.

The electrode skin impedance was measured using an Agilent E48980A LCR meter and customized LabVIEW software. The standard wet gel and CF–MN electrodes were placed on the anterior and posterior antebrachial region of the forearm to avoid hair shaft

interference and maintain consistent conditions. Both types of electrodes were applied with light pressure using thumb and index fingers. The impedance was recorded from six healthy volunteers over a wide frequency range of 20 Hz^{-1} kHz, with a 100 Hz interval. Although ECG bandwidth typically ranges from 0.05 Hz to 150 Hz, in this case, ESI was measured from 20 Hz due to equipment limitations. The skin surface was not shaved or abraded prior to recording, and measurements were performed at room temperature.

6.3.4 Skin Compatibility Test

To check for skin irritation, CF–MN, and wet-gel electrodes were placed adjacent to each other on the forearm of a healthy subject with a 5 cm distance between them and left for 48 h, while a medical grade tape was placed over the electrodes for additional support. The skin was then examined for signs of erythema. [48]

6.3.5 ECG Recording: Hardware and Signal Analysis

The performance of the CF–MN electrodes was assessed by recording ECG signals from the subjects in static and dynamic conditions using the customized dual-channel ECG device previously reported. [42] Schematic, PCB, CAD files, and PCB readout module details can be found in Figure S2A–D (Supporting Information). To test the anti-artifact capability of the CF–MN electrodes and wearable recording system, ECG signals were recorded simultaneously with CF–MN and gel electrodes on three volunteers (two males and one female: age – 35 ± 12 years; height – 168 ± 7 cm; weight – 68 ± 24 kg). The volunteers wore dual-channel ECG wireless recording systems with CF–MN and gel electrodes in the lead-I configuration. Medical grade tape was used to stabilize the recording system during ECG signal recording.

The recordings were performed at 500 samples per seconds (sps) for 1 min before and after exercise and for 2 min and 30 s during exercise (walking at 2, 4, and 6 km h^{-1}) as recommended by the American Heart Association and Nyquist criterion. [43] The two sets of electrodes were placed adjacently on the left and right chest, with a distance of ≈ 6.5 ± 0.4 and 6.4 ± 0.6 cm between the centers of the electrodes for left and right sides, respectively. Kurtosis (kSQI), signal-to-noise ratio (SNR), and the standard deviation (SD) of the QRS complex were used to assess the performance of the CF–MN electrodes. A kurtosis larger than five indicates clean, sinus rhythm ECG, [44] while a kurtosis ≈ 5 indicates muscle artifact, and a kurtosis lower than five indicates baseline wander and powerline interference. [45] A low kSQI usually indicates low-frequency noise such as Gaussian (thermal observation) noise, baseline wonder, and power-line interference.

$$\text{Kurtosis}, kSQI = \frac{E\{(x-\mu_x)^4\}}{\sigma^4} \qquad (1)$$

where kSQI represents the kurtosis as a signal quality index, μ_x and σ are empirical estimates of the mean and standard deviation of x respectively, and x is the ECG signal.

The SNR was calculated as follows:

$$SNR_{dB} = 20 \log_{10} \frac{A_{pp}^{signal}}{A_{pp}^{noise}} \qquad (2)$$

where A_{pp}^{signal} and A_{pp}^{noise} represent the peak-to-peak ADC counts of the QRS wave and noise in the isoelectric region between the T and P waves, respectively.

SD of the QRS complex could quantify the overall variability and dispersion of the amplitude values within the complex, which could be an indicator of the presence of noise. A higher SD suggests a greater variation and was often associated with a noisier signal. Conversely, a lower SD indicates less variability and a cleaner signal. [29] Labview 2020 SPI (32-bit) was used to calculate the values of kurtosis, SNR, and SD of the QRS complex.

6.3.6 EMG Recording: Hardware and Signal Analysis

A dual-channel EMG sensor (SEN0240 from DFRobot/OYMotion) was used for the simultaneous recording of EMG signals from both the wet gel and CF–MN electrodes. The EMG sensor was integrated with an ESP32-WROOM-32D microcontroller using a general-purpose PCB board for wireless transmission and processing, enclosed in a 3D printed housing and powered via USB. A custom-built Labview GUI software was used for real-time display and recording of the data. The device was lightweight (54.54 grams) and compact for ease of EMG signal recording (see Figure S3A,B, Supporting Information). This recording system was used to evaluate the performance of the CF–MN electrode against that of the gel electrode. CF–MN and wet gel electrodes were applied ≈ 6 cm apart in the flexor digitorum profundus (FDP) region of the forearm. [46] The EMG data was recorded from three subjects (three males with age, height, and weight of 32 ± 6 years, 167 ± 5 cm, and 79 ± 14 kg, respectively) for ≈ 70 s while subjects were performing various tasks like opening and closing of the fist, and flexing of the pinky, ring, middle, index, and thumb fingers. A 20 Hz high-pass FIR digital filter and full signal rectification were performed to remove the low-frequency motion noises and aggregate the negative part of the recorded raw EMG data. The high pass filter from 20 Hz was selected because normally 80% of the muscular energy is concentrated between 20 Hz

and 450 Hz. [47] Meanwhile, a 50 Hz digital notch filter was used to remove the power line interference. The root mean square (RMS) values of the signal and noise data of all extracted segments from each EMG signal were calculated to reflect the average amplitude. The SNR was estimated as follows:

$$SNR_{dB} = 20 \log_{10} \frac{RMS_{signal}}{RMS_{Noise}} \qquad (3)$$

where RMS_{signal} and RMS_{Noise} depict the root mean square values of signal and noise regions when the subject contracted and relaxed muscles.

The data analysis involved the use of Origin Pro (Origin 2021b) to perform calculations such as mean, standard error, and paired t-tests. Additionally, Labview 202 SPI (32-bit) was used to calculate root mean square (RMS) and SNR.

6.3.7 Electrode Construction

6.3.7.1 Materials

Sylgard 184 polydimethylsiloxane (PDMS) was purchased from Dow Corning Inc., USA. Medical grade EPO-TEK 353ND epoxy resin and medical grade MED-H20E conductive epoxy was acquired from Epoxy Technology Europe Ltd. Conductive fabric (NCS95R-CR, a nylon ripstop fabric covered by nickel, copper, silver, and a waterproof layer) with a thickness of 127 µm ± 15%, DC surface resistivity of < 0.01 Ω sq^{-1}., and temperature ranges of −40 to 100 °C was sourced from Marktek Inc. USA. Medical grade, double-sided, a conductive adhesive (ARcare 90 366, with a thickness of 1.3 µm and low volume resistance of ≈ 10Ω) was received as a sample from Adhesives Research, Inc., USA. We also bought Micropore Medical Tape, thickness 25 µm, from 3M Ireland Limited, Ireland

that was used for attaching the dry electrodes onto the skin. 3M Red Dot (2239) Monitoring Electrodes were procured from Promed, Tulligmore, Ireland. Male ECG snap buttons were purchased from PMSOEHT Professional Accessories, China.

6.3.7.2 Design, Fabrication, and Assembly of Electrodes

The flexible microneedle array structure for CF–MN electrodes was fabricated using a micromoulding process as shown in Figure 2. To create a mould, a 100 mm diameter silicon wafer was used as a master template, on which was etched an array of 500 µm tall microneedles consisting of eight (263) silicon planes, a base of (212) planes, and a height: base diameter aspect ratio of 3:2. [6], [41] The needle-to-needle pitch was 1750 µm and the tip radii were typically between 50 and 100 nm. PDMS was mixed according to the manufacturer's instructions, poured over the master template, and left to degas at room temperature for 24 h. The PDMS was then cured at 80 °C for 1 h, cooled, and peeled from the master template. Thereafter, a biocompatible epoxy resin (EPO-TEK 353ND) was mixed in a 10:1 ratio and poured onto this front mould. This material has previously been used for microneedle manufacture. [17], [35], [41] It was left in a vacuum chamber to degas the epoxy at 200 mTorr for ≈ 15–20 min. The mould was then placed on a vacuum table for ≈ 30–45 min, during which time a spatula was used to spread the epoxy resin and fill the microneedle pits.

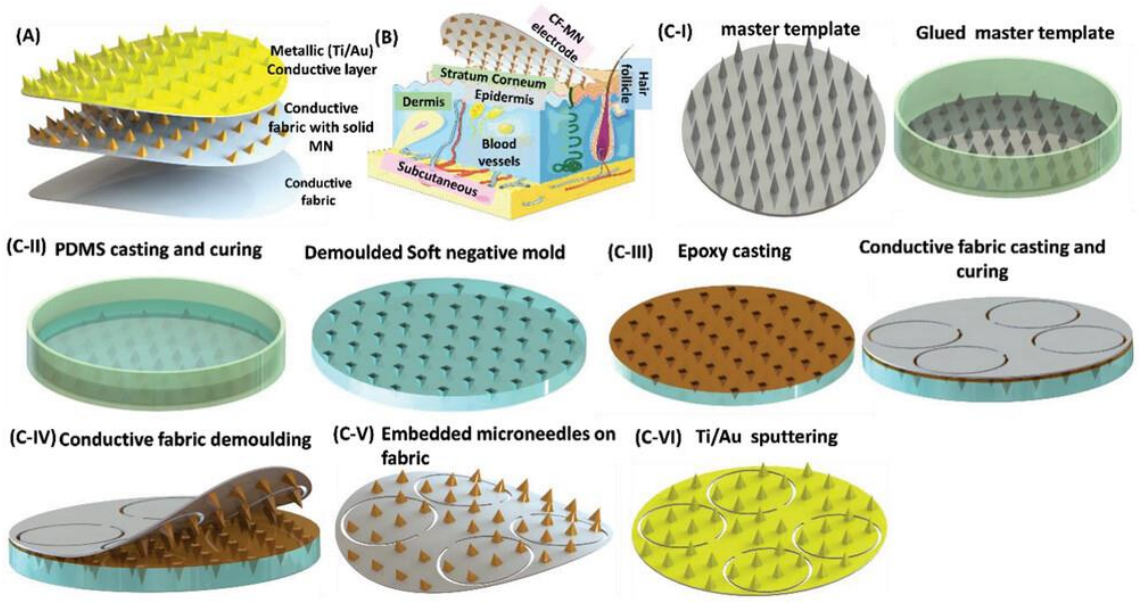


Figure 2. A) Schematic view of the structure and material of the CF–MN electrode. B) Principle of minimally invasive electrophysiological signal acquisition by a flexible CF–MN electrode. C) (I–VI) Manufacturing process flow of the CF–MN electrode.

While excess epoxy was removed after the microneedle pits were filled, in order to improve the adhesion of conductive fabric to the microneedles a thin layer of epoxy resin (≈ 40% of the original deposited volume) was left to remain on the front mould surface. To form a rear backing layer and define the geometrical dimensions of the electrodes, a circular ring shape with internal and external diameters of 18 and 19.14 mm was created using Microsoft PowerPoint and saved as a JPG file (Figure S1, Supporting Information). The file was then imported into Cricut Design Space (v7.20.88) and cut into the conductive fabric using a Cricut Maker cutting machine (CXPL301) equipped with a fine point blade.

Next, the cut CF sheet was placed over the filled front mould and left on a vacuum table for ≈ 30–45 min. A petri dish cover and weight were placed over the rear mould. After curing in an oven at 80 °C for an hour, the CF and microneedles were detached from the front mould. This process resulted in a substrate thickness of ≈ 165 ± 5 µm that had good flexibility.

Before metallization, the electrodes were cleaned with isopropyl alcohol and dried with a nitrogen gun. A Temescal UEFC-4900 e-beam system was used to deposit an adhesion layer of 20 nm thick titanium, followed by a 150 nm thick gold layer. The evaporation process was performed exclusively on the front side of the flexible CF–MN, while the electrical connection was established from the front to the rear side of the conductive fabric via the gap created by cutting out a circular ring from the fabric as presented in Figure S1 (Supporting Information).

The electrodes were cut from the rear backing layer using a scalpel or fine blade. For testing purposes, they were then affixed to 3M Red Dot Monitoring Electrodes, from which the wet gel pad was removed, using conductive adhesive. Sterilization was performed with UV–ozone for 5 min at a power of 1380 mW cm^{-2} before the electrodes were packed and stored in plastic cases.

6.4 Results and Discussion

6.4.1 Materials, Structural, and Fabrication Approach

Figure 2A shows the basic structure of the CF–MN electrode, which includes arranging ≈ 100 microneedles on an 18 mm diameter conductive fabric. The microneedles have a tip radius of ≈ 5 µm, height of 500 µm, and pitch of 1750 µm. The NCS95R-CR fabric worked well once the amount of epoxy resin necessary to ensure bonding between the

rigid microneedle and the fabric was optimized. Bonding was confirmed by casting epoxy resin onto a fabric sample (5 × 7 mm^2), curing it, and analyzing it using SEM. Figure S4A,B (Supporting Information) showed that the epoxy has diffused into the fabric, indicating a good bond between the fabric and the epoxy resin. Ti/Au metal layers were used for signal transmission on the front face of the electrodes, including the microneedles and sidewalls. This single-sided metallization approach reduces processing time and cost by 50% compared to earlier studies. [23], [41]

As depicted in Figure 2B, the CF–MN electrode, when placed on the skin, demonstrates the capability of the microneedles to effectively traverse the *stratum corneum* (SC) and establish direct contact with the epidermis. This contact is achieved without coming into contact with the underlying dermis and deeper tissues, which are home to nerves and blood vessels. The manufacturing process of the CF–MN electrode is illustrated in Figure 2C.

Figure 3A–D illustrates the fabricated CF–MN electrode, showcasing the metal coating on the front face (Figure 3A) as well as the nonmetallized rear side (Figure 3B). The figures also demonstrate the successful reproduction of the master template structures. Figure 3D and Figure S5, Table S1 (Supporting Information) show that the mean tip diameter of 4 ± 2 μm is consistent with previous studies [36], [49] and sharp enough to penetrate the skin. The robustness of the fabrication process was confirmed by repeatedly micromoulding the same silicon master template over 100 times, without any deformation or loss of morphology.

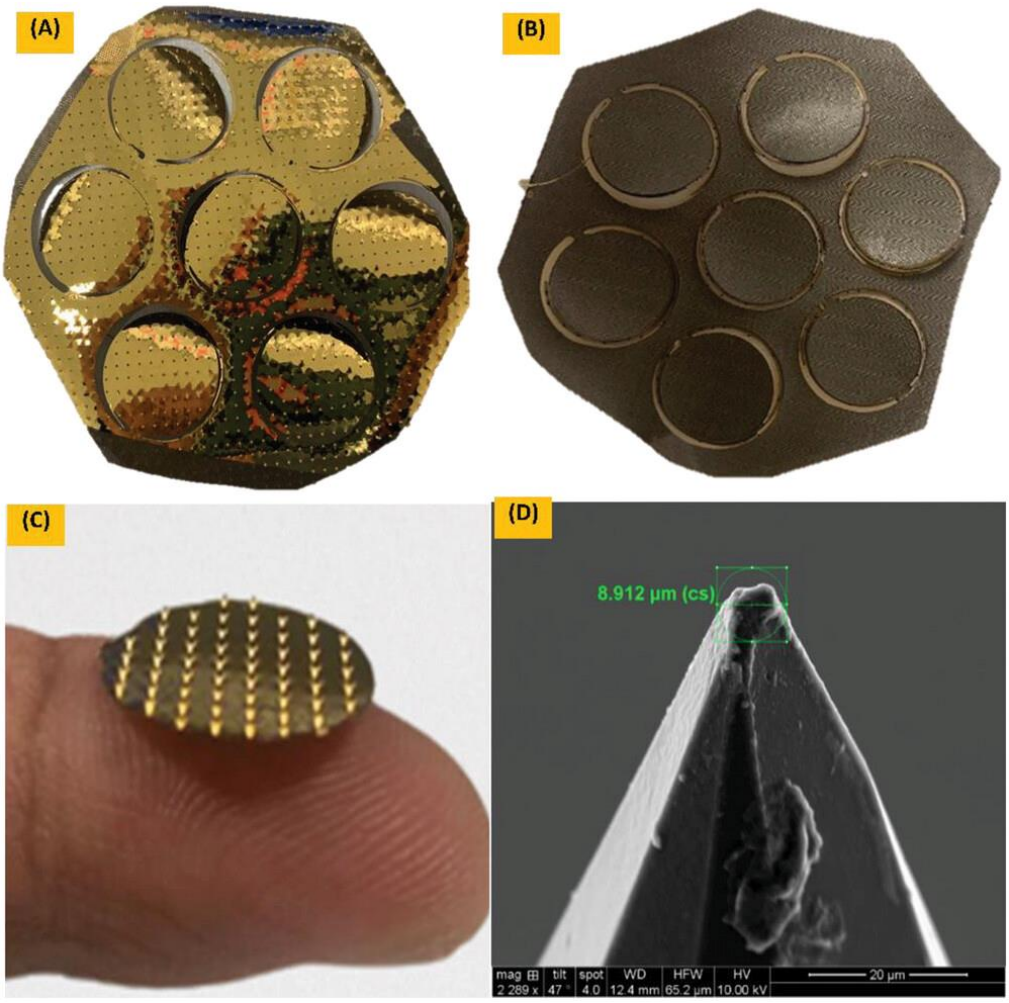


Figure 3. A) Front side of the metallized wafer; B) rear side of the conductive fabric (nonmetallized); C) image of the detached electrode; D) SEM image of 500 µm tall CF–MN microneedle array.

6.4.2 Mechanical Characterization

6.4.2.1 Flexibility Test

Figures 4A,B illustrate the experimental setup and the stress–strain curve concerning stretchability. In Figure 4B, it can be observed that three samples displayed a stretchability of (3.6 ± 0.6)%. Notably, Figure 4B shows a distinct reduction in stress at 11 N mm^{-2}, suggesting a failure in the fabric and epoxy. However, it is worth mentioning that the microneedles themselves remained intact, as depicted in the inset image of Figure

4A. Bending tests as shown in Figure 4C, D demonstrate that the electrodes may be deformed into shapes with small radii of curvature without damage or delamination of the materials. It should also be noted that forces or deformations such as those investigated here should never arise during routine application and use of the electrodes, thereby allowing for a significant margin of safety during normal wear.

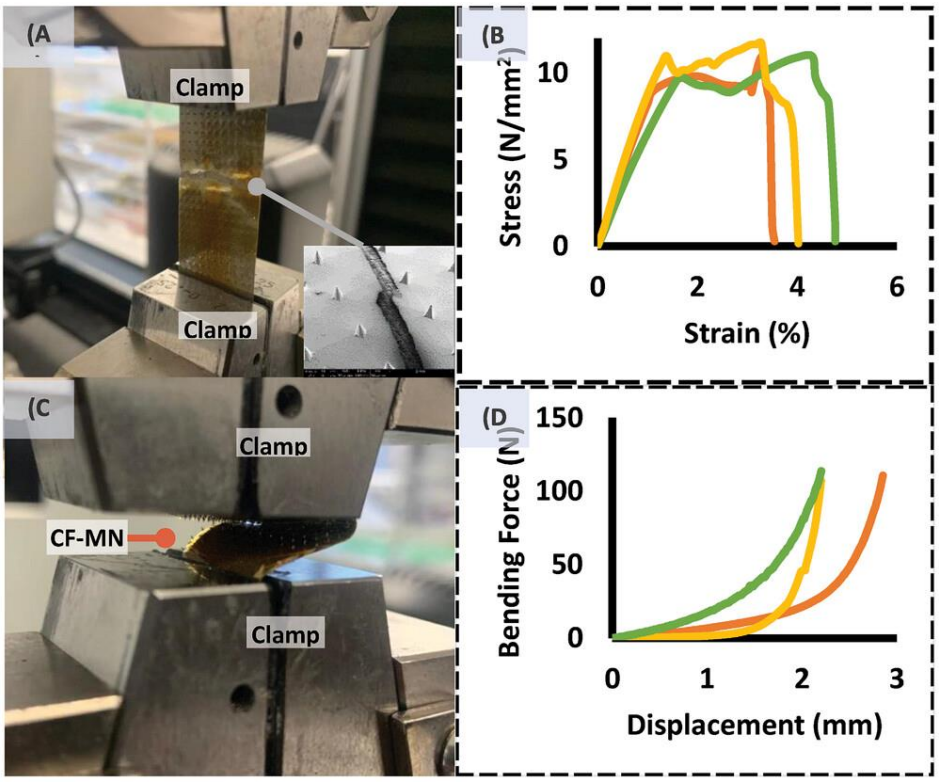


Figure 4. Illustration of the stretchability and bending tests. A) Experimental set-up for stretchability; inset: SEM Image after stretching of the sample; B) stress-strain relationship; C) experimental set-up for bending; D) force versus displacement curve of bending for one of the samples.

6.4.2.2 Compression Test

Compression force measurements were conducted on a 16-mm diameter array of 52 microneedles. The test revealed that microneedles remained intact even under forces significantly higher than those needed for skin penetration, as shown in Figure 5 (Left).

The combination of a polymeric microneedle tip and a strong flexible base prevented the microneedles from breaking, instead causing them to bend as shown in Figure 5 (Right).

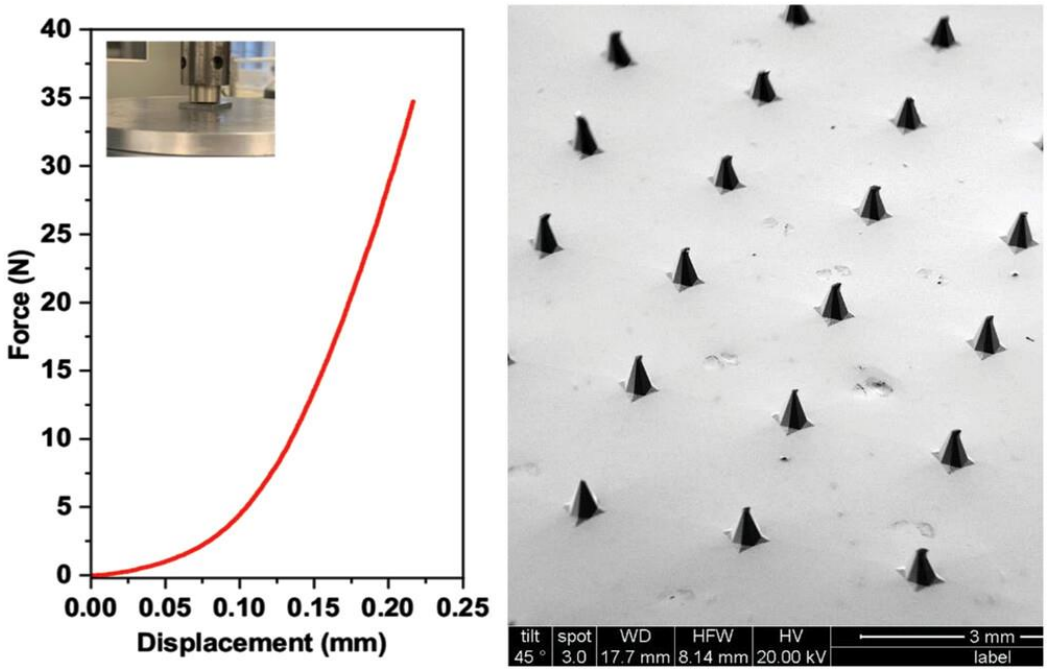


Figure 5. Representative examples of microneedle compression data. Left: force–displacement data obtained following compression of a CF–MN array using a cylindrical steel probe. Inset: experimental set-up. Right: post-compression SEM micrograph of the microneedles after application of a 35 N load to the array.

6.4.3 Skin Insertion Test

To verify skin penetration, 1% w/v methylene blue dye was applied to the skin after the insertion test and left for 2 h before being cleaned off. Methylene blue is a surgical dye with a high protein affinity, which binds to the epidermal tissue but not the hydrophobic *stratum corneum* layer. It is commonly used to assess microneedle penetration, as these blue marks indicate a successful breach of the *stratum corneum* layer. [40] In a sample of 16 microneedles, all 16 were able to penetrate the skin with a residual force of 5 N, indicating a 100% penetration efficiency, as shown in Figure 6. This suggests that a

maximum force of ≈ 0.31 N is required for a microneedle to penetrate the skin, which is in agreement with an earlier study. [36]

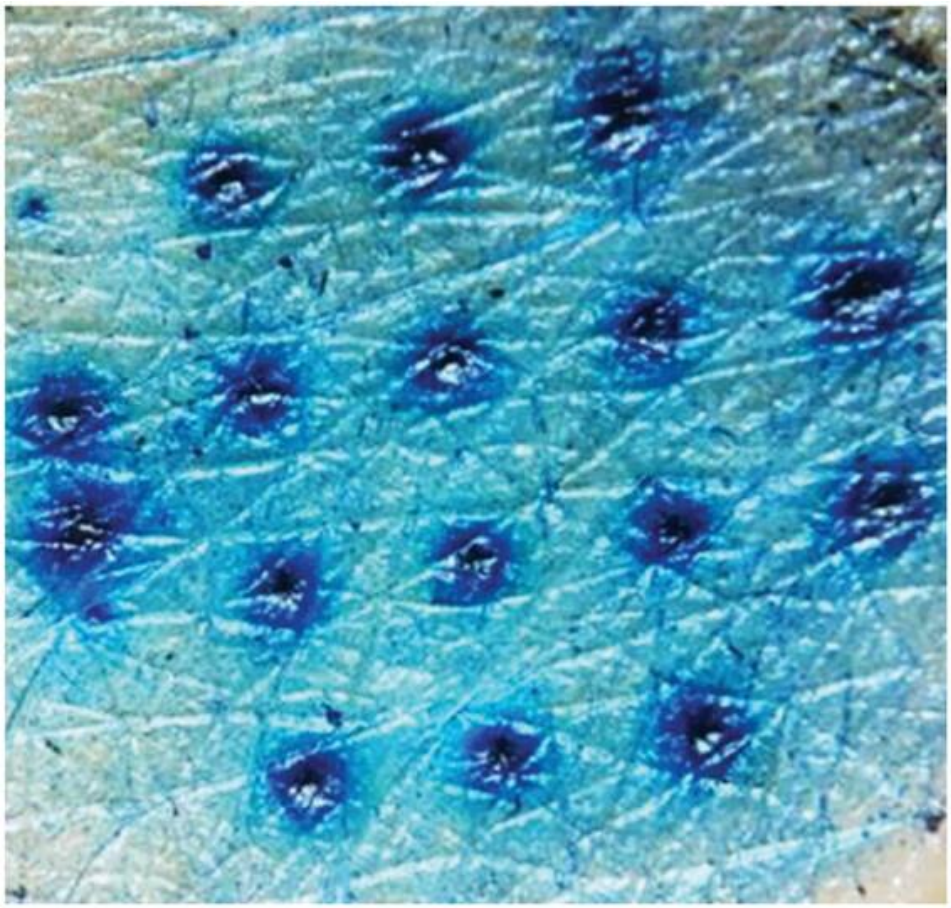


Figure 6. Skin penetration was assessed using methylene blue dye staining and an *ex vivo* human skin model: stained skin sample confirms successful microneedle penetration.

6.4.4 Electrical Characterization

6.4.4.1 Electrode Skin Impedance Measurement

The CF–MN electrode demonstrates a low impedance due to its microneedles effectively penetrating the highly resistant outer layer of the skin, known as the *stratum corneum* (SC). This penetration results in the formation of a coupling capacitance, which contributes to the overall impedance at the interface between the electrode and the skin. The impedance measurements were conducted within a frequency range of 20 Hz–1000

Hz, with data points collected at 20 Hz intervals. In Figure 7A, the impedance values (mean ± SE) obtained from six subjects using CF–MN and gel electrodes are displayed. Figure 7B illustrates the impedance values at specific frequencies, providing a clear representation of how the impedance changes as the frequency increases. To provide further insight, Figure 7C, D visually depict the appearance of microneedles after removal from one subject. Additionally, Figure S6A (Supporting Information) provides the impedance data for each individual subject.

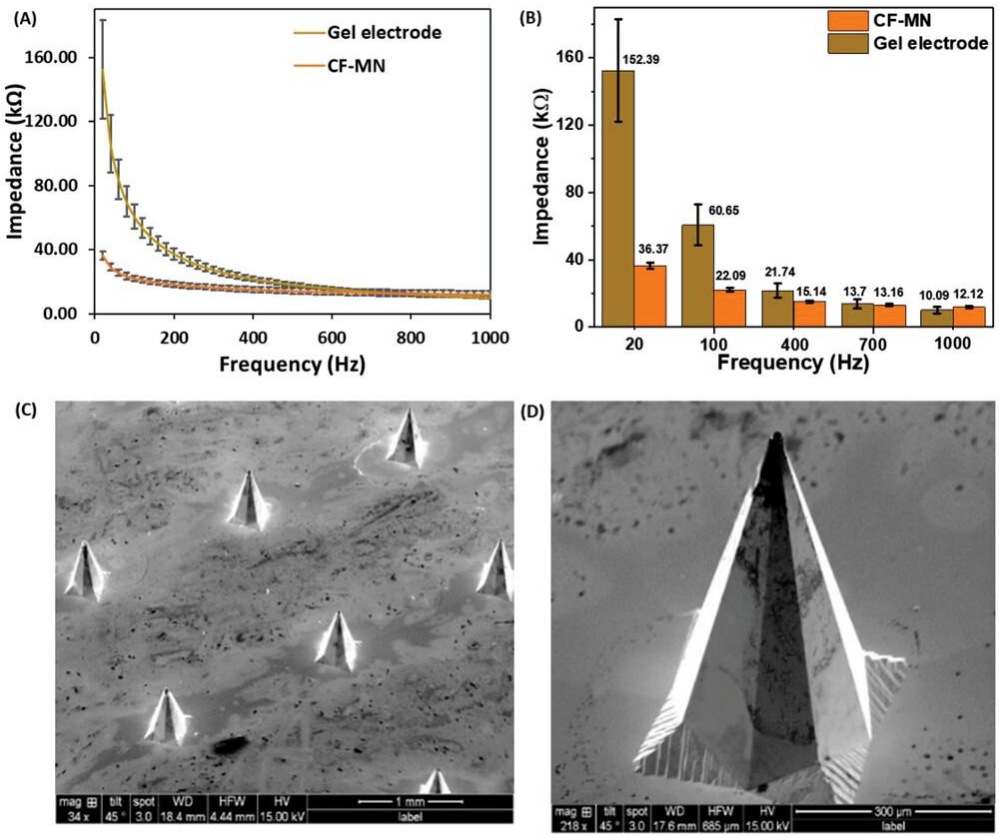


Figure 7. A) ESI spectra of clinical grade gel and CF–MN electrodes in the frequency range from 20 Hz to 1000 Hz with a step size of 20 Hz (n = 6 subjects, mean ± standard error); B) ESI values at specific spectra (n = 6 subjects, mean ± SE); C, D) SEM micrographs of the CF–MN electrode after ESI measurement.

The ESI analysis showed that the CF–MN electrodes with Au surface had superior performance compared to the gel electrodes, especially at low frequencies (≤ 700 Hz), with a lower estimated standard error. The impedance of both CF–MN and gel electrodes decreased with the increase in frequency. The microneedle structure and Au metallization contributed to an ESI of only (36.4 ± 2 kΩ) at 20 Hz for CF–MN electrodes, which was substantially lower than that of the gel electrode (152.4 ± 30 kΩ). Moreover, throughout the lower tested frequency range (<700 Hz), CF–MN electrodes consistently displayed lower total impedance than gel-based electrodes, and also had lower impedance values compared to previous studies [25], [26], [27], [30], [40], [41], [50], [54], and their dry nature makes them more suitable for long-term use. These advantages make CF–MN electrodes suitable for recording high-quality electrophysiological signals with short frequency ranges and low amplitude. [51]

6.4.4.2 Surface Resistance, and DC Offset Voltage

The surface resistance measured using a four-probe system (Figure S6B, Supporting Information) was ≈ 0.5 Ω, which is consistent with an earlier study. [52] This implies that the high conductivity of the Au metalized electrode allowed for high-quality signal recording. The schematic representation of the four-probe system for measuring surface resistance and DC offset voltage is illustrated in Figure S6B, C (Supporting Information), respectively. The wet electrode had a DC offset voltage of 12 mV, while the CF–MN electrodes exhibited DC offset voltages of ≈ 9 mV, which was lower than in an earlier study. [52]

6.4.4.3 Skin Compatibility Test

The materials used for CF–MN electrodes are biocompatible. A 48-h continuous test on a human volunteer showed no inflammation or allergies, and marks caused by the

microneedles disappeared within 30 min of removal (Figure S7, Supporting Information) which indicates the long-term usability of CF–MN electrode.

6.4.5 Electrophysiological Signal Measurement

Figure S8 (Supporting Information) illustrates the setup for ECG recording. As described in Section 16, seven activity states were considered and the data is shown in Figure 8. It is evident that the signals obtained from both types of electrodes exhibit a remarkable resemblance. The key features of the P, QRS, and T waves are clearly captured and visible under both static and dynamic conditions, with the exception of the ECG recorded at 6 km h^{-1}, where the P and T waves appear distorted and necessitate further processing. However, the R peak remains distinctly identifiable in this scenario. The Pearson correlation coefficient (r) [53] confirms that there is substantial similarity of more than 80% between the ECG signals acquired by the gel electrodes and the CF–MN electrodes across all activities, excluding walking at 6 km h^{-1}.

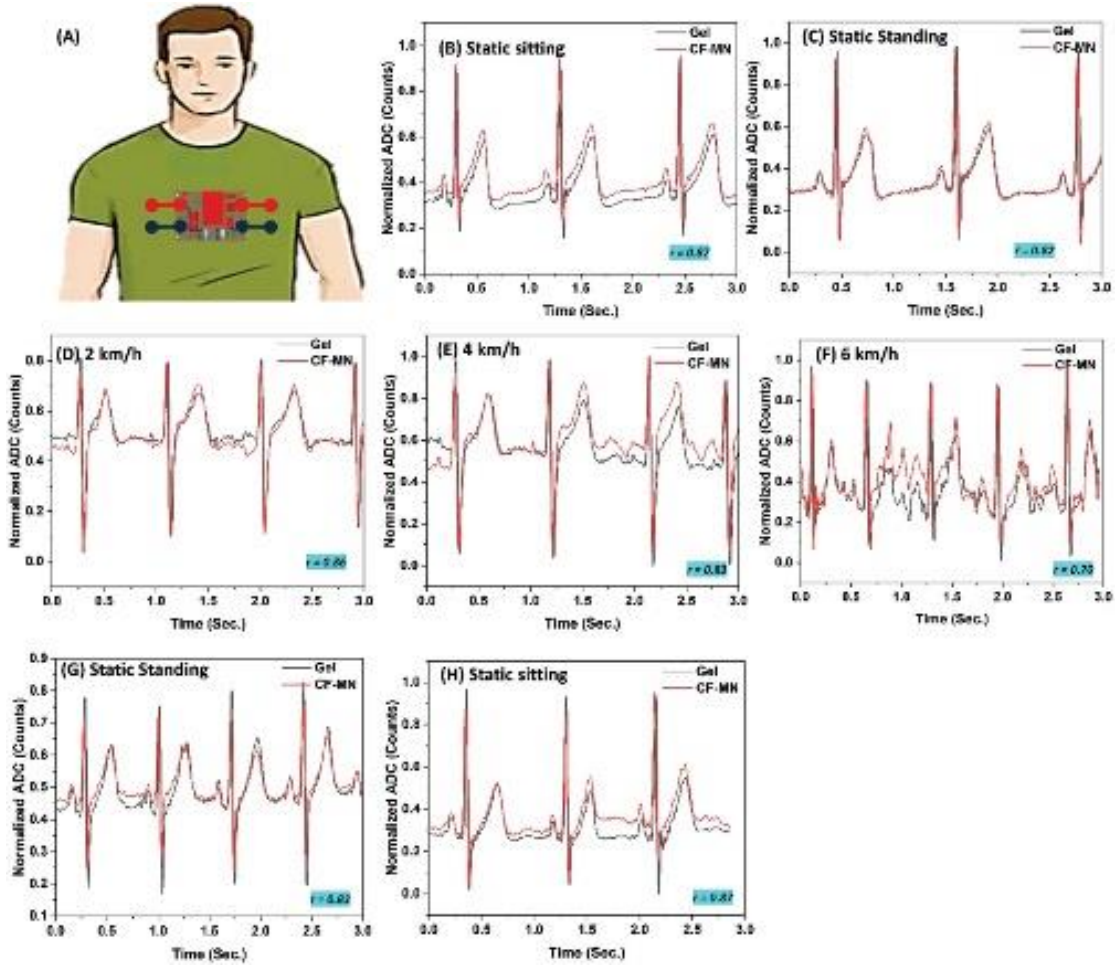


Figure 8. The 3 s segment of recorded ECG signal using CF–MN and gel electrodes of subject 1. A) Electrode placement scheme for ECG signal recording using CF–MN and gel electrodes. B) ECG signal in a sitting position before exercise, C) ECG signal when subject was standing on a treadmill before the exercise, D) ECG signal when subject was walking at 2 km h^{-1}, E) ECG signal when subject was walking at 4 km h^{-1}, F) ECG signal while subject walking at 6 km h^{-1}, G) ECG signal when standing on the treadmill after exercise, H) ECG signal when subject was sitting on a chair after exercise. r: linear correlation coefficient estimated for 3 s signal for distinct postures.

The slight variation in this particular case can be attributed to factors like motion artifacts, electrode movement, and muscle artifacts. Notably, the similarity observed during the sitting activity exceeds 87%, surpassing the findings of a recently published study. [54] These outcomes serve to affirm the effectiveness and efficiency of the newly developed electrodes. Figure 9A–C shows three quantitative methods for analysing the artifact level in recorded ECG: kurtosis, SNR, and standard deviation (SD) of QRS amplitude over a 15-s period. Data are presented in Figure 9A–C. All three methods indicate that CF–MN electrodes can acquire high-quality ECG signals. The overall mean kurtosis values, computed for all three subjects, for both wet and dry electrodes, were calculated across different activities.

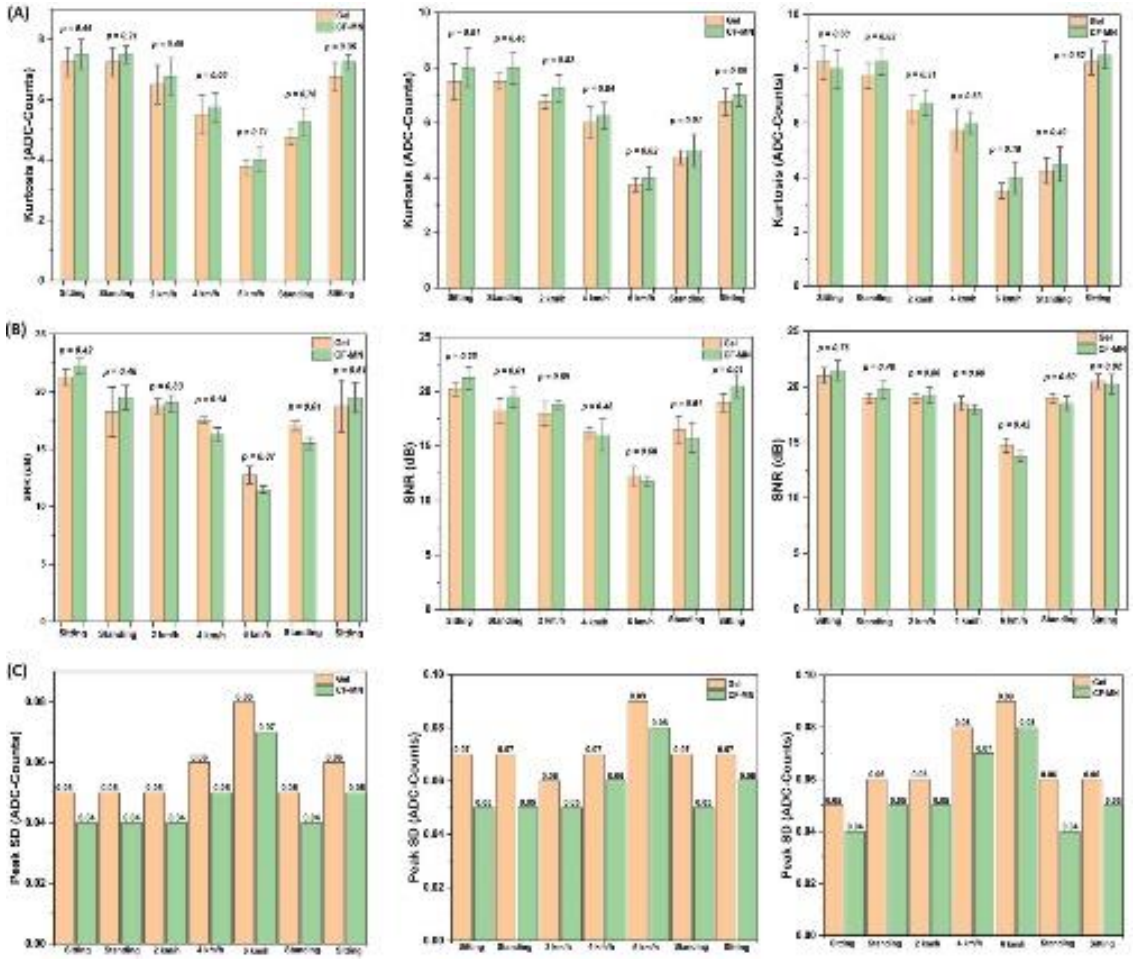


Figure 9. Quantitative comparison of 15 s of regular segments for each subject in sitting and standing positions before exercise, walking at speeds of 2, 4, and 6 km h^{-1}, and standing and sitting after exercise, from left to right, subject 1, 2, and 3; A) kurtosis estimated for each subject; B) SNR calculated for each subject; C) standard deviation (SD) of QRS complex for each subject.

Overall, the kurtosis values were generally higher for dry electrodes compared to wet electrodes. The kurtosis tended to decrease with increasing activity intensity, with the lowest values observed at the highest speed of 6 km h^{-1}. However, the kurtosis values increased after exercise, particularly in the standing and sitting positions. These findings

suggest that factors such as electrode type and activity level can influence the shape and distribution characteristics of the recorded ECG signals.

Based on the analysis presented in Figure 9A, the paired t-test results indicated no statistically significant difference ($p > 0.05$) in the average kurtosis values, except for certain cases. For subject one walking at 4 km h^{-1} and subject two in sitting and standing positions, higher kurtosis values were observed for the CF–MN electrodes. This could potentially be attributed to initial good contact with the skin and subsequent settling of the electrode against the skin over time.

The kurtosis values of the ECG signals recorded during various activities, except for walking at 6 km h^{-1} and subject three standing after exercise, were consistently higher than five. This suggests that the ECG signals remained relatively unaffected by artifacts like muscle interference, baseline wander, and power-line interference. However, for all subjects walking at 6 km h^{-1} and subject three standing after exercise, the kurtosis values were lower than five. This indicates that respiration and muscle activity had an impact on the ECG signals. Overall, the analysis demonstrates that the kurtosis values provide insights into the quality and characteristics of the ECG signals, with deviations observed in specific situations where factors like electrode settling and physiological activities influence the signal properties. The overall mean SNR, estimated for all three subjects, for both wet and dry electrodes varied across different activities.

The study found that motion artifacts had a significant impact on the ECG signal quality during physical activity (Figure 9B). The SNR tended to decrease with increasing activity intensity. As the speed increased, the ECG cycle became shorter, and signal quality tended to decrease due to myoelectric signals and noise from electrode friction, motion artifacts, and breathing, with the lowest values observed at the highest speed of 6 km h^{-1}. The CF–MN electrodes showed no statistically significant difference ($p \geq 0.05$) in SNR

compared to gel electrodes, except for subject one when walking at 6 km h^{-1} and standing after exercise, and subject two in a sitting position after exercise and standing before exercise, potentially due to the flexibility of the CF–MN electrode. However, the mean SNR values estimated for CF–MN were lower for all subjects when walking at 4, or 6 km h^{-1}, and standing on the treadmill, likely due to electrode displacement.

The mean SD values of the QRS complex for both wet and dry electrodes were also determined for various activities and exhibited slight variations across different activities and types of electrodes. The differences between wet and dry electrodes were minimal, with generally higher SD values observed at higher speeds. However, overall, the SD values remained relatively low, indicating that the shape and distribution characteristics of the recorded ECG signals were close to a normal distribution. These findings suggest that the influence of artifacts and nonstationary noise on the ECG signals was minimal, ensuring the quality and reliability of the recorded data. Overall, the study suggests that CF–MN-based dry electrodes can acquire clinically acceptable ECG signals during a range of activity levels.

Images were also taken to assess the impression left on the skin after removing the electrodes. Minor erythema marks (Figure 10A) were observed after the removal of both commercial and microneedle-based electrodes, consistent with previous findings. [41] These marks were highly transient and typically disappeared within 30 min as shown in Figure 10B. Digital microscopy images of CF–MN electrodes (Figure 10C,D) confirmed the microneedles' integrity without any signs of damage, detachment, or breakages during or after use.

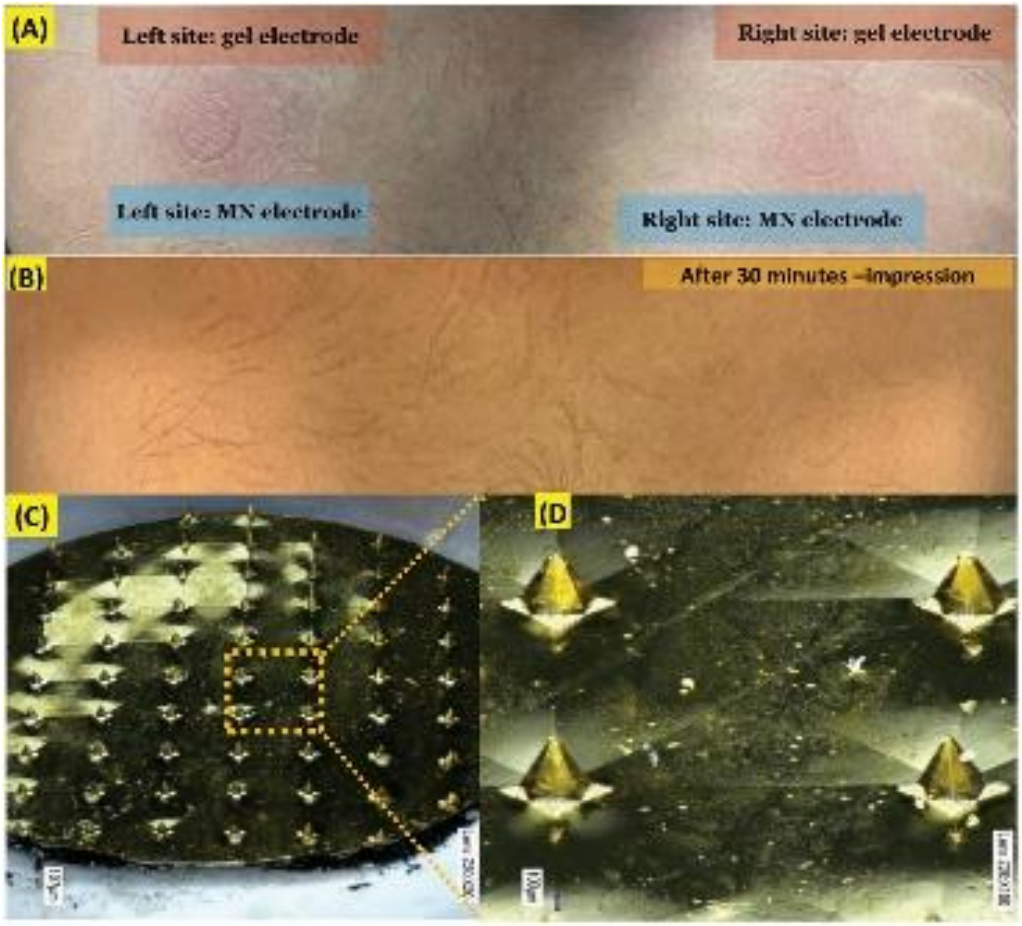


Figure 10. Effects of electrode wear on the skin: A) impressions on the chest of a subject immediately after removal of MN and gel electrodes; B) 30 min after removal of electrodes; C) 18 mm CF–MN flexible electrode after use; D) close-up view of four of microneedles, no deformation or breakage of the tip is observed.

For EMG recording as described in Section 17, the electrodes were placed on the forearm of the subjects (Figure 11A, see Figure S9, Supporting Information). Because the muscle activities were relatively intense, the raw data still showed obvious artifacts, and digital filtering methods were carried out to improve signal quality as described earlier. Figure 11B shows a ≈ 140 s segment recording, after filtering, that depicts EMG signals arising from the various hand and finger movements. Figure 11C illustrates the full rectified

signal. The calculated SNR values in Figure 11E were derived from the signal and noise regions.

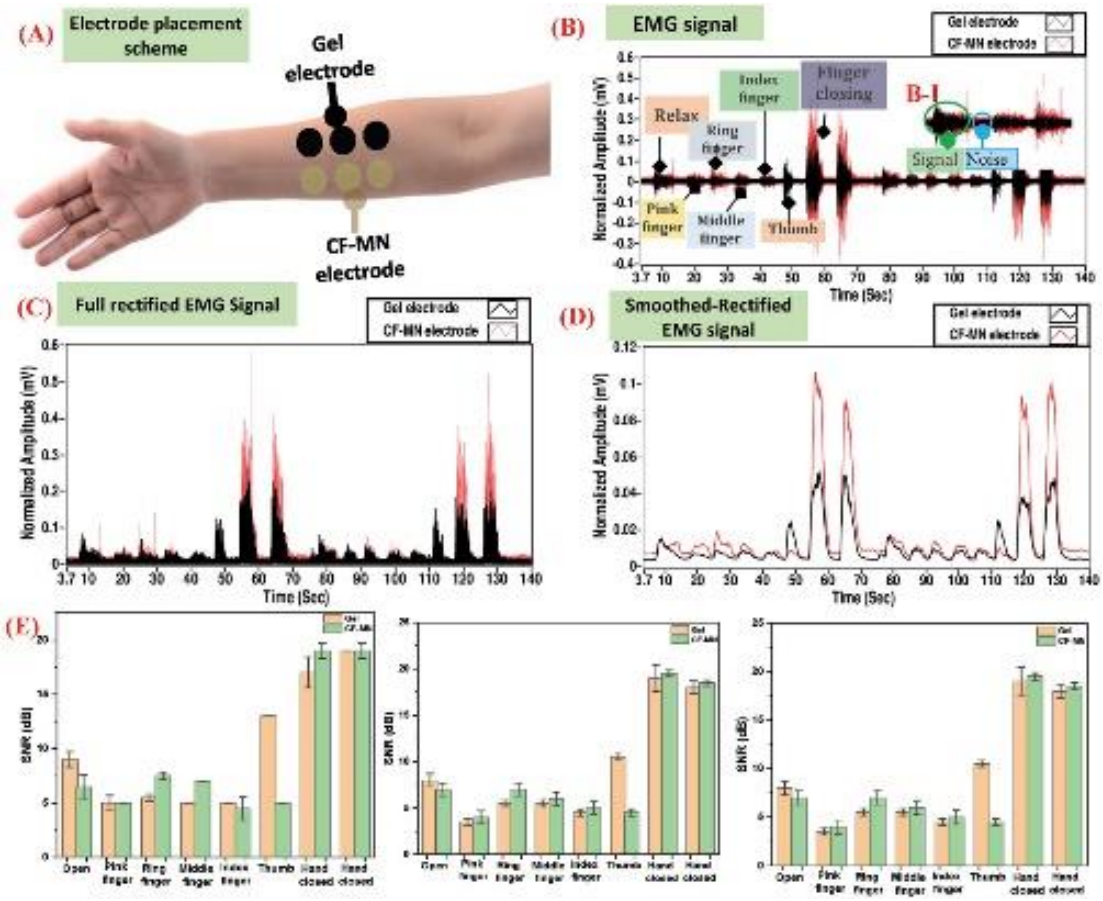


Figure 11. A) Electrode placed scheme on the forearm, B) Acquired EMG signal from eight gesture classes: hand open, pink finger extension, ring finger extension, middle finger extension, index finger extension, thumb extension, hand closed, C) Full rectified EMG signal, D) smooth EMG signal, each peak illustrates the distinct activities, E) SNR estimated for each subject while performing different activities.

As presented in Figure 11B–I inset, the CF–MN electrode exhibited an SNR comparable to that of commercial wet electrodes across all activities except for thumb movement. The reason for this is the inability to place both sets of electrodes close enough to simultaneously pick up the activity of the flexor pollicis longus (FPL) muscle of the

forearm, which is responsible for flexing the thumb. Nevertheless, the data suggests that the flexible CF–MN electrode can effectively record EMG signals associated with finger movements, followed by computationally inexpensive signal processing. The flexibility of the CF–MN allows it to conform closely to the muscles being monitored, enabling selective EMG signal recording and elimination of crosstalk. This is particularly important when multiple muscles are located in small spaces, making the flexible CF–MN a superior choice for EMG recording.

6.5 Conclusion

The CF–MN electrodes proposed in this work are suitable for wearable biopotential recording, and the acquisition of ECG and EMG signals has been demonstrated using customized electronic systems and a small sample of healthy volunteers. Using metrics such as SNR, SD of QRS complex, and kurtosis, it has been shown that these signals were comparable in quality to those obtained using conventional wet electrodes, but without the need for skin preparation or the use of wet gel. The low ESI, high mechanical strength, flexibility, and comfort of the CF–MN also represent significant performance advantages over standard wet electrodes and rigid microneedle electrodes. In addition, the use of a conductive textile as a rear backing layer means that metal deposition is required on just the front face of the electrode, thereby reducing metallization time and cost by 50% over comparable devices.

While no skin irritation or microneedle damage was observed during 48 h of wearing the electrodes during this assessment, longer-term studies will be necessary to fully evaluate their comfort and performance over extended periods. Future studies will include also involve recording electrophysiological signals from a greater number of subjects using CF–MN electrodes in order to gain further statistical proof of performance. It is also

anticipated that the performance of CF–MN electrodes can be enhanced by optimizing the assembly process and investigating the effects of electrode coating on the recording capabilities. Due to its high performance and low cost, this electrode shows potential for a wide range of applications, including sports and lifestyle monitoring, medical diagnostics, human-computer interaction, and long-term health assessments.

6.6 Supplementary Material

Supplementary material available in Appendix A.3.

6.7 References

[1] Y. Ling, T. An, L. W. Yap, B. Zhu, S. Gong, and W. Cheng, 'Disruptive, Soft, Wearable Sensors', *Adv. Mater.*, vol. 32, no. 18, p. 1904664, 2020, doi: 10.1002/adma.201904664.

[2] T. R. Ray *et al.*, 'Bio-Integrated Wearable Systems: A Comprehensive Review | Chemical Reviews', *Chem. Rev.*, vol. 119, pp. 5461–5533, 2019, doi: 10.1021/acs.chemrev.8b00573.

[3] Y. Wang *et al.*, 'Electrically compensated, tattoo-like electrodes for epidermal electrophysiology at scale', *Sci. Adv.*, vol. 6, no. 43, p. eabd0996, Oct. 2020, doi: 10.1126/sciadv.abd0996.

[4] "Arrhythmia". nhs.uk, 2018. Retrieved November 2022.

[5] K. R. Mills, 'The basics of electromyography', *J. Neurol. Neurosurg. Psychiatry*, vol. 76, no. suppl 2, pp. ii32–ii35, Jun. 2005, doi: 10.1136/jnnp.2005.069211.

[6] N. Wilke and A. Morrissey, 'Silicon microneedle formation using modified mask designs based on convex corner undercut', *J. Micromechanics Microengineering*, vol. 17, no. 2, p. 238, Dec. 2006, doi: 10.1088/0960-1317/17/2/008.

[7] C. D. Oster, Proper skin prep helps ensure ECG trace quality. 3 M Health Care, https://multimedia.3m.com/mws/media/358372O/proper-skin-prep-ecg-trace-quality-white-paper.pdf (accessed: July 2023).

[8] T. Wartzek, T. Lammersen, B. Eilebrecht, M. Walter, and S. Leonhardt, 'Triboelectricity in Capacitive Biopotential Measurements', *IEEE Trans. Biomed. Eng.*, vol. 58, no. 5, 2011, doi: 10.1109/TBME.2010.2100393.

[9] W. Li, R. N. Terry, J. Tang, M. R. Feng, S. P. Schwendeman, and M. R. Prausnitz, 'Rapidly separable microneedle patch for the sustained release of a contraceptive', *Nat. Biomed. Eng.*, vol. 3, no. 3, pp. 220–229, Mar. 2019, doi: 10.1038/s41551-018-0337-4.

[10] K. C. Tseng, B.-S. Lin, L.-D. Liao, Y.-T. Wang, and Y.-L. Wang, 'Development of a Wearable Mobile Electrocardiogram Monitoring System by Using Novel Dry Foam Electrodes', *IEEE Syst. J.*, vol. 8, no. 3, pp. 900–916, Sep. 2014, doi: 10.1109/JSYST.2013.2260620.

[11] R. Kaveh *et al.*, 'Rapid and Scalable Fabrication of Low Impedance, 3D Dry Electrodes for Physiological Sensing', *Adv. Mater. Technol.*, vol. 7, no. 11, p. 2200342, 2022, doi: 10.1002/admt.202200342.

[12] S. Park and S. Jayaraman, 'Smart textile-based wearable biomedical systems: a transition plan for research to reality', *IEEE Trans. Inf. Technol. Biomed. Publ. IEEE Eng. Med. Biol. Soc.*, vol. 14, no. 1, pp. 86–92, Jan. 2010, doi: 10.1109/TITB.2009.2025817.

[13] N. Meziane, J. G. Webster, M. Attari, and A. J. Nimunkar, 'Dry electrodes for electrocardiography', *Physiol. Meas.*, vol. 34, no. 9, p. R47, Aug. 2013, doi: 10.1088/0967-3334/34/9/R47.

[14] L. A. Geddes and M. E. Valentinuzzi, ‘Temporal changes in electrode impedance while recording the electrocardiogram with “Dry” electrodes’, *Ann. Biomed. Eng.*, vol. 1, no. 3, pp. 356–367, Mar. 1973, doi: 10.1007/BF02407675.

[15] C. Massaroni *et al.*, ‘Smart textile for respiratory monitoring and thoraco-abdominal motion pattern evaluation’, *J. Biophotonics*, vol. 11, no. 5, p. e201700263, 2018, doi: 10.1002/jbio.201700263.

[16] M. Alizadeh Meghrazi *et al.*, ‘Multichannel ECG recording from waist using textile sensors’, *Biomed. Eng. OnLine*, vol. 19, no. 1, p. 48, Jun. 2020, doi: 10.1186/s12938-020-00788-x.

[17] W. Lee and T. Someya, ‘Emerging Trends in Flexible Active Multielectrode Arrays’, *Chem. Mater.*, vol. 31, no. 17, pp. 6347–6358, Sep. 2019, doi: 10.1021/acs.chemmater.9b00165.

[18] S. Kusama *et al.*, ‘Transdermal electroosmotic flow generated by a porous microneedle array patch’, *Nat. Commun.*, vol. 12, no. 1, p. 658, Jan. 2021, doi: 10.1038/s41467-021-20948-4.

[19] K. T. M. Tran *et al.*, ‘Transdermal microneedles for the programmable burst release of multiple vaccine payloads’, *Nat. Biomed. Eng.*, vol. 5, no. 9, pp. 998–1007, Sep. 2021, doi: 10.1038/s41551-020-00650-4.

[20] D. Huang, J. Li, T. Li, Z. Wang, Q. Wang, and Z. Li, ‘Recent advances on fabrication of microneedles on the flexible substrate’, *J. Micromechanics Microengineering*, vol. 31, no. 7, p. 073001, Jun. 2021, doi: 10.1088/1361-6439/ac0513.

[21] L. Ren, B. Liu, W. Zhou, and L. Jiang, ‘A Mini Review of Microneedle Array Electrode for Bio-Signal Recording: A Review’, *IEEE Sens. J.*, vol. 20, no. 2, pp. 577–590, Jan. 2020, doi: 10.1109/JSEN.2019.2944847.

[22] M. Kim, T. Kim, D. S. Kim, and W. K. Chung, ‘Curved Microneedle Array-Based sEMG Electrode for Robust Long-Term Measurements and High Selectivity’, *Sensors*, vol. 15, no. 7, Art. no. 7, Jul. 2015, doi: 10.3390/s150716265.

[23] Y. Hou, Z. Li, Z. Wang, and H. Yu, ‘Miura-ori structured flexible microneedle array electrode for biosignal recording’, *Microsyst. Nanoeng.*, vol. 7, no. 1, Art. no. 1, Jul. 2021, doi: 10.1038/s41378-021-00259-w.

[24] R. Wang, X. Jiang, W. Wang, and Z. Li, ‘A microneedle electrode array on flexible substrate for long-term EEG monitoring’, *Sens. Actuators B Chem.*, vol. 244, pp. 750–758, Jun. 2017, doi: 10.1016/j.snb.2017.01.052.

[25] R. Wang, W. Zhao, W. Wang, and Z. Li, ‘A Flexible Microneedle Electrode Array With Solid Silicon Needles’, *J. Microelectromechanical Syst.*, vol. 21, no. 5, pp. 1084–1089, Oct. 2012, doi: 10.1109/JMEMS.2012.2203790.

[26] L. Ren *et al.*, ‘Flexible microneedle array electrode using magnetorheological drawing lithography for bio-signal monitoring’, *Sens. Actuators Phys.*, vol. 268, pp. 38–45, Dec. 2017, doi: 10.1016/j.sna.2017.10.042.

[27] L. Ren, K. Yu, and Y. Tan, ‘Monitoring and Assessing the Degradation Rate of Magnesium-Based Artificial Bone In Vitro Using a Wireless Magnetoelastic Sensor’, *Sensors*, vol. 18, no. 9, p. 3066, Sep. 2018, doi: 10.3390/s18093066.

[28] O. P. Singh, A. Bocchino, T. Guillerm, and C. O’Mahony, ‘Design, Fabrication and Performance Assessment of Flexible, Microneedle–Based Electrodes For ECG Signal Monitoring’, in *2022 44th Annual International Conference of the IEEE Engineering in Medicine & Biology Society (EMBC)*, Jul. 2022, pp. 846–849. doi: 10.1109/EMBC48229.2022.9871073.

[29] J. Li *et al.*, ‘High-Performance Flexible Microneedle Array as a Low-Impedance Surface Biopotential Dry Electrode for Wearable Electrophysiological Recording and Polysomnography’, *Nano-Micro Lett.*, vol. 14, no. 1, p. 132, Jun. 2022, doi: 10.1007/s40820-022-00870-0.

[30] F. Stauffer *et al.*, ‘Skin Conformal Polymer Electrodes for Clinical ECG and EEG Recordings’, *Adv. Healthc. Mater.*, vol. 7, no. 7, p. 1700994, 2018, doi: 10.1002/adhm.201700994.

[31] R. Bhandari, S. Negi, and F. Solzbacher, ‘Wafer-scale fabrication of penetrating neural microelectrode arrays’, *Biomed. Microdevices*, vol. 12, no. 5, pp. 797–807, Oct. 2010, doi: 10.1007/s10544-010-9434-1.

[32] H. Roh *et al.*, ‘Fabrication of High-Density Out-of-Plane Microneedle Arrays with Various Heights and Diverse Cross-Sectional Shapes’, *Nano-Micro Lett.*, vol. 14, no. 1, p. 24, Dec. 2021, doi: 10.1007/s40820-021-00778-1.

[33] K. Badnikar *et al.*, ‘Generic Molding Platform for Simple, Low-Cost Fabrication of Polymeric Microneedles’, *Macromol. Mater. Eng.*, vol. 305, no. 5, p. 2000072, 2020, doi: 10.1002/mame.202000072.

[34] F. Tjulkins *et al.*, ‘Towards Micropump- and Microneedle-based Drug Delivery using Micro Transdermal Interface Platforms (MicroTIPs)’, in *2022 44th Annual International Conference of the IEEE Engineering in Medicine & Biology Society (EMBC)*, Jul. 2022, pp. 3020–3023. doi: 10.1109/EMBC48229.2022.9871455.

[35] C. Plamadeala *et al.*, ‘Bio-inspired microneedle design for efficient drug/vaccine coating’, *Biomed. Microdevices*, vol. 22, no. 1, p. 8, Dec. 2019, doi: 10.1007/s10544-019-0456-z.

[36] S. P. Davis, B. J. Landis, Z. H. Adams, M. G. Allen, and M. R. Prausnitz, ‘Insertion of microneedles into skin: measurement and prediction of insertion force and needle fracture force’, *J. Biomech.*, vol. 37, no. 8, pp. 1155–1163, Aug. 2004, doi: 10.1016/j.jbiomech.2003.12.010.

[37] K. J. Krieger, J. Liegey, E. M. Cahill, N. Bertollo, M. M. Lowery, and E. D. O’Cearbhaill, ‘Development and Evaluation of 3D-Printed Dry Microneedle Electrodes for Surface Electromyography’, *Adv. Mater. Technol.*, vol. 5, no. 10, p. 2000518, 2020, doi: 10.1002/admt.202000518.

[38] L. Ren, Z. Chen, H. Wang, Z. Dou, B. Liu, and L. Jiang, ‘Fabrication of Bendable Microneedle-Array Electrode by Magnetorheological Drawing Lithography for Electroencephalogram Recording’, *IEEE Trans. Instrum. Meas.*, vol. 69, no. 10, pp. 8328–8334, Oct. 2020, doi: 10.1109/TIM.2020.2990523.

[39] K. Moussi, A. Bukhamsin, T. Hidalgo, and J. Kosel, ‘Biocompatible 3D Printed Microneedles for Transdermal, Intradermal, and Percutaneous Applications’, *Adv. Eng. Mater.*, vol. 22, no. 2, p. 1901358, 2020, doi: 10.1002/adem.201901358.

[40] J. Lozano and B. Stoeber, ‘Fabrication and characterization of a microneedle array electrode with flexible backing for biosignal monitoring’, *Biomed. Microdevices*, vol. 23, no. 4, p. 53, Oct. 2021, doi: 10.1007/s10544-021-00583-y.

[41] C. O’Mahony, K. Grygoryev, A. Ciarlone, G. Giannoni, A. Kenthao, and P. Galvin, ‘Design, fabrication and skin-electrode contact analysis of polymer microneedle-based ECG electrodes’, *J. Micromechanics Microengineering*, vol. 26, no. 8, p. 084005, Jul. 2016, doi: 10.1088/0960-1317/26/8/084005.

[42] O. P. Singh, Y. Hu, A. Bocchino, T. Guillerm, and C. O’Mahony, ‘Performance Assessment of Microneedle Dry and Wet Gel Electrodes Using a Dual-Channel,

Single Lead Wearable ECG Device', in *2022 IEEE 21st Mediterranean Electrotechnical Conference (MELECON)*, Jun. 2022, pp. 737–740. doi: 10.1109/MELECON53508.2022.9843060.

[43] C. E. KOSSMANN *et al.*, 'Recommendations for Standardization of Leads and of Specifications for Instruments in Electrocardiography and Vectorcardiography', *Circulation*, vol. 35, no. 3, pp. 583–602, Mar. 1967, doi: 10.1161/01.CIR.35.3.583.

[44] T. He, G. Clifford, and L. Tarassenko, 'Application of independent component analysis in removing artefacts from the electrocardiogram', *Neural Comput. Appl.*, vol. 15, no. 2, pp. 105–116, Apr. 2006, doi: 10.1007/s00521-005-0013-y.

[45] G. C. Clifford, F. Azuaje, and P. McSharry, *Advanced Methods and Tools for ECG Data Analysis*. Norwood, MA, UNITED STATES: Artech House, 2006. Accessed: Apr. 07, 2025. [Online]. Available: http://ebookcentral.proquest.com/lib/uccie-ebooks/detail.action?docID=338739

[46] M. S. Rodrigues *et al.*, 'Dry Electrodes for Surface Electromyography Based on Architectured Titanium Thin Films', *Materials*, vol. 13, no. 9, Art. no. 9, Jan. 2020, doi: 10.3390/ma13092135.

[47] H. J. Hermens, B. Freriks, C. Disselhorst-Klug, and G. Rau, 'Development of recommendations for SEMG sensors and sensor placement procedures', *J. Electromyogr. Kinesiol. Off. J. Int. Soc. Electrophysiol. Kinesiol.*, vol. 10, no. 5, pp. 361–374, Oct. 2000, doi: 10.1016/s1050-6411(00)00027-4.

[48] S. Liu *et al.*, 'The development and characteristics of novel microneedle arrays fabricated from hyaluronic acid, and their application in the transdermal delivery of insulin', *J. Controlled Release*, vol. 161, no. 3, pp. 933–941, Aug. 2012, doi: 10.1016/j.jconrel.2012.05.030.

[49] J.-H. Park, Y.-K. Yoon, S.-O. Choi, M. R. Prausnitz, and M. G. Allen, 'Tapered Conical Polymer Microneedles Fabricated Using an Integrated Lens Technique for Transdermal Drug Delivery', *IEEE Trans. Biomed. Eng.*, vol. 54, no. 5, pp. 903–913, 2007, doi: 10.1109/TBME.2006.889173.

[50] S. Md. Saleh, S. Md. Jusob, F. K. C. Harun, L. Yuliati, and D. H. B. Wicaksono, 'Optimization of Reduced GO-Based Cotton Electrodes for Wearable Electrocardiography', *IEEE Sens. J.*, vol. 20, no. 14, pp. 7774–7782, Jul. 2020, doi: 10.1109/JSEN.2020.2981262.

[51] C. Vidal Silva and V. Gatica Rojas, 'Design and implementation of a digital electrocardiographic system', *Rev. Fac. Ing. Univ. Antioquia*, vol. 55, pp. 99–107, 2010.

[52] M. F. Hossain, J. S. Heo, J. Nelson, and I. Kim, 'Paper-Based Flexible Electrode Using Chemically-Modified Graphene and Functionalized Multiwalled Carbon Nanotube Composites for Electrophysiological Signal Sensing', *Information*, vol. 10, no. 10, Art. no. 10, Oct. 2019, doi: 10.3390/info10100325.

[53] L.-D. Liao, I.-J. Wang, S.-F. Chen, J.-Y. Chang, and C.-T. Lin, 'Design, Fabrication and Experimental Validation of a Novel Dry-Contact Sensor for Measuring Electroencephalography Signals without Skin Preparation', *Sensors*, vol. 11, no. 6, Art. no. 6, Jun. 2011, doi: 10.3390/s110605819.

[54] Y. Liu, Y. Cheng, L. Shi, R. Wang, and J. Sun, 'Breathable, Self-Adhesive Dry Electrodes for Stable Electrophysiological Signal Monitoring During Exercise', *ACS Appl. Mater. Interfaces*, vol. 14, no. 10, pp. 12812–12823, Mar. 2022, doi: 10.1021/acsami.1c23322.

Chapter 7

Detection of Lactate via Amperometric Sensors Modified With Direct Electron Transfer Enzyme Containing PEDOT:PSS and Hydrogel Inks

Authors: Steffen Kurzhals, Eva Melnik, Paulina Plata, Esra Cihan, Peter Herzog, Alfons Felice, Andrea Bocchino, Conor O'Mahony, Giorgio C. Mutinati, Rainer Hainberger.

Journal: *IEEE Sensors Letters*, volume 7, article 4503104.

Publication Date: September 2023.

DOI: 10.1109/LSENS.2023.3307066

Contribution: I was responsible for developing and designing the sensors, characterised by one counter, one reference, and two working electrodes. Production and metallization was done using two of the modules of the core platform (Chapter 2). Subsequently, I chlorinated the silver reference electrode, forming Ag/AgCl, and cysteamine modified the working electrodes, facilitating the adhesion of the chemistry used to detect lactate. I have also developed the passivation technique (Chapter 3) and designed the geometrical layout of the film. The technique was then refined by AIT with laser cutting. AIT was also responsible for the biofunctionalization and testing of the sensors. The majority of these contributions are presented in Sections 7.3.2 and 7.3.4.

This exemplar is also the most complex out of the presented use cases.

Finally, I have also contributed to the writing and the reviewing of the paper.

Chapter shared from below link under the Creative Commons license 4.0 (CC BY-NC-ND 4.0). The Section numbers, Figures/Tables/References style has been adapted to conform to the style and numbering of the thesis.

https://ieeexplore.ieee.org/document/10225692

Link to license:

https://creativecommons.org/licenses/by-nc-nd/4.0/

7.1 Abstract

In this letter, we present amperometric sensors based on direct electron transfer (DET) enzyme for the detection of lactate, which is an important medical parameter present in blood and interstitial dermal fluid (ISF). For measurement in blood, we present a planar screen-printed biosensor with carbon working electrodes, whereas for the intended measurement in ISF, we investigated platinum-metallized epoxy microneedle sensors. On both sensor types, a bioink was applied, consisting of a DET enzyme mixed with poly(3,4-ethylenedioxythiophene) polystyrene sulfonate. As a second layer, a hydrogel layer is deposited to hold the enzyme on site. Local modification of the platinum microneedle sensors was performed by non-contact spotting. The developed modification enables the detection of lactate at a potential of 0 V with response times of 500–700 s. For carbon sensors, a limit of detection of 0.12 mM lactate was determined, and two linear ranges of 0.3–5 and 10–50 mM were observed with sensitivities of 319 and 9.6 nA/(mm^2 mM), respectively. For locally modified platinum microneedle sensors, two linear ranges of 0.3–2.5 and 5–30.5 mM were observed with sensitivities of 322.5 and 3.7 nA/(mm^2 mM), respectively. Given the low sensitivities in the higher concentration range, saturation for carbon sensors and locally modified platinum microneedle sensors starts at 10 and 5 mM lactate, respectively. Thus, both sensors allow sensitive measurements in the lower concentration range. Current densities at saturating lactate concentration are higher on freshly prepared carbon electrodes with 1.80 µA/mm^2 (10 mM) compared to platinum microneedle electrodes with 0.75 µA/mm^2 (10 mM) with full electrode modification. For platinum microneedle electrodes with optimized, dried local microneedle modification, a current density of 0.95 µA/mm^2 (5 mM) was measured. Detection of lactate in whole blood was demonstrated on carbon sensors, showing increasing currents after exercise, correlating with higher blood lactate levels, measured with a test strip reference system.

7.2 Introduction

L-lactate is an important marker in healthcare [1] and sports medicine [2], [3]. For sports medical purposes, a broad concentration range needs to be covered for lactate in blood, with levels at rest in the range of 0.5–1.5 mM and up to 25 mM under extreme exercise conditions [1], [3]. To allow for widespread use, mobile diagnostic devices suitable for blood lactate detection at the point-of-care are required. Electrochemical sensors [4] are well suited for this purpose, as they combine low production costs such as screen-printing with the possibility of small read-out devices. With the trend for non- or minimally invasive diagnostics, other body fluids are also of interest for lactate detection, such as interstitial dermal fluid (ISF), which can be accessed via microneedle technology [5], [6], [7], [8]. Early devices for lactate detection were based on lactate oxidase, requiring potentials of 0.7 V to detect generated hydrogen peroxide [5], [6]. With the development of direct electron transfer (DET) enzymes [9], [10], detection at significantly lower potentials can be performed, making the sensors more robust against electrochemical interferences. Amperometric sensors using DET lactate enzymes were reported in the literature [8], [11]. Freeman et al. [8] deposited DET lactate mixed with carbon inks on gold microneedles. Hiraka et al. [11] immobilized the DET-enzyme via polyethylene imine and polyethylene glycol (PEG) diglycidylether on planar MWCNT-modified gold electrodes. Detection of lactate was possible in these two reports at potentials of 0.2 V and 0.15 V versus AgCl, respectively. In both cases, a cellulose acetate film on top of the enzymatic layer was necessary to widen the linear range. Examples of DET lactate immobilization on environmentally more friendly platinum [12] electrodes were not found in the literature. To address the diagnostic needs for the detection of lactate in blood and ISF and reduce the environmental impact, we aim for two amperometric biosensors: 1) carbon screen-printed sensors for a fast single measurement of lactate in blood and 2)

platinum-metallized microneedle-based sensors for minimally invasive continuous monitoring of lactate in ISF. Functionalization should be done with a DET enzyme poly(3,4-ethylenedioxythiophene) polystyrene sulfonate (PEDOT:PSS) bioink covered with a protective hydrogel layer [15], which should enable biocompatible measurements at low potentials [13], [14]. We also report on an up-scalable dispensing process method for local microneedle functionalization: a topic often neglected in biosensing publications.

7.3 Materials and Methods

7.3.1 Materials

Lactazyme (DET), a recombinant enzyme derived from the previously characterized DET enzyme fcb2 [9], [10], was provided by DirectSens GmbH as stock solutions in phosphate buffer and stored at −20 °C. Proof of DET properties of the used enzyme were previously reported by Freeman et al. [8]. PEDOT:PSS (1.1wt%, neutral pH, high conductivity), cysteamine hydrochloride, glycerol, PEG dimethacrylate (PEG-DMA) (10 kDa), diethyleneglycol vinylether (DEGVE), lithium-phenyl-2,4,6-trimethylbenzoyl-phosphinate (LAP), and hypochlorite solution were purchased from Sigma Aldrich. ARcare 7759 was purchased from Adhesives Research. AgCl paste Loctite EDAG 7019 was purchased from Henkel.

7.3.2 Sensors

Figure 1 shows the two sensor types used in this letter. Screen-printed planar sensors with carbon counter electrode (CE), Ag/AgCl reference electrode (RE), and four carbon working electrodes (WE) (area: 0.74 mm^2) were provided by SCIO Holding GmbH, Linz, Austria. Metallized epoxy microneedle sensors (height 500 µm) were provided by

Tyndall National Institute, Cork, Ireland. Front-to-back connections (< 10 Ω) were enabled by filling the via holes with AgCl paste from Henkel. WEs, CE, and backside connection areas were metallized with platinum. REs were metallized with silver and then chlorinated by pipetting a 15% (v/v) sodium hypochlorite aqueous solution on the silver layer using an incubation time of 10 s, followed by a water rinsing step for cleaning.

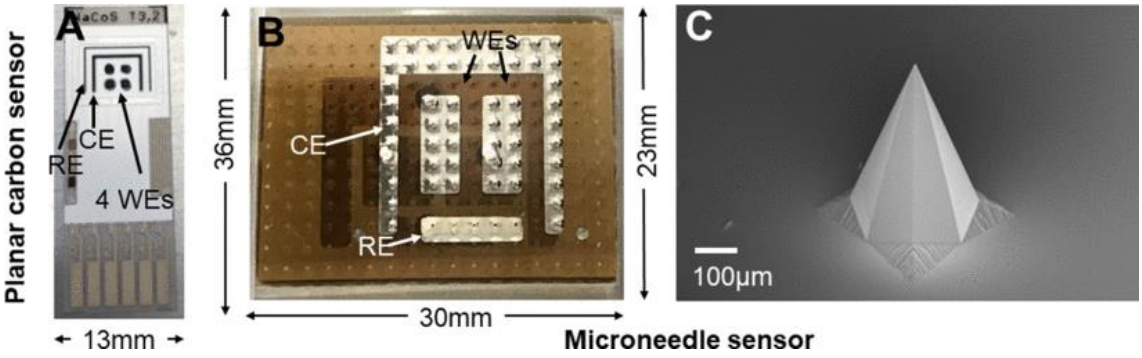


Figure 1. Images of sensor types used in this work. (a) Screen-printed planar sensor. (b) Microneedle sensor with ten microneedles per WE. (c) SEM image of platinum metallized microneedle.

7.3.3 Ink Preparation

The DET-PEDOT:PSS ink was prepared by mixing PEDOT:PSS 16.1% (v/v), water 20.7% (v/v), and a DET solution in different concentrations (63.2% (v/v)) in low protein binding Eppendorf vials to obtain 1–7.2 mg/mL DET enzyme in the ink. The hydrogel precursor ink was prepared by dissolving PEG-DMA in water (166.7 mg/mL) and mixing 30% (v/v) of this solution with DEGVE (60% (v/v), water (8% (v/v)), and LAP solution (2% (v/v)). LAP solution was prepared by dissolving 10 mg LAP in a mixture of 50 µL water and 50 µL ethanol under ultrasonication. After deposition of the hydrogel precursor ink on the sensor surfaces, the sensors were placed in a UV crosslinker (UVP CL-1000), (365 nm) and irradiated with 1 J/cm^2. After cross-linking, the sensors were washed with physiological PBS for 5 min and again for 10 min with fresh PBS.

7.3.4 Sensor Preparation

For the screen-printed sensors, a volume of 0.5 µL DET-PEDOT:PSS ink was manually drop cast twice on each WE. After each application, the layers were dried. Then, 15 µL of the hydrogel precursor ink was pipetted on the whole WE array. In the case of the microneedle sensors, the platinum WEs were treated with cysteamine hydrochloride solution (104 mg in a mixture of 7.6 mL physiological PBS and 2.4 mL glycerol) for improved adhesion of the DET-PEDOT:PSS. The microneedle sensors were modified on the WEs either by pipetting or by non-contact spotting with a BioDOT AD1520 dispenser (ceramic tip, orifice 190 µm). For sensors modified by pipetting, 18.7 µL of DET-PEDOT:PSS were manually drop cast twice on each WE, letting the ink dry after each layer. Then, 20 µL hydrogel ink was applied on each WE and cured and washed as described. For BioDOT dispensing, either the full WE or only the microneedles were modified. In the case of the full WE modification, 18 µL of DET-PEDOT:PSS were dispensed twice on each WE, letting the ink dry after each layer. Then, 20 µL hydrogel precursor ink was dispensed on each WE, cured, and washed as described. For the local modification of the microneedle sensors, they were first passivated using an ARcare 7759 passivation film [7]. The film had a regular hole pattern (*x*, *y* distance 1.75 mm, average hole diameter 764 µm) to leave the microneedles non-passivated. This hole pattern was fabricated with a laser cutter Speedy 360 from Trotec, Marchtrenk, Austria. For local modification, four layers of DET-PEDOT:PSS (4 × 150 nL per needle, with 10 min drying between the layers) were deposited on the WE microneedles. In a second step, the hydrogel precursor ink was dispensed on the WE microneedles and the microneedle row between (two layers of 2 × 250 nL per microneedle, in total 25 µL). After curing and washing the hydrogel layer with ultrapure water, the sensors were dried in a vacuum for

1 h and kept in a closed desiccator for a further 2 h. The sensors were then stored in aluminum bags with desiccant at 4 °C until measurement.

7.3.5 Electrochemical Lactate Measurement

The sensors were characterized by a lactate concentration series in physiological PBS. Chronoamperometric measurements in PBS and blood were performed at 0 V versus AgCl with the sensors connected to an Emstat3 4WE potentiostat from PalmSens. Measurements were performed at an interval of 0.5 s with the Multitrace 4.4 software. For the screen-printed sensors, measurements were started with 80 µL physiological PBS. After 500 s, the PBS buffer was replaced with lactate standards in 500 s intervals by carefully pipetting off the previous solution. For the microneedle sensors, measurements were started with 500 µL physiological PBS. After 700 s, the PBS buffer was replaced with lactate standards by careful pipetting off the previous solution. Current values were obtained by averaging the last 100 s before applying the next lactate standard. For measuring lactate in blood on screen-printed sensors, first, a calibration curve was generated by measuring lactate standards in physiological PBS (0.3, 1, 2.5, 5, 10, and 20 mM, one standard/sensor). To characterize the sensors, anonymized blood samples were collected at AIT-Molecular Diagnostics from finger pricks of volunteers, before and after light exercise. The collected blood was pipetted on dry sensors. Measurements were performed with 8 s equilibration time, 10 s run time, and averaging the last 5 s. For comparison, collected blood was also measured with the Roche Accutrend Plus lactate detection system.

7.4 Results

7.4.1 Screen-Printed Sensors: Ink Formulation and Optimization

In the first step, the DET-PEDOT:PSS ink was optimized by determining the highest enzyme concentration that still gave a stable ink formulation. Inks with more than 7.2 mg/mL DET enzyme started to precipitate very fast. Therefore, inks with 1, 3, 5, and 7.2 mg/mL were prepared and quickly screened by measuring lactate concentrations ranging from 0–50 mM on freshly prepared sensors with one WE/DET concentration [see Figure 2(a)] at 0 V versus AgCl. The current curves for 3, 5, and 7.2 mg/mL of DET enzyme exhibited two quasi-linear ranges, the first from 0.3–5 mM reaching a maximum of ~ 2 μA/mm^2 and the second from 10–50 mM. Sufficient current densities with short equilibration times could be achieved with DET-PEDOT:PSS inks comprising ≥ 5 mg/mL of the DET enzyme, although sensors prepared with a DET enzyme concentration of 7.2 mg/mL performed slightly poorer than with 5 mg/mL. For sensors with 1 mg/mL DET concentration, only very low currents (50 mM gave 47.5 nA/mm^2) were measured. Due to the high currents of the 5 mg/mL ink and the instability of the 7.2 mg/mL ink (which started to precipitate a few minutes after mixing), the 5 mg/mL ink was chosen for further studies. Measurements with the 5 mg/mL ink averaging four WEs [see Figure 2(b)] confirmed the quick screening results with the two quasi-linear ranges with sensitivities of 319 nA/(mm^2 mM) for 0.3–5 mM and 9.6 nA/(mm^2 mM) for 10–50 mM. Given the standard deviation in the higher concentration range, sensor saturation starts at 10 mM lactate. A limit of detection (LOD) of 0.12 mM was calculated. Measurements of 10 mM lactate on screen-printed sensors with and without hydrogel showed currents in the range of ~ 1 μA and 2 nA, respectively, proving that the hydrogel is crucial to keep the enzyme immobilized and prevent washout. The storability of the sensors was tested

by measuring 10 mM lactate using freshly prepared sensors and using sensors that were dried and then stored for 0–8 weeks at 4 °C. After 1 week of storage, the current dropped to 46% of the current of freshly prepared sensors. A further decrease in current is seen over 4 weeks to 32%. After 4 weeks, the current stays constant for at least up to 8 weeks. The initial steep current drop was mainly caused by the drying process, which could be confirmed by measuring freshly prepared sensors before and after drying.

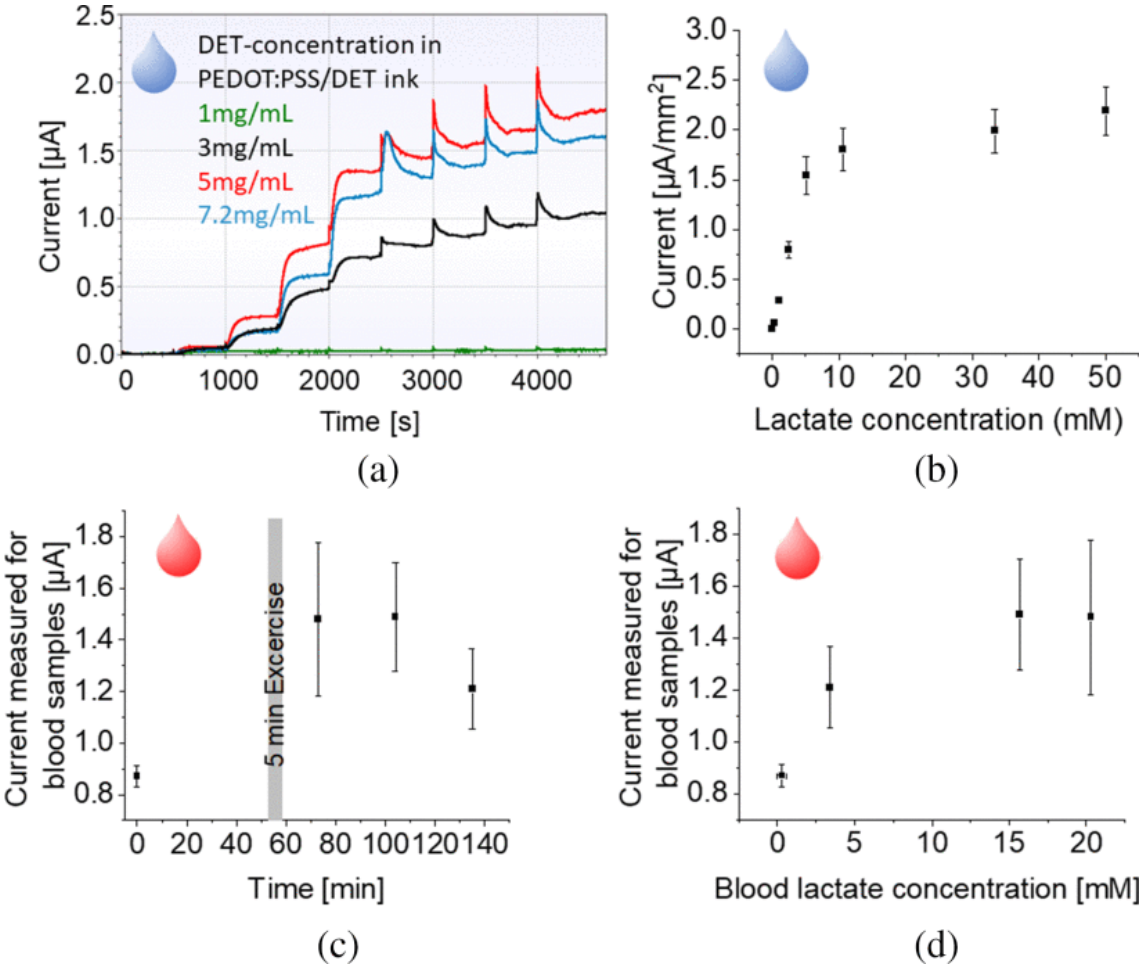


Figure 2. (a) Chronoamperometry (0 V versus AgCl) with different DET concentrations and 0-50 mM lactate in PBS. (b) Averaged current values (n = 4) versus lactate concentration with 5 mg/mL DET. (c) Time evolution of averaged currents (n = 2) for measured blood samples before and after exercise. (d) Correlation of currents measured versus blood lactate concentrations detected with the Roche Accutrend Plus.

7.4.2 Measurement of Lactate in Blood

For measurements in blood, a quick measurement procedure was adopted. The sample liquid was applied to the dried sensors and the measurement was run for 10 s. First, a calibration curve was created by measuring a concentration series (six lactate standards, 0.3–20 mM) with one lactate standard per sensor. A saturation of the signal could be found for a lactate concentration around 5–10 mM. For one volunteer, currents on screen-printed sensors and blood lactate concentrations via test strips were measured with blood samples collected before and starting 15 min after 5 min of light exercise. Baseline levels of blood lactate were below the detection limit of the test strip system (< 0.6 mM). Blood lactate levels up to 20.3 mM were measured after exercise. The current increased after exercise and then decreased, although not reaching the baseline level in the recorded time frame [see Figure 2(c)]. A correlation between measured currents and blood lactate levels is observed; however, a distinction between blood lactate concentrations of 15 and 20 mM was not possible due to the lower sensitivity in the higher concentration range [see Figure 2(d)]. Still, lactate measurements in whole blood could be demonstrated, showing the compatibility of the biofunctionalization with the complex body fluid, especially the developed hydrogel that prevents electrode blocking by cellular components in whole blood.

7.4.3 Microneedle Sensor Modification

In the first step, it was investigated if manually drop cast layers and layers applied with a BioDOT dispenser exhibited similar characteristics to ensure that the ink was not impacted by the deposition process. The measurement of lactate concentrations (0–80 mM lactate) showed a good match between the different processes. Currents for lactate concentrations of 10–80 mM were on average 15% higher for dispensed layers compared

to manually drop cast layers. Current densities measured for 10 mM lactate on a freshly prepared microneedle sensor (WE area of 25 mm^2) were in the range of 0.75 $\mu A/mm^2$ and, thus, lower compared to current densities on screen-printed carbon sensors with 1.80 $\mu A/mm^2$. Since only the microneedles will enter the skin and the modification of the area between the microneedles is prone to interaction with sweat under *in vivo* conditions, which would result in interference currents, we investigated a local functionalization of the microneedle tips. To define the microneedle area for modification, the sensor was passivated with a biocompatible film as described in Section 7.3.4. Four layers of 150 nL DET-PEDOT:PSS ink were dispensed in a 5 × 2 drop pattern on the needles of each of the two WEs per sensor. This resulted in a clean drop pattern, with the ink kept at the microneedle location with only low amounts of ink outside of the hole in the passivation film [see Figure 3(a)]. For the hydrogel layer, 1000 nL of precursor ink were dispensed on each needle of the WE, resulting in a hydrogel film that covered the entire area and prevented a washout of the DET enzyme from the PEDOT-PSS matrix.

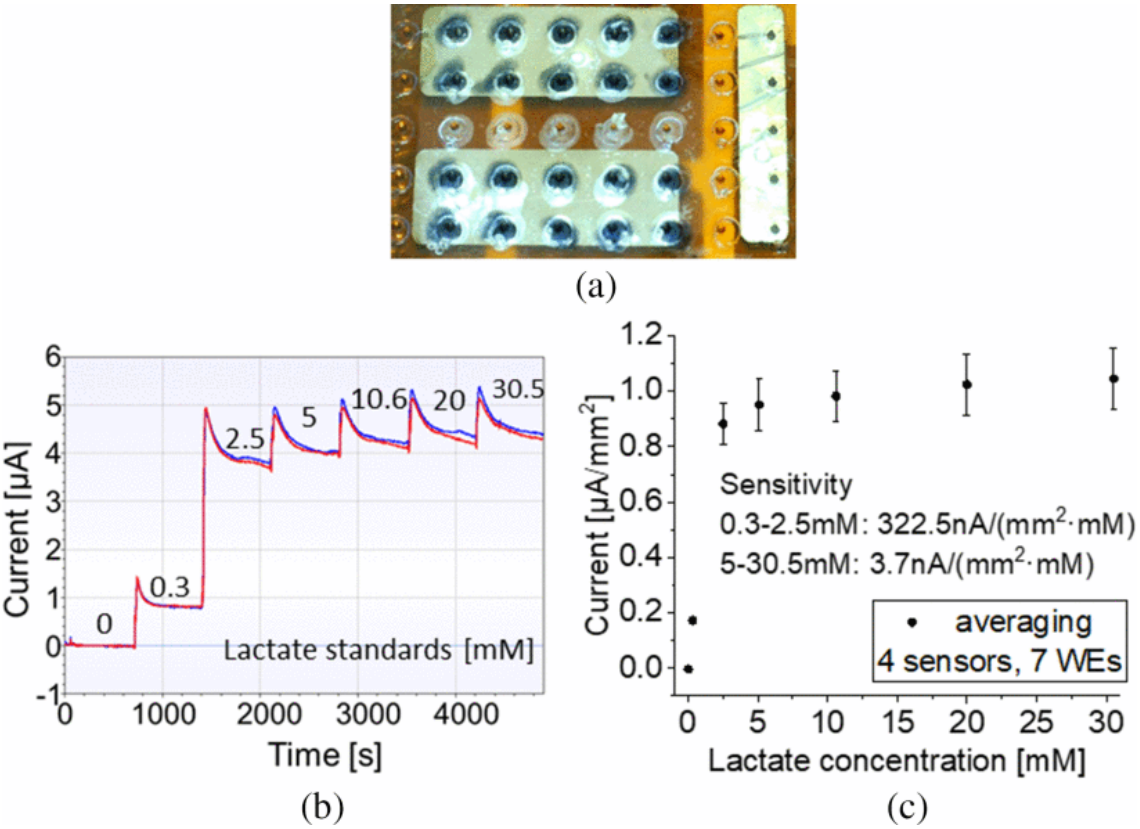


Figure 3. (a) Passivated, locally functionalized microneedle sensor (ten microneedles/WE), WEs and RE shown, rotated 90°. (b) Chronoamperometric curves for a microneedle sensor with two WEs at 0 V versus AgCl. (c) Calibration curve averaging seven WEs from four sensors, 0–30.5 mM lactate in PBS.

7.4.4 *In Vitro* Measurements of the Locally Functionalized Microneedle Sensor

After washing and drying, sensors were characterized by measuring lactate concentrations of 0–30.5 mM in PBS [see Figure 3(b)]. A baseline stabilization for the platinum microneedle sensors was achieved in the range from 500 to 1200 s. The current stabilization was improved compared to the modification covering the full electrode area, especially for higher lactate concentrations, and could be performed within 700 s. Similar to the screen-printed sensors, two linear ranges were found with different sensitivities,

the first ranging from 0.3 to 2.5 mM and the second ranging from 5 to 30.5 mM [see Figure 3(c)]; however, given the low sensitivity and the standard deviation for this second range, saturation at 5 mM can be stated. Current densities for 5 mM are in the range of 0.95 $\mu A/mm^2$ for the local modification and thus higher than for sensors with full electrode modification at a concentration of 10 mM, which we attribute to the optimized hydrogel washing with ultrapure water instead of PBS. Averaging seven WEs measured on four sensors [see Figure 3(c)] gave a calibration curve with coefficients of variations for the measurement signal of 0.075–0.107, showing good reproducibility of the dispensing process, which is a promising result for the intended *in vivo* measurements.

7.5 Conclusions

Two amperometric enzyme sensors based on direct electron transfer for lactate detection were investigated. The modification of screen-printed sensors and microneedle sensors allowed lactate detection at even lower potentials than previously reported sensors using the same enzyme [8]. The results achieved on the microneedle sensors are promising for the realization of a wearable sensor patch for lactate monitoring.

7.6 References

[1] K. Rathee, V. Dhull, R. Dhull, and S. Singh, 'Biosensors based on electrochemical lactate detection: A comprehensive review', *Biochem. Biophys. Rep.*, vol. 5, pp. 35–54, Mar. 2016, doi: 10.1016/j.bbrep.2015.11.010.

[2] P. Wahl, C. Zinner, Z. Yue, W. Bloch, and J. Mester, 'Warming-Up Affects Performance and Lactate Distribution between Plasma and Red Blood Cells', *J. Sports Sci. Med.*, vol. 9, no. 3, pp. 499–507, Sep. 2010.

[3] C. Brinkmann, W. Bloch, and G. C. Mutinati, 'ELSAH (electronic smart patch system for wireless monitoring of molecular biomarkers for healthcare and

wellbeing): definition of possible use cases', *Front. Bioeng. Biotechnol.*, vol. 11, May 2023, doi: 10.3389/fbioe.2023.1166857.

[4] E. Melnik *et al.*, 'Screen-printed amperometric biosensors: A balancing act of manufacturing properties, cost efficiency and sensitivity', in *2022 IEEE International Conference on Flexible and Printable Sensors and Systems (FLEPS)*, Jul. 2022, pp. 1–4. doi: 10.1109/FLEPS53764.2022.9781500.

[5] S. A. N. Gowers *et al.*, '3D Printed Microfluidic Device with Integrated Biosensors for Online Analysis of Subcutaneous Human Microdialysate', *Anal. Chem.*, vol. 87, no. 15, pp. 7763–7770, Aug. 2015, doi: 10.1021/acs.analchem.5b01353.

[6] D. K. Ming *et al.*, 'Real-time continuous measurement of lactate through a minimally invasive microneedle patch: a phase I clinical study', *BMJ Innov.*, vol. 8, no. 2, Apr. 2022, doi: 10.1136/bmjinnov-2021-000864.

[7] A. Bocchino *et al.*, 'Development and Characterization of Passivation Methods for Microneedle-based Biosensors', in *2022 44th Annual International Conference of the IEEE Engineering in Medicine & Biology Society (EMBC)*, Jul. 2022, pp. 1275–1278. doi: 10.1109/EMBC48229.2022.9871005.

[8] D. M. E. Freeman *et al.*, 'Continuous Measurement of Lactate Concentration in Human Subjects through Direct Electron Transfer from Enzymes to Microneedle Electrodes', *ACS Sens.*, vol. 8, no. 4, pp. 1639–1647, Apr. 2023, doi: 10.1021/acssensors.2c02780.

[9] O. Smutok, T. Kavetskyy, and E. Katz, 'Recent trends in enzyme engineering aiming to improve bioelectrocatalysis proceeding with direct electron transfer', *Curr. Opin. Electrochem.*, vol. 31, p. 100856, Feb. 2022, doi: 10.1016/j.coelec.2021.100856.

[10] O. Smutok, M. Karkovska, R. Serkiz, B. Vus, N. Čenas, and M. Gonchar, ‘A novel mediatorless biosensor based on flavocytochrome *b*2 immobilized onto gold nanoclusters for non-invasive *L*-lactate analysis of human liquids’, *Sens. Actuators B Chem.*, vol. 250, pp. 469–475, Oct. 2017, doi: 10.1016/j.snb.2017.04.192.

[11] K. Hiraka *et al.*, ‘Rational design of direct electron transfer type l-lactate dehydrogenase for the development of multiplexed biosensor’, *Biosens. Bioelectron.*, vol. 176, p. 112933, Mar. 2021, doi: 10.1016/j.bios.2020.112933.

[12] P. Nuss and M. J. Eckelman, ‘Life Cycle Assessment of Metals: A Scientific Synthesis’, *PLOS One*, vol. 9, no. 7, Jul. 2014, doi: 10.1371/journal.pone.0101298.

[13] F. Schachinger, H. Chang, S. Scheiblbrandner, and R. Ludwig, ‘Amperometric Biosensors Based on Direct Electron Transfer Enzymes’, *Molecules*, vol. 26, no. 15, Art. no. 15, Jan. 2021, doi: 10.3390/molecules26154525.

[14] S.-C. Luo *et al.*, ‘Poly(3,4-ethylenedioxythiophene) (PEDOT) Nanobiointerfaces: Thin, Ultrasmooth, and Functionalized PEDOT Films with in Vitro and in Vivo Biocompatibility’, *Langmuir*, vol. 24, no. 15, pp. 8071–8077, Aug. 2008, doi: 10.1021/la800333g.

[15] A. Herrmann, R. Haag, and U. Schedler, ‘Hydrogels and Their Role in Biosensing Applications’, *Adv. Healthc. Mater.*, vol. 10, no. 11, p. 2100062, 2021, doi: 10.1002/adhm.202100062.

Chapter 8

Conclusions & Future Work

8.1 Summary of key contributions

In this work, a platform for the rapid prototyping of polymer microneedle devices has been developed and characterized. The platform has been presented in Chapter 2, and published in *Sensors and Actuators A: Physical* [1]. The key novelties included the ability to merge materials of widely differing properties within a single array, and the compatibility with batch production capabilities, increasing the throughput at laboratory level. Moreover, a first fully dedicated characterization of metallization techniques for the challenging topography associated with MNs arrays was carried out. This analysis led to the development of new metal masking designs that reduced or eliminated unwanted spreading. By analysing and controlling the size of the openings in the shadow masks, the phenomenon was diminished by as much as 80%, while the subsequent introduction of wall-like features to the masks completely eliminated the problem. This enabled the patterning of highly accurate features, such as electrodes, on the arrays. Similarly, another key feature usable within the platform, the application of a passivation layer necessary for use with many diagnostic devices, was summarised in another publication presented in Chapter 3. A number of different deposition methods and passivation materials were characterised and compared, with a view towards providing a base for future research aimed at using or optimising such layers. Specifically, the passivation methods were direct brushing of varnish, spin coating of different polymers, deposition and etching of parylene, application of a patterned medical tape and sputtering of silicon oxide. This is,

to my knowledge, the most complete work on passivation for MN-based devices published to date, and it is published in *Sensors and Actuators Reports* [2].

The scalability of a moulding process was proven in Chapter 4, where a collaboration with STRATEC Consumables GmbH led to the development and testing of reservoir equipped injection moulded MN arrays. The needles pierced the skin, successfully delivering the formulation contained in the reservoir below the *stratum corneum*. This work also showed an industrial method used to fill the reservoir of the MNs, potentially giving a scalable way to coat or functionalise individual needles. This work has been published in the *Journal of Micromechanics and Microengineering* [3].

The platform may be quickly tailored towards a specific use case, and several examples (Chapter 5, 6, and 7) were provided to show this versatility in many aspects of MN technology. The exemplars were presented in order of complexity, from the simplest to the most difficult to produce.

In particular, initial work was focussed on drug delivery. The MNs produced with the platform were used to validate the biomechanical robustness of the epoxy moulded needles by showing that they were able to pierce porcine skin. Because they successfully pricked the skin, they allowed the passage of intact B12 loaded liposomes through the *stratum corneum*, maximising the amount of B12 that can reach systemic circulation [4].

Subsequently, Chapter 5 showed a more complex drug delivery application, where novel bio-inspired 3D printed needles designed at Johannes Kepler University (Austria) were successfully replicated using the platform, and used to generate fluid transport in specific directions [5]. Not only did this work prove the precision and reliability of the core moulding process and its ability to precisely copy intricate microstructures, but the produced MNs could be used for two main tasks by simply controlling the orientation of

the superficial pattern on the needle walls and substrate. By aligning the structures in one direction, liquid drugs could be guided into the skin. Contrarily, by reversing the orientation, the needles could be used for ISF extraction. This work was published in *Biomedical Microdevices* [5].

After drug delivery, dry MNs electrodes were developed for EEG monitoring [6]. Epotek 353ND, the same materials used for the previously discussed transdermal deliveries, was used to build these electrodes. A layer of titanium and a layer of gold were deposited on both sides of the electrodes, making them electrically conductive. These dry electrodes were able to effectively record EEG signals without the use of wet gel, skin abrasion or shaving. Notably, the MNs lowered the skin-electrode impedance in the frontal region of the scalp by more than 80% over commercially available dry alternatives, hence providing a more convenient solution.

Similarly, dry electrodes for ECG and EMG recording were also produced using the platform. Leveraging its capability to integrate polymers with non-adhesive materials, novel MN-based electrodes were fabricated. The needles were formed with a rigid, medical grade epoxy while a conductive textile, flexible in nature, was used as the substrate material. This allowed better conformance to the body of the volunteers they were tested on, providing an evolution over rigid dry electrodes. A layer of titanium and gold was used to metallise the MNs side of the electrodes. However, because the substrate fabric was electrically conductive, no metallization was needed for the rear side, reducing production time and cost over the previously developed EEG electrodes. This work, presented in Chapter 6, was published in *Advanced Materials Technologies* [7].

MNs were also used as electrochemical sensors to monitor different biomarkers and chemistries. Initially, MN-based sensors for real-time monitoring of pH and sodium were developed [8]. This not only showed how MNs could be used to analyse different aspects

of the physiological environment, but also how they could be used as point-of-care devices, potentially replacing centralized laboratory testing.

Finally, another biosensor, used to detect lactate in interstitial fluid, was developed and presented in Chapter 7. This work was published in *IEEE Sensors Letters* [9]. Developed as part of the EU-funded ELSAH project [10], this sensor combined moulding together with metallization, multi-electrode formation, chlorination, passivation, and functionalization, showing the integration of the different 'building blocks' of the platform, and demonstrating its full capabilities. Four electrodes were formed on a single array: two working, one counter, and one reference electrode. The electrodes were precisely shaped by implementing metal masks during the metallization step. Titanium and platinum were used in all cases except for the reference electrode, which was formed by layering titanium/nickel/silver followed by Ag chlorination. A medical grade tape was patterned, cut to size, and applied to the sensor to passivate it. Finally, at the Austrian Institute of Technology, a PEDOT-PSS ink was formulated, mixed with a novel lactate-sensitive DET enzyme provided by Austrian company DirectSens GmbH, and used to functionalise the MNs of the WEs. The functionalization was done by dispensing the ink through a piezoelectric BioDOT dispenser, enabling automatic deposition and process scalability at industrial level. As outlined in Chapter 2 [1], additional functionality was later added to the above mentioned lactate sensor by using one WE for lactate, and the other WE for glucose detection. Moreover, the sensors were sterilised, allowing their testing on 30 human volunteers in a trial run at the Medical University of Graz. To capture and record the data, the sensors were interfaced with electronics developed by Infineon Technology AG (Graz, Austria), and packaged in a wearable device designed by Sanmina Corp (Fermoy, Ireland), which was applied to the volunteers using adhesive tape and a customised applicator designed as part of this PhD. For this trial, several hundreds of

sensors were produced using the moulding, metallisation and passivation procedures described in Chapters 2 and 3. Not only could the platform handle the production of such a large number of sensors, but the arrays conformed to the standards required by our industrial systems integration partner Sanmina, both in terms of precision and reproducibility. This biosensor represents the most advanced application of the platform demonstrated to date. The innovative device could be used for several applications, including continuous biomarker monitoring to track the evolution of pathological conditions, to optimise athletes training to improve their performances, or simply to provide a strong evidence-based support to promote healthy living.

8.2 Critical review and future work

This work has provided a high-quality, laboratory-scale manufacturing solution for microneedle-based devices used in applications ranging from transdermal delivery and biomarker analysis to biopotential monitoring. It is intended to facilitate rapid prototyping of mixed-material devices in quantities suitable for pre-clinical or early clinical trials. However, additional research and development could be done to further advance this platform at laboratory level, as well as to make it fully scalable at industrial level.

Firstly, the majority of the process steps of the platform, such as moulding and passivation, are manual. Therefore, they heavily rely on the skill of the operator for production speed, reproducibility between different batches, and for fidelity of the replicated features. Since the throughput has been increased by enabling the handling of a batch of several wafers per process iteration, the platform could enable the fabrication of hundreds of arrays. These numbers are significant at laboratory level, but are not enough for industrial production or large-scale trials.

Secondly, although one of the core novelties of the platform is its ability to allow the integration of substrate and structural materials with different properties, there are two main limitations remaining. To start, the polymers must be mouldable. Therefore, the viscosity of the uncured material cannot be too high. Based on the tested materials, it was possible to mould up to 7500 cP, but more tests should be conducted to understand the viscosity limit of the usable materials. A second limitation is the inability to directly merge polymers which require drying, with preformed materials such as the fabric shown in Chapter 6. Degradable polymers and hydrogels are usually mixed within a solution, and, after filling the mould, the mixture is left to dry, becoming rigid. This means that they cannot be directly bonded to materials like films or cloths. The integration could be possible only by using a glue, additional polymer layer or similar material to bond the needles to the back substrate, increasing the complexity of the process. Alternatively, only a curable or adhesive material should be used as a substrate for polymers requiring drying.

To investigate the feasibility of scaling up the replica moulding process to industrial level, initial tests were performed in collaboration with STRATEC Consumables GmbH (Anif, Austria), successfully injection moulding dry electrodes [11]. These electrodes were then sputtered with 200 nm of gold, affixed to snap fasteners removed from commercial gel-based electrodes, and used to capture ECG signal on healthy volunteers. The tests were performed in different active and resting states. Specifically, sitting, standing, and walking at different speeds on a treadmill. The experiments showed that, although wet and dry electrodes have similar performances in static conditions, MN-based electrodes demonstrated marginally better results in dynamic conditions. This work has been submitted to *IEEE Access*. To demonstrate applicability in a second use case, the same injection moulding process was also used to replicate microstereolithography-fabricated conical MNs, designed with a cylindrical reservoir close to the tip [3]. Injection moulding

is a technique which forces melted plastic inside a metallic mould. After cooling the plastic down, the solid part can be removed from the mould [12]. A biocompatible cyclic olefin polymer was used to produce the replicated needles. The MN arrays were easy to de-mould, and maintained the sharpness observed in the original needles. Subsequently, the reservoirs were precisely filled with a fluorescein isothiocyanate (FITC) ink dispensed by a drop-on-demand inkjet printer, making also the loading of the ink compatible with industrial level production. The needles were tested on *ex vivo* skin samples, successfully penetrating the SC whilst sustaining no structural damage, and delivering the fluorescent dye in the dermis below. Although injection moulding is the natural evolution of the core process to reach industrial level production, the number of materials usable with this technique is much lower than the wide range of polymers compatible with micromoulding [12]. Another aspect that should be investigated during a study of injection moulding capabilities is the ability of the process to combine different materials for MNs and substrate production, together with the possibility to integrate preformed materials though a process such as overmoulding or inset moulding [13], [14].

Focussing now on the individual blocks of the platform, both passivation and metallization would benefit from additional work. The passivation layers investigated during this work showed several clear strengths and weaknesses: liquid layers were difficult to reliably deposit in a controlled fashion, while sputtering of SiO_2 was heavily affected by spreading of the material below the mask. However, both spin coating and sputtering would have been easily scalable at industrial level. The patterned tape was robust and flexible, but thicker than the other options, reducing the height of the needle available for skin penetration. Finally, parylene was thin and conformal, but the process to apply it was the most complex out of all the investigated materials. All passivation experiments showed the need for further optimization in order to reach an ideal deposition

process. In particular, it was very difficult to cover the entirety of the substrate with a thin layer while leaving the entirety of the MN bodies completely exposed. To reliably achieve such a result together with a uniform thickness covering the substrate, further research will be required.

While metallizing MN arrays, to form multiple electrodes or to selectively cover specific areas, masks must be used. This was characterised for both sputtering and ebeam evaporation. Ebeam worked very well, and precisely replicated the pattern of the mask. Sputtering instead required masks with wall features to achieve similar results. In both cases, the masks were 1 mm thick (excluding the wall depth) and placed 100 µm away from the tip of the needles. Considering this thickness, if the metal source is not centred directly above or below the wafer, the mask could act as a shield, shadowing some of the substrate, and reducing the size of the desired shape deposited on the wafers. Vice-versa, if the mask is too thin, some metal could leak under the mask, covering more area than required. Because of this, there is both a limit to the minimum size of the features that can be transferred to the wafers, and to the accuracy of patterns drawn on individual MNs. Potentially, these results could be achieved by blanket depositing metal, and then selectively removing it using laser ablation or similar techniques. Complex lithographic processes could also be explored. Otherwise, initial work has been started by Holicky et al., combining spray coating and photolithography to pattern graphene channels as small as 63 µm on top of MN arrays [15].

Stepping out from the platform itself, one limitation shared by many MN-based devices is that, once applied to a volunteer, there is no proof that all the needles are effectively embedded inside the skin. It has been shown that use of different application forces or directions, combined with the bed-of-nails effect, can strongly effect skin penetration and the depth reached by the MNs [16], [17]. Considering that skin composition and thickness

are highly variable, not just from person to person, but also from area to area of the same individual [18], [19], there is often uncertainty on whether the needles reach the viable epidermis or not. Commonly, this concern is mitigated using an applicator to apply a pre-determined and consistent amount of force/speed [20]. However, the only way to be sure would be to have a reliable way to determine if the MNs are correctly inserted.

This work started initial development of a penetration sensor for use with biodegradable microneedles. This sensor could be produced by leveraging the moulding, metallisation and passivation steps of the platform, and would be a fundamental step to potentially enable mass adoption of MN-based devices. The sensor would involve the deposition of a narrow strip of degradable metal over a row of needles, and a passivation layer applied to leave only the needles exposed. A proof of concept, developed using a biodegradable microneedle array made from a PVP-PVA mixture, and titanium/platinum sputtering on the MNs to create the metal trace, has shown that the resistance of the metal strip increases as the polymer degrades (Figure 1).

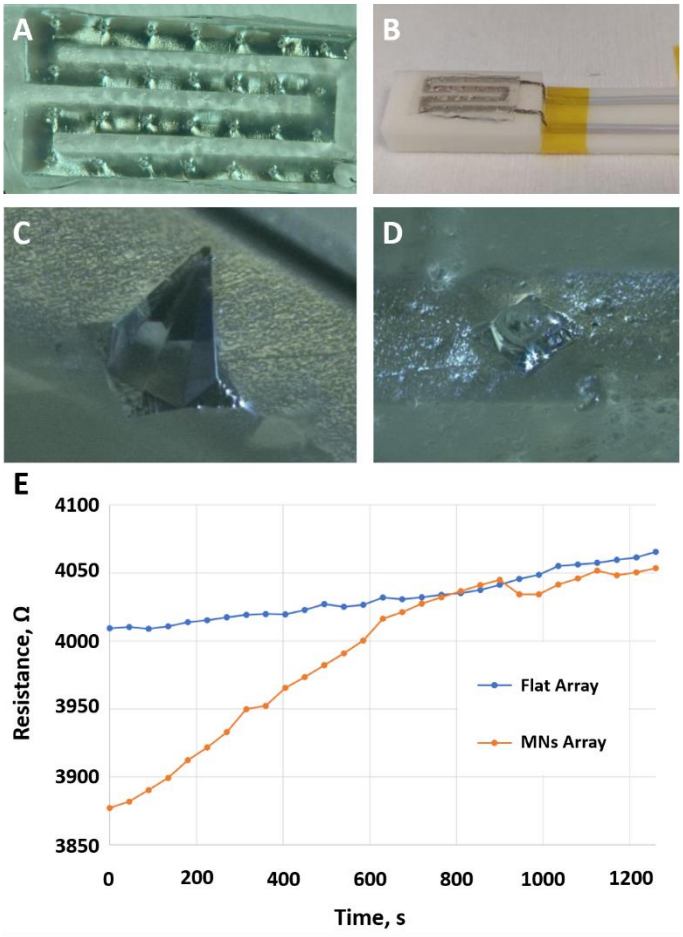


Figure 1. Developed proof of concept for the penetration sensor: a top view of the sensor (A) and the same sensor mounted on a 3D printed support for testing on *ex vivo* skin samples (B). A close up of a MN before (C) and after (D) insertion is shown as well: after skin application, the MNs are showing complete dissolution. Finally, a graph is showing the changes in resistance of a MN-based array vs a flat array (E). Both were applied to *ex vivo* skin.

Considering the use of degradable polymers for the sensor, drugs could be loaded inside the needles, achieving transdermal delivery together with active penetration detection. This indicates the potential of the platform in combining active sensors with passive delivery devices. Future work could focus on the designing of new devices, produced

using a biodegradable metal such as magnesium or zinc, passivated, and tested to potentially be used in *in vivo* trials.

8.3 Conclusion

Microneedle arrays have significant potential for use in a wide range of transdermal delivery and diagnostics applications. However, since arrays intended for different use cases may also have divergent material, structural, biomechanical or functional requirements, the corresponding fabrication process is often specific to each particular device. In response to that limitation, this work successfully developed a multifunctional platform for the rapid prototyping of polymer MN-based devices.

The key contribution of the thesis was the creation and characterisation of a highly versatile fabrication process that allowed for the micromoulding of polymer microneedle arrays with varying materials, structural properties and functionalities. Other contributions to the state of the art included the development of new masking procedures for the precise deposition of metallic patterns on the three-dimensional MN array surface, and a study of passivation methods necessary for use with biosensor devices.

In addition, major contributions have been made towards published works that describe use of the moulding process in exemplars such as drug delivery devices, biosensors, and biopotential monitoring electrodes.

It is intended that the process will facilitate the rapid development and iteration of polymer-based microneedles at laboratory scale, as well as producing the quantities necessary for early-stage research and small volume trial needs. In this manner, the platform could assist in accelerating the pace of research and development of microneedle technologies and applications.

8.4 References

[1] A. Bocchino *et al.*, 'A multifunctional platform for the production and customization of polymer-based microneedle devices', *Sens. Actuators Phys.*, vol. 388, p. 116491, Jul. 2025, doi: 10.1016/j.sna.2025.116491.

[2] A. Bocchino *et al.*, 'Strategies for passivating microneedle-based sensors: development, characterization and comparison', *Sens. Actuators Rep.*, vol. 9, p. 100328, Jun. 2025, doi: 10.1016/j.snr.2025.100328.

[3] C. O'Mahony *et al.*, 'Piezoelectric inkjet coating of injection moulded, reservoir-tipped microneedle arrays for transdermal delivery', *J. Micromechanics Microengineering*, vol. 29, no. 8, p. 085004, Jun. 2019, doi: 10.1088/1361-6439/ab222b.

[4] A. J. Guillot *et al.*, 'Exploration of Microneedle-assisted skin delivery of cyanocobalamin formulated in ultraflexible lipid vesicles', *Eur. J. Pharm. Biopharm.*, vol. 177, pp. 184–198, Aug. 2022, doi: 10.1016/j.ejpb.2022.06.015.

[5] C. Plamadeala *et al.*, 'Bio-inspired microneedle design for efficient drug/vaccine coating', *Biomed. Microdevices*, vol. 22, no. 1, p. 8, Dec. 2019, doi: 10.1007/s10544-019-0456-z.

[6] M. O'Sullivan, A. Temko, A. Bocchino, C. O'Mahony, G. Boylan, and E. Popovici, 'Analysis of a Low-Cost EEG Monitoring System and Dry Electrodes toward Clinical Use in the Neonatal ICU', *Sensors*, vol. 19, no. 11, Art. no. 11, Jan. 2019, doi: 10.3390/s19112637.

[7] O. P. Singh, A. Bocchino, T. Guillerm, Y. Hu, F. Stam, and C. O'Mahony, 'Flexible, Conductive Fabric-Backed, Microneedle Electrodes for Electrophysiological

Monitoring', *Adv. Mater. Technol.*, vol. 9, no. 3, p. 2301606, 2024, doi: 10.1002/admt.202301606.

[8] F. Rahman, A. Ryan, A. Bocchino, P. Galvin, and S. R. Teixeira, 'Microneedle-based electrochemical sensors for real-time pH and sodium monitoring in physiological environments', *Sens. Bio-Sens. Res.*, vol. 48, p. 100777, Jun. 2025, doi: 10.1016/j.sbsr.2025.100777.

[9] S. Kurzhals *et al.*, 'Detection of Lactate via Amperometric Sensors Modified With Direct Electron Transfer Enzyme Containing PEDOT:PSS and Hydrogel Inks', *IEEE Sens. Lett.*, vol. 7, no. 9, pp. 1–4, Sep. 2023, doi: 10.1109/LSENS.2023.3307066.

[10] 'WELCOME TO ELSAH'. Accessed: Feb. 13, 2023. [Online]. Available: https://www.elsah.researchproject.at/home.php

[11] C. O'Mahony *et al.*, 'Characterisation of Microneedle-Based ECG Electrodes Fabricated Using an Industrial Injection-Moulding Process', in *2019 IEEE 32nd International Conference on Micro Electro Mechanical Systems (MEMS)*, Jan. 2019, pp. 557–560. doi: 10.1109/MEMSYS.2019.8870721.

[12] 'What Are the Limitations of Injection Molding? -', https://zetarmold.com/. Accessed: Jan. 05, 2025. [Online]. Available: https://zetarmold.com/limitations-of-injection-molding/

[13] 'Overmolding and Insert Molding: From Prototyping to Production', Formlabs. Accessed: Jan. 05, 2025. [Online]. Available: https://formlabs.com/eu/blog/overmolding-insert-molding/

[14] ‘Insert Molding vs. Overmolding: What’s the Difference?’ Accessed: Jan. 05, 2025. [Online]. Available: https://www.xometry.com/resources/injection-molding/the-differences-between-insert-molding-vs-overmolding/

[15] M. Holicky, B. Fenech-Salerno, A. E. G. Cass, and F. Torrisi, ‘Fabrication of graphene field effect transistors on complex non-planar surfaces’, *Appl. Phys. Lett.*, vol. 125, no. 11, p. 113301, Sep. 2024, doi: 10.1063/5.0226780.

[16] M. Razzaghi and M. Akbari, ‘The Effect of 3D Printing Tilt Angle on the Penetration of 3D-Printed Microneedle Arrays’, *Micromachines*, vol. 14, no. 6, Art. no. 6, Jun. 2023, doi: 10.3390/mi14061157.

[17] Y. Zhang, S. A. Campbell, and S. Karthikeyan, ‘Finite element analysis of hollow out-of-plane HfO2 microneedles for transdermal drug delivery applications’, *Biomed. Microdevices*, vol. 20, no. 1, p. 19, Feb. 2018, doi: 10.1007/s10544-018-0262-z.

[18] H. Yousef, M. Alhajj, A. O. Fakoya, and S. Sharma, ‘Anatomy, Skin (Integument), Epidermis’, in *StatPearls*, Treasure Island (FL): StatPearls Publishing, 2024. Accessed: Sep. 19, 2024. [Online]. Available: http://www.ncbi.nlm.nih.gov/books/NBK470464/

[19] W. Lopez-Ojeda, A. Pandey, M. Alhajj, and A. M. Oakley, ‘Anatomy, Skin (Integument)’, in *StatPearls*, Treasure Island (FL): StatPearls Publishing, 2025. Accessed: Jan. 23, 2025. [Online]. Available: http://www.ncbi.nlm.nih.gov/books/NBK441980/

[20] M. Leone *et al.*, ‘Universal Applicator for Digitally-Controlled Pressing Force and Impact Velocity Insertion of Microneedles into Skin’, *Pharmaceutics*, vol. 10, no. 4, Art. no. 4, Dec. 2018, doi: 10.3390/pharmaceutics10040211.

Appendices

A.1 Supplementary Information – Chapter 3

Exposed Area

The calculation of the exposed area was performed using ImageJ to analyse the captured SEM pictures as follows:

1. If the MN was entirely exposed, A_l was calculated using the known s and h of the needle. ImageJ was used to calculate the additional exposed area (A_{ex}) around the MN as shown in Figure 1, measuring the area outlined by the yellow line. This was repeated for 6 needles and then average A_{ex} and standard deviations were calculated. When proceeding with TSA calculation, A_b was removed from A_{ex}, and A_l added.

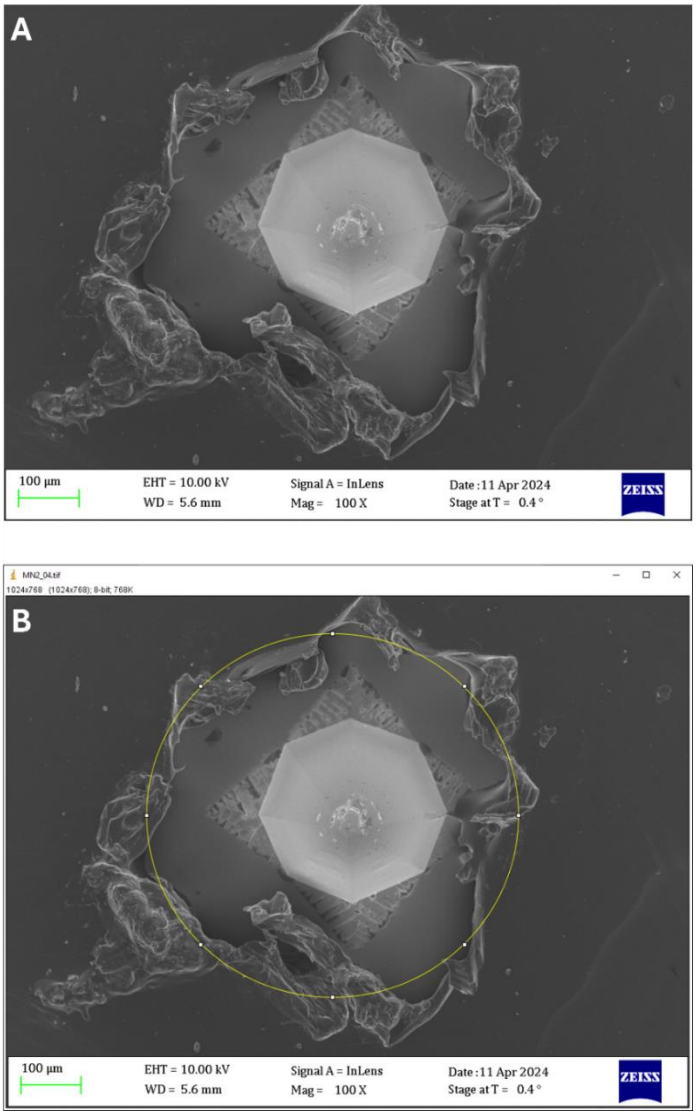


Figure 9. Original SEM picture of an ARcare passivated needle (A) together with the same image processed with ImageJ (B).

This method was used for both ARcare and parylene.

2. If only part of the MNs' lateral surface was exposed, the SEM pictures were used to calculate the height of the not passivated area (h) and the base edge of the corresponding octagonal pyramid (s). Figure 2 shows how the SEM image (Figure 2A) was loaded on ImageJ and, firstly, the base radius (r) of the circumference circumscribed to the exposed part octagonal base was measured (Figure 2C). The measurement was repeated 8 times (one for each of the visible edges of the triangular faces) and an average value found. The MNs have a 2:3 base:height ratio (equation (1)). Therefore, considering this ratio, the cross section passing from the centrepoint of the pyramid (outlined in the schematic on Figure 2B) and the average r, h was calculated with equation (2):

$$2r : h = 2 : 3 \qquad (1)$$

$$=> h = \frac{r}{3} \qquad (2)$$

For the base edge, all 8 base edges of the exposed part were measured with ImageJ (Figure 2D), and the average value used as s.

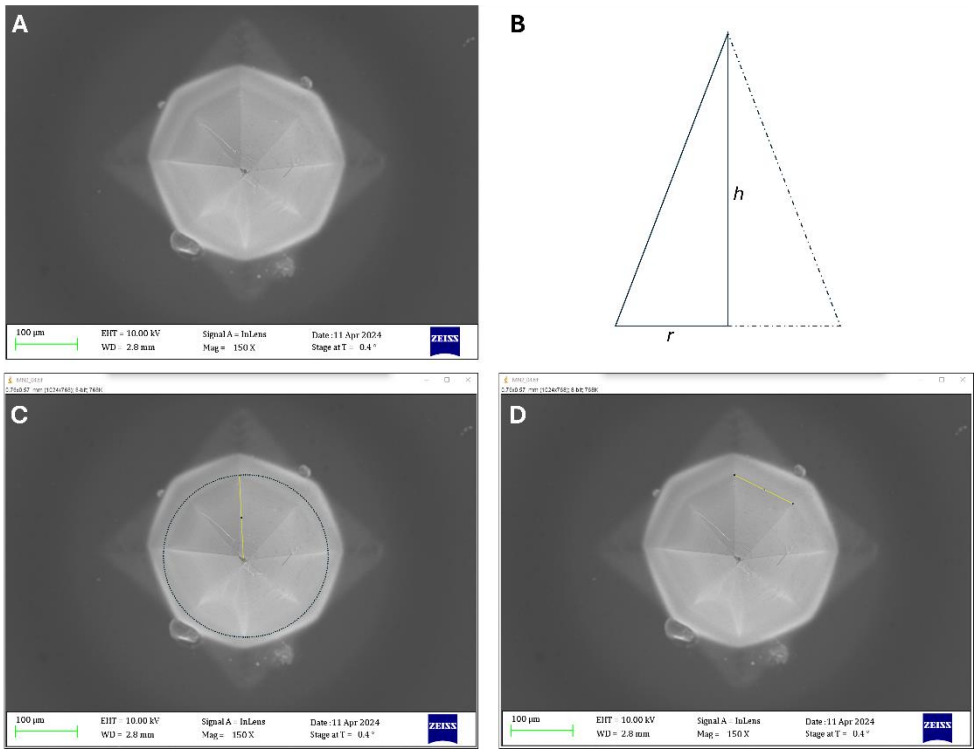


Figure 10. Original SEM picture of a PMMA passivated needle (A) together with the schematic representation of the central cross section of the octagonal pyramid (B). Also, measurement of a single radius (yellow line) done with ImageJ together with representation of the associated base circumference (circumscribed to the base of the pyramid - dashed line. C). Finally, measurement of an individual base edge for the exposed part using ImageJ (D).

These *h* and *s* were then used to calculate A_l. This method was used for PMMA and Epotek.

3. For the Varnish passivated MNs, no clear edge was visible. Therefore, the exposed part was modelled with a cone.

The SEM pictures were imported in ImageJ (Figure 3A) and the circular area measured with the software (Figure 3B). The radius associated with this area was calculated. Considering the 2:3 base:height ratio of the MNs, h was found from r and A_l calculated.

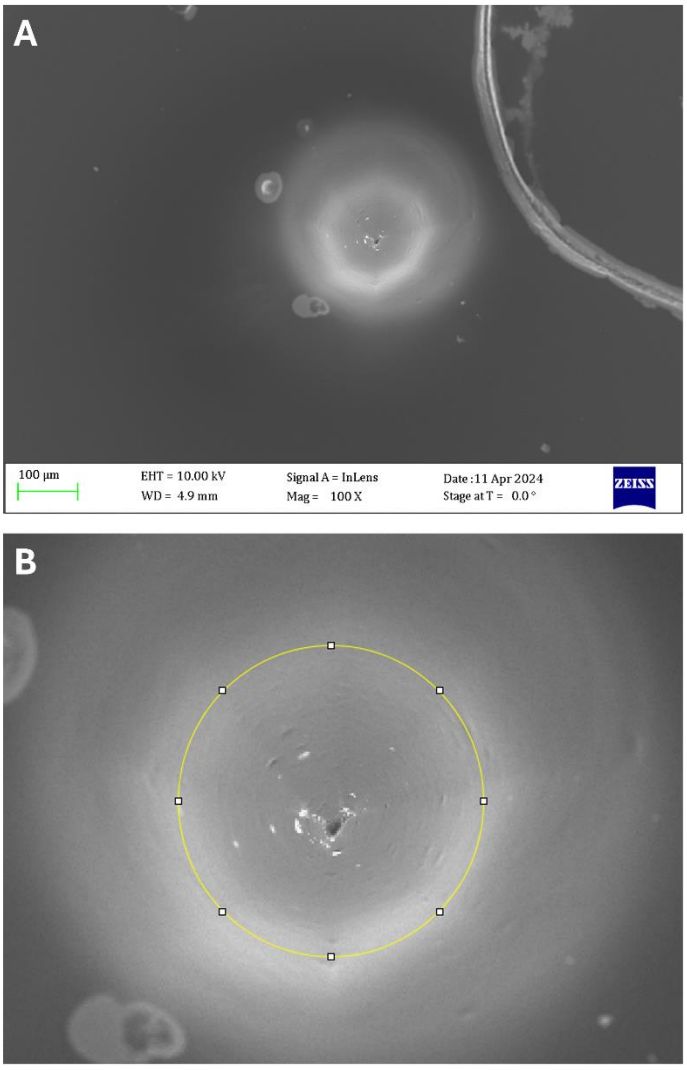


Figure 11. Original SEM picture of the varnish passivated needle (A) together with magnification of the circular area measured with ImageJ (B).

Spin Coating

In regards to spinning PMMA and Epotek 353ND, a preliminary optimization was performed before choosing which recipe to use.

Specifically, the following steps were used for the materials:

1. PMMA: Seven different 2x2 cm silicon chips were used to characterise the polymer spin curve. Speeds of 2000, 2500, 3000, 3500, 4000, 5000, and 6000 rpm were tested, checking thickness and uniformity of the coating. A polynomial curve was then use to fit the data, estimating a thickness of the passivation layer covering the substrate around the MNs of more than 3 µm. The substrate showed a uniform coating and the MN tips appeared exposed.

The data is represented in Figure 4.

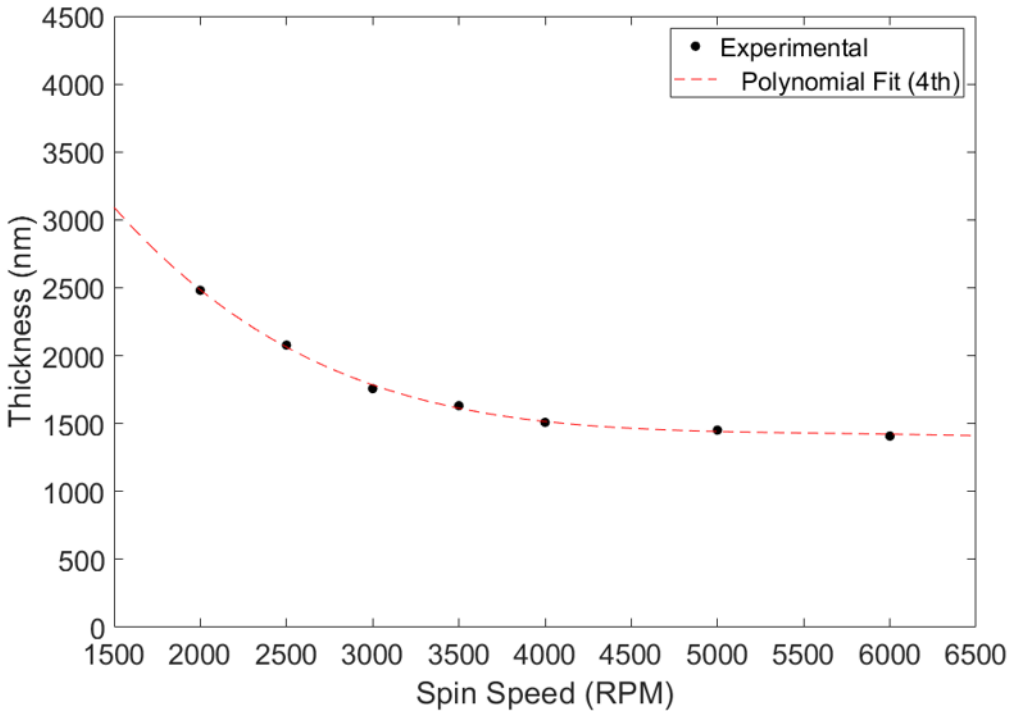


Figure 12. Thickness recorded at different speeds for the PMMA layers. The polynomial curve is also represented by a dashed red line.

2. Epotek 353ND: the higher viscosity of the Epotek made harder to find a way to properly spin coat the samples, creating thick layers of material. Considering this, the majority of the spinning tests were performed directly on the MN samples, having an immediate feedback on wheatear the tip were exposed or not.

Speeds of 2000, 2500, 3000, and 4000 rpm were tested. At 4000 rpm, the tips of the MNs were exposed. However, the spun layer was not uniform, and the passivation left exposed areas close to the edges of the arrays. Considering this would defy the purpose of the passivation layer, the Epotek was firstly pre-heated, lowering its viscosity, and then spin coated on the material. Although, as observed within the manuscript, the cover was not ideal, greatly reducing the viable height of the MNs, the passivation was still tested and characterised. The main reason behind this was to show the witnessed problem, highlighting the need to properly choose the spinning material while demonstrating one of the possible issues caused by a wrong pick.

A.2 Supplementary Information – Chapter 5

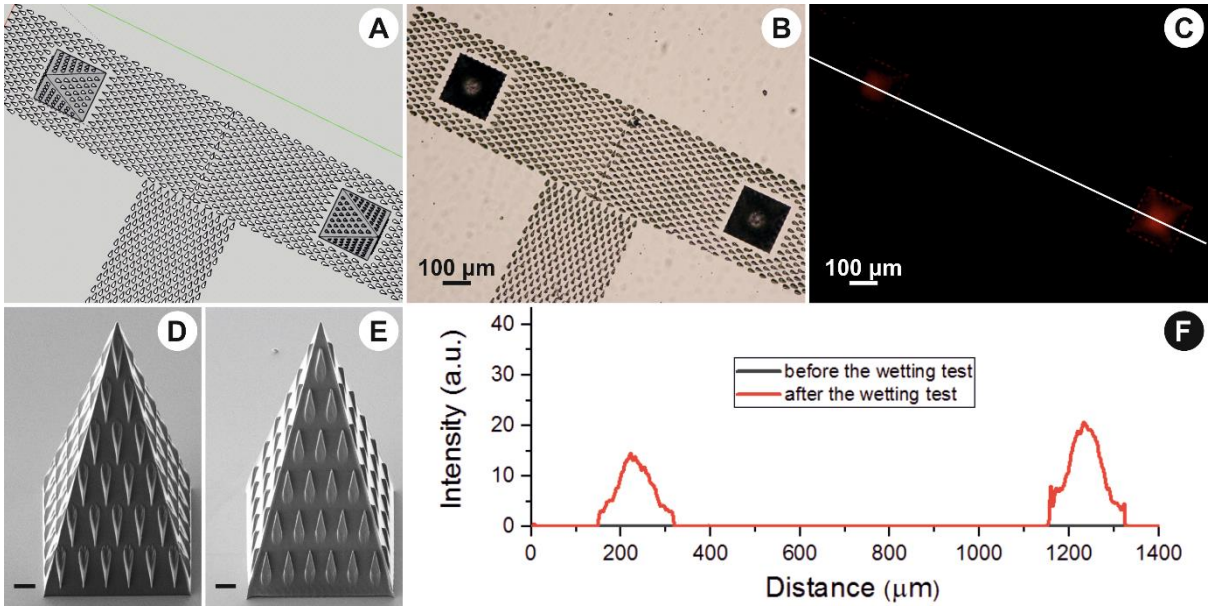
Not owning supplementary video 1 and 2, they can be found at the following link:

https://link.springer.com/article/10.1007/s10544-019-0456-z#additional-information .

Video 1 (Supplement 1): Video showing a z-stack of confocal microscope images of the non-structured MN after the wetting test. First, one sees the structures in the guiding channel. Later on, one sees the non-structured MN's lateral faces and corners from the bottom ($z = 0$ μm) till $z = 60$ μm.

Video 2 (Supplement 2): Video showing a z-stack of confocal microscope images of the structured MN after the wetting test. First, one sees the structures in the channels. Later on, one sees the structured MN's lateral faces and corners from the bottom (z = 0 µm) till z = 90 µm. Note that the height range here is considerably larger than in Supplement 1.

(Supplement 3)



A T-shaped guiding channel containing two different structured MNs (structures pointing downwards MN on the left, and structures pointing upwards on the right-hand side). (A) The CAD design of the test sample. (B) Optical microscope image of the T-shaped channel and the two MNs before the wetting test. (C) Fluorescent microscope image taken in the red channel after the wetting test performed with a fluorophore-soap-water solution. Scanning electron microscope (SEM) images of the (D) MN with surface structures pointing downwards, and of the (E) MN with the surface structures pointing upwards, taken at a 45° view angle (scale bar corresponds to 20 µm). (F) Intensity profile along the white line in Supplement 3E (grey plot - before the wetting test, red plot - after the wetting

test). For this certain wetting test a fluorophore concentration of 1 to 100 was used, therefore the signal intensity in image (C) is lower than in the Figure 4 (Section 5.4).

A.3 Supplementary Information – Chapter 6

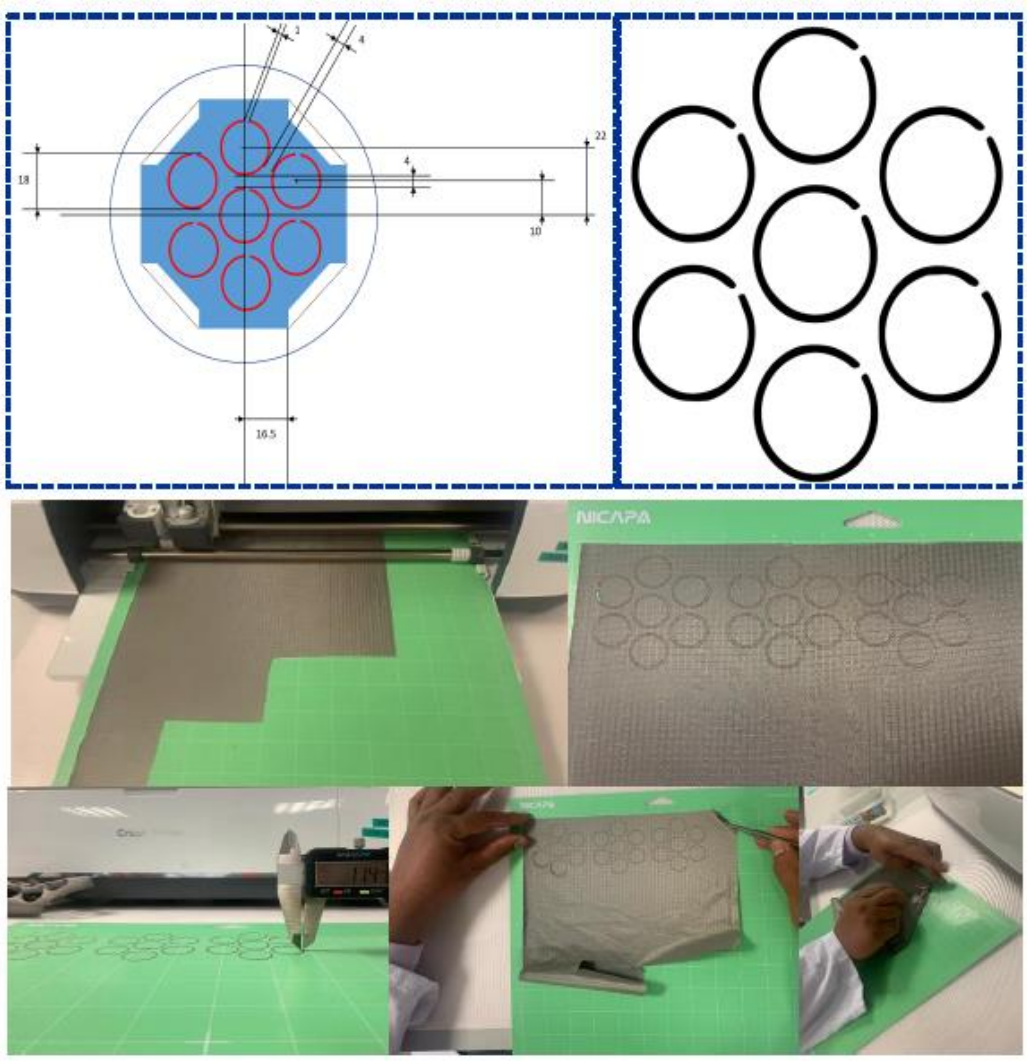


Figure S13. Left: A circular shapes wafer with a diameter of 18 mm reflects the shape and dimension of electrode and acts as a backing layer too, right: redesigned the wafer into Cricut Design Space.

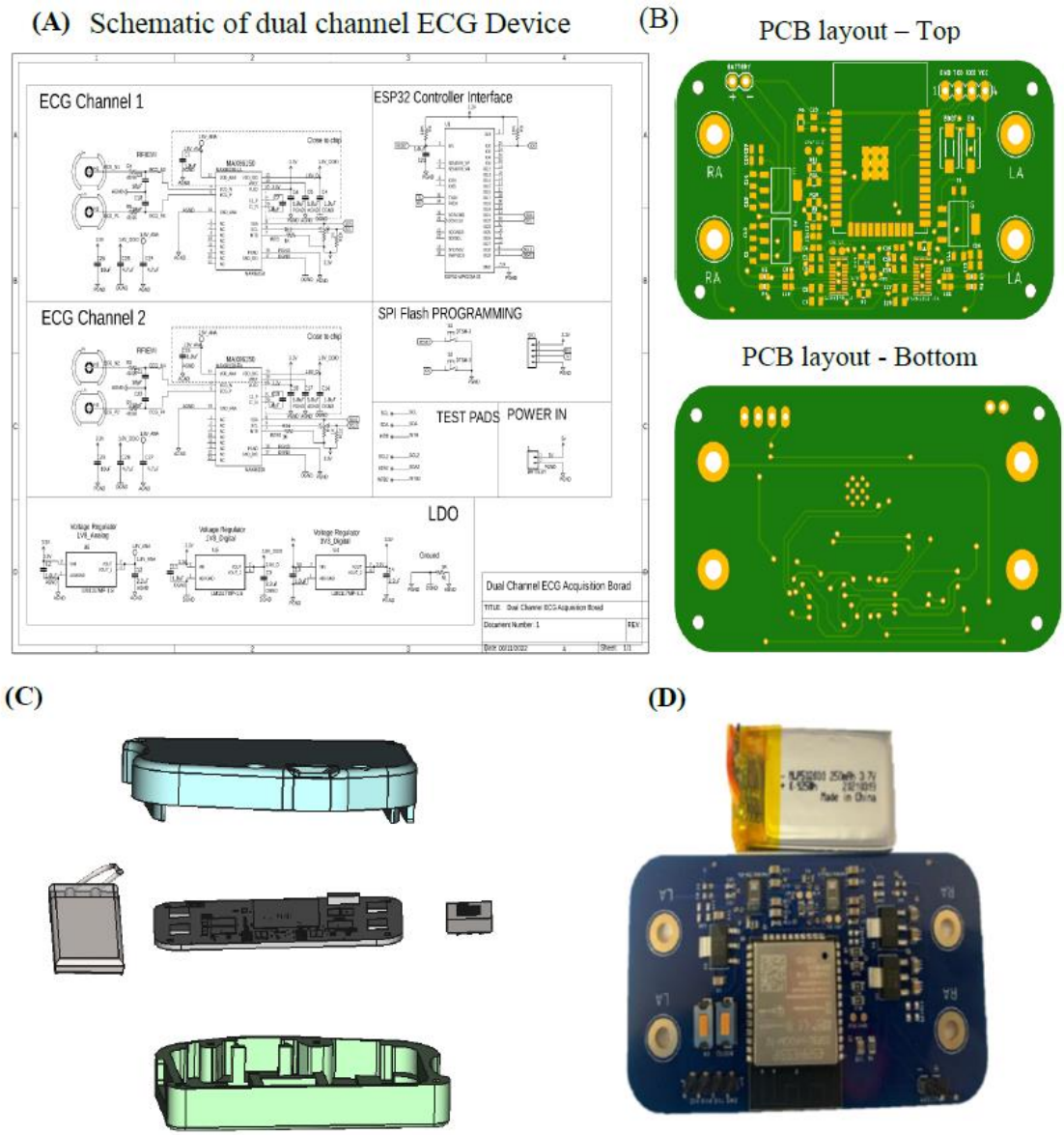


Figure S14. (A) Schematic layout- dual channel ECG acquisitions, (B) PCB layout (Top and Bottom), (C) CAD file for dual channel ECG wearable system includes housing, step file for dual channel wearable ECG system, battery, and switch. (D) Readout module PCB fabricated on the fourth grade of retardant material (7 x 3 cm^2).

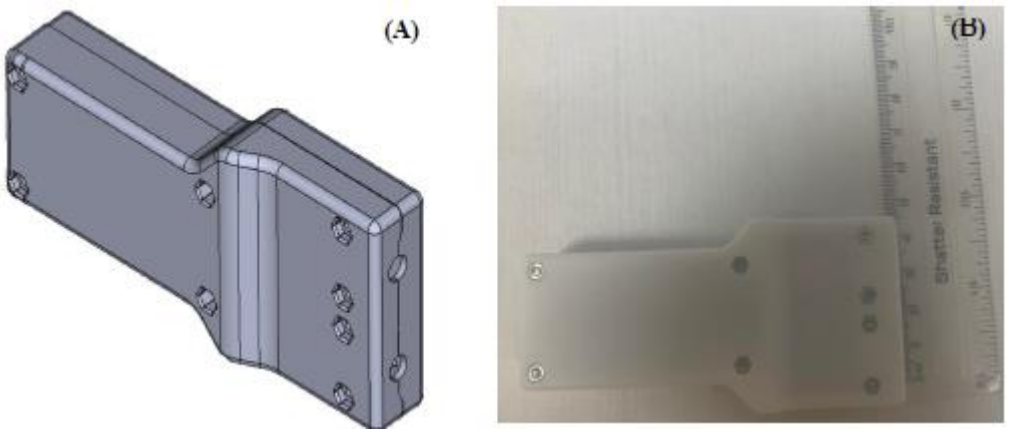


Figure S15. (A) CAD file for dual channel EMG system includes housing (Isometric view); (B) EMG recording device enclosed into a 3-D printed housing, comprises dual channel analog EMG sensor from DFRobot and OYMotion (SEN0240, DFRobot, China), weight of 54.54 gram.

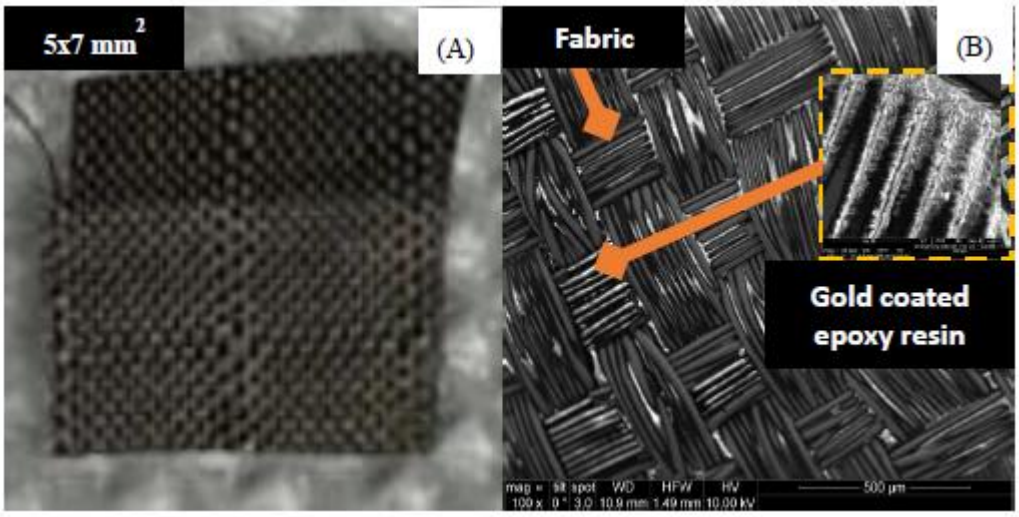


Figure S16. Illustrates the bonding of epoxy resin with the fabric; (A) Fabric sample with the dimension of 5x7 mm^2, (B) SEM image of fabric with gold coated epoxy resin, inset: Zoom-In of metallised area.

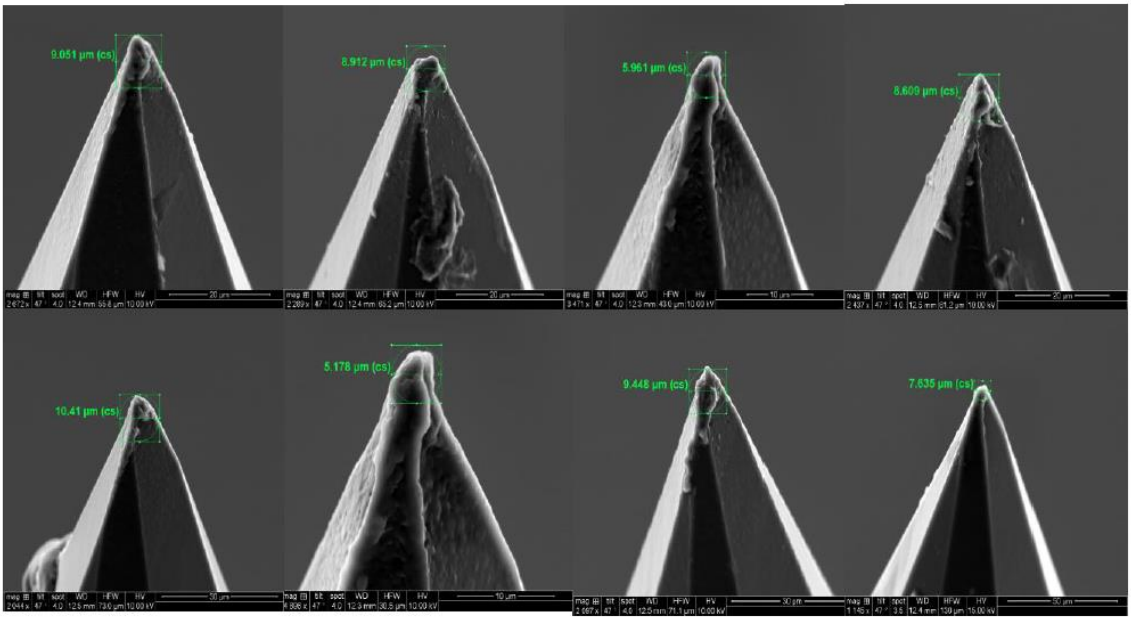


Figure S17. SEM image of microneedles arrays, shows variation in tip diameters of microneedles.

Table 2. Illustrate the tip diameter in terms of mean and standard deviation.

No. of Microneedles	**Microneedle Tip (Diameter - µ)**
1	8.9
2	9
3	5.9
4	10.4
5	5
6	8.6
7	9.4
8	7.6
Mean	8.1
SD	1.8

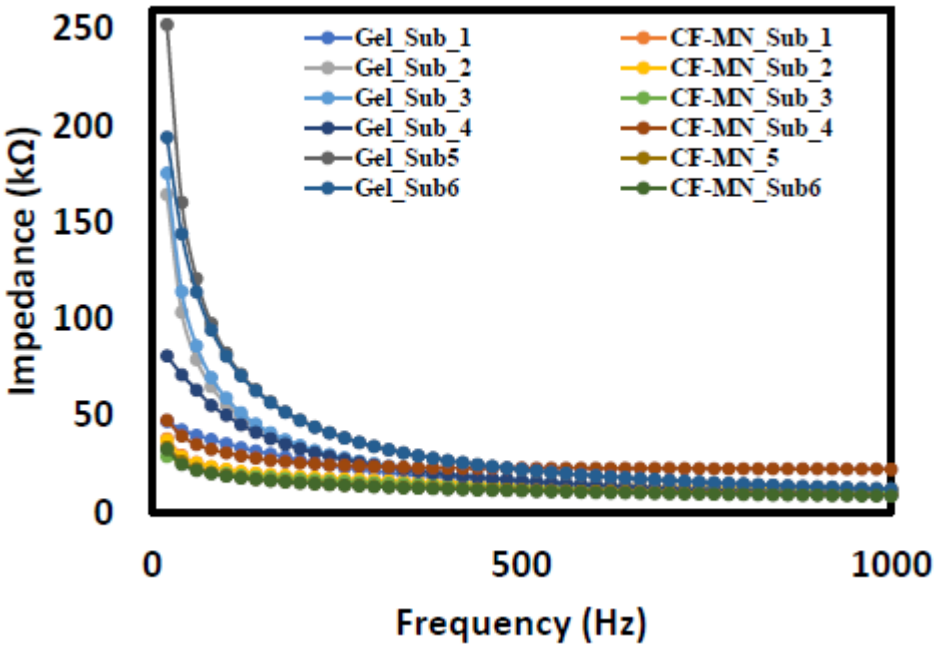


Figure S18. (A) Impedance represents the six subject individual impedance at distinct frequency from 20 Hz – 1000 Hz with swap of 20 Hz.

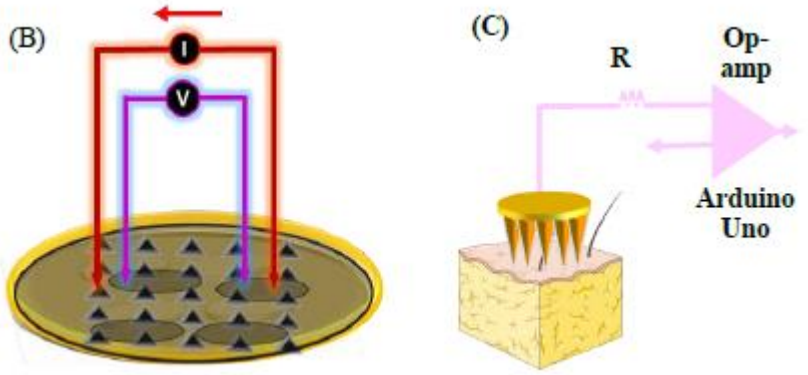


Figure S6. (B) Four probe system for measurement of surface resistivity, and (C) direct current (DC) offset potential.

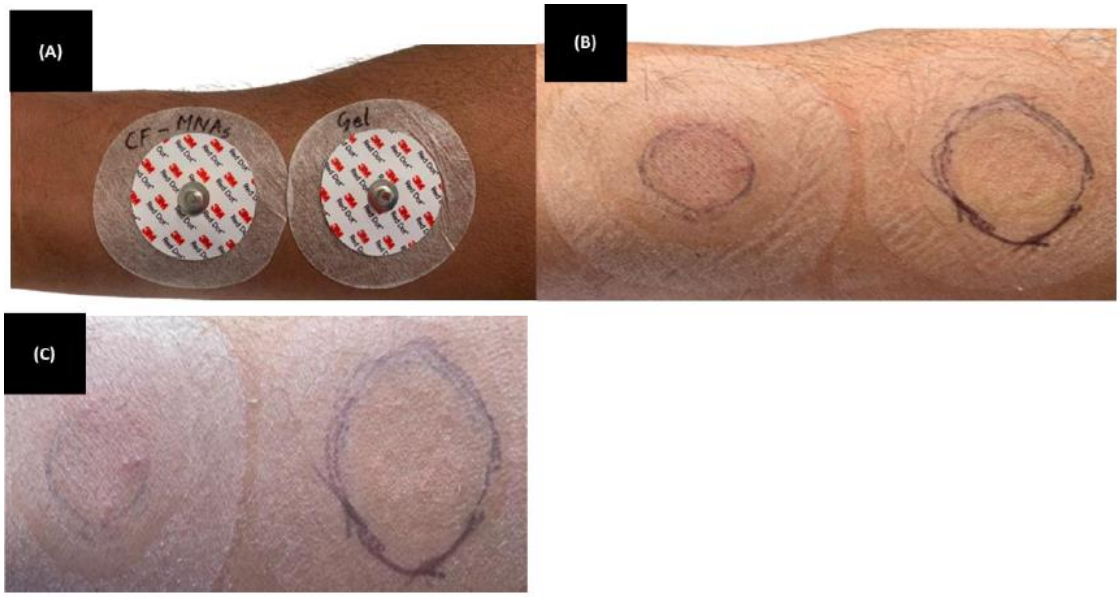


Figure S19. Illustration of skin irritation test analysis. (A) skin irritation test set-up conducted for 48 hours; (B) immediately after removal of electrode (left: CF-MN; right: gel electrode); (C) after 30 minutes (left: CF-MN; right: gel electrode).

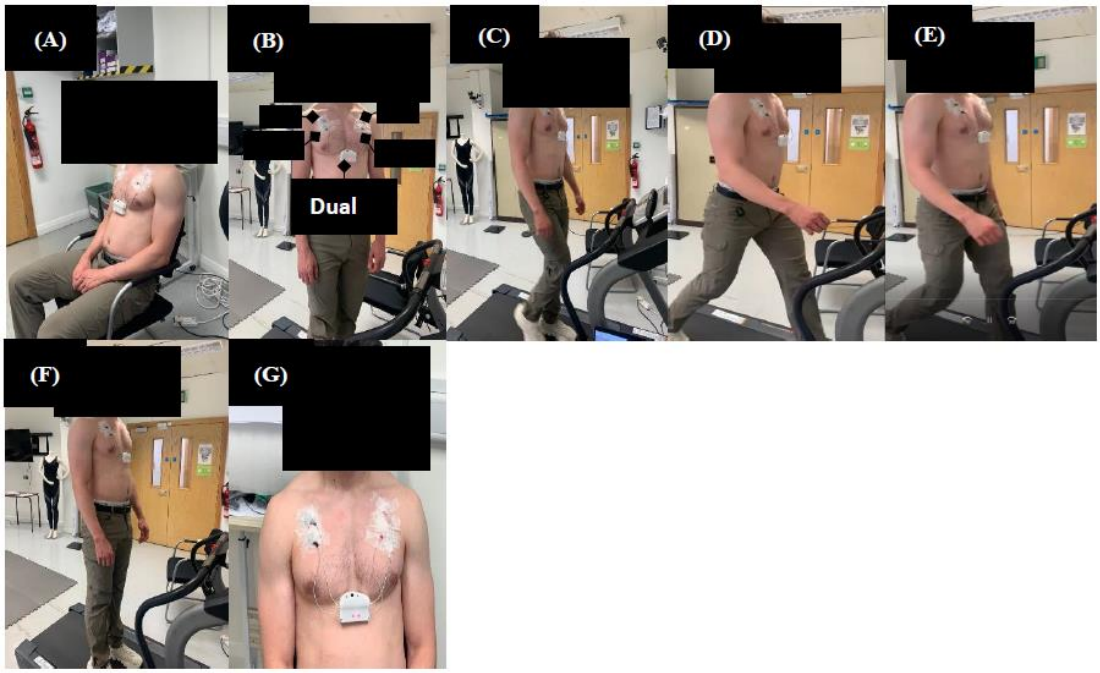


Figure S20. Distinct postures of a subject during the ECG data recording. (A) Sitting on a chair prior to exercise, (B) Subject's worn ECG monitoring device while standing on a treadmill before the exercise, (C) Posture of subject walking at 2 km/h, (D) Posture of the subject walking at 4 km/h, (E) Posture of the subject walking at 6 km/h, (F) Standing posture on the treadmill after exercise, (G) Sitting position of the subject after walking on treadmill.

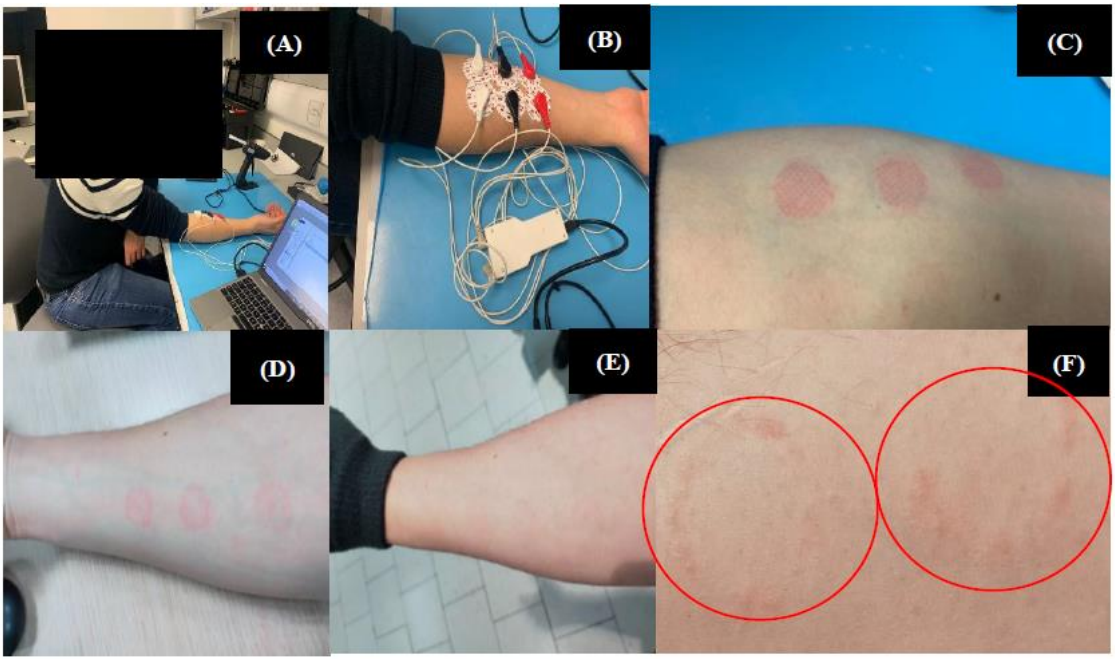


Figure S21. (A) Experiment set-up for EMG recording using gel and CF-MN electrodes, (B) Posture of the subject during EMG recording, (C) impression of MN and gel immediate after removal of electrodes, (D) impression of MN and gel after 30 minutes, (E) impression of MN and gel after 60 minutes, (F) erythema causes due to gel after more than an hour.

A.4 Journal Papers

1. O. Singh, **A. Bocchino**, D. Cherian, Y. Hu, M. J. Haslinger, D. Fechtig, I. Prinz, S. Brandstätter, P. Galvin, C. O'Mahony, "Quantitative Comparison of the Performance of Injection-Moulded Polymeric Microneedle Dry Electrodes and Traditional Gel Electrodes for ECG Signal Acquisition", Submitted to *IEEE Access*, March 2025.

2. **A. Bocchino**, C. Marquez-Grana, O. Singh, E. Melnik, S. Kurzhals, G. C. Mutinati, S. Coulman, C. Martin, K. W. Ng, M. Massufero Vergilio, J. Birchall, P. Donovan,

P. Galvin, C. O'Mahony, "A Multifunctional Platform for the Production and Customization of Polymer-Based Microneedle Devices", *Sensors and Actuators A: Physical*, **388**, 116491, July 2025.

DOI: 10.1016/j.sna.2025.116491

3. **A. Bocchino**, S. Teixeira, F. Barry, C. Thatte, A. Ryan, F. Rahman, Y. Hu, S. Iadanza, P. Galvin, S. Kurzhals, E. Melnik, G. C. Mutinati, P. Galvin, C. O'Mahony, "Strategies for Passivating Microneedle-based Sensors: Development, Characterization and Comparison", *Sensors and Actuators Reports*, **9**, 100328, June 2025.

   DOI: 10.1016/j.snr.2025.100328

4. F. Rahman, A. Ryan, **A. Bocchino**, P. Galvin, S. Teixeira, "Microneedle-Based Sensors for Ph and Sodium Detection", *Sensing and Bio-Sensing Research*, **48**, 100777, June 2025.

   DOI: 10.1016/j.sbsr.2025.100777

5. M. Sica, O. T. Varnosfaderani, C. Crowe, L. Kenny, **A. Bocchino**, B. O'Flynn, S. Mueller, S. Tedesco, S. Timmons, J. Barton, "Design of a multi-sensors wearable system for continuous home monitoring of people with Parkinson's", *IEEE Access*, **12**, pp. 38436-38455, March 2024.

   DOI: 10.1109/ACCESS.2024.3375871

6. O. Singh, **A. Bocchino**, T. Guillerm, Y. Hu, F. Stam, C. O'Mahony, "Flexible, Conductive Fabric-Backed, Microneedle Electrodes for Electrophysiological Monitoring", *Advanced Materials Technologies*, **9**, 3, December 2023.

DOI: 10.1002/admt.202301606

7. S. Kurzhals, E. Melnik. P. Plata, E. Cihan, P. Herzog, A. Felice, **A. Bocchino**, C. O'Mahony, G. C. Mutinati, R. Hainberger, "Detection of Lactate via Amperometric Sensors Modified With Direct Electron Transfer Enzyme Containing PEDOT:PSS and Hydrogel Inks", *IEEE Sensors Letters*, **7**, 9, September 2023.

DOI: 10.1109/LSENS.2023.3307066

8. C. O'Mahony, R. Sebastian, F. Tjulkins, D. Whelan, **A. Bocchino**, Y. Hu, J. O'Brien, J. Scully, M. Hegarty, A. Blake, I. Slimi, A. J. P. Clover, A. Lyness, A. M. Kelleher, "Hollow silicon microneedles, fabricated using combined wet and dry etching techniques, for transdermal delivery and diagnostics", *International Journal of Pharmaceutics*, **637**, 122888, April 2023.

DOI: 10.1016/j.ijpharm.2023.122888

9. A. J. Guillot, P. Merino, **A. Bocchino**, C.O'Mahony, R. Mª Giner, Mª Carmen Recio, T. M Garrigues and A. Meleroa, "Ultraflexible Lipid Vesicle and Microneedle-based Delivery of Cyanocobalamin Permeability through intact Skin", *European Journal of Pharmaceutics and Biopharmaceutics*, **177**, pp. 184-198, August 2022. DOI: 10.1016/j.ejpb.2022.06.015

10. C. Plamadeala, SR. Gosain, F. Hischen, B. Buchroithner, S. Puthukodan, J. Jacak, **A. Bocchino**, D. Whelan, C. O'Mahony, W. Baumgartner, J.Heitz, "Bio-inspired microneedle design for efficient drug/vaccine coating", *Biomedical Microdevices*, **22**, 8, December 2019.

DOI: 10.1007/s10544-019-0456-z

11. C. O'Mahony, **A. Bocchino**, M. J. Haslinger, S. Brandstätter, H. Außerhuber, K. Schossleitner, A. J. P. Clover, D. Fechtig, "Piezoelectric Inkjet Coating of Injection Moulded, Reservoir-Tipped Microneedle Arrays for Transdermal Delivery", *Journal of Micromechanics and Microengineering*, **29**, pp. 085004, August 2019.

DOI: 10.1088/1361-6439/ab222b

12. M. O'Sullivan, A. Temko, **A. Bocchino**, C. O'Mahony, G. Boylan, E. Popovici, "Analysis of a Low-Cost EEG Monitoring System and Dry Electrodes toward Clinical Use in the Neonatal ICU", *Sensors*, **19**, 11, June 2019.

DOI: 10.3390/s19112637

13. M. Leone, B. H. Van Oorschot, M. R. Nejadnik, **A. Bocchino**, M. Rosato, G. Kersten, C. O'Mahony, J. Bouwstra, K. Van Der Maaden, "Universal Applicator for Digital-Controlled Pressing Force and Impact Velocity Insertion of Microneedles into Skin", *Pharmaceutics*, **10**, 4, November 2018.

DOI: 10.3390/pharmaceutics10040211

[Published before starting the PhD]

14. C. O'Mahony, L. Hilliard, T. Kosch, **A. Bocchino**, E. Sulas, A. Kenthao, S. O' Callaghan, A. James, P. Clover, G. Bared, "Accuracy and Feasibility of Piezoelectric Inkjet Technology for Application in Microneedle-based Transdermal Delivery Applications", *Microelectronic Engineering*, **172**, pp. 19-25, March 2017.

    DOI: 10.1016/j.mee.2017.02.018

    [Published before starting the PhD]

A.5 Reviewed Conferences (Oral Presentation)

1. **A. Bocchino**, S. Teixeira, S. Iadanza, E. Melnik, S. Kurzhals, G. Mutinati, C. O'Mahony, "Development and Characterization of Passivation Methods for Microneedle-based Biosensors", *44th Annual International Conference of the IEEE Engineering in Medicine and Biology Society (EMBC 2022)*, Glasgow, Scotland, UK, July 11-15th 2022. (Oral Presentation).

    DOI: 10.1109/EMBC48229.2022.9871005

2. O. Singh, Y. Hu, **A. Bocchino**, T. Guillerm and C. O'Mahony, "Performance Assessment of Microneedle Dry and Wet Gel Electrodes Using a Dual-Channel, Single Lead Wearable ECG Device", *21st Mediterranean Electrotechnical Conference (IEEE MELECON 2022)*, Palermo, Italy, June 14-16th 2022.

    DOI: 10.1109/MELECON53508.2022.9843060

3. O. Singh, T. Guillerm, **A. Bocchino** and C. O'Mahony, " Design, Fabrication and Performance Assessment of Flexible, Microneedle–Based Electrodes For ECG Signal Monitoring", *44th Annual International Conference of the IEEE Engineering in Medicine and Biology Society (IEEE EMBC 2022)*, Glasgow, Scotland, July 11-15th 2022.

   DOI: 10.1109/EMBC48229.2022.9871073

4. C. O'Mahony, **A. Bocchino**, M.J. Haslinger, D. Fechtig, K. Schossleitner, P. Galvin and S. Brandstätter, "Characterisation of microneedle-based ECG electrodes fabricated using an industrial injection-moulding process", *MEMS 2019*, Seoul, South Korea, pp. 557-560, January 27-31st, 2019.

   DOI: 10.1109/MEMSYS.2019.8870721

5. M. O'Sullivan, E. Popovici, **A. Bocchino**, C. O'Mahony, G. Boylan and A. Temko, "System level framework for assessing the accuracy of neonatal EEG acquisition" *40th Annual International Conference of the IEEE Engineering in Medicine and Biology Society*, Hawaii, USA, July 17-21st 2018.

   DOI: 10.1109/EMBC.2018.8513246

   [Published before starting the PhD]

6. M. O'Sullivan, J. Poveda Pena, **A. Bocchino**, C. O'Mahony, D. Costello, E. Popovici and Andriy Temko, "Comparison of Electrode Technologies for Dry and Portable

EEG Acquisition", *7th IEEE International Workshop on Advances in Sensors and Interfaces (IWASI)*, Trieste, Italy, 15-16th June 2017.

DOI: 10.1109/IWASI.2017.7974202

[Published before starting the PhD]

7. C. O'Mahony, **A. Bocchino**, E. Sulas, A. Ciarlone, G. Giannoni, S. O'Callaghan, A. Kenthao, A. J. P. Clover, P. Galvin and K. Grygoryev, "Embedded Sensors for Micro Transdermal Interface Platforms (MicroTIPs)", *2016 Symposium on Design, Test, Integration and Packaging of MEMS/MOEMS (DTIP)*, Budapest, Hungary, 30th May- 2nd June 2016.

   DOI: 10.1109/DTIP.2016.7514859

   [Published before starting the PhD]

A.6 Invention Disclosure Forms

1. IDF UCC-21-069: Combined Hollow and Solid Microneedle Device for Drug Delivery and Sensing. C. O'Mahony, **A. Bocchino**, R. Sebastian. 18th January 2021.

A.7 Patents and Licenses

1. *US Patent Application 63/542, 655*, filed October 5th 2023: Needle Arrays, Wearable Medicament Delivery Devices, And Methods Of Medicament Delivery Utilizing Sensing Microneedles. A. Lyness, C. O'Mahony, C. Webster, B. Yan, L. Magara, **A. Bocchino**, R. Sebastian, and F. Tjulkins

This technology was licensed to West Pharmaceuticals, a multinational American company, technology agreement reference LOA 22-034. This achievement was recognised with the University College Cork License of the Year Award (see below).

A.8 Awards

1. *Wrixon Research Excellence Bursary 2024*, recipient: **A. Bocchino**. Cork, November 2024.

2. Shortlisted finalist for Innovation at the *EARTO Innovation Awards 2024*, nominees: **MicroTIPs team**. Brussels, October 2024.

3. License of the Year Award, *UCC Research & Innovation Awards 2023*, Winners: C. O'Mahony, C. Webster, **A. Bocchino**, R. Sebastian, F. Tjulkins. Cork, May 2024.

4. Shortlisted finalist for 'Collaboration in Medtech' at the *Irish Medtech Awards 2023*, nominees: **Tyndall National Institute** and West Pharmaceutical Services.

5. Collaboration Achievement Award, *Irish Laboratory Awards 2018*. Winners: M. O'Sullivan, E. Popovici, A. Temko, C. O'Mahony, **A. Bocchino**. Dublin, April 2018. [Obtained before starting the PhD]

A.9 Posters (Oral Presentation)

1. A. Attiguppe, C. MV, R. Sebastian, **A. Bocchino**, A. Bußmann, O. Zett, C. Gärtner, E. Töpfer, J. Redmond, K. Carroll, D. Scaini, J. L. Pedraz, S. R. Alonso, C. O'Mahony, "Development of a smart lid system for next-generation skin-on-chip platforms", *Microfluidic Workshop 2025*, Dublin, Ireland, 20-21st March 2025.

2. **A. Bocchino**, S. Teixeira, S. Iadanza, E. Melnik, S. Kurzhals, P. Plata, G. Mutinati, C. O'Mahony, "Passivating microneedle-based biosensors: strategies, characterization and application", *Microneedles 2023*, Seattle, USA, 15-17th May 2023.

3. O. Singh, T. Guillerm, **A. Bocchino**, C. O'Mahony, "High quality EMG signal measurement from Lower back muscle using dry microneedle electrodes", *Microneedles 2023*, Seattle, USA, 15-17th May 2023.

4. **A. Bocchino**, S. Teixeira, E. Melnik, S. Kurzhals, G. Mutinati, C. O'Mahony, "Microneedle-based Biosensors: Comparison of Passivation Strategies", *European Technology Platform on Nanomedicine (ETPN 2022)*, Braga, Portugal, 20-23rd July 2022.

5. S. R. Teixeira, T. Guillerm, R. Sebastian, Y. Hu, **A. Bocchino**, S. Krishnamorthy and C. O'Mahony, "Microneedle Arrays for Enhanced Light Transmission through Skin", *44th Annual International Conference of the IEEE Engineering in Medicine and Biology Society (IEEE EMBC 2022)*, Glasgow, Scotland, 11-15th July 2022.

6. O. Singh, T. Guillerm, **A. Bocchino** and C. O'Mahony, "Design And Fabrication Of Microneedle–Based Electrodes With Flexible Surface For ECG Signal Monitoring", *Bioengineering in Ireland (BINI 2022),* Galway, Ireland, 20-21st May 2022.

7. **A. Bocchino**, S. Teixeira, E. Melnik, S. Kurzhals, G. Mutinati and C. O'Mahony, "Passivation Strategies for Microneedle-Based Biosensors", *Bioengineering in Ireland (BINI 2022),* Galway, 20-21st May 2022. (Oral Presentation).

8. R. Sebastian, I. Slimi, **A. Bocchino**, F. Tjulkins, A. James P. Clover and C. O'Mahony, "Microneedle and Micropump Systems For Interstitial Fluid Sampling", *Perspectives in Percutaneous Penetration (PPP 2022)*, La Grande Motte, France, April 19-22nd 2022.

9. D. M. E. Freeman, E. Melnik, S. Kurzhals, A. Felice, P. Herzog, **A. Bocchino**, C. O'Mahony, C. Brinkmann, W. Bloch, G. C. Mutinati, Rainer Hainberger, Tony Cass "ELSAH Patch: A Microneedle Biosensor for Continuous Glucose and Lactate Detection", *Sensors in Medicine 2021*, online, 8-12th November 2021.

10. S. Kurzhals, E. Melnik, P. Plata, E. Cihan, C. Derntl, A. Felice, P. Herzog, **A. Bocchino**, C. O'Mahony, G. Mutinati and R. Hainberger, "Towards an electronic smart patch for glucose and lactate monitoring", *Swiss Symposium in Point-of-Care Diagnostics 2021*, Davos, 21st October 2021.

11. E. Melnik, S. Kurzhals, P. Plata, E. Cihan, C. Derntl, A. Felice, P. Herzog, **A. Bocchino**, C. O'Mahony, G. Mutinati and R. Hainberger, "Novel surface modification of platinum microneedle sensors for interference-less detection of glucose and lactate", Point-of-Care, *Biosensors & Mobile Diagnostics Europe 2021*, Rotterdam, 28th-30th June 2021.

12. J. Heitz, C. Plamadeala, W. Baumgartner, F. Hischen, J. Jacak, B. Buchroithner, C. O'Mahony, **A. Bocchino** and B. Heise, "Laser-induced and laser-fabricated drop-shaped microstructures for directional fluid transport", paper H.6a.8, *E-MRS 2021 Spring Meeting*, Online, May 31- June 4th, 2021.

13. **A. Bocchino**, J. Madden, C. Robinson, S. Teixeira, A. O'Riordan, P. Galvin, C. O'Mahony, "Scalable micromoulding process for microneedles-based diagnostics", *Microneedles 2020*, Online, 10-11th November 2020.

14. R. Kern, T. Chuang, S. Schork, C. O'Mahony, **A. Bocchino**, A. Ernst, "Reliable microneedle coating with a non-contact and drop-on-demand nano dispensing technology", *SLAS 2020*, San Diego, 25-29th January 2020.

15. C. Plamadeala, S.R. Gosain, F. Hischen, B. Buchroithner, S. Puthukodan, J. Jacak, **A. Bocchino**, D. Whelan, C. O'Mahony, W. Baumgartner and J. Heitz, "Bio-inspired

microneedles for efficient drug/vaccine coating made by 2-PP", *Medical 3D-Printing and Innovative Technologies,* Vienna, Austria, 6-7th December 2019.

16. **A. Bocchino**, C. Robinson, J. Madden, S. Teixeira, A. O'Riordan, P. Galvin and C. O'Mahony, "A scalable, double-sided micromoulding process with enhanced electrical functionality for microneedle-based diagnostics", *Polymer Replication at the Nanoscale,* Dublin, Ireland, May 9-10th 2019.

A.10 Posters before PhD (Oral Presentation)

1. M. O'Sullivan, E. Popovici, **A. Bocchino**, C. O'Mahony, and A. Temko, "Comparative assessment of microneedle electrodes for use in EEG applications" *Microneedles 2018,* Vancouver, Canada, May 28-June 1st 2018.

2. **A. Bocchino**, C. Robinson, J. Madden, A. O'Riordan, P. Galvin and C.O'Mahony, "A scalable, double-sided micromoulding process with enhanced electrical functionality for microneedle-based sensing and diagnostics", *Microneedles 2018,* Vancouver, Canada, May 28-June 1st 2018.

3. C. O'Mahony, **A. Bocchino**, M. Rosato, R. Lembo, D. Cocco, S. O'Callaghan, D. Demarchi, A. J. P. Clover and P.Galvin, "MicroTIPs - Micro Transdermal Interface Platforms for wearable drug delivery and diagnostics", *Microneedles 2018,* Vancouver, Canada, May 28-June 1st 2018.

4. C. O'Mahony, **A. Bocchino**, M. J. Haslinger, V. M. Reddy, S. Brandstätter, A. J. P. Clover, and D. Fechtig, "Piezoelectric filling of reservoir-tipped, injection-

moulded microneedle arrays", *Microneedles 2018*, Vancouver, Canada, May 28-June 1st 2018.

5. **A. Bocchino**, M. Taj-Eldin, K. Grygoryev, P. Galvin and C. O'Mahony, "Microneedle-based 'dry electrodes' for ECG monitoring", *Microneedles 2018*, Vancouver, Canada, May 28-June 1st 2018.

6. **A. Bocchino**, M. Taj-Eldin, P. Galvin and C. O´Mahony, "Microneedle-based ECG Monitoring – Part 1: Dry Electrodes", *Design of Medical Devices Europe (DMD Europe 2017),* Eindhoven, Netherlands, 14-15th November 2017. (Oral Presentation).

7. M. Taj-Eldin, **A. Bocchino**, P. Galvin and C. O´Mahony, "Microneedle-based ECG Monitoring – Part 2: A Wearable System", *Design of Medical Devices Europe (DMD Europe 2017),* Eindhoven, Netherlands, 14-15th November 2017.

8. C. O'Mahony, **A. Bocchino**, R. Lembo, D. Coco, S. O'Callaghan, P. Vazquez, R. Houlihan, A. O'Riordan, A. J. P. Clover, T. Moore, D. Demarchi and P. Galvin, "Breaking Barriers: Wearable Micro Transdermal Interface Platforms (MicroTIPs) for Transdermal Delivery and Diagnostics", *Design of Medical Devices Europe (DMD Europe 2017),* Eindhoven, Netherlands, 14-15th November 2017.

9. M. J. Haslinger, V. M. Reddy, H. Außerhuber, A. Fuchsbauer, **A. Bocchino**, S. Brandstätter, C. O´Mahony and D. Fechtig, "3D printed Micro Needles for Drug delivery and sensor applications", *43rd International Conference on Micro and NanoEngineering (MNE 2017),* Braga, Portugal, 18th-22nd September 2017.

10. M. J. Haslinger, V. M. Reddy, H. Außerhuber, **A. Bocchino**, C. O´Mahony and D. Fechtig, "3D printed Micro Needles for Drug delivery", *8th International Congress in Nanotechnology in Biology & Medicine,* Krems, Austria, 20-22nd March 2017.

11. **A. Bocchino**, M. Taj-Eldin, D. Cocco, P. Galvin, C. O'Mahony, "Ambulatory System for Monitoring and Detection of ECG Arrthymias", *Insight augmented human demonstrator event*, Dublin, 23 March 2017.

12. **A. Bocchino**, k. Grygoryev, A. Ciarlone, G. Giannonui, A. Kenthao, P. Galvin, C. O'Mahony, "Microneedles-based Dry Electrodes for ECG Monitoring", *Workshop on wearable and implantable antennas and propagation*, ECIT Institute, Belfast, UK, 16th March 2017.

13. S. O'Callaghan, L. Hilliard, T. Kosch, **A. Bocchino**, E. Sulas, A. Kenthao, A. J. Clover, G. Bared and C. O'Mahony, "Piezoelectric Inkjet Coating of Silicon and Polymer Microneedles", *Micromechanics Europe 2016*, Cork, Ireland, August 28-30th 2016.

14. C. O'Mahony, **A. Bocchino**, E. Sulas, A. Ciarlone, G. Giannoni, S. O'Callaghan, A. Kenthao, A. J. P. Clover, P. Galvin and K. Grygoryev, "Towards Intelligent Micro Transdermal Interface Platforms (MicroTIPs)", *Third International Conference on Microneedles (Microneedles 2016),* London, England, May 23-25th 2016.

15. C. O'Mahony, L. Hilliard, T. Kosch, **A. Bocchino**, E. Sulas, A. Kenthao, S. O'Callaghan, A. J. P. Clover and G. Bared, "Accuracy and Feasibility of Piezoelectric Inkjet Technologies for Microneedle Coating Applications", *Third International Conference on Microneedles (Microneedles 2016)*, London, England, May 23-25th 2016.